Kazuyoshi Takayama
Ozer Igra *Editors*

Frontiers of Shock Wave Research

Springer

Frontiers of Shock Wave Research

Kazuyoshi Takayama · Ozer Igra
Editors

Frontiers of Shock Wave Research

Published in celebration of the One-Hundred Year Birthday
of Professor Akira Sakurai

Springer

Editors
Kazuyoshi Takayama
Sendai, Japan

Ozer Igra
Metar, Israel

ISBN 978-3-030-90734-1 ISBN 978-3-030-90735-8 (eBook)
https://doi.org/10.1007/978-3-030-90735-8

© The Editor(s) (if applicable) and The Author(s), under exclusive license to Springer Nature Switzerland AG 2022
This work is subject to copyright. All rights are solely and exclusively licensed by the Publisher, whether the whole or part of the material is concerned, specifically the rights of translation, reprinting, reuse of illustrations, recitation, broadcasting, reproduction on microfilms or in any other physical way, and transmission or information storage and retrieval, electronic adaptation, computer software, or by similar or dissimilar methodology now known or hereafter developed.
The use of general descriptive names, registered names, trademarks, service marks, etc. in this publication does not imply, even in the absence of a specific statement, that such names are exempt from the relevant protective laws and regulations and therefore free for general use.
The publisher, the authors and the editors are safe to assume that the advice and information in this book are believed to be true and accurate at the date of publication. Neither the publisher nor the authors or the editors give a warranty, expressed or implied, with respect to the material contained herein or for any errors or omissions that may have been made. The publisher remains neutral with regard to jurisdictional claims in published maps and institutional affiliations.

This Springer imprint is published by the registered company Springer Nature Switzerland AG
The registered company address is: Gewerbestrasse 11, 6330 Cham, Switzerland

Preface

This monograph is published for the one-hundred years of Professor Akira Sakurai, born on April 27th 1921. International shock wave researchers who know him well wish to mark this memorable opportunity and publish their works in the present book. Professor Akira Sakurai served in Tokyo Denki University from 1948 to 1991. During his long career, he contributed immensely to international shock wave research. In 1995 he initiated the First International Workshop on Shock Vortex Interaction in Tokyo. The second one was held in 1997 at Zao and since then this workshop has been held biannually in various cities. Meantime, due to addition of relevant topics in shock wave research, the name was changed to the International Symposium of Shock Wave Interaction and at the same time, this workshop merged with the Mach Reflection Symposium, which was initialed in 1981 by Professor John Dewey and held at Victoria, Vancouver Island, Canada. This Symposium boosted support for the International Shock Wave Symposium, thereby widening the shock wave research area.

Therefore, we are very pleased to express our celebration and thanks on the one-hundred year birthday of Professor Sakurai, a pioneer in shock wave research.

Sendai, Japan — Kazuyoshi Takayama
Metar, Israel — Ozer Igra

Contents

My Walk in the Field of Shock Waves 1
Ozer Igra

My Adventure with Mach Reflection—A Tribute to Professor Sakurai 21
Zbigniew A. Walenta

The Background of My Studies of Shock and Blast Waves 33
John M. Dewey

Research Activities at the Wisconsin Shock Tube Laboratory 57
Riccardo Bonazza

Flow Formation Around a Body in the Area of Interference of Two Blast Waves 83
Irina V. Krassovskaya

Interaction of Small Scale Blast Waves with a Sphere, Cones, and an Ellipsoid 97
Kazuyoshi Takayama and Koji Tamai

Mach Waves Occurring Over a Backward Facing Edge in Supersonic Flow 109
V. Sridhar, F. Seiler, R. Hruschka, H. Kleine, S. Gai, and J. Srulijes

Medical Application of Miniaturized Underwater Shock Wave Focusing 133
Hiroaki Yamamoto and Kazuyoshi Takayama

Experimental Demonstration on High-Speed Gas Gun Driven by a Gaseous Detonation 147
Shinichi Maeda and Tetsuro Obara

Shock Interactions with Solid Objects; from Simple to Complex Geometries 161
Charles E. Needham

Experimental Study of Generation and Mitigation of Weak Shock Waves Induced in Intake and Exhaust Pipe Lines of Automobile Engines 175
Noriaki Sekine

Equation of State for Water Based on the Shock Hugoniot Data 201
Kunihito Nagayama

General Solution of the 2D Navier–Stokes Equations and Its Application to Shock Wave Problems 213
Akira Sakurai and Susumu Kobayashi

My Walk in the Field of Shock Waves

Ozer Igra

I entered the shock waves field in Aug. 1967 when I was accepted as a Ph.D. student at the Institute for Aerospace Studies, University of Toronto, Canada. My theses supervisor was the famous scientist Professor I. I. Glass. My knowledge in gasdynamic and especially in shock waves was almost zero. The Ph.D. research work assigned for me by my supervisor was to develop a reliable way for evaluating the recombination rate constant of ionized Argon, K_R. At that time the available data regarding K_R for Argon was to accuracy of $\pm$ 400 percent! The novel way for measuring the recombination rate constant of ionized Argon was to use a shock tube in which the driven section will contain diluted Argon. A very strong shock wave will be sent into the Argon gas and thereby raising the post shock temperature to very high level; over 9,000 °K. At such temperature, significant amount of the Argon is ionized. Generating such flow conditions was possible in the 4 by 7 inch shock tube; its photo is given in Fig. 1.

A wedge having 15° expansion was installed inside the shock tube test section; a schematic description of the expansion wedge and the expansion wave is given in Fig. 2. The required ionized Argon flow over the 15-degrees expansion corner was generated by normal shock waves having the following ranges: shock Mach numbers $13 \leq M \leq 18$; electron number densities $10^{16} \leq n_e \leq 10^{17\,\text{cm}^{-3}}$ electron temperatures $9{,}000 \leq \text{Te} \leq 12{,}000$ °K. The initial (pre shock) channel pressure was $1 \leq p_i \leq 10$ Torr and the initial temperature $T_0 \approx 300$ °K.

Experiments were conducted using a Mach–Zehnder interferometer having a nine inch diameter field of view. The interferometer had a dual frequency laser light source. Typical interferograms are shown in Figs. 3 and 4. In Fig. 3 the relaxation zone prevailing behind the strong incident shock wave is shown; in Fig. 4 the expansion of the ionized Argon plasma is exhibited. In the experimental range of electron density and temperature prevailing behind the strong incident shock wave, the dominant recombination process is due to the three-body, electron–ion-electron collisions.

O. Igra (✉)
Department of Mechanical Engineering, Ben Gurion University, Jerusalem, Israel

© The Author(s), under exclusive license to Springer Nature Switzerland AG 2022

K. Takayama and O. Igra (eds.), *Frontiers of Shock Wave Research*,
https://doi.org/10.1007/978-3-030-90735-8_1

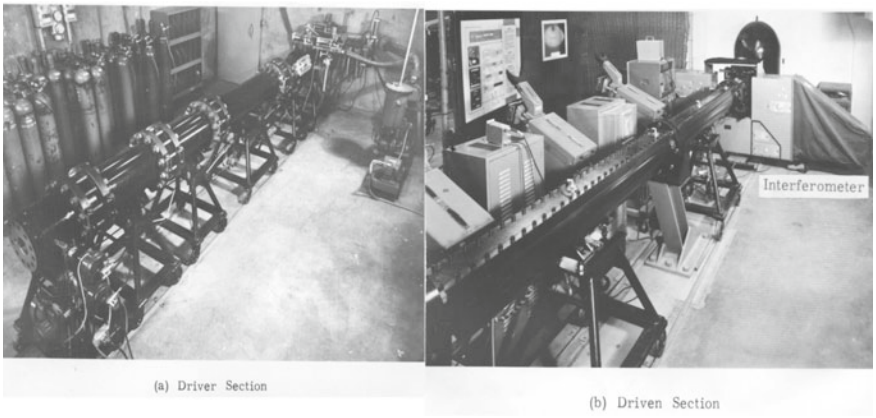

(a) Driver Section

(b) Driven Section

Fig. 1 Photo of the 4 × 7 inches UTIAS shock tube

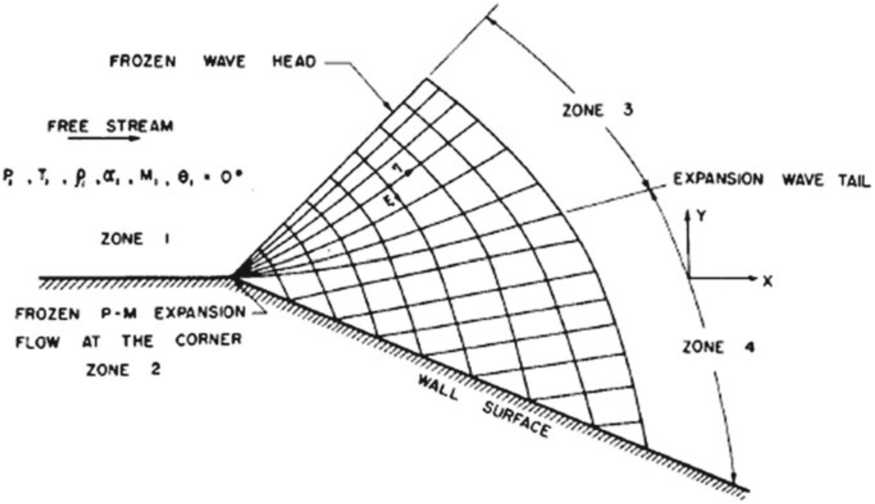

Fig. 2 Schematic diagram of characteristic net for a corner- expansion flow

That is:

$$\mathrm{A} + \mathrm{e} \underset{K_\mathrm{R}}{\overset{K_\mathrm{I}}{\longleftrightarrow}} \mathrm{A}^+ + \mathrm{e} + \mathrm{e}$$

where A is a neutral Argon atom, A^+ an Argon ion, e an electron, K_I, the ionization rate constant, and K_R the recombination rate constant.

The rate equation for the production of electrons is expressed by $\frac{\mathrm{d}n_\mathrm{e}}{\mathrm{d}t} = K_\mathrm{I} n_\mathrm{a} n_\mathrm{e} - K_\mathrm{R} n_\mathrm{e}^3$.

where, n_a and n_e are number densities of neutral atoms and electrons, respectively.

Fig. 3 Relaxation zone behind strong shock wave in Argon. P1 = 1.83 torr, T1 = 296.1 K and Ms = 19.05

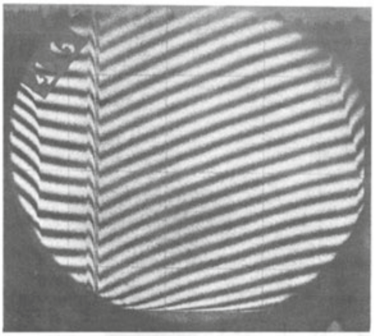

(a) λ = 10,600 Å

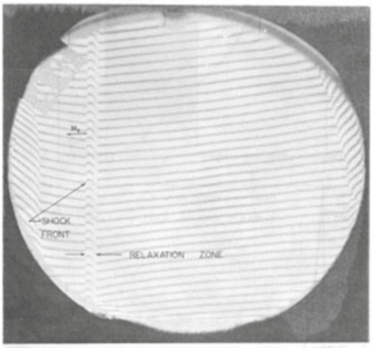

(b) λ = 5,300 Å

The used light source, a laser, provides a giant pulse (–30 MW) and very short exposure times (15–30 ns); it had two different wave's lengths; 6943 Å and 3471.5 Å. From two simultaneously taken interferograms the total plasma density ρ, and the degree of ionization α, or the electron number density, n_e, were evaluated. Detailed

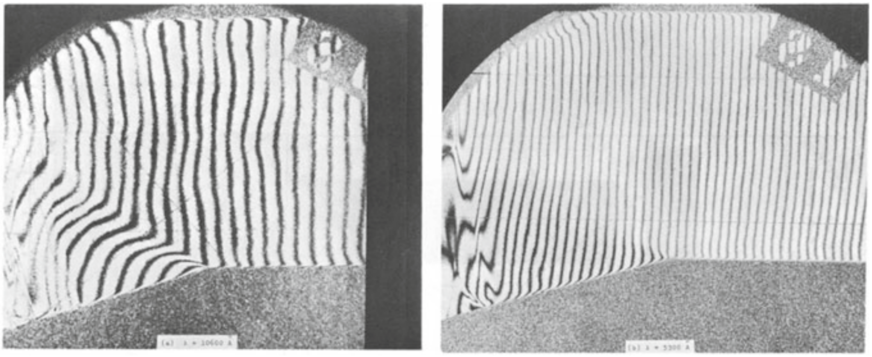

Fig. 4 Interferograms of expansion Argon plasma. P1 = 8.60 torr, T1 = 298.2 K and Ms = 13.3 taken with two different light's wave lengths

Fig. 5 Recombination rate constant variations, for a three-body collision, versus temperature

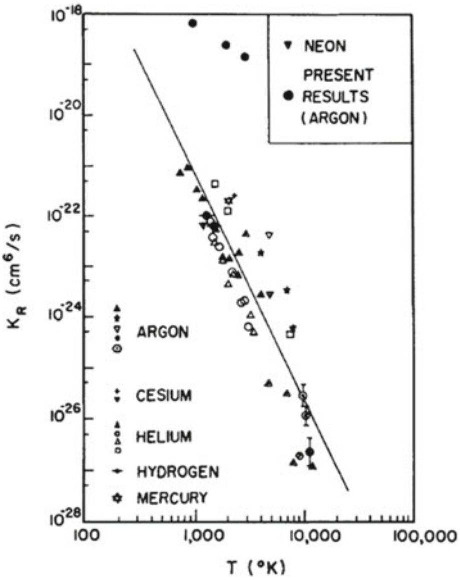

results are available in Igra and Glass [1]. Based on these findings, finally the recombination rate constant was evaluated. The obtained results are shown in Fig. 5 where results of other experimenters are also plotted.

Upon completing my Ph.D. studies I returned to Israel and I Joint the newly established Ben Gurion University. My first efforts were centered on building a respectable shock tube laboratory. At that time I was the only person among the academic staff who knows what is a shock wave or, a shock tube and therefore, could not expect any advice/support; not to mention the symbolic financial support I received from my university for this project. It is not surprising that the first shock tube in the present Shock Wave Laboratory in the Ben Gurion University was built using available material. For the driver an old British cannon from the Second World War was used, see in Fig. 6. Being a canon it was planned to be operated either by firing a piston toward the metal diaphragm separating between the driver and the driven sections of the shock tube, or just generating the required high pressure by simply exploding the explosive powder in a bullet free shell. The high pressure, generated between the moving piston and the metal diaphragm will decelerate the piston and will break/open the metal diaphragm. Once the diaphragm opened, a shock wave is transmitted into the shock tube driven section. Details describing the design of this piston driven shock tube appear in [2]. A general view of the piston driven shock tube appears in Fig. 7.

It took about 3 years to make this shock tube operational. However, for conducting experiments one needs, in addition to the shock tube, additional facilities; such as recorders, optical diagnostics, pressure gauges etc. Lack of support for purchasing such basic facilities further expanded the time needed for turning the newly build shock tube useful. It became fully operational only in the early nineties. The present

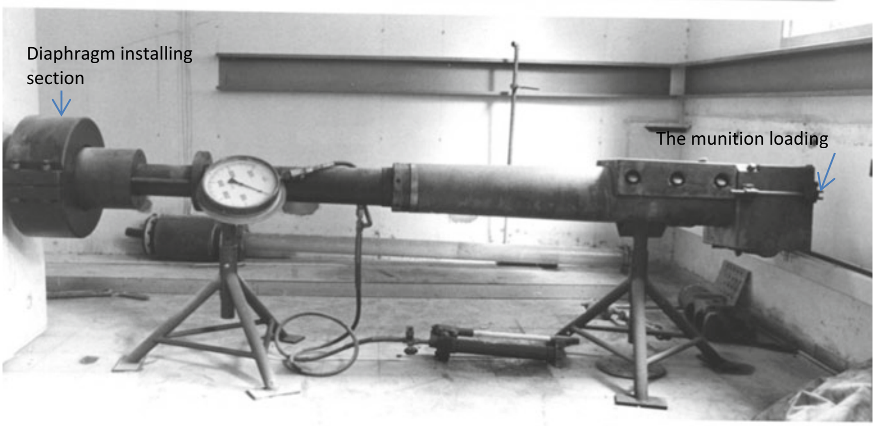

Fig. 6 The 25 lb British cannon that was modified to be used as the shock tube driver

shock tube laboratory, whose humble start is shown in Figs. 6 and 7 contains 6 different shock tubes three of the six are seen in Fig. 8. A brief description of these shock tubes is summarized in the following table.

But time was not wasted; in parallel to bringing the shock tube to be operational I used my connection with colleagues around the world for conducting joint research works. In the following my cooperation with the Shock Waves Laboratory in the institute of Fluids Science, Tohoku University, Japan; in the Ernst Mach Institute in Freiburg, Germany and with the Shock Tube Laboratory, IUSTI-CNRS, in Aix-Marseille Universit´e, Marseille, France is briefly described.

The BGU Shock Tube Laboratory consists of the following six shock tubes:

Shock tube	Cross-section [mm × mm]	Driver length [m]	Driven length [m]	Driver/driven separation	Vacuum Sealed?	Shock mach number range
ST-I[a]	80 × 80	2	3.6	Mylar diaphragm	Yes	$1 < M_S \leq 6$
ST-II	80 × 80	2	3.5	Mylar diaphragm	No	$1 < M_S \leq 2$
ST-III	56 × 56	2	3	Fast valve	No	$1 < M_S \leq 2.5$
ST-IV	32 × 32	1.8	3	Fast valve	No	$1 < M_S \leq 2$
ST-V[b]	31 × 31	1	2	Mylar diaphragm	No	$1 < M_S \leq 1.4$
ST-VI[c]	200	2	10	Mylar diaphragm	No	$1 < M_S \leq 2$

[a] This is a vertical shock tube

[b] The test section of this shock tube is transparent

[c] The cross section of this shock tube is round. The walls of all the shock tubes are equipped with numerous flush-mounted piezoelectric pressure transducers (PCB, Kistler, Endevco) that are used for both pressure history and shock wave velocity measurements and triggering purposes. Schlieren and shadowgraph photography methods are used to record the various shock wave related phenomena. High-speed photography is applied using a shutterless rotating-prism camera (Vivitro Hi-Spin) that is coupled with the following lasers: I. A 25-Watt Nd:YAG frequency doubled laser, which can be pulsed at intervals of about 20 to 200 μs. II. A 1-Watt Nd:YAG frequency doubled laser, which can be pulsed at intervals of about 10 to 200 μs or operated in a continues mode. III. A 2-Watt copper-vapor laser, which can be pulsed at intervals of about 100 μs

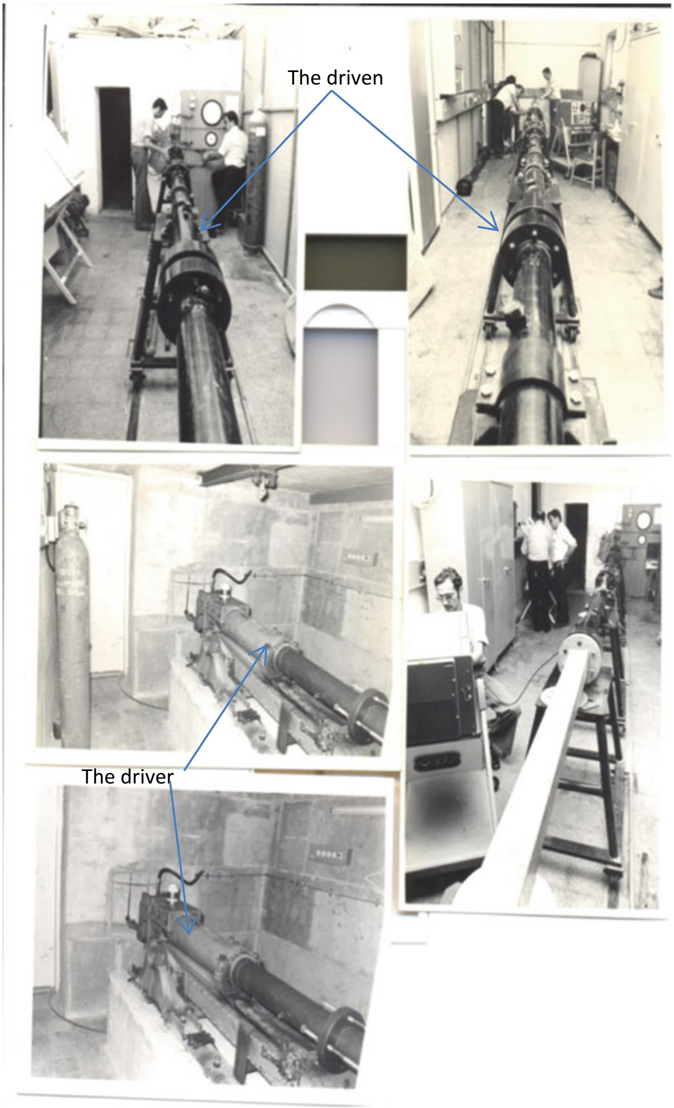

Fig. 7 The piston driven shock tube

With Professor K. Takayama from the institute of Fluids Science, Tohoku University, Japan the following topics were investigated: Experimental study checking the influence of surface roughness on the transition from regular to Mach reflection in pseudo-steady flows [3]; shock tube investigation of the drag coefficient of a sphere in a nonstationary flow [4] and experimental and theoretical studies of shock wave propagation through double-bend ducts [5]. In the following some highlights/results from this cooperation is briefly presented. In [3] the effect of the wedge surface

Fig. 8 Photo showing 3 out of 6 different shock tubes in the shock tube laboratory of the Dept. Mech. Eng., Ben Gurion University

roughness on the transition from regular reflection (RR) to Mach reflection (MR) in pseudo-steady flows was investigated both experimentally and analytically. A model for predicting the RR ↔ MR transition in the (M_i, θ_w)-plane was developed (M_i is the incident shock wave Mach number and θ_w, is the reflecting wedge angle). Its validity was checked against experimental results. Summary of obtained results are shown in Fig. 9.

Another fruitful cooperation with Professor Takayama was in evaluating the drag coefficient of a sphere in a non-steady flow. While variations in the drag coefficient of a sphere as function of Reynolds number, in a steady flow is well known and it appears in textbooks, there was no reliable information regarding its magnitude in a non-steady flow. In order to offer a reliable estimate for the Sphere's drag coefficient in a non-steady flow the following experiments were conducted. A small sphere or a few small spheres of different diameters were placed on the floor of the shock tube test-section. Their motion, induced by the passing incident shock wave was recorded and from the available sphere's trajectories the appropriate sphere's drag coefficient was evaluated; for details see in Ref. 4. As is apparent from Fig. 10 there is a significant difference between the drag coefficient in a steady and a non-steady flows.

A third joint research work conducted with Professor Takayama was studying shock wave propagation inside a double-bent duct. The aim of this work was evaluating the efficiency in using such geometry for reaching quick shock attenuation. For investigating the effect played by the duct's wall roughness, experiments were conducted by using two similar models. One had a smooth surface while the second had a very rough surface. A sample of recorded interferograms, obtained for the smooth surface duct is shown in Fig. 11a. In Fig. 11b, results obtained while using the rough surface duct are shown. A detailed description of this research is available in [5]. It is clear from Fig. 11 that the conducted simulations accurately reconstructed the recorded wave patterns. Based on this good agreement we were able to compute the pressure distribution inside the duct for the two cases, smooth and rough duct's walls. Obtained results are shown in Fig. 12.

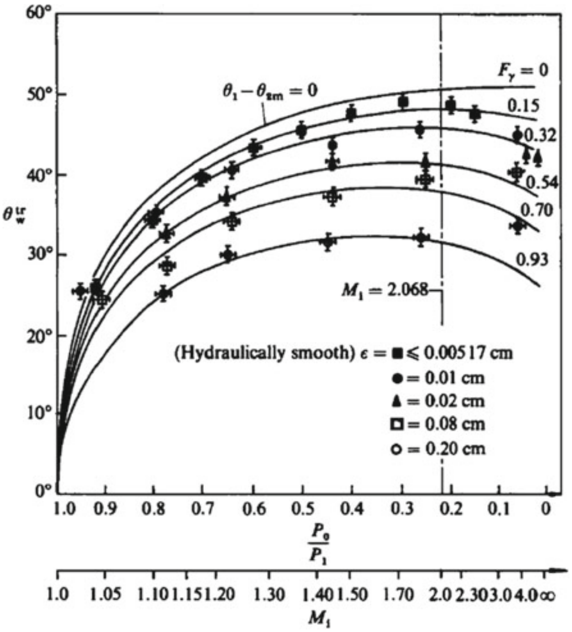

Fig. 9 The experimental results as well as the prediction of the present model for the RR $\rightleftarrows$ MR transition over rough wedges

It is apparent from Fig. 12 that a lower pressure is reached, at the duct exit, in the smooth surface case. This is expected, as in the rough surface case shock waves are generated at every collision of the transmitted shock wave with the steps (roughness) along its way.

I had also a fruitful cooperation with Professor Reichenbach, Drs. Heilig and Amann from the Ernst Mach Institute in Freiburg, Germany covering the following topics: An experimental and numerical study of shock wave diffraction into a square cavity [6], uni-axial strain loading of a rubber rod by planar shock waves [7], numerical simulation of the starting flow in a wedge-like nozzle [8], numerical and experimental study of shock wave propagation in a branched duct [9] and blast wave reflection from wedges [10].

Example for a research conducted jointly in three different countries is the one discussed earlier and summarized in the paper: Experimental and theoretical studies of shock wave propagation through double-bend ducts [5]. In this research the propagation of a shock wave through a double-bend duct was investigated experimentally (in Japan and in Germany) and numerically (in Israel). The German contribution, not seen in Figs. 11 and 12, checked the shock attenuation when the double bent duct had an expansion chamber as shown in Fig. 13; details in [9].

Another joint research conducted with the Ernst Mach group was investigating the starting process of the flow in a wedge-like expansion nozzle of a shock tunnel. Based on the experimental findings conducted at the Ernst Mach Institute (shadowgraphs),

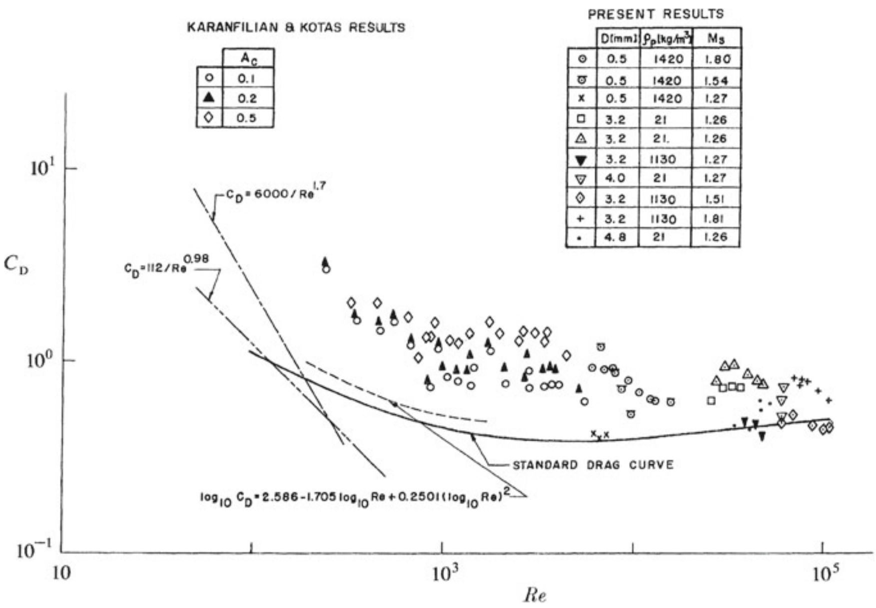

Fig. 10 The sphere drag coefficient versus Reynolds number

the flow was simulated using an un-split 2-D GRP scheme on an unstructured grid [8]. As shown in Fig. 14 the simulated pattern of reflected and transmitted shock waves in the nozzle inlet region and inside the nozzle is found to agree well with the experimental data.

Another joint research activity conducted with the Ernst Mach institute was studying blast wave reflection from wedges [10].

While a lot of attention was given to shock wave reflections from wedges, only little work was published regarding the similar case of blast wave reflection from wedges. In our joint research this subject was studied experimentally and theoretically/numerically.

Experiments where conducted in a specially arranged shock tube (detailed in [10]), a wedge was placed inside the shock tube test section, see in Fig. 15 and pressures where recorded along the wedge surface and the shock tube walls.

Typical results are shown in Fig. 16. It is apparent that the geometry of the reflected wave pattern is similar in the two cases when both incident waves have the same initial pressure jump across their fronts. However, different reflected pressure signatures (history) are observed in these two cases. The pressures obtained behind a reflected shock wave are always higher than those obtained behind the corresponding similar blast wave. In the considered case differences as high as 17% were observed, see Fig. 16.

The third research group with whom I had intensive cooperation included Dr. Lazhar Houas, Dr. Georges Jourdan and their graduate students, from the Shock

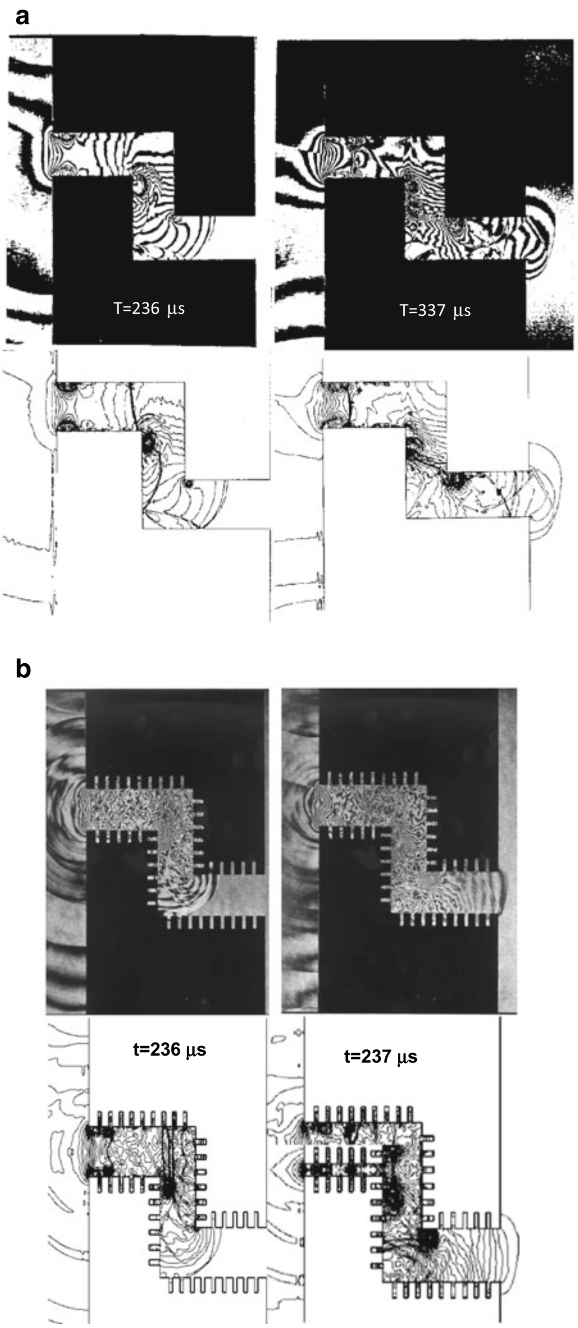

Fig. 11 **a** Shock wave propagation inside a smooth surface, double bent duct; recorded interferograms and its simulations. **b** Shock wave propagation inside a roughed surface, double bent duct; recorded interferograms and its simulations

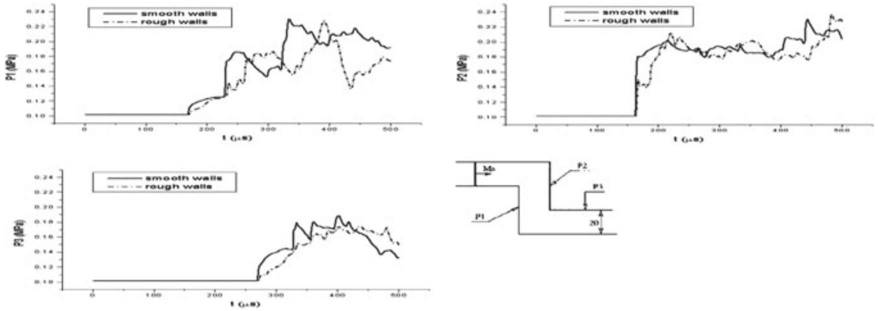

Fig. 12 Calculated pressure histories at various positions along the duct's wall

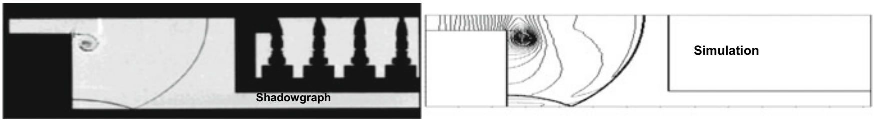

Fig. 13 The double bent model investigated in the Ernst Mach Institute

Tube Laboratory, IUSTI-CNRS, in Aix-Marseille Universit´e, Marseille, France. We were investigating the following topics: Experimental investigation of door dynamic opening caused by impinging shock wave [12]; flow generated inside a duct after it expels a shock wave [13]; effects that changes in the diaphragm aperture have on the resulting shock tube flow [14]; drag coefficient of a sphere in a non-stationary flow; new results [11]; simulation of sphere's motion induced by shock waves [15]; effect of an impinging shock wave on a partially opened door [16]; experimental investigation of shock wave propagation in a 90° branched duct [17] and investigation of blast wave interaction with a three level building [18].

As mentioned earlier, due to the lack of knowledge about the drag coefficient of a sphere in a **non-steady flow**, Professor Takayama and I recorded, in the early nineties, spheres trajectories behind on-coming shock waves; from which the appropriate drag coefficient was deduced [4]. However, in those experiments, the investigated spheres were laid on the shock tube floor and therefore they started their motion in the thin post-shock boundary layer. For eliminating the negative boundary layer effect on the sphere motion, new experiments were conducted in the Shock Tube Laboratory, of Aix-Marseille Universit´e, Marseille. In these experiments the investigated spheres were hanged at the center of the shock tube by a light wire taken from a spider web. Obtained results, including those obtained previously, in Japan [4] are shown in Fig. 17. It is clear from this figure that there is a significant difference between the drag coefficient of a sphere in a steady flow (the standard drag curve) and that obtained in non-stationary flow conditions. Based on results shown in Fig. 17, (the solid line) Jourdan et al. [11] suggested the following correlation for the sphere's drag coefficient:

Fig. 14 The flow field inside a wedge-like nozzle at $t = 75$ μs. The top is a shadowgraph photo, at the center is an isopycnic plot and on the bottom an isobar plot

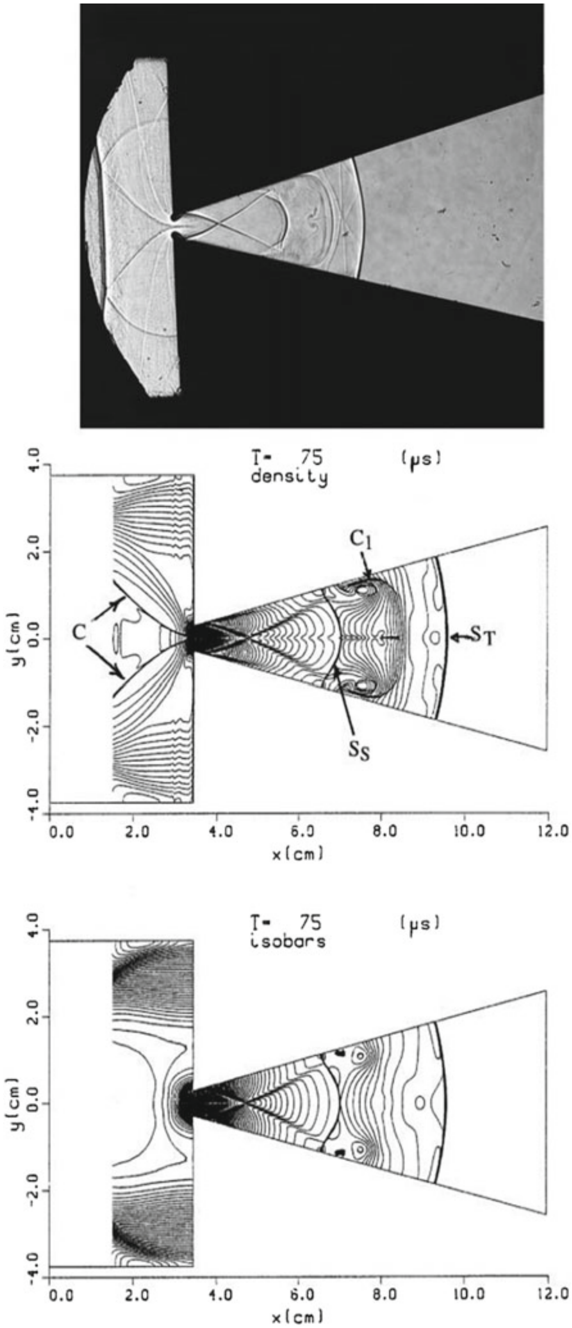

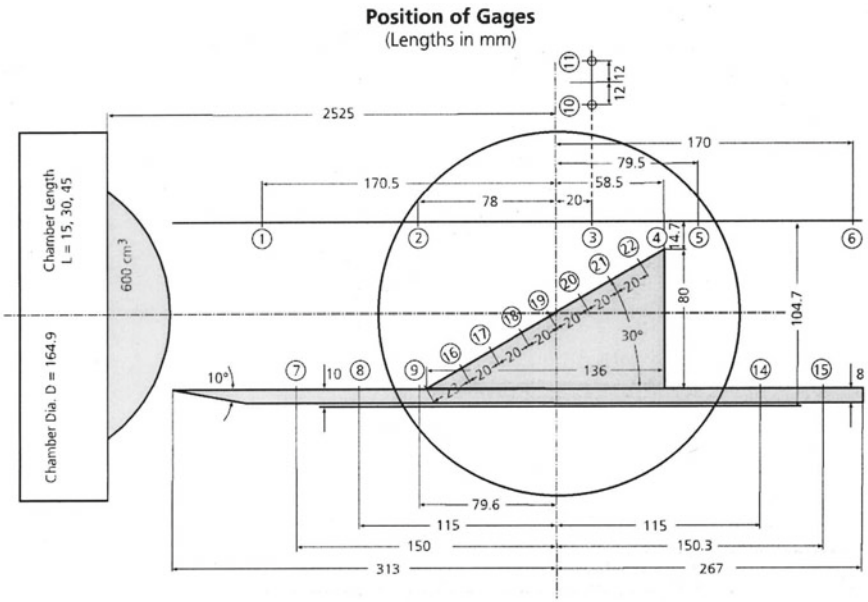

Fig. 15 Schematic description of the wedge location inside the shock tube test section

$$\log_{10}C_D = -0 : 696 + 1.259 \text{ X } \log_{10}Re_p - 0.465 \text{ X } \left(\log_{10}Re_p\right)^2 + 0.045 \text{ X } \left(\log_{10}Re_p\right)^3,$$

where Re_p stands for the Reynolds number based on the particle relative velocity.

Another example of the cooperation with the Shock Tube Laboratory, of Aix-Marseille Universit´e, Marseille is the investigation of blast wave interaction with a three level building [18]. It was shown in this investigation that weak blast waves that are considered as being harmless can turn to become fatal upon their reflections from walls and corners inside a building. In the experimental part, weak blast waves were generated by using an open-end shock tube. A three level building model was placed in vicinity to the open-end of the used shock tube; as shown in Fig. 18. The evolved wave pattern inside the building rooms was recorded by a sequence of schlieren photographs; also pressure histories were recorded on the rooms' walls. In addition, numerical simulations of the evolved flow field inside the building were conducted [18]. Typical results are shown in Fig. 19. It is apparent from the results shown in [18] that blast wave damages are higher for people standing near a wall, or even higher when near corners. Furthermore, at a late time, the overpressure behind reflected blast wave from a room corner is significantly higher than that experienced in the open atmosphere.

The good agreement obtained between numerical and experimental results shows the potential of the used code for identifying safe and dangerous places inside a building rooms penetrated by the weak blast wave.

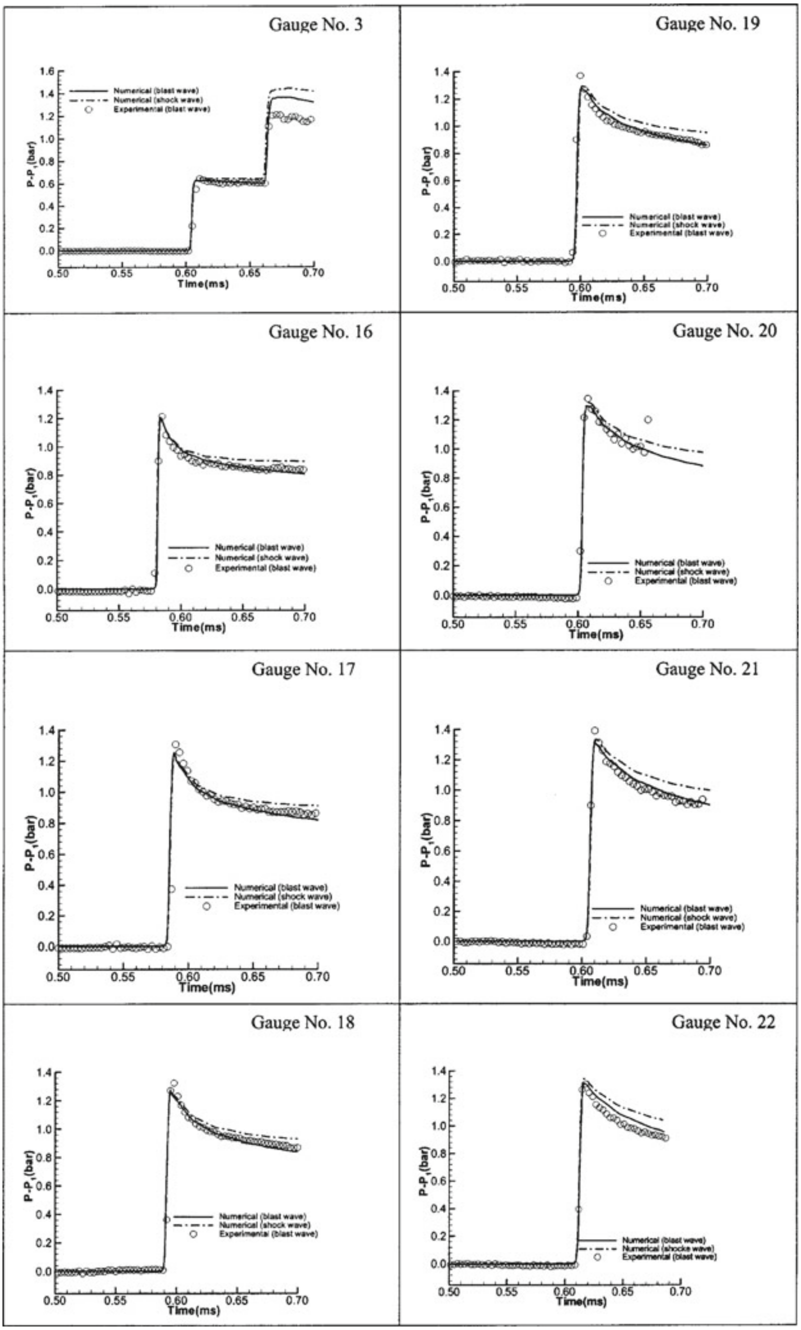

Fig. 16 Recorded and computed pressure signatures over the wedge. Initial conditions are: the driver length is 45 mm $P_4 = 5$ bars, $P_1 = 748$ torr, and $T_1 = 20.1$ °C. The driver and the driven gases are air

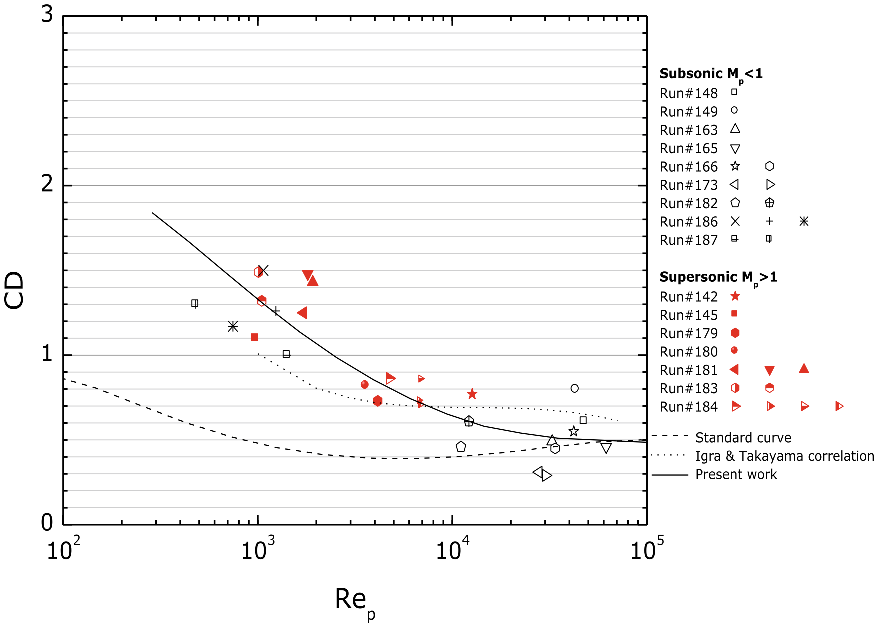

Fig. 17 Variations in the spheres' drag coefficient with Reynolds

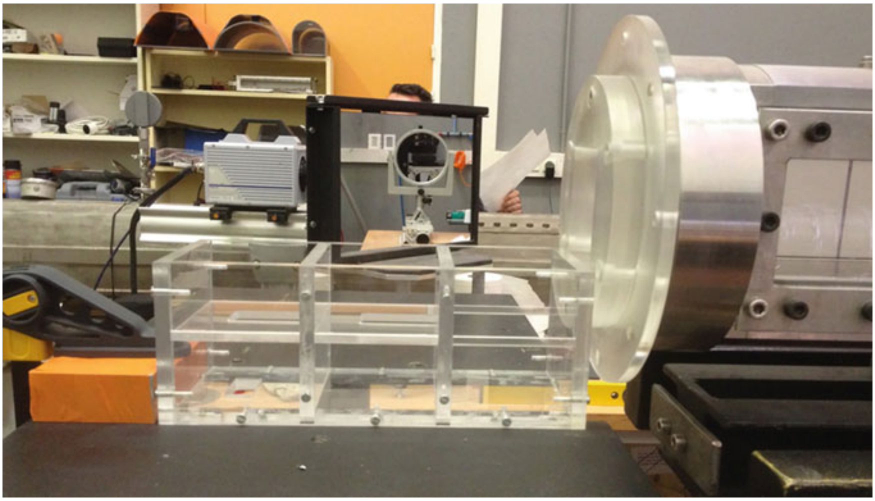

Fig. 18 View of the Plexiglas building model placed close to the shock tube exit

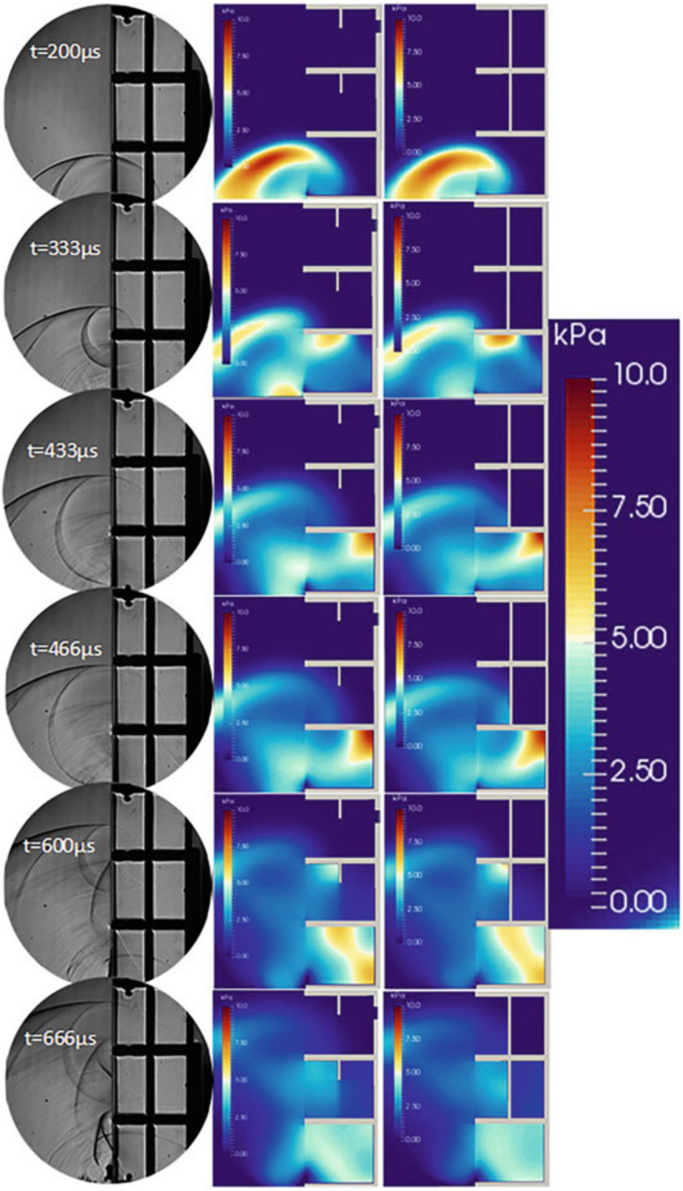

Fig. 19 Overpressure prevailing inside the three floor building model impeached by a blast wave (generated by an incident shock wave, M = 1.17). Experimental results are shown on the left and appropriate simulations appear on the right

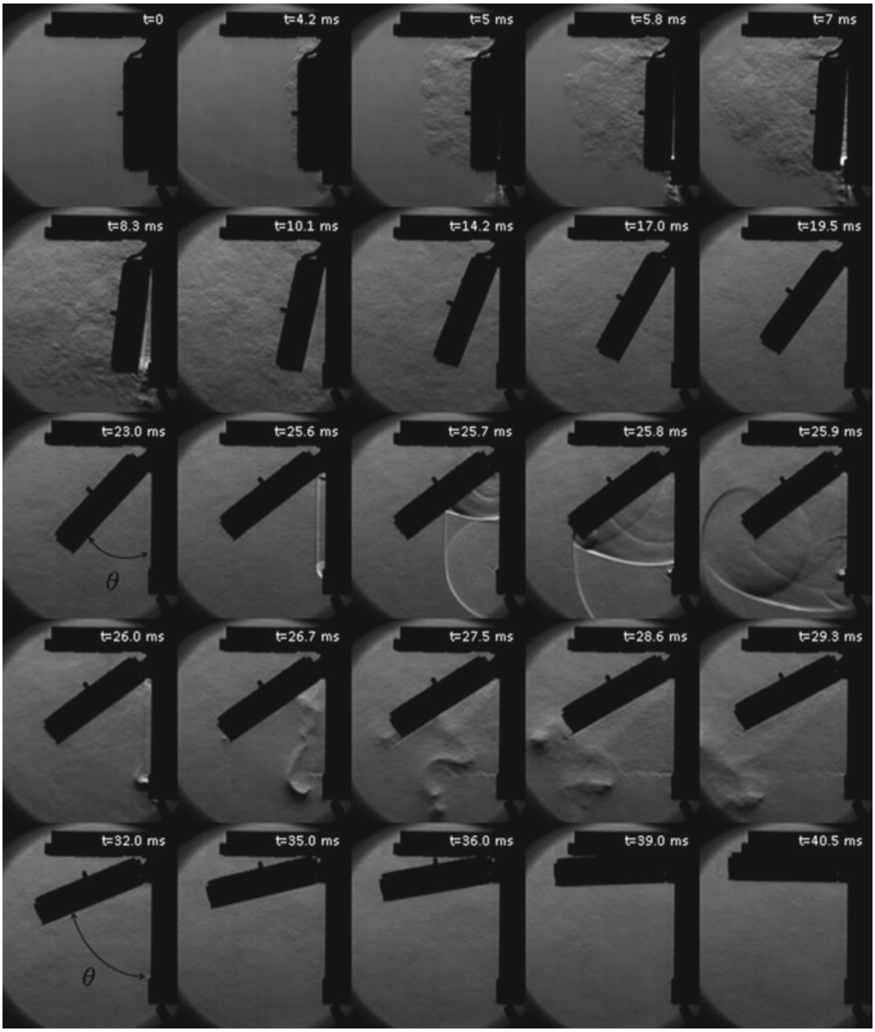

Fig. 20 Sequence of schlieren photos showing the impact of a normal shock wave ($M_{is} = 1.1$), moving initially from right to left inside the shock tube, on an aluminum door. θ is the angle between the door and its initial position

Another example of cooperation with the Shock Tube Laboratory in Marseille University was experimental investigation of door dynamic opening caused by impinging shock wave [12]. In this investigation the dynamic opening of a door, placed at the end of a shock tube driven section was checked. The door was hung on an axis and was free to rotate, thereby opening the tube. The evolved flow and wave pattern due to the door collision with the on-coming incident shock wave, causing the door opening, is studied by employing a high speed schlieren system and recording pressures at different places inside the shock tube, as well as on the rotating door. A typical schlieren records showing the interaction between the door and the on-coming shock wave is shown in Fig. 20.

Analyzing this data sheds light on the air flow evolution and the behavior of the opening door. In this research work [12], emphasis was given to understanding the complex, unsteady flow developed behind the transmitted shock wave as it diffracts over the opening door. It was shown that both the door inertia and the shock wave strength influence the opening dynamic evolution, but not in the proportions that might be expected.

So far a brief description of joint research work done with leading shock wave laboratories in Japan, Germany and France was outlined. Additionally, during the past 25 years I was involved in variety of shock wave investigations conducted in Israel. Among the covered topics were: Interaction between weak shock waves and granular layers [19]; gas filtration during the impact of weak shock waves on granular layers [20]; mechanism of compressive stress formation during weak shock waves impact with granular materials [22]; nonstationary compressible flow in ducts with varying cross-section [23]; dusty gas flow in a converging–diverging nozzle [25]; shock wave reflections in dusty-gas suspensions [26]; shock wave diffraction by a square cavity filled with dusty gas [27]; general attenuation laws for spherical shock waves in pure and particle laden gases [28]; shock wave interaction with perforated plates [30]; shock wave interaction with porous compressible foam [38]; shock wave propagation in non-uniform gas mixtures [39]; shock wave mitigation by different combination of plate barriers [42] and shock wave interaction with a polygonal bubble containing different gases [43]. Detailed description of these research activitie is available in Ref. [8, 19–44].

References

1. Igra O, Glass II (1971) Corner expansion flow of ionized argon. Canad J Phys 49:2671–2679
2. Ben-Dor G, Igra O (1978) Analysis of a piston-driven shock tube. Aeronaut J 82:178–181
3. Ben-Dor G, Mazor G, Takayama K, Igra O (1987) Influence of surface roughness on the transition from regular to mach reflection in pseudo-steady flows. J Fluid Mech 176:333–356
4. Igra O, Takayama K (1993)Shock tube study of the drag coefficient of a sphere in a nonstationary flow. In: proceedings of the royal society, vol A 442. London, pp 231–247
5. Igra O, Wu X, Falcovitz J, Meguro T, Takayama K, Heilig W (2001) Experimental and theoretical studies of shock wave propagation through double-bend ducts. J Fluid Mech 437:255–282
6. Igra O, Falcovitz J, Reichenbach H, Heilig W (1996) Experimental and numerical study of the interaction process between a planar shock wave and a square cavity. J Fluid Mech 313:105–130
7. Igra O, Wang L, Ben-Dor G, Reichenbach H, Heilig W (1997) Uni-axial strain loading of a rubber rod by planar shock waves. Acta Mech 120(1–4):91–107
8. Igra O, Wang L, Falcovitz J, Amann OH (1998) Simulation of the starting flow in a wedge-like nozzle. Shock Waves Int J Shock Waves Detonations Expl 8(4):235–242
9. Igra O, Wang L, Falcovitz J, Heilig W (1998) Shock wave propagation in a branched duct. Shock Waves Int J Shock Waves Detonations Expl 8(6):375–381

10. Igra O, Hu GQ, Falcovitz J, Heilig W (2003) Blast wave reflection from wedges. ASME J Fluids Eng 124:510–519
11. Jourdan G, Houas L, Igra O, Estivalezes J-L, Devals C, Meshkov EE (2007) Drag coefficient of a sphere in a non-stationary flow; new results. In: Proceedings of the royal society, vol A 463, no. 2088. London, pp 3323–3345.
12. Biamino L, Jordan G, Mariani C, Igra O, Massol A, Houas L (2011) Experimental investigation of door dynamic opening caused by impinging shock wave. Shock Waves Int J Shock Waves Detonations Expl 21(1):19–28
13. Biamino L, Igra O, Jourdan G, Massol A, Houas L (2012) The flow generated inside a duct after it expels a shock wave. Proc Inst Mech Eng Part G J Aerosp Eng 226(4):395–412
14. Houas L, Biamino L, Mariani C, Igra O, Jourdan G, Massol A (2012) The effects that changes in the diaphragm aperture have on the resulting shock tube flow. Shock Waves Int J Shock Waves Detonations Expl 22(4):287–293
15. Igra D, Igra O, Houas L, Jourdan G (2012) Simulation of sphere's motion induced by shock waves. ASME J Fluids Eng 134(10):104502–1–104502–4
16. Biamino L, Igra O, Jourdan G, Houas L (2013) Effect of an impinging shock wave on a partially opened door. Shock Waves Int J Shock Waves Detonations Expl 24(2):115–121
17. Biamino L, Jourdan G, Igra O, Mariani C, Tosello R, Leriche D, Houas L (2014) Experimental investigation of shock wave propagation in a 90° branched duct. Shock Waves Int J Shock Waves Detonations Expl 24(3):307–315
18. Massoni J, Biamino L, Jourdan G, Igra O, Houas L (2017) Experimental and numerical investigation of blast wave interaction with a three level building. ASME J Fluids Eng 139(11):111106–1–111106–9
19. Ben-Dor G, Britan A, Elperin T, Igra O, Jiang JP (1997) Experimental investigation of the interaction between weak shock waves and granular layers. Exp Fluids 22:432–443
20. Britan A, Jiang JP, Igra O, Elperin T, Ben-Dor G (1997) Gas filtration during the impact of weak shock waves on granular layers. Int J Multiph Flow 23(3):473–491
21. Schotz M, Levy A, Ben-Dor G, Igra O (1997) Analytical prediction of the wave configuration size in steady flow mach reflections. Shock Waves Int J Shock Waves Detonations Expl 7(6):363–372
22. Britan A, Ben-Dor G, Elperin T, Igra O, Jiang JP (1997) Mechanism of compressive stress formation during weak shock waves impact with granular materials. Exp Fluids 22:507–518
23. Igra O, Wang L, Falcovitz J (1998) Nonstationary compressible flow in ducts with varying cross-section. J Aerosp Eng Proc Inst Mech Eng Part G 212:225–243
24. Miron G, Igra O, Rosenwaks S, Falcovitz J (1999) Parametric study of a supersonic unsteady flow in a nozzle for a potential lead azide laser. Int J Fluid Mech 26(2):172–194
25. Igra O, Elperin I, Ben-Dor G (1999) Dusty gas flow in a converging-diverging nozzle. ASME J Fluids Eng 121:908–913
26. Ben-Dor G, Igra O, Wang L (2001) Shock wave reflections in dusty-gas suspensions. ASME J Fluids Eng 123:145–153
27. Wang BY, Wu QS, Wang C, Igra O, Falcovitz J (2001) Shock wave diffraction by a square cavity filled with dusty gas. Shock Waves Int J Shock Waves Detonations Expl 11:7–14
28. Aizik F, Ben-Dor G, Elperin T, Igra O (2001) General attenuation laws for spherical shock waves in pure and particle laden gases. AIAA J 9:969–971
29. Igra O, Wu X, Hu GQ, Falcovitz J (2002) Shock wave propagation into a dust-gas suspension inside a double-bend conduit. ASME J Fluids Eng 124:483–491
30. Britan A, Karpov V, Vasiliev EI, Igra O, Ben-Dor G, Shapiro E (2004) Experimental and numerical study of shock wave interaction with perforated plates. ASME J Fluids Eng 126:399–409
31. Britan A, Igra O, Ben-Dor G, Shapiro H (2006) Shock wave attenuation by grids and orifice plates. Shock Waves Int J Shock Waves Detonations Expl 16(1):1–15
32. Britan A, Ben-Dor G, Igra O, Shapiro H (2006) Development of a general approach for predicting the pressure fields of unsteady gas flows through granular media. J Appl Phys 99(9):093519

33. Igra D, Igra O (2007) Enhancement of shock waves. Shock Waves Int J Shock Waves Detonations Expl 16(3):199–207
34. Glam B, Igra O, Britan A, Ben-Dor G (2007) Dynamics of stress wave propagation in a chain of photoelastic discs impacted by a planar shock wave; part I, experimental investigation. Shock Waves Int J Shock Waves Detonations Expl 17(1–2):1–14
35. Igra D, Igra O (2008) Gas combination for shock wave enhancement. Shock Waves Int J Shock Waves Detonations Expl 18(1):77–78
36. Igra O, Jiang JP (2008) Head on collision of a planar shock wave with a dusty gas layer. Shock Waves Int J Shock Waves Detonations Expl 18(5):411–418
37. Falcovitz J, Igra O (2008) Model for shock interaction with sharp area reduction. J Aerosp Eng Proc Inst Mech Eng part G J Aerosp Eng 222:789–800
38. O. Igra. and J. P. Jiang, “Simulation of shock wave interaction with porous compressible foam”, Proceedings of the Institution of Mechanical Engineers, Vol. 223, part G: J. Aerospace Engineering,, pp. 297–306, 2009.
39. Falcovitz J, Igra O, Igra D (2012) Shock wave propagation in non-uniform gas mixtures. Proc Inst Mech Eng Part G J Aerosp Eng 226(2):123–130
40. Igra D, Igra O (2014) Simulation of shock wave propagation in a duct with a side branch. Proc Inst Mech Eng Part G J Aerosp Eng 228(12):2226–2236
41. Igra D, Igra O (2016) Planar shock wave diffraction into a square cavity filled with different gases. AIAA J 54(5):1798–1802
42. Igra D, Igra O (2016) Shock wave mitigation by different combination of plate barriers; a numerical investigation. Eur J Mech B/Fluids 59:115–123
43. Igra D, Igra O (2018) Numerical investigation of the interaction between a planar shock wave with square and triangular bubbles containing different gases. Phys Fluids 5:1449–1457
44. Igra D, Igra O (2020) Shock wave interaction with a polygonal bubble containing two different gases, a numerical investigation. J Fluid Mech 889:A 26

My Adventure with Mach Reflection—A Tribute to Professor Sakurai

Zbigniew A. Walenta

The first time I encountered the problem of weak Mach reflection in early seventies of the twentieth century, when reading Professor Sakurai's paper "On the problem of weak Mach reflection" [1]. The problem really fascinated me. I started studying more papers on this subject and in the paper by Guderley [2] I found a suggestion that, in order to make the weak Mach reflection possible, an additional rarefaction wave should be present behind the triple point to equilibrate the pressures behind the reflected and the Mach stem shocks. However, nobody ever detected experimentally such rarefaction wave. It was argued then, that probably the linear dimensions of this wave were so small, that it was impossible to detect with standard optical methods commonly used at that time.

It occurred to me, that such rarefaction wave might be spotted if the linear scale of the phenomenon was sufficiently increased—this could be done by increasing the mean free path of the gas molecules, i.e. by decreasing the gas density.

Fortunately, we were then in the process of building a new shock tube for the Department of Fluid Mechanics, Institute of Fundamental Technological Research, where I worked. This shock tube was cylindrical, of 250 mm internal diameter and about 17 m long. Its low pressure part could be evacuated down to 0.00001 Tor. To produce strong shocks, aluminium foil diaphragms could be used. For the weakest shocks, a special quick-opening valve with a narrow throat was designed. For measuring shock speed, two electron beam densitometers, placed 0.5 m apart, were used as shock detectors [3].

In this shock tube it was possible to investigate shock waves of Mach number as low as Ms = 1.1 in a rarefied gas at densities corresponding to mean free path equal to about 2 mm.

Z. A. Walenta (✉)
Department of Fluid Mechanics, Institute of Fundamental Technological Research, Polish Academy of Sciences, Warsaw, Poland
e-mail: zwalenta@ippt.pan.pl

© The Author(s), under exclusive license to Springer Nature Switzerland AG 2022

K. Takayama and O. Igra (eds.), *Frontiers of Shock Wave Research*,
https://doi.org/10.1007/978-3-030-90735-8_2

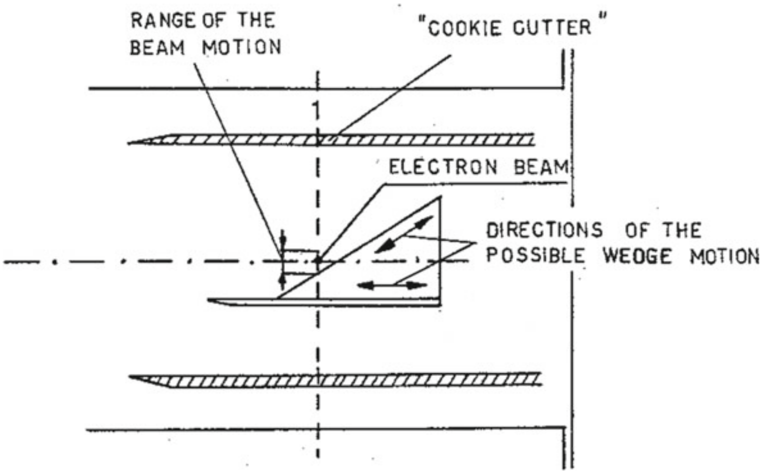

Fig. 1 Shock tube test section with “cookie cutter” and shock reflecting wedge

Unfortunately, under low density conditions no standard optical method could be used for visualization of the flow field. Instead, we decided to use the electron beam densitometer (working on the beam attenuation principle). This device was able to register in one test run the density distribution along one line. To obtain the picture of the whole flow field it was necessary to superimpose a number of such distributions, registered at different positions of the electron beam. Of course, it was only possible if repeatability of the phenomenon was sufficiently good.

The initial calibration runs indicated, that scatter of velocities of the shock waves, generated at the same initial conditions, was about 2 per cent—which seemed to be satisfactory.

In the first series of experiments the Mach reflection of moderately strong shock ($Ms = 3.22$) from a wedge of 25° angle was investigated. The test gas was Argon at room temperature and initial pressure 13.9 Pa (mean free path of the molecules 0.534 mm) [4]. Figure 1 shows schematically the test section of the shock tube with reflecting wedge and electron beam inside.

Quasi—stationary Mach reflection of the shock wave in a shock tube is usually described in the frame of reference connected with the moving triple point. Under standard conditions trajectory of the triple point is a straight line intersecting the surface of the wedge at its leading edge. To make sure, that in the considered case of low density conditions this is also true, we performed the experiment twice, with electron beam at two different distances from the wedge tip. To our surprise, the straight line connecting positions of the triple point intersected the surface of the wedge about 100 mean free paths behind the leading edge. (Later we found out, that this phenomenon was reported, independently, by Henderson and Gray [5] and explained theoretically by Hornung [6]).

Figure 2 presents a view of density distributions along the lines parallel to the triple point trajectory, when the triple point is 263 mean free paths from the leading

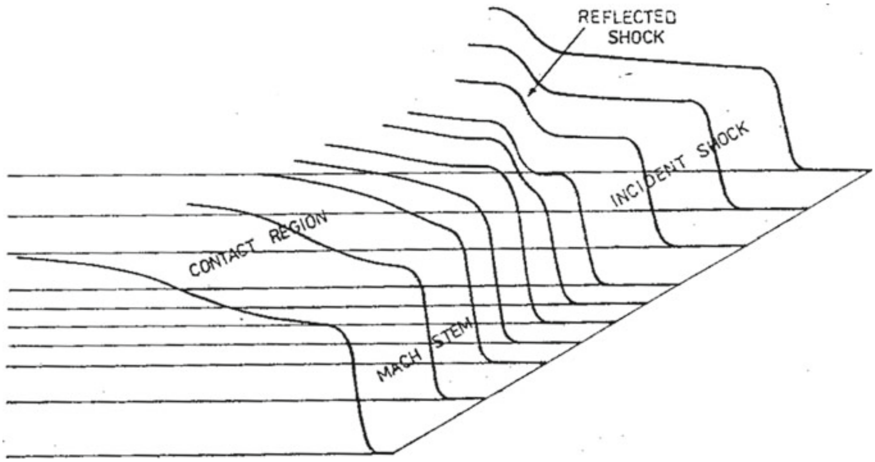

Fig. 2 Density distributions along lines parallel to the triple point trajectory

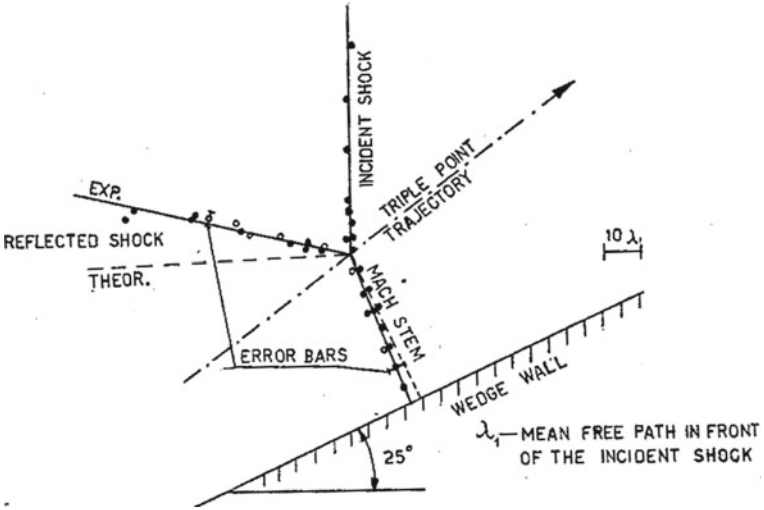

Fig. 3 Positions of shocks, corresponding to density distributions shown in Fig. 2

edge. The regions corresponding to incident shock, reflected shock, Mach stem and "contact region" are clearly visible. The thickness of the "contact region" is quite large—much larger than the thickness of any of the shocks. It seems conceivable, that such thick layer of gas may support some finite pressure difference, contrary to the assumption of von Neumann's theory and supporting the Sternberg's suggestion [7].

Figure 3 shows positions of the inflection points of the density distribution curves from Fig. 2 (these points may be taken as characteristic for positions of thick

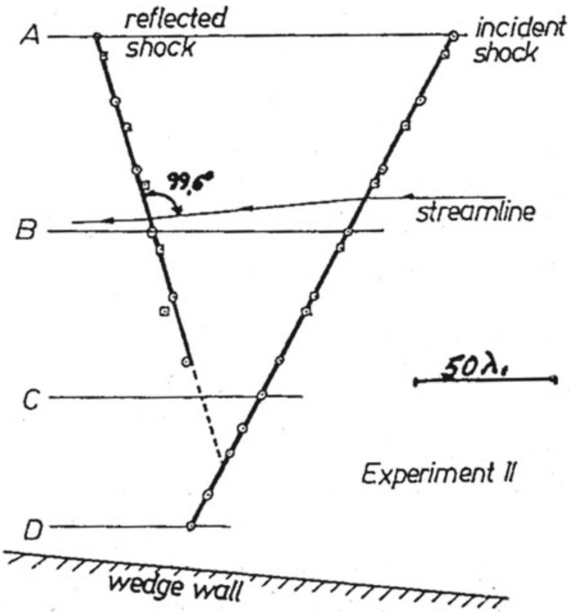

Fig. 4 Mach reflection of a very weak shock, of Mach number Ms = 1.14

shock waves). Theoretical (von Neumann's) position of the reflected shock has also been marked there. The visible distance between experimental and theoretical position of the reflected shock is appreciable—much above the estimated experimental inaccuracy.

At this point we decided to look at the reflection of the weakest shocks, to see whether the rarefaction wave predicted by Guderley actually exists. The experimental setup was the same as before (Fig. 1), only for producing shock waves the quick-opening valve was used instead of a diaphragm. The test gas was Argon at room temperature and pressure 34.0 Pa (mean free path of the molecules about 0.215 mm). Two sets of runs were done—for incident shock Mach numbers Ms = 1.28 and Ms = 1.14 [8].

As was mentioned before, according to von Neumann's theory under such conditions no Mach reflection is possible. If it is present nevertheless, then according to Guderley, behind the triple point an additional, rarefaction wave should appear in order to equilibrate the pressures behind the Mach stem and reflected shock. Apart from that, close to the triple point the reflected shock should be "inclined forward" and strongly curved.

The results of our experiment for Ms = 1.14 are presented in Figs. 4 and 5. Figure 4 shows the registered positions of all three shocks: incident, reflected and Mach stem (as before, the inflection points of the density distribution curves were taken as points characterizing positions of the shocks). According to this figure:

- the system of shocks undoubtedly has the character of Mach reflection,
- none of the shocks seems to be curved,

Fig. 5 Density distributions along lines A, B, C, D in Fig. 4

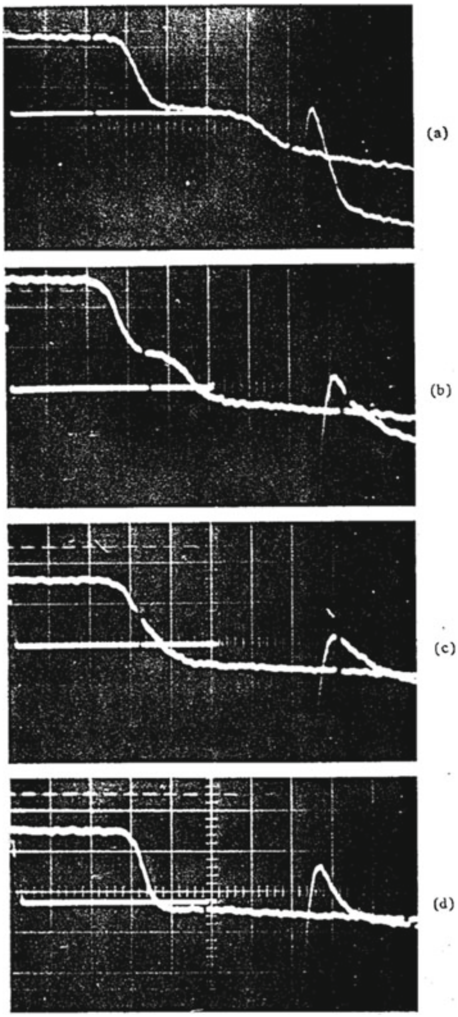

– the reflected shock is definitely inclined "backwards".

Figure 5 shows four oscilloscope traces, corresponding to density distributions along lines A, B, C, D of Fig. 4 (note, that in the traces, density increases downwards). None of these traces seems to show the existence of a rarefaction wave.

Next step of our investigation was aimed at the case of slightly stronger shocks, where the von Neumann's theory does predict the existence of Mach reflection, but the reflected shock is "inclined forward". The incident shock Mach number was equal to 1.42, test gas—Argon at room temperature and initial pressure 27.2 Pa (mean free path equal to 0.271 mm) [9]. Figure 6 shows the experimentally obtained positions of the three shocks—incident, reflected and Mach stem—with respect to

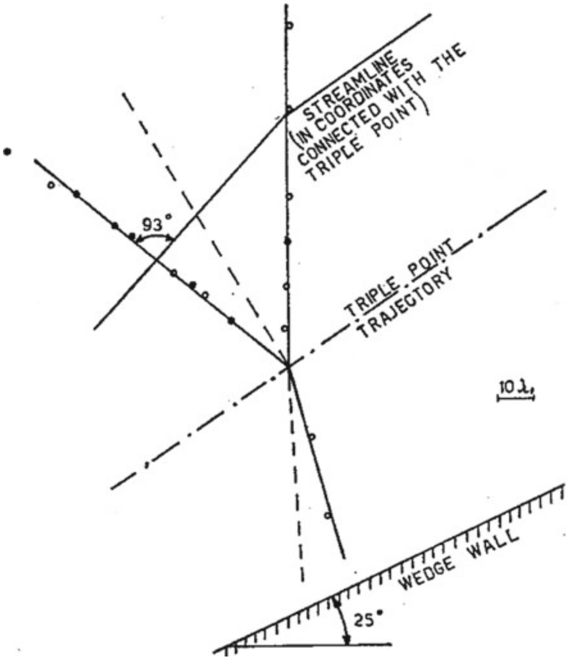

Fig. 6 Mach reflection 515 mean free paths from leading edge. Argon, Ms = 1.42

the wedge, for triple point 515 mean free paths behind the wedge tip. Theoretical (von Neumann's) positions of the reflected and Mach stem shocks are marked there with dashed lines. The reflected shock is evidently not "inclined forward", although it is nearly perpendicular to the streamline.

It was interesting to know how development of the Mach reflection proceeds in time. Figure 7 [10] shows configurations of shocks at several distances from the leading edge (conditions of experiment the same as those specified for Fig. 6). In this figure, positions of all shocks from experiment are drawn with solid lines. The circular shapes with radii:

$r(t) = Ur^{*}t + r_0$.

and centres at the points:

$x_c(t) = u_2{}^{*}t + x_{c0}$.

are drawn there with a dashed line. In the above expressions:

$t = x(t)/U$.

x(t)—distance from the wedge tip to the incident shock.

U—speed of the incident shock.

Ur—speed of reflected shock with respect to gas in front of it.

u_2—flow velocity behind the incident shock.

r_0 and x_{c0}—constants accounting for delay in formation of the reflected shock.

The shape and the inclination angle of the reflected shock seem to be reasonably well described by the above formulae everywhere, except in the region very close to the

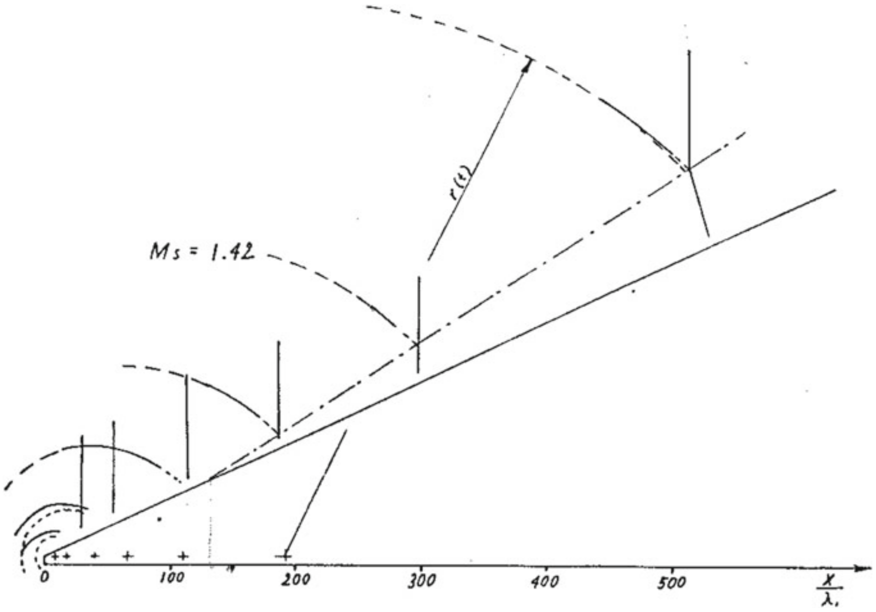

Fig. 7 Development of Mach reflection—weak shock case. Argon, Ms = 1.42

leading edge. It should be noted, that in this case the triple point trajectory intersects the wedge surface about 130 mean free paths behind the leading edge.

Figure 8 [10] presents similar picture of development of the Mach reflection of moderately strong shock wave of Ms = 2.75 in Krypton gas. Here the shape of the reflected shock can no longer be described in the way similar to the previous case, however it is far from prediction of the von Neumann's theory (the dashed line).

Trajectory of the triple point looks here (Fig. 8) similarly to that in the case of weak shock. The dotted line shows position of this trajectory according to a model, proposed for strong shocks by Hornung [6]. Agreement between Hornung's result and our experiment seems to be quite satisfactory.

The known geometry of the shock waves in the neighbourhood of the triple point, together with Rankine-Hugoniot conditions for the shocks, make it possible to calculate the flow velocities in the area behind the triple point. The calculation indicates, that for Mach reflection of a weak shock (Ms = 1.42, wedge angle 25° Fig. 6) the flow velocities behind the reflected and the Mach stem shocks diverge (Fig. 9a).

If the reflecting shock is strong, then flow velocities behind the reflected and the Mach stem shocks converge (Fig. 9b). To check it, calculation was done on the basis of our old result: Mach reflection in Argon, 25° wedge, initial pressure 15 Pa (mean free path 0.5 mm), incident shock Mach number Ms = 4.7, distance from the leading edge 290 mean free paths (Fig. 10).

Having found the above we decided to look at the density distributions just behind the Mach stem and the reflected shock (exactly, at the rear edge of the shock structure),

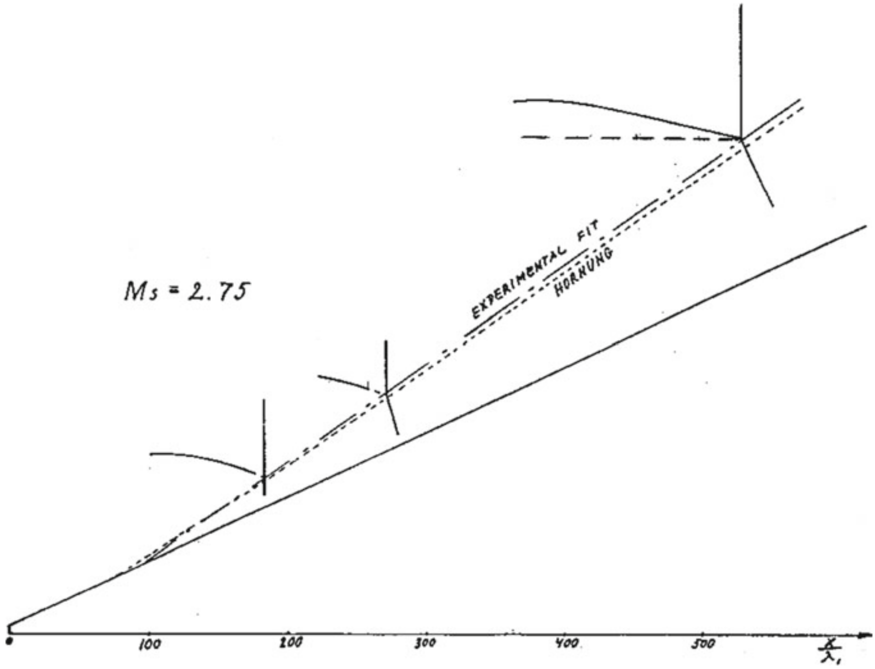

Fig. 8 Development of Mach reflection—strong shock case. Krypton, Ms = 2.75

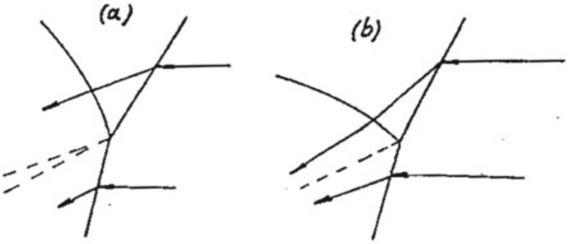

Fig. 9 Mach reflection—streamlines in the neighbourhood of triple point: **a** —weak shock case, **b** —strong shock case

as measured by our densitometer. The results are presented in Figs. 11 and 12. Figure 11 shows densities in the case of weak incident shock, Ms = 1.42 and Fig. 12—in the case of strong shock, Ms = 4.7.

In the weak shock case the diverging streams evidently produce no noticeable density (and presumably pressure) difference, making it possible for the reflected shock to keep its cylindrical shape arbitrarily long. In the strong shock case the converging streams do produce a local density (and pressure) maximum behind the triple point. Such local maximum of pressure might, presumably, influence the wave angles, slowly changing them to the limiting values, for which the theoretical (von Neumann's) conditions at the contact surface are satisfied.

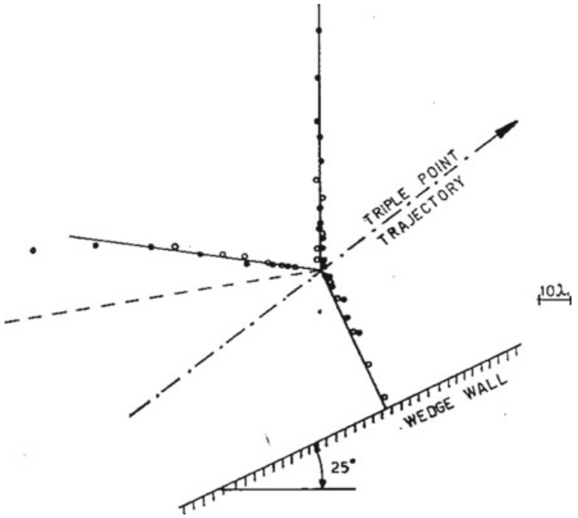

Fig. 10 Mach reflection 290 mean free paths from leading edge, Ms = 4.7, Argon

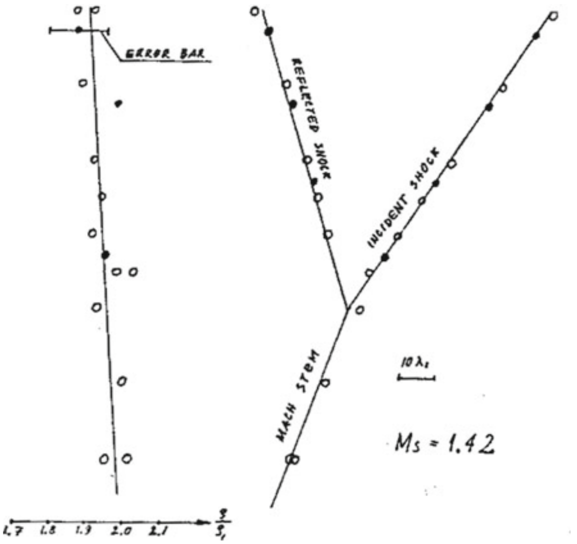

Fig. 11 Density distribution behind wave system, Ms = 1.42, 25° wedge

It should be noted here, that even at high density (i.e. very far from the wedge tip, as measured in mean free paths) Ben-Dor et al. [11] found experimentally a hot spot (presumably connected with local maxima of other gas parameters) just behind the triple point. Recently Sakurai et al. [12] presented a theoretical paper, suggesting possibility of existence of maximum of density behind the triple point.

The next problem to investigate was the structure of the flow field close to the leading edge of the reflecting wedge—in the range of "apparent regular reflection" as it was called sometimes. To obtain the picture of flow in this whole area it was

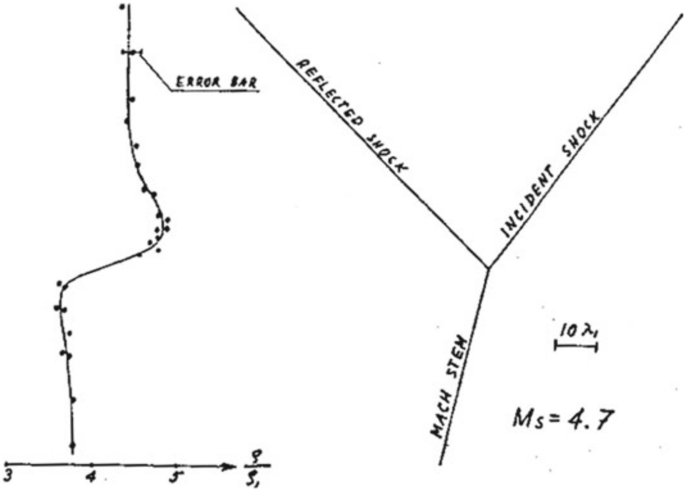

Fig. 12 Density distribution behind wave system, Ms = 4.7, 25° wedge

Fig. 13 Typical positions of the electron beam with respect to the wedge

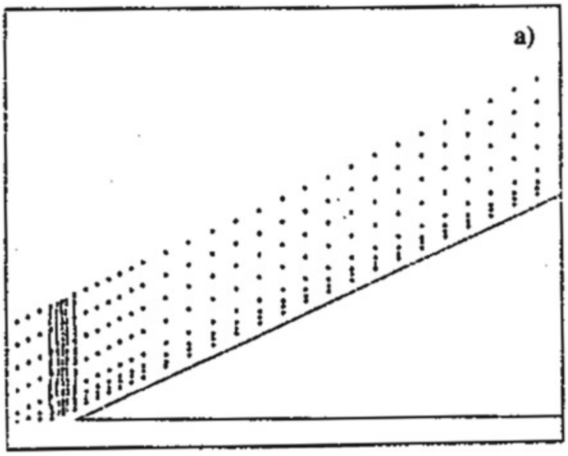

necessary to register (with the electron beam densitometer) the density history at a number of points in front and above the shock reflecting wedge. Figure 13 shows typical positions of the electron beam with respect to the wedge. For each position of the beam at least one test run of the shock tube was done.

The signals from the densitometer were recorded digitally and then fed to a computer to calculate the density history at each point. The matrices of momentary values of density for selected positions of the incident shock were then used to draw pictures of constant density lines in the flow field.

The experiments were performed in Argon and Sulphur Hexafluoride (SF_6) [13]. The reflecting wedge angle was equal to 25°. The incident shock Mach numbers

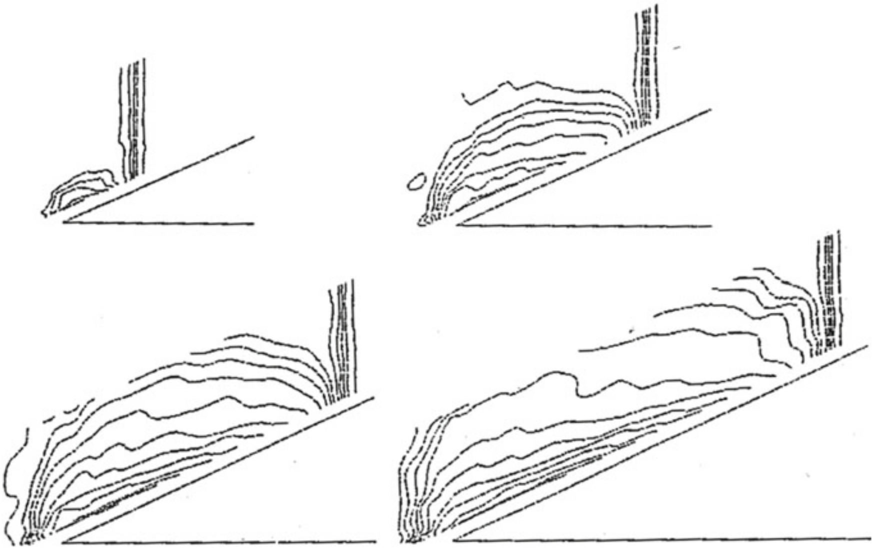

Fig. 14 Maps of constant density lines for four positions of incident shock in Argon

were close to Ms = 2.80. The initial temperature (equal to room temperature) was about 298 K. The initial pressure of Argon was 7.33 Pa; under such conditions the mean free path of the molecules of Argon was equal to 0.95 mm and the maximum slope shock thickness to 3.75 mm. For Sulphur Hexafluoride the initial pressure was equal to 2.65 Pa. Such pressure was necessary to produce shocks of thickness similar to that in Argon.

Figure 14 shows the maps of constant density lines for four positions of the incident shock in Argon. The shapes of these lines at the "foot" of the incident shock suggest, that in this place we might actually have a very short Mach stem. Density increase across it is higher than that for the incident shock, its structure stays unchanged with time, however its thickness is larger than that for the incident shock. Anyway, it may perhaps be concluded, that the "apparent regular reflection" is in fact Mach reflection with very short Mach stem.

Figure 15 presents behaviour of the triple point in the range of "apparent regular reflection". We assume, that intersections of the lines connecting "wave heads" of the incident and reflected shocks represent positions of the triple point (definition of the "wave head" given in the figure). Subsequent positions of the triple point for Mach reflections in Argon and Sulphur Hexafluoride have been marked as circles and squares, respectively. Trajectory of the triple point, as can be seen there, is a concave curve, nearly parallel to the surface of the wedge at its tip, and far downstream tending asymptotically to a straight line, known as trajectory at high densities (not shown in the picture).

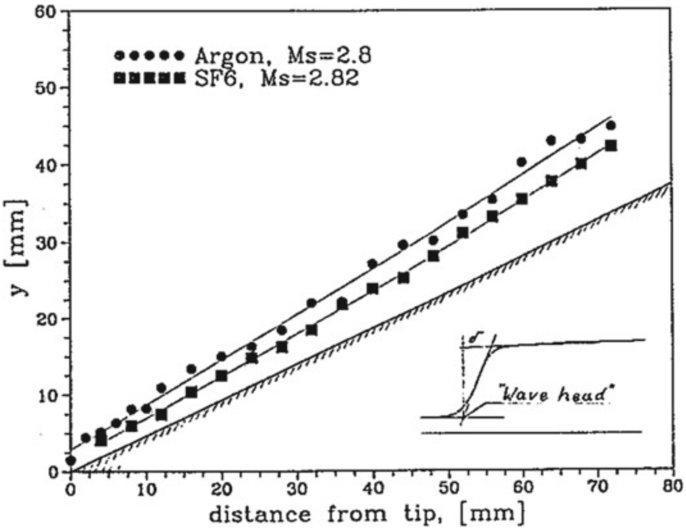

Fig. 15 Trajectories of the triple point in vicinity of the leading edge for Argon and SF_6

References

1. Sakurai A (1964) On the problem of weak mach reflection. J Phys Soc Japan 19(8):1440–1450
2. Guderley KG (1957) Theorie schallnaher stroemungen. Springer, Berlin, Goettingen, Heidelberg
3. Walenta ZA, Gmurczyk AS, Harasimowicz WW, Leśkiewicz EM, Tarczyński M, Orzeński J, Sałgut KJ (1976) Rura uderzeniowa ZMCiG, Prace IPPT, p 47 (in Polish)
4. Walenta ZA (1980) Microscopic structure of the Mach-type reflexion of the shock wave. Arch Mech 32(5):819–825
5. Henderson LF, Gray PM (1981) Experiments on the diffraction of strong blast waves. Proc R Soc Lond A 377:363–378
6. Hornung H (1986) The effect of viscosity on the Mach stem length in unsteady strong shock reflection. Lecture Notes 235, flow of real fluids. Springer
7. Sternberg J (1959) Triple−shock−wave intersections. Phys Fluids 2(2):179–206
8. Walenta ZA (1981) Microscopic structure of the Mach-type reflection of weak shock waves. In: Treanor CE, Hall JG (eds) Proceeding of 13th international symposium on shock tubes and waves. Niagara Falls, pp 335–341
9. Walenta ZA (1983) Formation of the Mach-type reflection of shock waves. Arch Mech 35(2):187–196
10. Walenta ZA (1987) Mach reflection of a moving, plane shock wave under rarefied flow conditions. In: Groenig H (ed) Proceedings of 16th international symposium on shock tubes and waves. Aachen, pp 535–541
11. Ben-Dor G, Takayama K, Needham CE (1987) The thermal nature of the triple point of a Mach reflection. Phys Fluids 30(5):1287–1293
12. Sakurai A, Kobayashi S, Tsukamoto M (2018) Internal structure of triple point in Mach reflection. In: 23rd International shock interaction symposium. Kruger National Park, South Africa
13. Walenta ZA (1993) Formation of the Mach reflection in vibrationally relaxing gases. In: Brun R, Dumitrescu LZ (eds) Proceedings of 19th international symposium on shock waves. Marseille, pp 181–186

The Background of My Studies of Shock and Blast Waves

John M. Dewey

1 Introduction

It is an honour to have the opportunity to contribute to this book commemorating the 100th birthday of Professor Sakurai. Professor Sakurai has made major contributions to the study of the physical properties of shock and blast waves, and has been an inspiration to scholars in this field both internationally, and particularly in Japan. Beyond the technical aspects, Professor Sakurai has inspired all those who have met him by his dignified demeanour and his humility. He is the epitome of a gentle man. One cannot help but relax in his presence, and perhaps it is this characteristic that has contributed to his longevity. The contribution of Mrs Sakurai and their daughter should also be acknowledge for their hard work and kindness while organising tours and social occasions for the delegates and their spouses attending international meetings in Tokyo (Fig. 1).

Professor Sakurai witnessed the atomic explosion over Hiroshima, fortunately from a long distance. During one of our social meetings, and in response to my enquiry, he told me the following that I now relate to the best of my memory. At 8:15 am on the morning of the attack on Hiroshima he observed a brilliant flash that illuminated the sky over the horizon, and assumed that a conventional bombing attack may have struck a munitions storage facility. About 20 min later he was startled by some loud booms like thunder, although the sky was clear. These were the sounds of the nuclear blast transmitted by refraction and reflection in the lapse-rate inversion layer that occurs in the atmosphere at altitudes above about 25 km, a topic I later studied following the eruption of Mount St Helen [1]. Because of the long delay between the two events Professor Sakurai did not associate the two phenomena.

Once the nature of the Hiroshima explosion was known, as a young physics graduate Akira Sakurai was called upon to explain this event, and it was his studies

---

J. M. Dewey (✉)
Department of Physics and Astronomy, University of Victoria, Victoria, BC, Canada
e-mail: jdewey@uvic.ca

© The Author(s), under exclusive license to Springer Nature Switzerland AG 2022

K. Takayama and O. Igra (eds.), *Frontiers of Shock Wave Research*,
https://doi.org/10.1007/978-3-030-90735-8_3

Fig. 1 Professor Sakurai and Mrs Sakurai at a BBQ in my garden, 1994

of the literature to answer these questions that initiated his lifetime interest in the physics of shock and blast waves. Professor Sakurai typically chose the more difficult problems for his analysis, problems that his peers elected to avoid. The primary example of this was his attempted analytical solution of the infamous so-called point source solution. One of the simplest problems to define in fluid mechanics is "What are the physical properties of the pressure wave generated when a finite amount of energy is suddenly released at a point in a uniform ideal gas?" Few scientists have attempted to achieve an analytical solution to this problems, but the ones that have been most successful are Sir Geoffrey Taylor, Hans Bethe, John von Neumann and Akira Sakurai [2–4]. A truly august company.

2 Defence Research Establishment Suffield

The following is an autobiographical summary of my studies of the physical properties of shock and blast waves. Rather than supplying details only of the technical aspects of those studies I will try to relate information about the background and environment that influenced the direction of my research activities, and this will provide an opportunity to acknowledge the many scientists and others who have been my mentors and colleagues.

In 1950 I graduated from the University of London with an honours degree in physics, pure and applied mathematics. My first employment was as the physics and mathematics master at De La Salle College on the Island of Jersey. There followed six most enjoyable years as I taught physics and mathematics to the Advanced and Scholarship levels to small classes of enthusiastic students, some of whom I remain in contact with to this day. Teaching these subjects at a level equivalent to that of the first two years of a North American university program provided me with a knowledge and understanding of basic physics and mathematics that has served me well throughout the rest of my career.

By 1956 I recognised my desire to create new knowledge, rather than merely pass it on to my young prodigies, by having the opportunity to do basic research. At that time the United Kingdom was still struggling to recover its economy after the Second World War, and offered few career opportunities. My wife, Jean, and I decided that because we had few ties we would emigrate to Australia or Canada for a few years before returning to Great Britain. Tossing a coin we decided to try our fortunes in Canada and I had no difficulty in obtaining a position with the Canadian Defence Research Board as an analyst in the Planning and Reporting Section of the Suffield Experimental Station in Alberta.

My job, under the wise direction of the Head of Section, Hub Fish, consisted principally of analysing the results of large scale field trials of chemical and biological agents. I found the work enthralling after the repetitive and demanding responsibilities of school teaching. As the analysis of each field experiment was completed a detailed technical report needed to be written and under the rigorous mentorship of Hub Fish I honed my writing skills. I am sure that the numerous reports I authored remain classified to this day.

My analysis was carried out using a state-of-the-art electrical calculator, but there was a rumour at that time of a new device called a digital computer, and at least three of these machines were now operating in Canada. I was given the task of investigating this new phenomenon and recommending whether or not such a device would be of benefit to Suffield Experimental Station. After visiting and talking to those who were operating Canada's three computers I recommended that the Station purchase the Stantec ZEBRA that was manufactured in Britain based on Dutch and German designs. ZEBRA is the abbreviation, in German, of Very Elementary Binary Reckoning Apparatus. And so this state-of-the-art machine was installed at Suffield, and in the pre-solid-state era contained 3000 electronic valves or tubes that generated an enormous amount of heat, and a memory of 32 kB stored on a spinning metal drum. It had the computing power almost equivalent to that of a present day wristwatch, but at that time was a state-of-the-art wonder that served the Station well for many years.

In the late 1940s and early 1950s it was discovered that a number of people involved in the American, British and Canadian Manhattan Project had been providing the Soviet Union with information about the development of nuclear weapons, and the most significant of these was probably Klaus Fuchs, a scientist who had been studying and working in the United Kingdom after fleeing Germany in the early 1930s. This resulted in a cessation of the exchange of information about nuclear weapons between United States and the United Kingdom, and the United Kingdom continued its own independent development of nuclear weapons with the participation of Canada in the measurement of thermal and nuclear radiation, and of the blast wave. The blast wave measurements were made under the direction of Dr Ross Harvey from the Suffield Experimental Station.

In 1955, the United Nations Disarmament Commission brought together the United States, the United Kingdom, Canada, France, and the Soviet Union to begin negotiations on ending nuclear weapons testing. This was supported by the United States in 1956, and in 1958 a moratorium banning the atmospheric testing of nuclear weapons was signed by the US, UK, Canada and the Soviet Union. In order to continue the study of nuclear blasts, simulated by using conventional chemical explosives, there was a renewed cooperation between the US, UK and Canada, and it was decided to initiate a tripartite collaborative experimental programme at Suffield. In order for Canada to participate in this program a Shock and Blast Group was formed, initially under the direction of Dr Henry Watson. With Ross Harvey being the only scientist with experience in this field, Dr Watson recruited four young scientists: Trevor Groves; John Muirhead; Gareth Jones, and myself, stealing me from Hub Fish who did not appreciate my defection.

None of the newcomers had any direct experience in fluid mechanics, and we were sent off to a two week intensive short course at the University of Toronto Institute of Aerospace Studies under the direction of Prof Irvine Glass. This was an inspiring and exhausting experience, and for the next few years Prof Glass became my primary mentor, even though officially I was not one of his students. In those years he critically reviewed all my papers before they were submitted for publication, and we became good friends as well as colleagues. He visited my wife and me at our home in Victoria, and demonstrated his bravery by helping me deal with a swarm of bees from one of my hives.

As the new shock and blast program at Suffield developed, Ross Harvey became Head of Section, and responsibilities were assigned as follows. Trevor Groves continued to develop the photogrammetric techniques that Ross Harvey had used to study the British nuclear tests in Australia, and to administer the piezoelectric measurements of hydrostatic overpressure. John Muirhead was responsible for the development of the shock tube laboratory, which he did with great skill and energy, producing more reports and open literature publications than the rest of the group combined. Gareth Jones, whose background was in geophysics, assumed responsibility for seismic measurements and particularly the study of the crater production. What was left for me to study?

One of the reading assignments for Professor Glass at the short course at UTIAS was the papers by Sir G. I. Taylor, and one particular statement caught my attention and excited me, and is paraphrased as follows. The expanding primary shock from a centred explosion leaves the air in a state of radially decreasing entropy and temperature. As a result, there are no simple thermodynamic relationships between the physical properties measured at a fixed point. This means, for example, that if the hydrostatic overpressure is measured as a function of time, it is not possible to use that information to determine the time histories of other physical properties such as density, temperature and particle velocity. In order to determine all the physical properties at a fixed point in a blast wave it is necessary to measure, independently, at least three of the properties. Since Trevor Groves was measuring the hydrostatic pressure I set myself the challenge of measuring two other properties, and chose density and particle velocity.

At this point I receive a serendipitous reward. With the end of atmospheric nuclear testing it was decided to close the nuclear radiation program at Suffield. The senior members of that team moved to Edmonton to establish a department at the University of Alberta, but several of the technicians decided to remain at Suffield. One of those technicians, Bill Anson, approached me and offered his services as I did not have anyone reporting directly to me at that time. There followed eight years of collaboration that had a major impact on my career that could not have been achieved without Bill Anson's skilled assistance and guidance.

We decided that one of the physical properties of blast waves that we would attempt to measure would be density. This was achieved by using a radioactive source of weak beta radiation, Erbium-169. The radiation was measured by a photomultiplier placed about 5 cm from the source. As a blast wave passed through that gap the reduction of the signal generated by the photomultiplier was directly related to the density of the air in the blast wave. The gauge was used extensively and successfully on several of the large scale TNT tests carried out at Suffield [5]. With my limited knowledge of radioactivity and electronic circuitry most of the credit for the development of the density gauge must go to Bill Anson, although the results subsequently formed a significant part of my Ph.D. thesis.

The second blast wave property that I set out to measure was the particle velocity. This was achieved by using high-speed photography to measure the velocity of flow tracers released into the air immediately before the arrival of the primary shock. The first flow tracers that I evaluated were ping-pong balls. These were easily visible on the high-speed films, but the measured peak velocities were significantly lower than the Rankine Hugoniot values, and so this technique was discarded in favour of using smoke as the flow tracer. The smoke was released from mortar shells fired in an array up to an altitude of several hundred metres in a vertical plane containing the charge centre and parallel to the film planes of the high-speed cameras running at more than a thousand frames a second, giving a time resolution of a millisecond (Fig. 2).

This technique proved to be very successful, and I was able to measure the particle velocities as functions of radius and time from surface burst TNT charges ranging in size from 30 kg to 500 tons [6]. There were two ancillary results of these studies, one of which I was initially unaware of. The first was a clear demonstration of the effect of afterburning from TNT explosions. TNT is an oxygen deficient explosive so that after detonation the detonation products continue to burn as they mix with atmospheric oxygen, burning with a black body temperature of about 2500 K after detonation. I seem to recall that the burning continued for about 25 s after initiation in the case of a 500 ton TNT explosion. Afterburning has little effect on the pressure profile of a blast wave, and was therefore thought be of little importance. However, it has a major effect on the time-history of the particle velocity that does not reverse direction until the beginning of the inward and upward flow that generates the classical mushroom cloud, and is caused because the blast wave leaves the air in a state of radially decreasing temperature and therefore of radially increasing density.

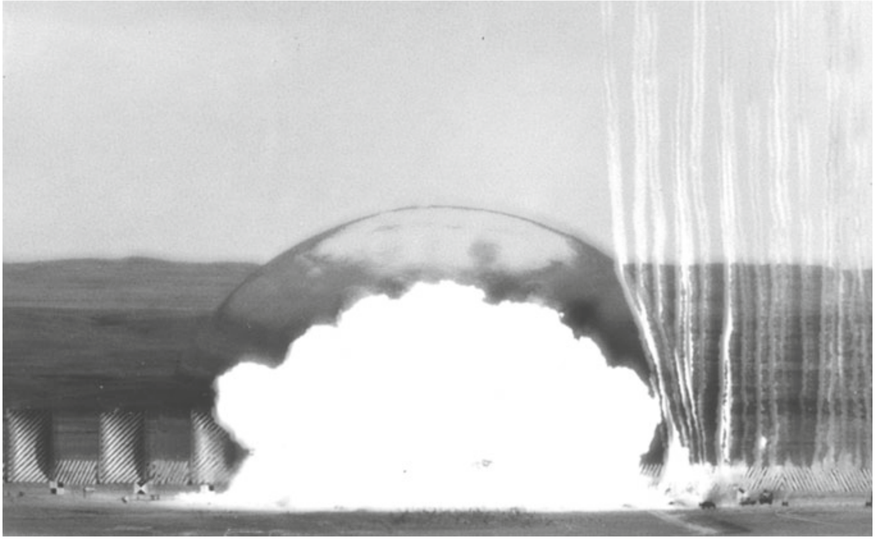

Fig. 2 A 200 ton hemispherical surface-burst explosion showing the refractive image of the shock front and an array of particle-flow smoke tracers

The second ancillary result arising from the particle velocity measurements was brought to my attention when I attended a short course, several years later, given by Wilf Baker, an authority on blast effects. Much to my surprise, at the beginning of the workshop Mr Baker introduced me to the audience as the first person to validate Sachs' scaling of time within a blast wave. Apparently, due to the unreliability of measuring the positive duration of hydrostatic pressure using the piezoelectric gauges that were available at that time, it had never been clearly established that Sachs' scaling could be applied validly to blast wave time histories. However, he said, my measurements of particle velocity time-histories from charges ranging from 30 kg to 500 tons had clearly established that validity. I was treated to undeserved respect for the remainder of the short course.

In the early 1960s it was realised that the large surplus supplies of TNT, left over from the Second World War, was nearly exhausted and a search was initiated for a cheaper explosive that could be used to simulate the blast waves from nuclear explosions. I was tasked to evaluate the possibility of using ammonium nitrate. Ammonium nitrate is manufactured in the form of a prill of small pellets that is easy to transport and use for agricultural purposes. Bill Anson and I made piles of bags of ammonium nitrate around booster charges that we tried to detonate, but all we did was fertilise the prairie, and to this day it is still possible to recognise the old ammonium nitrate test site because the grass there grows to two or three times the height of the normal prairie grass. But there was a serendipitous result from our failure.

The only means we had to measure and evaluate blast waves was to use piezoelectric transducers. At that time the outputs from the transducers were recorded as analogue signals on magnetic tape. The tapes were taken back to the laboratory,

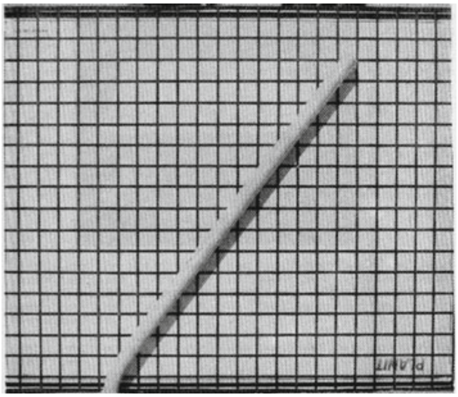

Fig. 3 A 2.5 cm diameter aluminium rod cantilever after exposure to a blast wave, showing that the rod bends only at the end where it was held in concrete

played back through an oscilloscope and the signals recorded by a Polaroid camera for subsequent analysis. This process took a minimum of 24 h. So that we could carry out and evaluate several explosions on the same day we needed a device that would provide an immediate measure of the blast wave. I recalled from the reading proscribed by Prof Glass that Lord Penny had analysed the blast waves from the Hiroshima and Nagasaki explosions using the bending of metal fence posts and overturned gravestones. Based on that work, Bill Anson and I developed a cantilever gauge from which the angle of bend of a wire exposed to a blast wave could be compared to the bending produced by a TNT explosion. This device was subsequently patented [7] and later further developed by Alex van Netten [8] to provide a measure of the peak value and impulse of dynamic pressure. It was deployed on all the large scale ANFO explosions carried out at White Sands Missile Range, and was particularly valuable in studying the boundary layers from those explosions (Fig. 3).

Soon after my arrival at Suffield Experimental Station I realise that to make progress as a scientific researcher, and to achieve my long-term goal of a position at a university, it was necessary to have a Ph.D. degree. Fortunately, because I had obtained a first class honours bachelor's degree, I was able to enroll in a Ph.D. program at the University of London without first acquiring a Master's degree. Professor Gaydon was assigned as my adviser, and it was agreed that I could use my research at Suffield for my thesis. And so my thesis title was "The air velocity and density in blast waves from TNT explosions". My oral examination was held at Imperial College in early 1964. Much to my surprise one of my examiners introduced himself as "Hi, I'm Bill Penny". This heightened my anxiety because I did not know how to address him. Should I say "my Lord"? I elected just to use "Sir". For two hours I struggled inadequately to answer the examiners technical questions, and I became appalled at my own ignorance. At the end of the exam the examiners bade me farewell with no indication of my success or failure. And so I decided to play my wild card. I addressed his Lordship and described how I use his analysis of fence posts to develop the cantilever gauge. He seemed genuinely pleased to hear my story, which I think played a big part in my obtaining a Ph.D.

3 Operation Sailor Hat

In 1964 I was given responsibility to manage a major research project on behalf of Canada, known as Operation SAILOR HAT. This was a US operation in which a number of naval vessels were exposed the blast waves from 500 ton TNT charges detonated on the shore of Kahoolawe, one of the smaller Hawaiian islands. I am not sure that Canada ever received an official invitation from the US to participate in this operation. During the preparation for SNOWBALL, a 500 ton test at Suffield, I was working closely with John Keefer from the US Ballistic Research Laboratory, since we were both responsible for the basic blast measurements for our respective countries. In casual conversation he told me about the plans for SAILOR HAT and suggested that Canada might seek an invitation to participate if we had ship's structures that could be exposed or even a whole ship. This possibility seemed very unlikely, but I passed on the suggestion to Archie Pennie, the Chief Superintendent of Suffield.

Much to my surprise he liked the idea and told me to prepare a presentation for the Admirals in Ottawa. One week later I was on my way by rail, that's how we travelled in those days, to meet with the Naval Chiefs of Staff. I gave my briefing to a room full of people, none of whom I knew, but I remember that there was a lot of gold braid on display. I assumed that they knew nothing about what was going on at Suffield, and so briefed them on the shock and blast programme; told them about SNOWBALL, and what little I knew about SAILOR HAT, and that we would like to participate if we could borrow some of their equipment, namely a warship.

The first question they asked was,

> Would there be any damage to the ship?

I explained that when studying blast loading on structures, anyone can place a structure where there will be major damage or where there will be no damage. Our job as blast scientists was to find the distance from an explosion where the threshold of damage occurs. That's why we would like to borrow a ship for two tests. In the first we would place the ship at what we thought would be a safe distance and measure the blast loading to see if our predictions were valid. Based on those findings we would then station the ship on the second test where we would expect minor damage, particularly to components such as radio and radar antennae, without which the ship would not be fully operational. We would not expect any significant damage to the main superstructure or the hull.

> How long would you require this ship?
>
> From the 1st January until the middle of May.
>
> Where will the tests be carried out?
>
> Off Kahoolawe, one of the smaller Hawaiian Islands.
>
> Would any of the senior staff from Ottawa be allowed to attend as observers?

> Oh yes sir. I think it would be essential to have senior Canadian Naval representatives present as there are certain to be numerous senior US Navel Staff witnessing the tests, and our technical team will be too busy to properly represent our county at that level.
>
> Thank you Dr Dewey. We shall consider your request and let you know our decision in a few days.

When I arrived back in Suffield a few days later I was called immediately to the Chief's office to be informed that the Admirals would let us use HMCS Fraser, a destroyer under the command of Capt. Carlé, for the first two tests, on the assumption that there would be only minor damage, and that on the first test Fraser would be escorted by HMCS Qu'Appelle, another destroyer, to carry the VIP observers. I was told to manage the project, and from that point on was given complete freedom to do whatever I wanted.

This was my first opportunity for such a role. At that time a wise man from the East had come to Suffield to give a short course on P. E. R. T., Project Evaluation and Review Technique, that had been developed by the US for planning and building their first nuclear submarines. This was a godsend for me because Fraser was to leave Esquimalt on 1st January in three months' time and P. E. R. T. soon shown what we could, and more importantly what we couldn't achieve in that time.

The first task was to select the team: Dr Mike Ward, a civil engineer; senior technician Fred Winfield; Joe Vesso, our strain-gauge expert; Bill Anson, who had been my technician for several years, and Rich Campbell and Howard Johnson to handle all the electronics. The problem was that none of us had any experience with ships' structures, but we were able to have Bill Hart, a marine constructor from Rosyth in Scotland whom we knew from his work with the British team for SNOWBALL, seconded to us until the end of the first test.

The first thing that Bill asked us to do was to obtain from Ottawa the "As Fitted" plans of Fraser from which he and Mike Ward could analyse all the components of the ship. Bill Anson and I, under the guidance of John Muirhead, used pressure gauges and schlieren photography in a shock tube to measure the blast loading on 200th scale cross-sectional models of Fraser's hull and superstructure.

The shock tube measurements were scaled up and used by Mike Ward and Bill Hart to estimate the structural response of the ship's components.

Bill Hart was a very quietly spoken Scottish gentleman. Soon after beginning his analysis he insisted that we visit Fraser because he had a number of concerns, the specifics of which he did not mention. And so Bill and I flew to Victoria, rented a car and drove to Esquimalt dockyard where Fraser was moored. As we approached the vessel, still in the car, Bill said to me,

> That's not Fraser.
>
> What do you mean, I said.
>
> The As-Fitted drawings show Fraser to have a welded aluminum superstructure, but that vessel has a riveted superstructure, which means that it is almost twice as strong as that shown in the drawings.

Subsequent analysis revealed that Fraser was one of the first Canadian ships designed with a welded aluminum superstructure. Welding aluminum is not a simple process because it must be done in an inert atmosphere, otherwise it catches on fire. Apparently, the shipyard building Fraser had struggled with this problem and eventually gave up and riveted the superstructure, but this detail was never conveyed to the as-fitted drawings (Fig. 4).

We determined that the best place on the ship for the electronics would be in the ammunition storage facility, which was also the safest place, and had an access chute through which we could lower our sizeable equipment. In this area there was just sufficient room to accommodate the pre-amplifiers, amplifiers and tape recorders for 72 instruments divided between strain gauges and piezoelectric gauges. All the piezoelectric gauges were designed and built at Suffield. This was before the solid state era and the many vacuum tubes generated a considerable amount of heat. Also, the size of the individual pieces of equipment meant that there were only millimetres to spare when the equipment was lowered into the ship. We marvelled at the skill of the crane operator as he lowered the equipment without ever touching anything, only

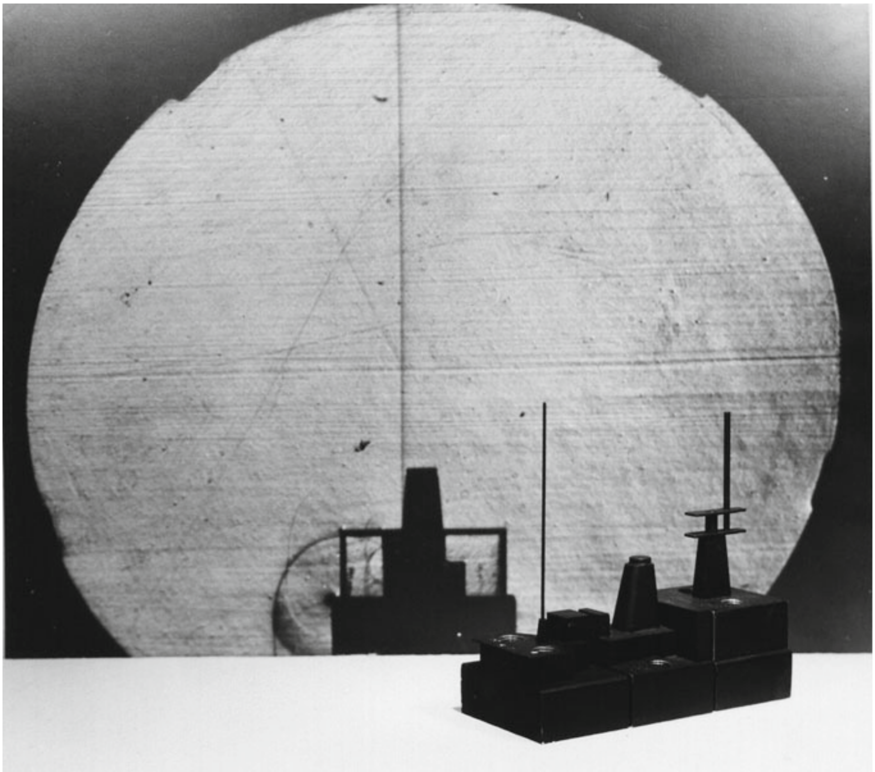

Fig. 4 A schlieren photograph taken in a shock tube of a shock interacting with a 1/200th scaled model of HMCS Fraser

guided by the finger signals from his colleague on the deck. The analogue signals from the gauges were stored on six 13-channel high-speed tape recorders, with one channel on each used as a timing comb.

Every day while at sea there would be some form of naval exercise: a man overboard rescued; a jack-stay transfer of the Captain’s steward back and forth between Qu‘Appelle and Fraser, both in daylight and at night, or a towing exercise between the two ships. The technical team was included in some of these exercises. On one occasion we activated the strain gauge recorders to measure the stress on the hull caused by the explosion of two depth charges detonated as close as possible to the ship. The mortar well from which the depth charges were fired was at the stern of the ship. From there the two depth charges were launched over the superstructure and the bridge to land in front of the vessel so that they would detonate immediately under the ship. This seemed to me to be a pretty dangerous operation, but it was carried out successfully and we obtained our gauge records.

On arrival at Pearl harbour Fraser was given a premier birth immediately adjacent to the Post Exchange, a large department store for US naval personnel with very low prices to which we were given access. Alongside was the US carrier Iwo Jima loading equipment enroute to Vietnam. From there, Fraser proceeded to the Kahoolawe test site. The US Navy provided four deep sea moorings at our selected distance from GZ. Unfortunately, the provided cables were too thick to go around Fraser’s capstan, and she had to be man-handled into position. Everyone on board, including the captain and the technical team, was called on deck and provided with a pair of thick leather gloves (I still have mine) and we took a long day to haul Fraser into position.

Late in the evening of the day on which we had man-hauled Fraser into position I was called to the Captain’s cabin. He had just received a message from the US Admiral in control of the project stating that there was a tsunami warning, and all ships were to drop their moorings and make steam. I pointed out that we were in deep water in which tsunamis are difficult to detect, and that tsunamis are only a danger in shallow shelving water. Captain Carlé decided that it was appropriate to emulate Nelson’s decision before the Battle of Copenhagen and put his telescope to his blind eye. The signalman was recalled and told not to awaken the sleeping captain, and to deliver the message in the morning. I called Rich Campbell and Howard Johnson who fired up their electronics and we sat and watched the regular sinusoidal oscilloscope signals from some of the strain gauges reacting to the gentle swells of a calm Pacific Ocean. Within a minute of the predicted time of arrival of the tsunami we saw a sudden change in the oscillation of the strain gauge signals. No one else on any of the ships was aware of the passage of the tsunami. Captain Carlé’s decision had been vindicated.

The first test was very successful. All 72 channels of instrumentation gave us good results in line with what we had predicted. The only damage we could identify was to the gyroscopic compasses that had to be re-calibrated.

We had three weeks before it was necessary to start preparing for the second test, and so on 13 February, 1965 we left Pearl Harbor enroute for Esquimalt. This meant that on the next day, when Canada flew the maple leaf flag for the first time, Fraser was the most westerly Canadian ship and therefore the last to fly the white ensign.

Fig. 5 14 February 1965, the lowering of the last white ensign to be flown on a Canadian ship

There was an appropriate ceremony on the after deck, and precisely at noon the last white ensign was lowered and replaced by the maple leaf. That ensign is now retained at the Maritime Museum in Victoria (Fig. 5).

With our experience on the first test, things went very smoothly for the second event. We had time to establish an array of black-smoke particles tracers and tower-mounted high-speed cameras on the island that subsequently allowed me to do a particle tracer analysis of the blast wave. We also set out an array of wire drag gauges, the results of which could be compared to those from SNOWBALL.

Fraser suffered more damage than had been predicted. In particular, one side of the riveted superstructure had been pierced. This was entirely my fault. In my shock tube determination of the blast loading on the superstructure I had failed to note that the Bofors deck projected 6 ft beyond the superstructure, overlapping the main deck. This meant that when the blast struck the side of the superstructure the high reflected pressure remained for approximately 6 ms longer than my predictions and added significantly to the impulse on the superstructure, thus causing the unexpected damage. Subsequent work at Suffield and the in the US demonstrated the blast enhancing effects of re-entrant structural components and is the reason why modern warships are designed without these features.

Another unexpected result was the distance travelled by the lava rock ejected from the crater. We had been accustomed to the distances travelled by the ejector from the craters at Suffield that consisted of easily fractured loam. In contrast, the large blocks of lava ejected from the Kahoolawe crater not only reached Fraser but were filmed passing over the VIPs in the observational vessels. It was a miracle that no one was killed (Fig. 6).

Fig. 6 SAILOR HAT, Shot No. 2 as the blast wave has just enveloped HMCS Fraser. The line of black smoke puffs can be seen to the left of the fireball. The two vessels outside of the blast wave are observational platforms thought to be at safe distances, but were struck by lava ejecta seen as the dark corona around the fireball

4 University of Victoria

My involvement with operation SAILOR HAT meant that in late 1964 and early 1965 I passed through Victoria on several occasions and took the opportunity to visit the Physics Department at the recently established University of Victoria. As a result of those meeting, I was offered a faculty position in the Department of Physics, commencing on 1st July 1965. This was an opportunity I had been seeking since obtaining my Ph.D. in early 1964, triggered by the observation that the structure of the Canadian Defence Research Board was changing. The direction of the research was becoming less the responsibility of the scientists and more under the direction of the military.

My first task at the University was to establish a shock tube laboratory, hoping to emulate the work that John Muirhead had been doing at Suffield and that I had seen in Professor Glass' laboratory at UTIAS. I was allowed by the Defence Research Board to take with me from Suffield one of the small valve driven shock tubes that had been used primarily to calibrate pressure gauges. This allowed me to quickly start an experimental shock research programme. I was also given funding to build a 12 × 4 inch cross-section shock tube specifically designed to obtain high quality schlieren, shadowgraph and interferometric photographs of shock wave reflections and interactions. The person primarily responsible for the development of this state of the art piece of equipment was my senior technician at the University, Larry Scotten. Larry worked with me for several years and enabled the laboratory to produce many unrivalled schlieren and shadowgraph records of shock reflections.

One technique that we developed at that time, and which provided a wealth of very accurate information, was contact shadowography. Traditional schlieren and shadowgraph techniques for the study of shock waves use a Z shaped optical system involving two parabolic mirrors. This results in a slight optical distortion of the resulting photographs. With contact shadowography a 5 × 4 inch film is pressed against the second window on the opposite side of the shock to the short duration laser light source. This means that the resulting image is without optical distortion, and is identical in scale to that of the shock phenomena being photographed.

5 Particle Trajectory Analysis

Shortly before leaving Suffield the paper describing the measurements of particle velocity in blast waves that have formed a major part of my Ph.D. thesis, was published in the Proceedings of the Royal Society [6]. At the end of that paper it was noted that from a measurement of the time resolved particle trajectories in a blast wave it may be possible to derive other physical properties in addition to the particle velocity. I continued that analysis at the University of Victoria and came to the conclusion that it was possible to determine all of the physical properties in a blast wave from the measured trajectories.

This comes about because a knowledge of the particle trajectories means that a blast wave can be analysed in Lagrangian coordinates. In Lagrangian coordinates along the particle trajectories between the primary and second shocks of a blast wave there is no change of entropy so that the simple thermodynamic relationships can be applied, which is not possible in Eulerian coordinates. When the particle trajectories initiated at a series of radial distances from the centre of the explosion are known, the spacing between two trajectories at any time can be compared with their spacing in the ambient atmosphere before the arrival of the shock, and this is directly related to the ratio of the density in the blast wave to that in the ambient air, assuming spherical symmetry, viz.,

$$\frac{\rho}{\rho_0} = \frac{R_0^2}{R^2}\frac{\Delta R_0}{\Delta R}, \tag{1}$$

where ρ and ρ_0 respectively are the density in the blast wave and the density in the ambient atmosphere; R and R_0 respectively are the radial position of a fluid element in the blast wave and its radial position before the arrival of the primary shock, and

ΔR and ΔR_0 respectively are the radial distances between two elements in the blast wave and between those elements before arrival of the primary shock. Thus, the density can be determined throughout the radius-time plane of the blast wave.

The Mach number of the primary shock, using the Rankine-Hugoniot relationships, can be used to determine the ratio of the pressure and density immediately behind the shock. From that point, each fluid element travels isentropically and adiabatically until it is overtaken by the second shock. In which case

$$\frac{P}{P_S} = \left(\frac{\rho}{\rho_S}\right)^{\gamma}, \tag{2}$$

where P and ρ respectively are the hydrostatic pressure and density of an element within a blast wave; P_s and ρ_s respectively the hydrostatic pressure and density of that element immediately behind the shock, and γ is the ratio of specific heats. Thus, knowing the density from (1), the hydrostatic pressure could be determined throughout the blast wave.

Alternatively, albeit less simply, the hydrostatic pressure could be obtained from the particle trajectories using conservation of momentum, viz.,

$$P = P_S + \rho_0 \int_{R_0}^{R_{0S}} \frac{R_0^2}{R^2} \frac{\delta^2 R}{\delta t^2} dR_0, \tag{3}$$

where R is the radial position of a particle; R_0 is the radial position of that particle before the arrival of the primary shock; ρ_0 the ambient density; $\delta^2 R/\delta t^2$ the acceleration of each particle along the constant time path of integration, and the other symbols are as defined above.

The particle velocity can be determined from the high-speed photogrammetry of the flow tracers, and so the hydrostatic pressure, density and particle velocity can be determined throughout the blast without the requirement for any other measurement. This analysis was applied to the particle trajectory measurements of two 500 ton surface burst explosions, SNOWBALL and SAILOR HAT, and the results were published in the Proceedings of the Royal Society [9].

At about this time, the Department of National Defence in Ottawa decided that their knowledge and understanding of blast waves was adequate for the defence of Canada, and the shock and blast programme at Suffield was terminated. All the shock tubes were dismantled and the state-of-the-art blast simulators were welded apart. At the same time the Defense Nuclear Agency (DNA) of the United States realise that some of the shock precursor phenomena observed on blast waves from nuclear weapons were in fact due to double Mach reflection, and a number of new projects were initiated to resolve this conflict. The test sites at Suffield were refurbished for these studies, funded entirely by DNA and without any Canadian Government scientific input.

The long term plan for my career at the University of Victoria was to phase out the studies of shock and blast waves in favour of a research programme in oceanography.

However, because of the closure of the shock and blast program at Suffield I was approached by DNA and invited to continue my high-speed photogrammetry studies on their series of height of burst experiments that were to be carried out at Suffield, for which they awarded me generous contracts. And so my oceanographic dreams were put aside.

At about this time I was approached by one of my previous undergraduate students, Douglas McMillin, who had since obtained his MSc. from Simon Fraser University, and who was seeking employment. And so he became my Research Associate for the next more than twenty years. Our respective skills complemented each other, and our collaboration was the most fruitful aspect of my research career.

Under contracts with DNA, Doug McMillin and I continued to develop high-speed photogrammetric techniques for the study of blast waves. These consisted of refractive image analysis (RIA) of shock fronts visualised against various backdrops, and particle trajectory analysis (PTA) of particle flow tracers. These techniques were used to map flow fields of blast waves in the DNA experimental series DIPOLE WEST, MIGHTY MACH, and DIAMOND ARC, all carried out at the Suffield test site. These experiments use primarily nominal 1000 lb spherical TNT charges, at a wide range of heights of burst and over different types of surfaces. From the wealth of data obtained from these experiments we were contacted by DNA and Suffield to collate all the results from over 300 explosive test, which were then used to develop the intelligent database known as *AirBlast*.

AirBlast was subsequently licensed to more than 30 international agencies studying blast waves. Unfortunately, this application is no longer compatible with modern computer operating systems, even in compatibility mode. An attempt is therefore being made to reproduce the capabilities of *AirBlast* using Excel interfaces such as that use to reproduce the blast properties from propane public/oxygen explosions [10, 11].

These early applications of PTA required large arrays of smoke tracers covering the whole flow field of the blast waves being studied. At this point, my friend and colleague Professor James Gottlieb of UTIAS, while visiting my laboratory, demonstrated a new technique that he had been developing. At that time numerical simulation was becoming a powerful tool for predicting the physical properties of blast waves. Professor Gottlieb's suggestion was to use numerical simulation to calculate blast properties; to compare those properties to experimental measurements, and then to iteratively adjust the initial conditions of the simulation until an optimum match between the calculated and measured properties was obtain. To do this he was using a technique called the random choice method.

In the simplest form of numerical simulation of blast flows, the calculated physical properties are assigned to the centre of each computational cells, but this assumes a linear relationship between the properties as functions of radius and time. This means that there is a small spatial error in each cell, which is always in the same direction. As a result, over a calculational grid of many thousand cells, the error always accumulates, thus resulting in a significant error of the final results. This can be overcome by using second or third order spatial relationships, but these relationships may not be accurately known and a considerable increase of computing is required, which was a significant problem in those days.

Professor Gottlieb had discovered that, using the random choice method, in which the physical properties calculated for a cell were randomly assigned to a position in that cell, appeared to stop the accumulation of error, even over very large computational grids, and did not add significantly to the amount of computation required. This technique was an immediate success when applied to the particle trajectory measurements. The method we used was to numerically calculate the properties of a blast wave generated in a conical channel by a moving spherical piston. The piston path was iteratively adjusted until the simulation optimally predicted the radius-time trajectories of all the measured flow tracers in a blast wave.

After applying this procedure to the analysis of several blast waves, Doug McMillin observed that in each case the optimum radius-time piston path was well described by a form of the modified Friedlander equation [12], viz.,

$$x - x_0 = \chi e^{-\propto(t-t_0)}\left(1 - \frac{t - t_0}{\tau}\right), \tag{4}$$

where x is the radial position of a point on the piston path, x_0 is the initial radial position of the piston at a point on the primary shock, t the time after initiation, t_0 the time at which the piston leaves the shock trajectory, and χ, α and τ are the fitted coefficients of a least squares fit to the equation describing the piston path.

The piston path is, of course, a particle trajectory. The piston path could therefore be described by the trajectory of a flow tracer close to the turbulent contact zone in which the detonation products mix with the ambient air. Having that information removed the need for an iterative process to determine the piston path for the random choice analysis. The validity of this procedure is demonstrated by the analysis of the blast wave from operation MINOR UNCLE. MINOR UNCLE was carried out at the White Sands Missile Range, NM USA, at 0910 h on 10 June 1993 using a 2.65 kt hemispherical surface burst ANFO charge in order to simulate the blast wave from a 4 kt surface burst nuclear explosion. The piston path method was used to determine all the physical properties of the blast wave as functions of radius and time, based only on the piston path determined by a smoke tracer initiated close to the charge and immediately outside the contact zone. The pressure–time histories determined from the analysis were compared with the electronic transducer measurements made at many distances from the explosion [13].

The outstanding agreement between the results from the two measurement procedures, shown in Figs. 7 and 8, was typical of that made at hundreds of radial positions on all the large scale ANFO explosions carried out at White Sands Missile Range. This agreement demonstrated the remarkable reliability of the physical relationships use in the two measurement techniques. One technique used a small piezoelectric crystal, coupled to a charge amplifier and other electronics, before being recorded as a voltage that was subsequently translated to a pressure using a calibration relationship. The other technique used high-speed photogrammetry to measure the trajectory

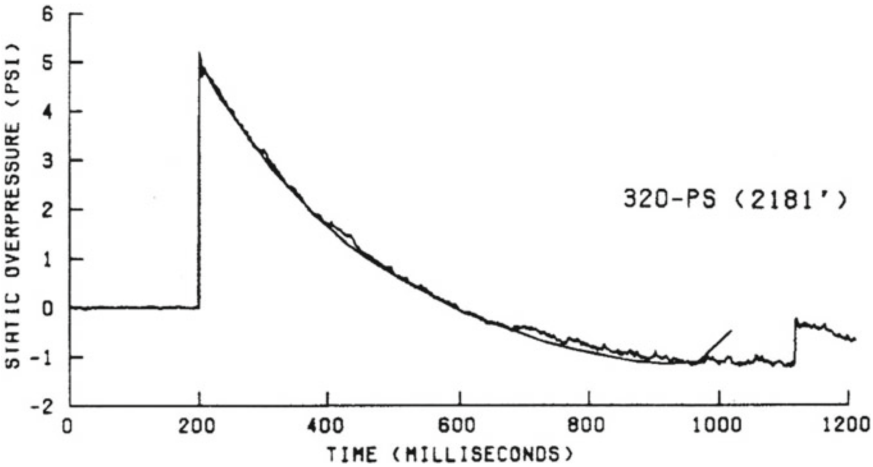

Fig. 7 The hydrostatic overpressure versus time at a radial distance of 2181 ft from the MINOR UNCLE explosion. The noisy curve is the electronic gauge measurement and the smooth curve the piston-path analysis

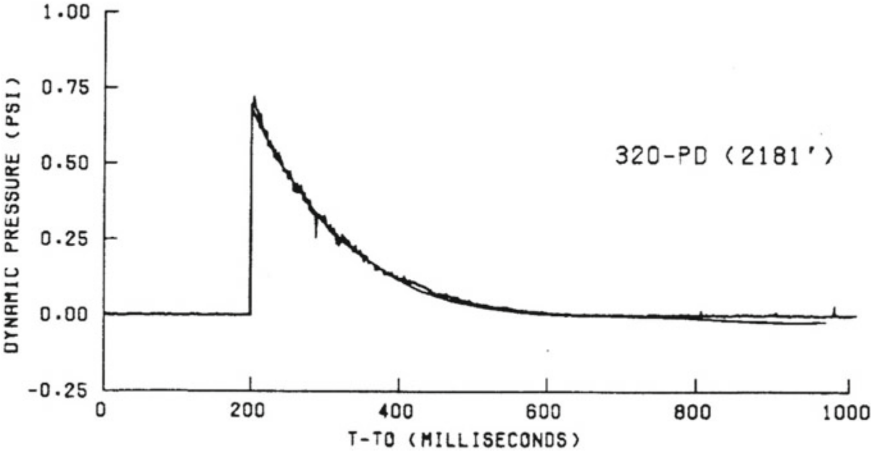

Fig. 8 The dynamic pressure versus time at a radial distance of 2,181 ft from the MINOR UNCLE explosion. The noisy curve was calculated from the electronically measured total and hydrostatic pressures, and the smooth curve is from the piston-path analysis

of a smoke puff generated close to the charge a fraction of a second before detonation, providing the radius-time trajectory of a spherical piston that was analysed to provide the physical properties of the blast wave. The two identical results gives one faith in the laws of physics.

Figure 9 shows the refractive image of the primary shock and some of the black and white smoke tracers used to analyse the blast wave produced by a 2.445 kt surface

Fig. 9 The refractive image of the primary shock and the smoke tracers used to analyse the blast wave from a 2.218 Mkg surface burst ANFO explosion (MISERS GOLD)

burst ANFO explosion (MISERS GOLD). The most left side black smoke trail was subjected to the turbulence of the contact zone between the detonation products and the ambient air. The white smoke trail to its right shows no turbulence, and its radius-time trajectory was used as the piston path in the subsequent analysis. The smoke trails were initially equidistance apart. The spacing between the trails behind the shock compared to that in front of the shock illustrates how the density within the shock wave can be calculated.

6 Shock Wave Reflection

In parallel with the study of the physical properties of blast waves generated by small and large scale explosions, the shock tube at the University of Victoria was in continued use, principally to study shock wave reflections. Again, high-speed photogrammetry was the principal tool used in these studies. Facilities were developed for shadowgraph, schlieren and interferometric photography producing both single and multiple time-resolve images. Only a monochromatic laser light source

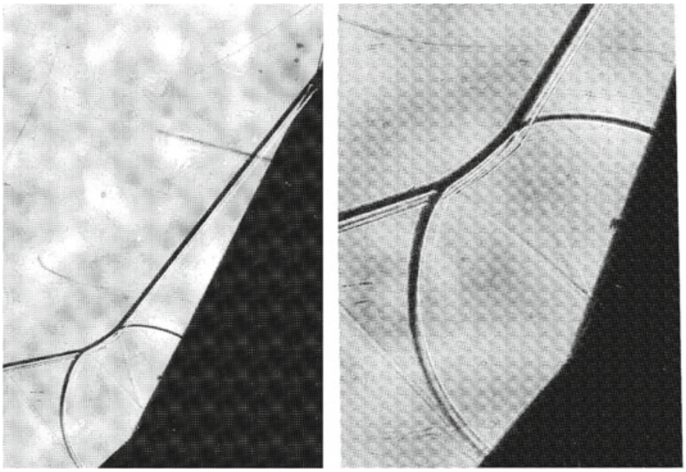

Fig. 10 Contact shadowgraphs of shock reflection from a double wedge

was use, providing very high resolution images that cannot be obtained when a broad spectrum light source is employed.

A technique using contact shadowography was developed in which large format film was pressed against the shock tube window so that the resulting image required no scaling and was without optical aberrations. Coupled with the use of monochromatic light the diffraction patterns around the shock images could be analysed to determine the shock position with high spatial resolution. An example is shown in Fig. 10 that was part of a study made in collaboration with Professor Ben-Dor [14–16].

It was essential also have the ability to use multiple time-resolve images because many of the reflection processes being studied were time dependent, a process that cannot be studied using single photographs taken on multiple experiments because of the impossibility of exactly matching the Mach number and the ambient conditions in a sequence of experiments.

Much of the work using the shock tube was directed to the study of the two-shock and three-shock theories that had been developed by John von Neumann when he was the consultant scientist to the Targeting Committee planning the nuclear attacks on Hiroshima and Nagasaki. The measurement of plane shocks reflecting from straight wedges, in general, showed good agreement with the two-shock theory in the regular reflection region. However, there was only good agreement with the three-shock theory when the speed of the incident shock was close to Mach 2. It was eventually shown that the reason for the disagreement with the three-shock theory at other shock strengths was because of the curvature and obliqueness of the reflected and Mach stem shocks, whereas von Neumann had assumed these shocks to be normal and plane.

Nearly all the shock-tube based projects were carried out by graduate students, and the results from the experiments provided the materials for their theses. These students provided invaluable support, as well as keeping me on my toes, inspiring and teaching me so much. They included: Brian Whitten (Calibration of a shock tube by analysis of the particle trajectories, 1969); Robert Johnson (Measurement of temperature in unsteady gas flows, 1969); David Walker (Particle trajectory analysis of a two-dimensional shock tube flow, 1970 and Study of two-dimensional shock tube flows by following particle trajectories using a multiply pulsed laser schlieren system, 1974); Gary Lock (An experimental investigation of the sonic criterion for transition from regular to Mach reflection, 1985); Roberto Racca (A method for automatic particle tracking in a three-dimensional flow field, 1988 and Time resolved holography for the study of shock waves, 1990); Moshe Olim (Least energy as a criterion for transition between regular and Mach reflection, 1991), and Alex van Netten (The design of a holographic interferometer and its use for the study of curved oblique shocks produced by shock reflections, 1988 and The use of cantilevers as blast wave gauges, 1995).

7 International Symposia

International conferences played a major role in my scientific career, partly because they kept me informed of the latest developments in my areas of interest, but more importantly because of the friendships and collaborations that were initiated with so many scientists from all over the world. The importance of spouses programs associated with these conferences must also be stressed. Conference delegates, when meeting socially, typically continue discussing scientific matters. In contrast, the spouses on their tours, discuss home and family matters, and this leads to familial friendships, visits and shared holidays. Relationships developed in this way have had a significant impact on my scientific work.

The conferences I attended most regularly were the International Shock Wave Symposia; the International High-Speed Photography and Photonics Congress, which I hosted in Victoria in 1994; the International Mach Reflection Symposia, and the Military Aspects of Shock and Blast Symposia (MABS). I am pleased to have played a part in the initiation of the latter two of these symposia.

While involved in the shock and blast programme at Suffield in the 1960s, the only specialist symposium for the presentation of blast research was the International Shock Tube Symposium, as it was then called, but this was not always a suitable forum. I therefore made a suggestion to the Chief Superintendent of Suffield that we might host an International Blast Wave Symposium. Subsequently, after discussion with American colleagues, it was decided to plan a conference called Military Applications of Blast Simulation (MABS), examining the use of conventional explosives to simulate nuclear blast waves. The first MABS was held at Suffield in 1967. As nuclear tensions decreased this conference expanded its emphasis to all forms of blast phenomena and changed its tile but retained the acronym MABS.

In the early 1980s, when interest in shock reflection was mounting, I invited a group of scientists involved in this field to a meeting at my laboratory that I called the International Mach Reflection Symposium. Because it was a relatively small group of researchers, the meeting was held in a workshop format in which each attendee was invited to describe their most recent research activity, any problems they were encountering, and their planned research for the next year. There were no time limits on the presentations, and participants were encouraged to interrupt the speaker with questions at any time. In lieu of Proceedings, each speaker was invited to provide copies of their PowerPoint slides that were duplicated and given to all attendees. This format proved so successful, and generated so much discussion and collaborative research, that many subsequent meetings were held, sometimes twice a year at different international locations. Eventually the name of this symposium was changed to the International Shock Interaction Symposium, and reverted a more conventional format.

Acknowledgements In concluding this autobiographical summary of my research career, I would like to acknowledge some of the distinguished scientists with whom I have been privileged to collaborate: Drs Heinz Reichenbach and Werner Heilig of the Ernst Mach Institute in Freiburg, Germany; Professors Irvin Glass and James Gottlieb of UTIAS; John Keefer, Ralph Reisler and Noel Etheridge of the Ballistic Research Laboratory, USA; Dr George Ullrich, Associate Director of the Defense Nuclear Agency; Arnfinn Jensen of the Norwegian Defence Construction Service; David Ritzel of DynFX; Professor Gabi Ben-Dor of the Ben-Gurion University of the Negev, Israel; Professor Kazu Takayama of Sendai University, Japan; Professor Beric Skews of the University of Witwatersrand, South Africa; Charles Needham of Applied Research Associates, USA; Professor Harald Kleine of the University of New South Wales, Canberra, Australia, and Professor Isabelle Sochet of INSA Centre Val de Loire, Bourges, France.

References

1. Dewey JM (1985) The propagation of sound from the eruption of Mt. St. Helens on 18 May 1980. Northwest Sci 59(2):79–96
2. Sakurai A (1953) On the propagation and structure of a blast wave, Pt I. J Phys Soc Japan 8(5):662–669
3. Sakurai A (1954) On the propagation and structure of a blast wave, Pt II. J Phys Soc Japan 9(2):256–266
4. Sakurai A (1982) Solution of point source blast wave equation. J Phys Soc Japan 51(5):1355–1356
5. Dewey JM, Anson WA (1963) A blast wave density gauge using beta radiation. J Sci Instr 40:568–572
6. Dewey JM (1964) The air velocity in blast waves from t.n.t. explosions. Proc Roy Soc A 279:366–385. https://doi.org/10.1098/rspa.1964.0110
7. Dewey JM, Anson WA (1966) Wire blast gauge. Can Pat No 748(640):66–0157
8. van Netten AA, Dewey JM (1997) A study of blast loading on cantilevers. Shock Waves 7:175–190
9. Dewey JM (1971) The properties of blast waves obtained from an analysis of the particle trajectories. Proc Roy Soc A 324:275–299. https://doi.org/10.1098/rspa.1971.0140
10. Dewey JM (2019) An interface to provide the physical properties of blast waves generated by propane explosions. Shock Waves 29(4):583–587. https://doi.org/10.1007/s00193-018-0866-5

11. Dewey JM (2020) Addendum: an interface to provide the physical properties of blast waves generated by propane explosions. Shock Waves 30:439–441. https://doi.org/10.1007/s00193-020-00945-0
12. Dewey JM (2018) The Friedlander equations, Chapter 3 in blast effects: physical properties of shock waves, Ed. I. Sochet. Springer Nature
13. Dewey JM, McMillin DJ (1995) Smoke trail photo diagnostics, Chapter 2, MINOR UNCLE Symposium Report, vol. 2, Event diagnostics and calculations, Def. Nuc. Agency, POR 7453–2
14. Ben-Dor G, Dewey JM, Takayama K (1987) The reflection of a plane shock wave over a double wedge. J Fluid Mech 176:483–520
15. Ben-Dor G, Takayama K, Dewey JM (1987) Further analytical considerations of weak planar shock wave reflections over a concave wedge. Fluid Dyn Res 2(2):77–85
16. Ben-Dor G, Dewey JM, McMillin DJ, Takayama K (1988) Experimental investigation of the asymptotically approached mach reflection over the second surface in a double wedge reflection. Exp In Fluids 6:429–434

Chronological Bibliography

Dewey JM (1965) Precursor shocks produced by a large-yield chemical explosion. Nature 205(4978):1306

Dewey JM (1968) Methods of studying the effects of blast waves on ships' superstructures. Marine Tech 6(3):268–273

Dewey JM, Anson WA (1969) Density measurements in a valve driven shock tube. Rev Sci Instr 40(3):451–455

Dewey JM, Patterson AM, Kingery CN, Rowe RD, Petes J (1972) Fireball and shock wave anomalies observed in chemical explosions. Comb Flame 19:25–32

Beer GA, Dewey JM, Mathie EL, Walker DK (1975) Velocity of ruptured window material in accelerator beam lines. Nucl Intrum Methods 129:353–355

Dewey JM, Walker DK (1975) A multiply pulsed double-pass laser schlieren system for recording the movement of shocks and particle tracers within a shock tube. J Appl Phys 46(8):3454–3458

Dewey JM, Whitten BT (1975) Calibration of a shock tube flow by analysis of the particle trajectories. Phys Fluids 18(4):437–445

Dewey JM, McMillin DJ, Classen DF (1977) Photogrammetry of spherical shocks reflected from real and ideal surfaces. J Fluid Mech 81(4):701–717

Dewey JM (1979) The Mach reflection of spherical blast waves. Nucl Eng Des (Netherlands) 55(3):363–373

Dewey JM, McMillin DJ (1981) An analysis of the particle trajectories in spherical blast waves reflected from real and ideal surfaces. Can J Phys 59(10):1380–1390

Walker DK, Dewey JM, Scotten LN (1982) Observations of density discontinuities behind reflected shocks close to the transition from regular to Mach reflection. J Appl Phys 53(3):1398–1400

Dewey JM, McMillin DJ (1985) Efficiency of energy conversion using shock waves. Can J Phys 63(3):339–345

Dewey JM, McMillin DJ (1985) Observation and analysis of the Mach reflection of weak uniform plane shock waves, part 1. Observations. J Fluid Mech 152:49–66

Dewey JM, McMillin DJ (1985) Observation and analysis of the Mach reflection of weak uniform plane shock waves. part 2. Analysis. J Fluid Mech 152:67–81

Ben-Dor G, Dewey JM (1985) The Mach reflection phenomenon: a suggestion for an international nomenclature. AIAA 23(10):1650–1652

Racca RG, Dewey JM (1988) A method for automatic particle tracking in a three-dimensional flow field. Expt Fluids 6:25–32

Racca RG, Dewey JM (1989) Time-resolved holography for the study of shock waves. Proc Soc Photo Opt Instrum Eng 1032:578–586

Lock GD, Dewey JM (1989) An experimental investigation of the sonic criterion for transition from regular to Mach reflection of weak shock waves. Expts Fluids 7:289–292

Racca RG, Dewey JM (1989) Time smear effects in spatial frequency multiplexed holography. Appl Optics 28(17):3652–3656

Dewey JM (1989) Explosive flows: shock tubes and blast waves, Chapt. 29. Yang W-J (ed) Handbook of flow visualization, Hemisphere. New York

Racca RG, Dewey JM (1990) High speed time-resolved holographic interferometer using solid-state shutters. Optics Laser Tech 22(3):199–204

Olim M, Dewey JM (1991) Least energy as a criterion for transition between regular and Mach reflection. Shock Waves 1:243–249

Olim M, Dewey JM (1992) A revised three-shock solution for the Mach reflection of weak shocks (1.1 < Mi < 1.5). Shock Waves 2:167–176

Dewey JM (1997a) Shock waves from explosions, Chapt. 16. In: Ray SF (ed) High speed photography and photonics. Focal Press, Oxford, pp 245–253

Dewey JM (1997b) Explosive flows: shock tubes and blast waves, Chapt.29. In: Yang W-J (ed) Handbook of flow visualization, 2nd edn. Hemisphere, New York

Dewey JM (2000) Spherical expanding shocks (blast waves). In: Handbook of shock waves 13.1, vol 2. Academic Press, pp 441–481

Kleine H, Dewey JM, Ohashi K, Mizukaki T, Takayama K (2003) Studies of the TNT equivalence of silver azide charges. Shock Waves 13:123–138

Dewey JM (2005) The TNT equivalence of an optimum propane-oxygen mixture. J Phys D Appl Phys 38:4245–4251

Dewey JM (2007) The TNT equivalence as a function of distance from the explosion of an optimum propane-oxygen mixture. Expl Eng 19–23

Dewey MC, Dewey JM (2014) The physical properties of the blast wave produced by a stoichiometric propane/oxygen explosion. Shock Waves 24:593–601. https://doi.org/10.1007/s00193-014-0521-8

Dewey JM (2016) Measurement of the physical properties of blast waves. In: Igra O, Seiler F (eds) Experimental methods of shock wave research. Springer

Dewey JM (2018a) The Rankine-Hugoniot equations: their extensions and inversions related to blast waves, Chapt. 2 in Blast Effects: physical properties of shock waves, ed. I. Sochet. Springer Nature

Dewey JM (2018b) The Friedlander equations, Chapt. 3 in Blast Effects: physical properties of shock waves, ed. I. Sochet. Springer Nature

Dewey JM (2020) Studies of the TNT equivalence of propane, propane/oxygen and ANFO. Shock Waves 30(5):483–489. https://doi.org/10.1007/s00193-020-00949-w

Dewey JM, Sochet I (2021) Analysis of the blast waves from the explosions of stoichiometric. rich and lean propane/oxygen mixtures. Shock Waves 31(2):165–717. http://link.springer.com/article/10.1007/s00193-021-01005-x

Research Activities at the Wisconsin Shock Tube Laboratory

Riccardo Bonazza

1 History

The Wisconsin Shock Tube Laboratory (WiSTL) was established by the author in the late 1990s. The main apparatus is a downward-firing, vertical shock tube with large internal square cross section. The shock tube is described in detail in [1]. The shock tube was designed specifically to study shock-accelerated gas interfaces of the kind typically observed in the Richtmyer-Meshkov instability (RMI) [2, 3], viz. nominally flat interfaces with small perturbations (to be described in detail in Sect. 2). This informed the first criterion in the design of the shock tube: a cross section large enough to minimize the effect that the boundary layers that develop on the shock tube walls would have on the behavior of the interface.

Next was the need for parallel walls to perform flow visualization in both line-of-sight and planar arrangements. Historically, because of structural considerations, shock tubes had always been built with circular cross section. If the need arose to perform flow visualization, the common solution had been the use of an extension (sometime referred to as a “cookie cutter”) with square or rectangular cross section that was mounted at the end of the circular tube. Brad Sturtevant, of the California Institute of Technology, was the first one, in the mid 1980s, to design and build a shock tube with square internal cross section to eliminate the need for a cookie cutter. For the WiSTL shock tube, these two criteria (minimization of wall effects and need for parallel walls) led to a square cross section of 25 cm 25 cm.

The third consideration in the design of the shock tube involved the preparation of a gas interface. Since the available shock tube facilities were all horizontal, the early experimental studies of the RMI [e.g. 3, 4] relied on very thin membranes (typically

---

R. Bonazza (✉)
Wisconsin Shock Tube Laboratory, Department of Engineering Physics, University of Wisconsin-Madison, 1500 Engineering Drive, Madison, WI 53706, USA
e-mail: riccardo.bonazza@wisc.edu

© The Author(s), under exclusive license to Springer Nature Switzerland AG 2022

K. Takayama and O. Igra (eds.), *Frontiers of Shock Wave Research*,
https://doi.org/10.1007/978-3-030-90735-8_4

nitrocellulose) to prepare an interface for shock-acceleration. This posed two problems: the possibility that the membrane fragments, with density about 1,000 times that of the gases, would alter the post-shock flow at the interface; and the certainty that the fragments would severely interfere with any kind of flow visualization. Once again, it was Sturtevant that came up with a solution: orient the shock tube vertically to rely on gravitational effects to separate gases of different density and form an initial condition. The WiSTL shock tube is vertical, with the driver section at the top (circular, 42 cm ID, 1.9 cm thick), and the test section near the bottom.

The final unique property of the WiSTL shock tube is its structural capability. The tube and the test section are designed to withstand a pressure of 20 MPa, a value that would be reached behind the reflection off the tube end wall of $M = 5$ shock wave initially launched into air at standard conditions. Historically, the approach to achieving high Mach numbers in shock tubes with lesser structural capabilities was to lower the pressure in the driven section. The problem with this approach is that the driven gas density is correspondingly decreased leading to an increase in the kinematic viscosity () which in turn causes the boundary layer thickness (which is proportional to) to be larger than it would be if a shock wave of the same Mach number were released into a driven gas at atmospheric pressure.

The inside of the WiSTL shock tube's driven section is a square liner (25 cm 25 cm) consisting of four stainless steel plates welded together. The liner is supported by a concrete matrix contained in a circular carbon steel pipe. The test section is made of four steel plates, 7.5 cm thick. It contains window- and instrumentation-ports on all four sides. The entire driven section consists of flanged segments of different length. This modular structure allows to vary the initial position of a gas interface relative to both the diaphragm and the end wall, thus making it possible to observe the shocked and re-shocked interface over large time intervals. The combined driven and test sections have a total length of about 7 m. A sketch and a photograph of the facility are shown in Fig. 1.

2 Richtmyer-Meshkov Instability

The Richtmyer-Meshkov instability is the unbounded growth of perturbations initially present on an interface between media of different density (or, more generally, acoustic impedance) that is impulsively accelerated by a shock wave. It is caused by the baroclinic generation of vorticity consequent to the misalignment between the pressure and density gradients associated with the shock wave and the material interface, respectively (The simplest configuration is that of a discontinuous, two-dimensional, single-mode sinusoidal interface with initial amplitude and wavelength. Initially, the perturbation grows linearly according to what is commonly called the "impulsive model": where is the dimensionless density difference across the interface (the Atwood number), k is the wavenumber, and t is time. This linear regime persists until. After that, the growth becomes non-linear with exponent <1 and the shape of the interface changes from sinusoidal to a combination of spikes/bubbles of the

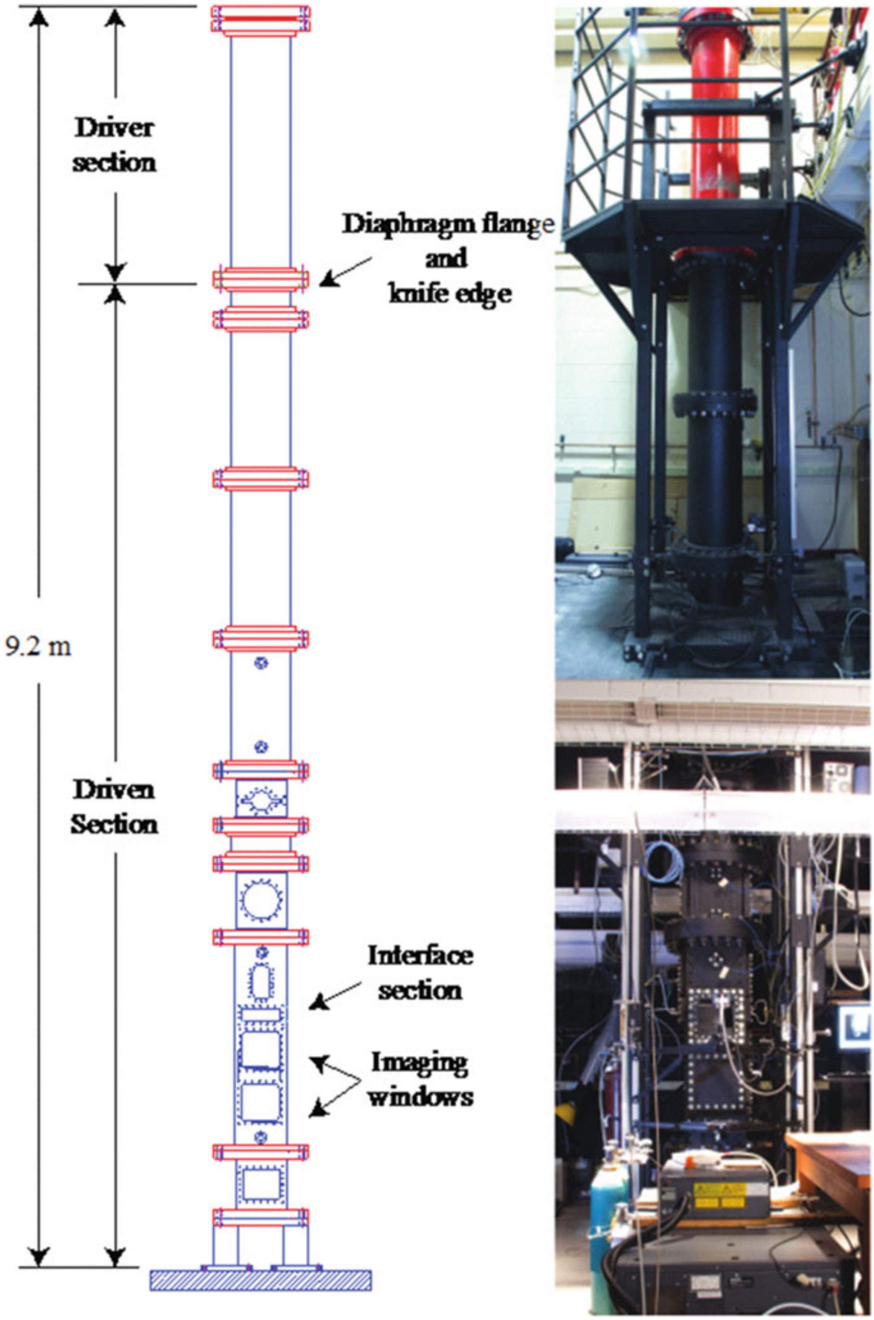

Fig. 1 Schematic and images of the WiSTL shock tube

heavy/light material penetrating into the other one. At even later times, secondary instabilities lead to the complete break-up of the interface and the transition to a mixing zone.

The RMI is known to occur over very large ranges of length, time, and energy scales, from astrophysical phenomena [5], to conceptual hypersonic combustion systems [6], to small-scale/high-energy-density laser-driven experiments like those at the National Ignition Facility (NIF) at Lawrence Livermore National Laboratory [7].

In man-made applications, the effect of shock-induced mixing can be advantageous, as in the case of hypersonic combustion systems [6]; or severely unfavorable, as in ICF implosion experiments where the shell material mixes with the nuclear fuel leading to no ignition or reduced yield [7]. A very comprehensive review of many years of RMI studies is in [8, 9].

In all the cases (natural or man-made) where the RMI occurs in practice, the pre-shock interface is actually much more complicated than the simplified version described above. Typical interfaces are three-dimensional, multimode, sometimes diffuse. While all modes are in the linear regime, the impulsive model can be applied via linear superposition to determine the overall amplitude of the perturbation. But once some modes break the linearity condition, non-linearities and mode coupling become important and linear superposition is no longer applicable.

Accordingly, over the years the focus in the study of the RMI has shifted from the amplitude (of a single-mode interface) to the thickness (of a fully developed mixing layer) to the details of the turbulent flow within the layer. Correspondingly, the experimental study of the RMI at institutions all over the world has evolved in two main respects: the approach used to prepare the initial interface and the diagnostic techniques utilized to measure the quantities of interest.

Below are the milestones of this evolution in our laboratory.

Experiments with Membranes

In our first experiments (late 1990s) [1] the interface was prepared using a nitrocellulose membrane and the flow was visualized using the shadowgraph technique. These experiments were used to check the basic functionality of the new shock tube and were carried out in full awareness of the adverse effects caused by the membrane.

Experiments with Retracting Plate

In our first experiments without a membrane (early 2000s) [10] preparation of the gas interface relied on the use of retractable plate with a 2D sinusoidal perturbation impressed on it (See Fig. 2a, taken from [10]). Carbon dioxide and air (the latter seeded with cigarette smoke for visualization purposes) were initially introduced

Fig. 2 **a** retractable plate with sinusoidal perturbation. **b** imaging schematic

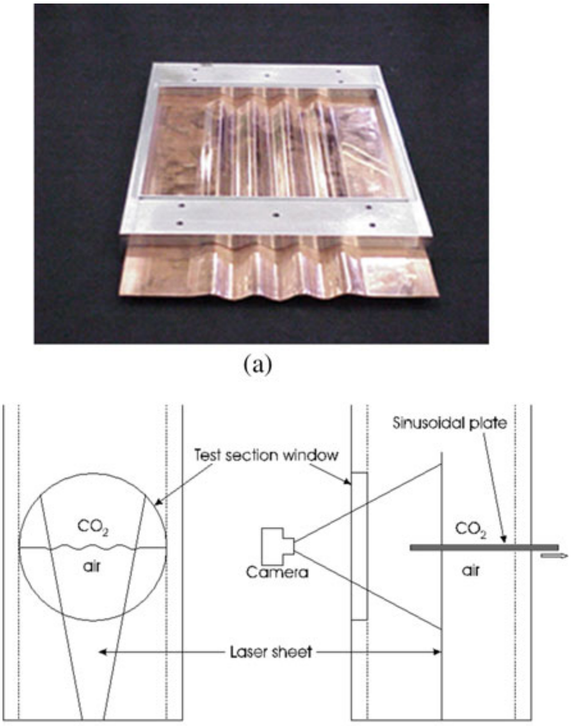
(a)

(b)

above and below the plate, respectively. Flow visualization (both before and after shock-acceleration) consisted of planar Mie scattering implemented by illuminating a vertical cross section of the flow with a light sheet generated using an Nd:YAG laser emitting at 532 nm (see Fig. 2b, taken from [10]).

Upon plate retraction, the Rayleigh-Taylor instability onset leading to an initial condition that evolved in time until the arrival of the shock wave. Samples of the interface cross section before shock arrival are in Fig. 3 (taken from [10]). The images in Fig. 3 suggest that the plate retraction technique afforded the ability to vary the initial condition by simply allowing different times to elapse between plate retraction and shock arrival at the interface. A short time delivered a “linear” initial condition while a long delay produced a highly non-linear initial condition. But the advantage of this versatility was adversely affected by the motions in the third direction (the one of the plate retraction itself). These caused the entire interface surface to have a much more irregular, unpredictable shape that would require 3D characterization immediately before shock arrival.

Fig. 3 Initial condition based on Rayleigh–Taylor instability. Times after plate retraction: **a**, 0 **ms**; **b**, 60 **ms**; **c**, 250 ms

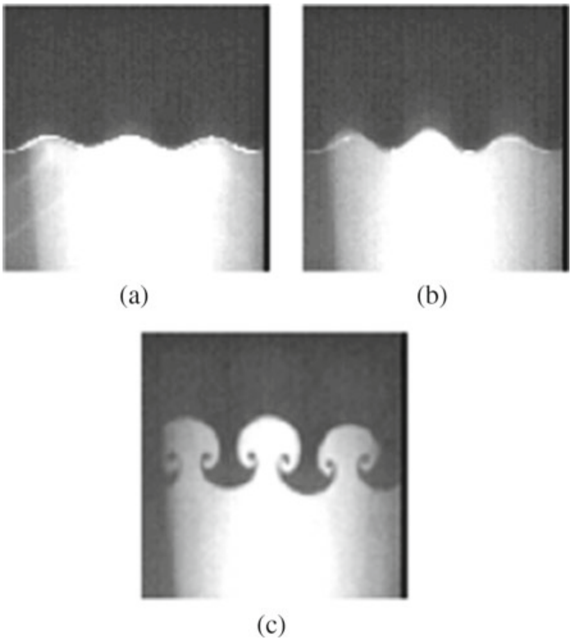

Experiments with Pistons

Because of these difficulties, a new approach for the preparation of an initial condition was developed [11]. It was based on a technique first developed by Jeff Jacobs at the University of Arizona [12]. Two gases are injected in a vertical, square shock tube: one (of lower density) flowing downward from just below the diaphragm, the other (of higher density) flowing upward from near the end wall. The two streams meet at a vertical location that can be adjusted by varying the two inlet flows. At that location, suction is provided through one or two ports in the shock tube sides to remove any excess gas and maintain the desired pressure (typically atmospheric). This results in a nominally flat, gravitationally stable interface. To impose a perturbation, the Arizona group oscillated the shock tube about a pivot point near the diaphragm. At WiSTL, a perturbation was imposed by horizontally oscillating two pistons imbedded in the shock tube walls as shown in Fig. 4. (taken from [11]).

The pistons contained slots connected to the vacuum line. They were oscillated at a frequency of 2.1 Hz, with a total travel of 2.86 cm using a computer-controlled stepper motor. This resulted in a 2D interface with a six-mode perturbation, with mode 3 being highly dominant. The flow was visualized on a vertical cross section with planar Mie scattering implemented in the same way as for the retractable plate case (cigarette smoke; ND:YAG laser sheet at 532 nm). The experimental campaign [13] covered large ranges of the Atwood and Mach numbers, for interfaces accelerated by a single shock and observed to very late times. By normalizing the interface

Fig. 4 Schematic of oscillating pistons used to impose initial perturbations

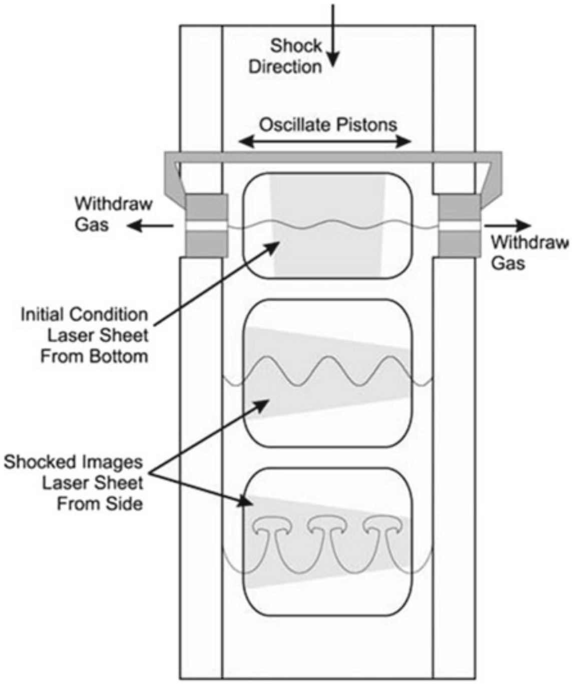

amplitude as) (where k is the wavenumber and the 0-subscript and 1-superscript represent the initial condition and the value immediately after shock acceleration, respectively) and time as (where is the amplitude growth rate immediately after shock acceleration), an excellent collapse was observed for the amplitude time history data for several different combinations of A and M.

For the case of $A = 0.29$ and $M = 1.92$, the interface was also studied after acceleration by the shock wave reflected off the shock tube end wall (reshock) [14].

Experiments with Shear Layer (Single-Shot PLIF)

While the oscillating pistons provided a very interesting and well-controlled initial condition, the system was not well suited to generate an interface with richer modal content. This type of initial condition is very important as it is more closely representative of the interfaces present in the actual occurrences of the RMI. It was for this purpose that a new method was devised to set up an interface. The entire campaign is described in [15, 16]. A schematic of the initial condition generation and imaging systems is shown in Fig. 5 (taken from [16]). The technique starts with the same gravitationally stable interface as in the previous case. To force broadband perturbations on it, a shear layer is superposed on it. The same two gases separated by the

Fig. 5 Interface generation by means of a shear layer

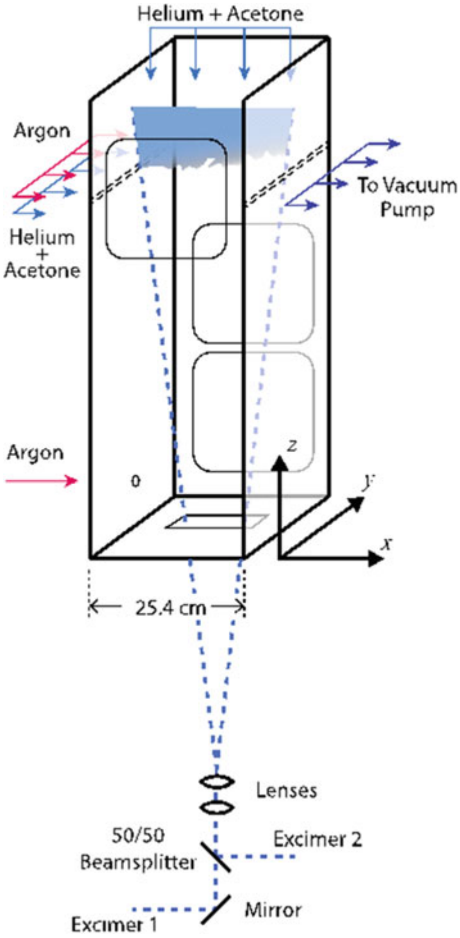

stagnation surface are injected horizontally immediately above and below its plane but in reversed order, with the heavy gas on top and the light one below. This was the result of prolonged tests to assess which configuration would produce the more "interesting" initial conditions. In all the campaigns performed with this setup, the light and heavy gases were helium and argon, respectively.

The resulting interface is described in Fig. 6 (taken from [16]). This initial condition was studied extensively, utilizing planar laser-induced fluorescence (PLIF) implemented by seeding the helium above the stagnation plane and in the shear layer with acetone (resulting in an Atwood number $A = 0.7$) and by illuminating a cross section of the flow with a vertical laser sheet generated using an excimer laser emitting at 308 nm. It was found that the amplitude spectrum of this interface was highly repeatable in time while the phase spectrum was not.

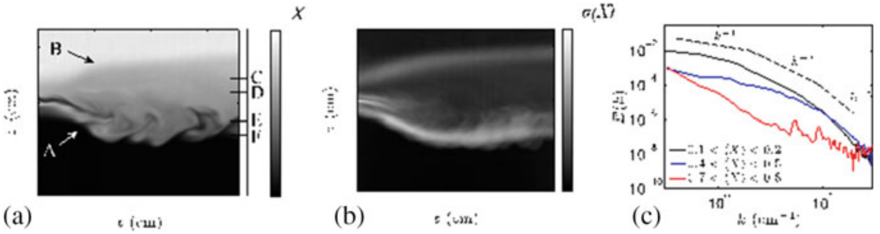

Fig. 6 Initial condition image and spectrum. **a** A sample initial condition image, processed so intensity corresponds to light-gas mole fraction. **b** Mole fraction standard deviation from 100 images. **c** Mole fraction energy spectra from three spanwise averaged mole fraction ranges

Use of PLIF provides access to the 2D concentration (i.e. density) field. This was a major advance with respect to planar Mie scattering experiments from which only macroscopic quantities (like amplitude and thickness) could be extracted. Analysis of this field allows for the evaluation of several integral properties (the thickness being only one of them) and of many statistical and spectral quantities.

In early experiments [15, 16], PLIF was carried out in single-shot mode, meaning one or two images were recorded in each run. The laser sheets were generated using excimer lasers delivering up to 500 mJ/pulse at 308 nm, resulting in images with very high signal-to-noise ratio. Data were collected at four post-shock times, for two different Mach numbers, $M = 1.6$ and $M = 2.2$. Samples of the concentration field for $M = 1.6$ are shown in Fig. 7 (taken from [16]).

The images show clearly the main stages of the interface evolution: compression; amplification of the larger wavelengths; appearance of smaller wavelengths; turbulent-looking zone. One of the most important results of the analysis of the concentration field was that the macroscopic Reynolds (obtained using three distinct approaches) had crossed a threshold value of about 10,000 indicated by Dimotakis [17] as a lower limit for the transition to fully developed turbulent mixing.

Experiments with Shear Layer (Concurrent, Single-Shot PLIF/PIV)

While many other conclusions could be reached from the PLIF data, important turbulence metrics involving the cross correlation of density and velocity fields remained elusive because of the lack of velocity measurements. Implementing particle image velocimetry (PIV) by itself (even at the same post-shock times at which PLIF had been performed) would not help since the initial condition's phase spectrum was not very repeatable. The only way to generate useful measurements of density and velocity is to perform PLIF and PIV concurrently. This was achieved in another highly successful campaign [18, 19]. Particle image velocimetry (PIV) was carried out by seeding both gases in the shear layer and the volumes immediately above

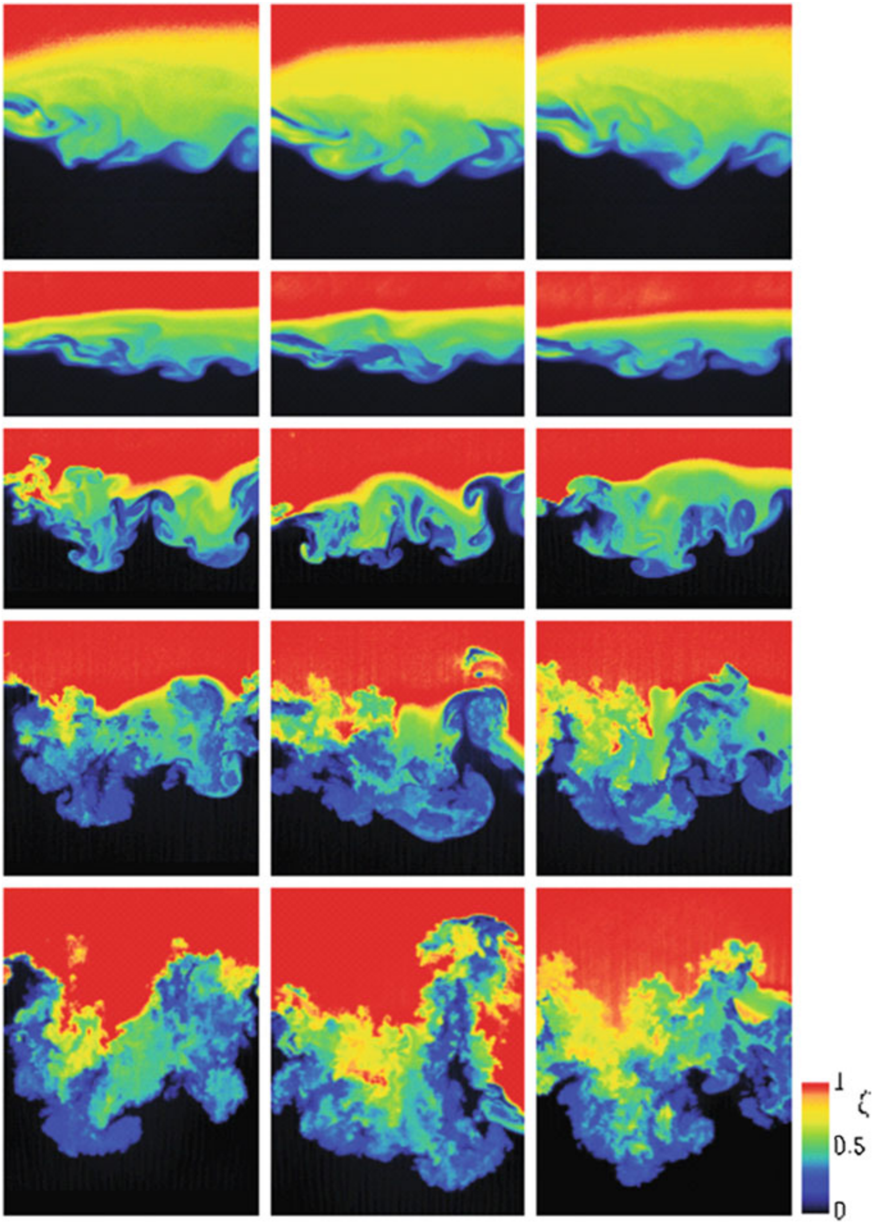

Fig. 7 Selected images from $M = 1.6$ experimental sequence. First row: initial condition images. Second row: PS1, 0.14 ms after shock interaction. Third row: PS2, 0.88 ms after shock interaction. Fourth row: PS3, 2.16 ms after shock interaction. Fifth row: PS4, 3.84 ms after shock interaction. The width of each image is 14.0 cm

and below the interface with TiO_2 particles (200 nm in diameter) and illuminating a vertical cross section of the flow with an Nd:YAF laser. Simultaneous acquisitions of density and velocity were performed in single-shot mode at four post-shock times and at the same two Mach numbers as before. The diagnostics required the co-propagation of two laser beams, one at 308 nm (for PLIF) and one at 532 nm (for PIV). A schematic of the experiment is in Fig. 8 (taken from [19]).

The PLIF and PIV images required a registration process (described in detail in [19]) to ensure that concentration and velocity data were made available at the same points in physical space. A sample of the data is in Fig. 9 (taken from [19]).

Analysis techniques similar to those that had been used in [15, 16] were employed in this campaign (integral, statistical, spectral) but this time quantities like the turbulent mass-fraction velocity and the Reynolds stresses (where indicates spanwise averaging and primes indicate fluctuations) could be studied in detail. The results confirmed that the flow transitions into a fully turbulent mixing regime towards the late times, and some of the most salient properties of this state could be quantitatively extracted from the data.

Experiments with Shear Layer (High-Speed PLIF)

The next frontier was time resolution. In single-shot experiments, a single data field (concentration from PLIF) or two data fields (concentration from PLIF and 2D-velocity from PIV) are collected at each run. In the case of a highly unsteady flow, as that for a shock-accelerated interface, the evolution equations for all relevant quantities involve time derivatives and no time derivatives can really be extracted from data acquisitions at discretely-spaced times. What is necessary is high-speed acquisition. All this became possible as a pulse-burst mode laser (designed and built by David Rothamer of the ME department of UW-Madison) became available to our lab. The laser provides a pulse train, at 20 kHz repetition rate, 10 ms in duration, at 266 nm, with an energy of 30 mJ/pulse and pulse duration of 10 ns. Here it must be remarked that even such high repetition rate would not be adequate to time-resolve the motion of the shock-accelerated interface (traveling at about 500 m/s or more) since the interframe displacement would be much too large (2.5 cm or more) to perform any kind of correlation. Furthermore, the interface would be visible in a test section window only for a very short time. What is feasible instead is to study the interface upon reshock. In this case, the interface moves upwards at about 60 m/s and 20 kHz is adequate to track its motion in detail.

Experiments were performed with the usual (He + acetone)/Ar interface, with an incident shock of $M = 1.9$ [20, 21]. Samples of the concentration fields are shown in Fig. 10 (taken from [20]). A time of 0 ms indicates the arrival at the interface of the reflected shock. The images on the far left represent the initial condition for the interaction that is about to take place. It is clearly visible that, although all experiments are started with the same nominal shear layer, the time fluctuations of

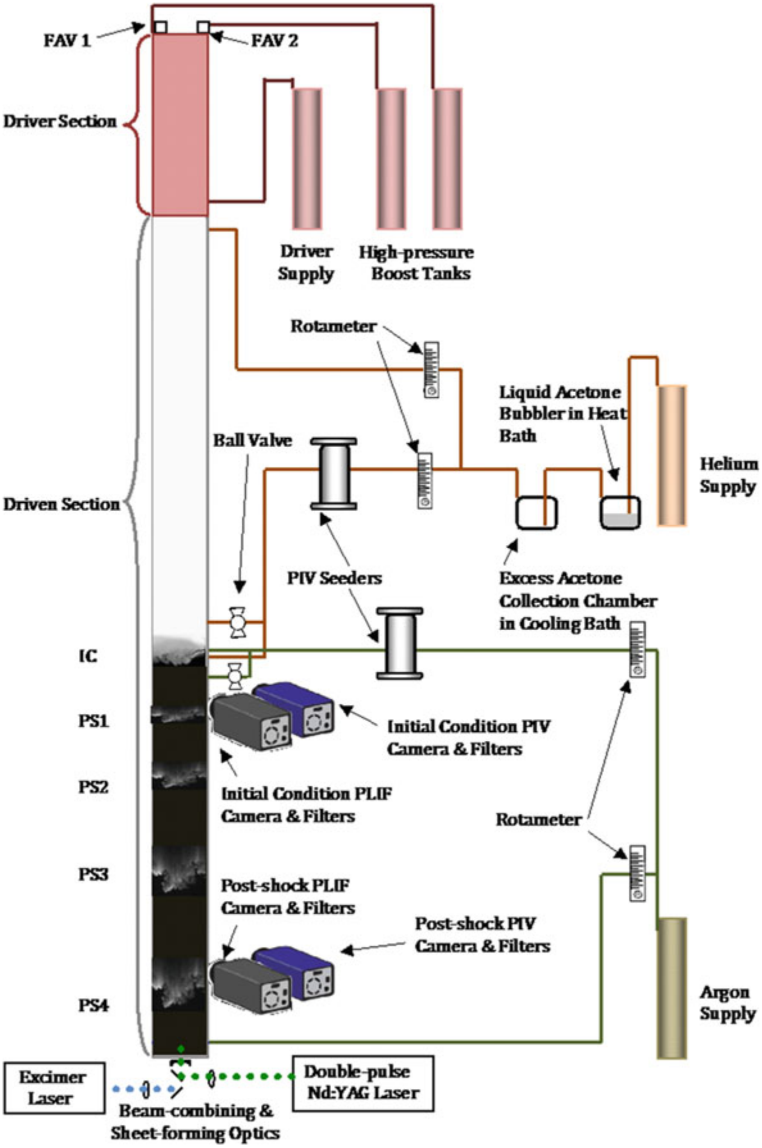

Fig. 8 Schematic of experimental setup for concurrent PLIF and PIV

the phase spectrum cause the actual initial condition seen by the reshock to vary significantly from one experiment to the next one.

Once again, the data were analyzed with statistical and spectral techniques. For the first time, it was possible to observe the time evolution of the structure functions and power spectra of the density fluctuations, elucidating the transition of the flow

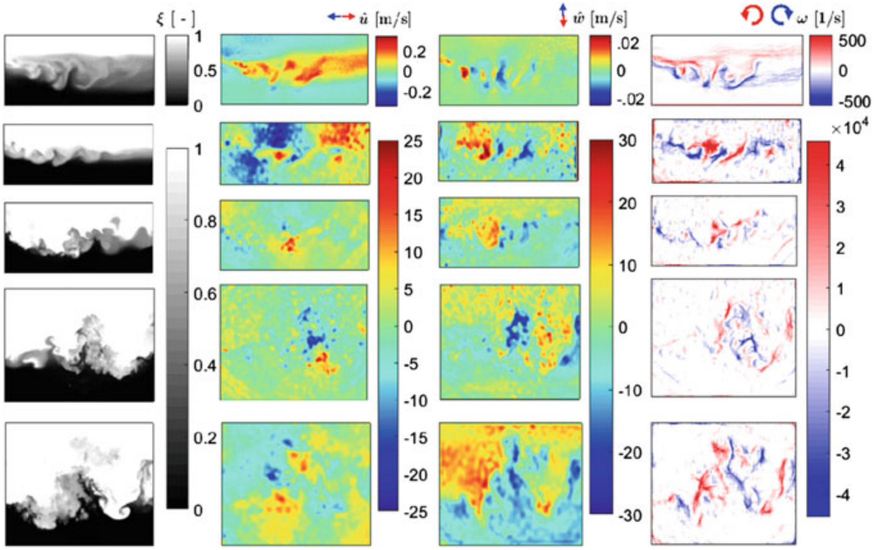

Fig. 9 Representative field evolution results for the $M = 1.6$ case. From top to bottom: IC, PS1, PS2, PS3, PS4. From left to right: concentration, global-fluctuation of spanwise velocity, global-fluctuation of streamwise velocity, and vorticity

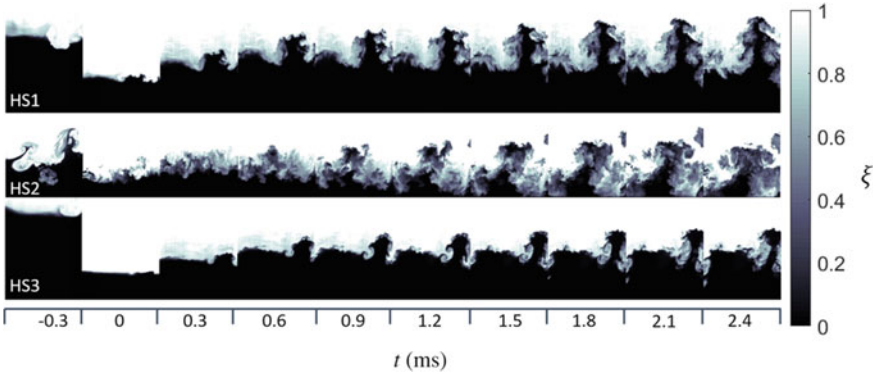

Fig. 10 He-concentration fields from three different high-speed PLIF experiments. Images acquired at 20 kHz. The images on the far left side represent initial conditions for the interface-reshock interaction

towards a turbulent state and quantifying the effect of the initial conditions on these time histories.

Experiments with Shear Layer (Concurrent, High-Speed PLIF/PIV)

In precisely the same way as it had been for the single-shot experiments, the need to measure concentration and velocity simultaneously became apparent in the high-speed configuration. The same approach that was used in the single-shot experiments was followed, with co-propagation of two different laser wavelengths for PLIF and PIV, respectively. Since only one pulse-burst laser system was available, the two wavelengths were 266 nm for PLIF and 532 nm for PIV. While co-propagating two wavelengths from the pulse-burst laser system and using two high-speed CMOS cameras certainly makes the experiment much more challenging, the experimental logic is conceptually the same as for the single-shot case.

At the time of this writing (August 2021), a large campaign, involving two series with $M = 1.6$ and $M = 2.2$ has been completed and will be reported in a future journal article. A sample of simultaneously acquired concentration and velocity fields is in Fig. 11.

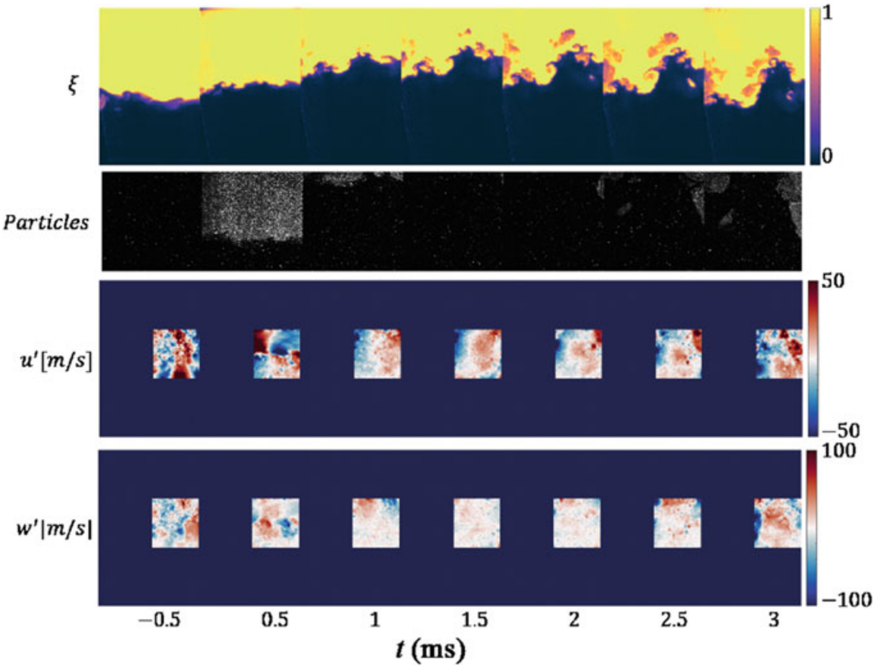

Fig. 11 Examples of concurrent high-speed PLIF and PIV measurements

3 Shock-Accelerated Bubbles

In the years 2002–2011, another area of activity at the WiSTL was the study of shock-bubble interactions (SBI) [22–27, 31, 34]. Within the general field of shock-accelerated density inhomogeneities, the interaction of a planar shock wave with a spherical bubble offers a very simple, fundamental geometry whose understanding can be used as a building block for the study of more complicated (and realistic) situations. This kind of interaction is fully three-dimensional but axial symmetry makes its study significantly more approachable.

The details of the shock refraction process depend on the difference between the acoustic impedance of the gases inside and outside the bubble, as shown in Fig. 12 for the case of a shock wave propagating from left to right. In the slow/fast/slow case (LHS in Fig. 12) a shock is transmitted into the bubble and a rarefaction reflected off its surface. Counterclockwise and clockwise vorticity is baroclinically deposited on the upper and lower hemispheres, respectively. In the fast/slow/fast case (RHS in Fig. 12) both transmitted and reflected waves are shocks, and the deposited vorticity has opposite signs than in the SFS case.

Non-Reactive Bubbles

The issues faced in designing the experiment were the same as those that had been confronted in the RMI studies: how to prepare the interface and what diagnostics to use. A schematic of the interface generation and imaging systems is given in Fig. 13 (taken from [24]) (showing the most advanced version of the latter). A retractable

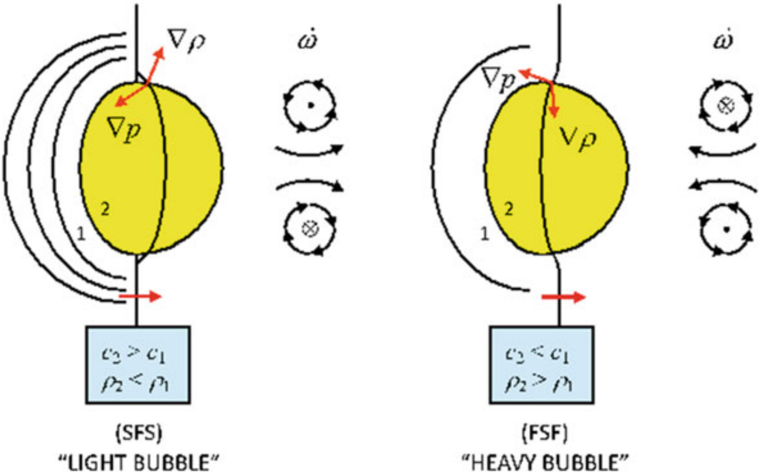

Fig. 12 Shock refraction at a gas bubble

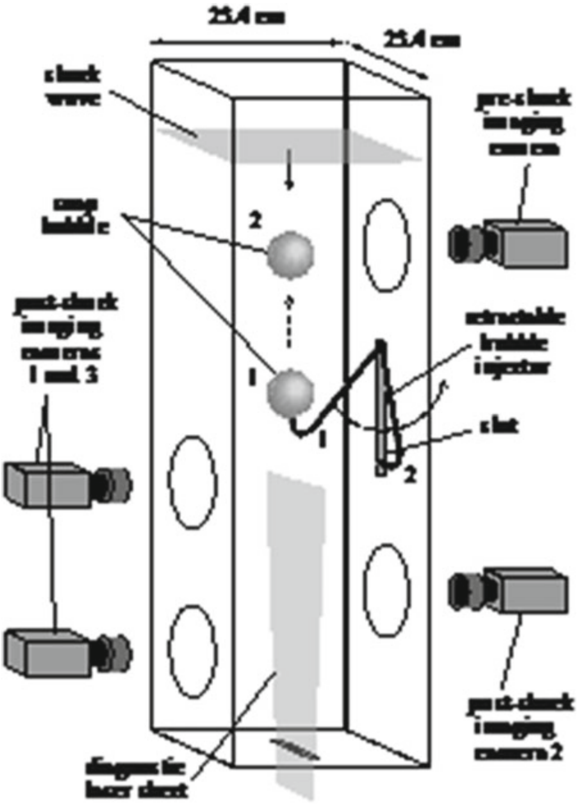

Fig. 13 Interface preparation and diagnostic system for shock-bubble interaction experiments. In this particular case, a helium bubble is released to rise freely in the shock tube. Laser sheets illuminate a bubble cross section, and four cameras capture images of the initial conditions and at three post-shock times

injector was used to prepare and release a bubble filled with a gas different than the one surrounding it. It consisted of a 6 mm ID tube, with a 90° bend near one of its ends. The tube could be tilted about a pivot and retracted into a cavity in one of the inner shock tube walls.

To prepare a bubble, the injector was initially extended inside the shock tube and a thin soap film was deposited on its open end. The test gas was slowly flowed into the injector and a bubble was formed with a typical diameter of 5 cm. If the bubble gas was lighter than the ambient, the injector tip faced upward (as in Fig. 13, taken from [24]). Conversely for a heavy gas bubble. At the start of each experiment, the injector was retracted very quickly into the shock tube wall causing the bubble to separate from its tip. Depending on the density difference between the bubble and ambient gases, the bubble would rise or fall freely along a vertical trajectory. A downward-propagating shock wave impulsively accelerated the bubble. The immediate effects of this interaction included: atomization of the soap film into droplets of 10–60 μm diameter; compression of the bubble; deposition of vorticity on the bubble periphery; formation of a vortex ring at the bubble equator. At later times, the flow developed a large wake and, for certain combinations of the Atwood and Mach numbers, secondary and tertiary vortex rings.

Extensive attempts were made at deploying the same two diagnostic techniques (PLIF and PIV) that had been used in the study of the RMI. Unfortunately, neither proved feasible. Doping of the gas bubble with a fluorophore did not work because the compound would either chemically attack the soap film (e.g. acetone) or dissolve in it (e.g. biacetyl). And even if seeding a fluorophore into the bubble had been possible, the soap droplets would have themselves fluoresced upon excitement by the laser light, with a much stronger signal than the bubble gas because of the much larger number density in the liquid than in the gas phase. Similarly, introducing solid particles of diameter small enough to faithfully follow the flow to perform PIV would have resulted in a Mie scattering signal much weaker than that produced by the soap droplets (whose diameter was about 100–600 times larger than that of the TiO_2 particles typically used for PIV).

Incident Shock

In conclusion, the soap droplets were used as flow tracers and planar Mie scattering was performed by illuminating the droplets with a laser sheet generated using both Nd:YAG and excimer lasers. All data acquisition was in single-shot mode with one image per run collected at each window. Experiments were performed over a large array of Atwood and Mach number combinations. Many of these were also studied computationally using the *Raptor* code of Lawrence Livermore National Laboratory. Examples of experimental and computational results are shown in Figs. 14 and 15 (taken from [24]) which demonstrate outstanding agreement between the experiments and the calculations. Quantitative measurements of macroscopic geometrical properties (major and minor vortex ring diameters, streamwise extent) were extracted from the digital images. Normalizing all dimensions by the original bubble diameter D (e.g., $L_h = h/D$, where h is the axial extent of the bubble), and time by, where W_t is the velocity of the shock transmitted into the bubble ($\tau = t/t'$), led to excellent collapse and showed the effect of compressibility (quantified by the Mach number) and of the density contrast (quantified by the Atwood number), as shown in Fig. 16. The importance of appropriate normalization appears in Fig. 17: the experiments by Klein [28] are for a copper sphere impulsively accelerated by a laser-generated shock wave on the NOVA facility at Lawrence Livermore National Laboratory. The data show unequivocally that the universal scaling covers a very large range of the dimensionless parameters.

The combination of experiments and calculations also allowed for the evaluation of several total circulation models and to understand in detail the differences in the shock refraction processes between the light and the heavy bubble cases. The appearance of a tertiary vortex ring in the He/air case with $M = 2.95$ (see Fig. 15, taken from [24]) was the first experimental evidence of a prediction by Norman Zabuski and his group [29, 30].

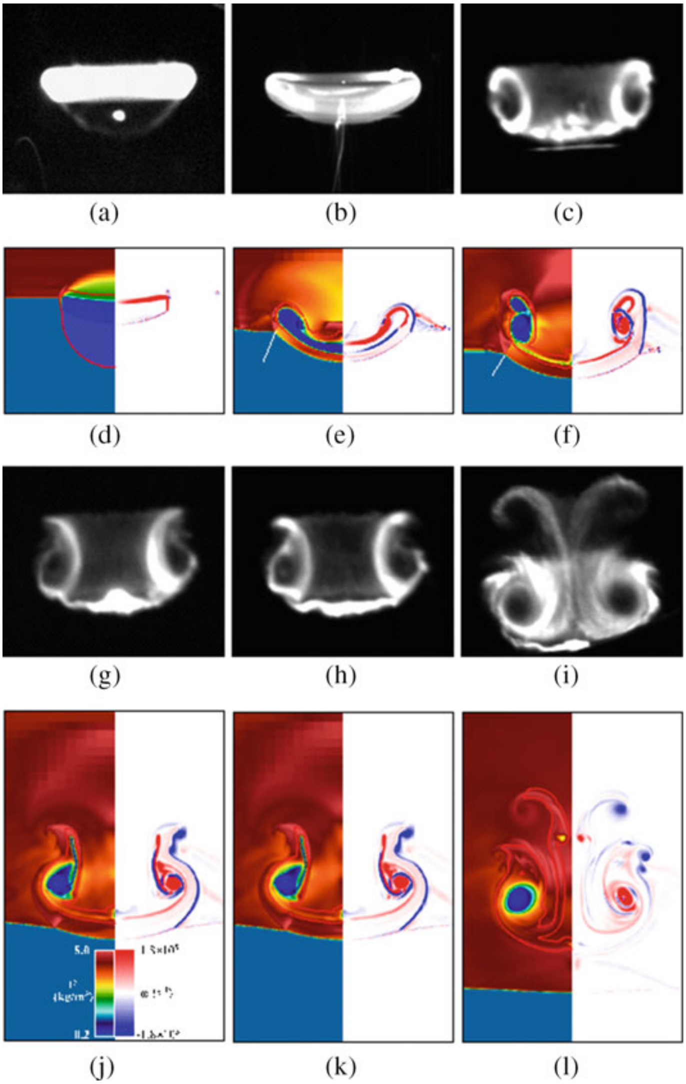

(a) (b) (c)

(d) (e) (f)

(g) (h) (i)

(j) (k) (l)

Fig. 14 Helium bubble in air ($A = 0.8$), $M = 2.08$. 1st and 3rd rows: planar Mie scattering. 2nd and 4th rows: numerical simulations with density on the left and vorticity magnitude on the right. Dimensionless times (tW_t/R): (**a**), (**d**) 1.3; (**b**), (**e**) 4.0; (**c**), (**f**) 7.7; (**g**), (**j**) 11.4; (**h**), (**k**) 11.7; (**i**), (**l**) 23.7. The width of the field of view in each image is 8 cm

Reshock

Since the upward velocity of a reshocked bubble is much smaller than the downward velocity of a singly-shocked one, it is possible to perform useful high-speed imaging of a reshocked bubble. In the present case, since imaging was based on

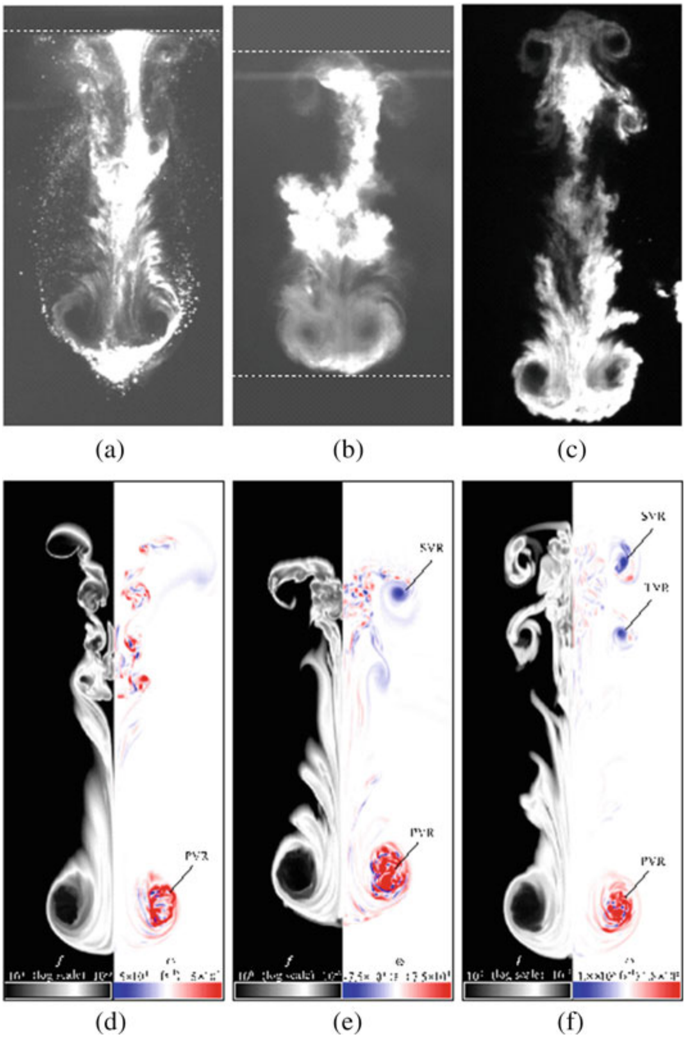

Fig. 15 Helium bubble in air. Top row: planar Mie scattering. Bottom row: numerical simulations with He volume fraction on the left and vorticity magnitude on the right. Left, middle, right columns: $M = 1.45, M = 2.08, M = 2.95$. Dimensionless times ($tW_t/R$): (**a**), (**d**) 105.8; (**b**), (**e**) 63.5; (**c**) 69.5; (**f**) 63.5. PVR, SVR, TVR stand for principal, secondary, tertiary vortex ring, respectively to the non-reactive case were the composition of the bubble and an additional diagnostic to track the progress of the combustion. Our experiments are described in detail in [34]

Fig. 16 Time histories of the bubble axial extent for several *A, M* combinations. **a** Ar bubble in N_2; **b** He bubble in N_2

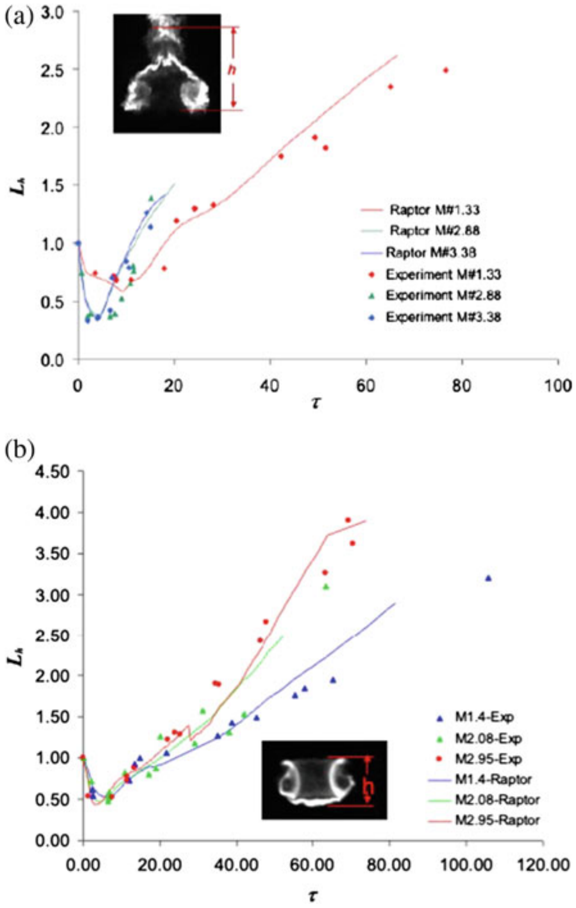

Fig. 17 Time histories of the bubble axial extent for several *A, M* combinations. The data by Klein are for a copper sphere studied in the NOVA facility at Lawrence Livermore National Laboratory

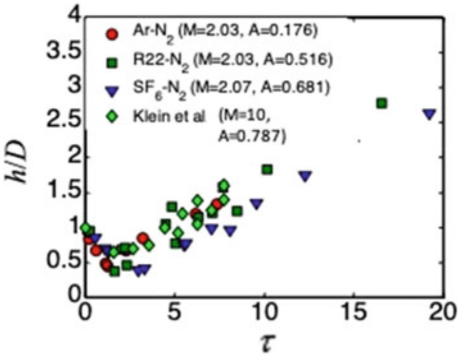

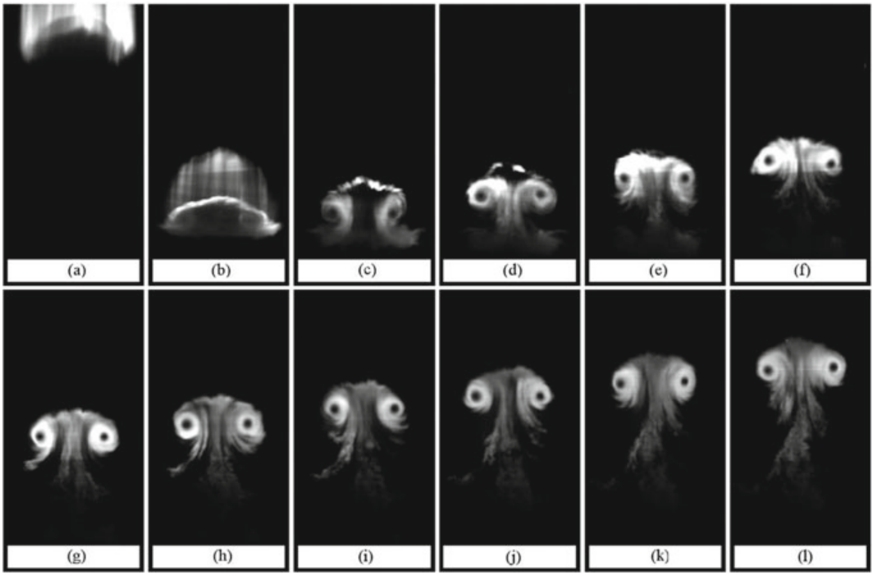

Fig. 18 Reshocked Ar bubble in N_2 ($A = 0.176$), $M = 2.07$. Imaging at 10,000 fps. **a** singly-shocked bubble still in downward motion. **b** reshocked bubble immediately after interaction; (**c**)–(**l**) images separated by 300 µs. Each image corresponds to physical dimensions of 9 cm by 22 cm

planar Mie scattering, no high-repetition rate laser was necessary. A cross section of the bubble could be illuminated with a CW Ar^+ laser and imaged with a high-speed CMOS camera. Experiments were performed for several Atwood and Mach numbers [31] and, again, several circulation models (including a new one) were successfully tested against the experimental data. An example of high-speed planar Mie scattering images is shown in Fig. 18 (taken from [31]).

Chemically-Reactive Bubbles

The interaction of a shock with a density inhomogeneity (like, e.g., a bubble) is often accompanied by a chemical or nuclear reaction (e.g. in conceptual hypersonic combustion systems [6], supernova explosions [5], or inertial confinement fusion implosion experiments on laser-driven facilities [7]). While the coupling between the RMI and nuclear reactions has been studied extensively, by the early 2000s very little experimental work had been carried out to study the coupling of shock propagation and chemical reaction. Among the few examples is work by Markstein [32, 33]. The SBI offers a simple platform to study the combined effect of shock acceleration and chemical reaction. Working with a heavy bubble, one can use the focusing of the portion of the shock transmitted into the bubble to cause an appropriate gas mixture to ignite.

The non-reactive SBI experimental setup described in the previous section represented an excellent starting point to design a chemically-reactive SBI experiment. The two main changes with respect.

Instead of a pure gas, the bubble was now filled with a stoichiometric mixture of hydrogen and oxygen, diluted in xenon. The relative proportion of Xe was selected to balance two conflicting needs: a higher proportion of the H_2-O_2 mixture makes the overall mixture more reactive; a larger presence of Xe increases the density of the bubble, the Atwood number of the bubble gas/ambient gas combination, and the strength of the shock-focusing effect. The final composition used in all the experiments was 56% Xe, 29% H_2, 15% O_2. The bubble was released in ambient nitrogen, resulting in an Atwood number $A = 0.48$.

To visualize the flow, the same planar Mie scattering diagnostic used in the non-reactive SBI experiments was employed to track the evolution of the bubble. Two Mie scattering images were collected in each run. To follow the progression of the combustion, the chemiluminescence of the OH^* radical (peaked at 307 nm) was imaged with a dual-frame ICCD camera fitted with a UV-lens and the necessary filters to reject the 532 nm light from the Mie scattering. The Mie scattering images had a 10 ns exposure set by the duration of the Nd:YAG laser flashes. The chemiluminescence images had an exposure set using the amplifier gate on the ICCD camera (times in the 3-1000 μs were used). Examples of superimposed Mie scattering and chemiluminescence images are shown in Fig. 19 (taken from [34]). The gray scale is the image of the Mie scattering while the yellow and red portions are the images of

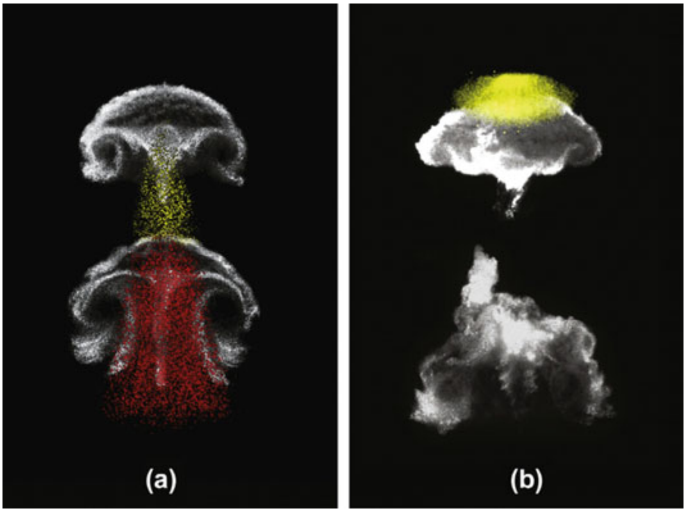

Fig. 19 Composite images showing the development of a shock-accelerated bubble filled with a reactive mixture initially free-falling in N_2. Each image consists of two chemiluminescence exposures in yellow and red overlaid upon two planar Mie scattering images in grayscale. For clarity, the signal levels have been adjusted and do not reflect the intensity of the chemiluminescence signal. **a** $M = 1.65$, **b** $M = 2.83$

the chemiluminescence. The Mie scattering images look qualitatively similar to their non-reactive counterparts for the case of a heavy bubble. For the low Mach number case (Fig. 19a), the chemiluminescence trace indicates that the H_2–O_2 mixture ignites at a point and the combustion proceeds with a spherical front whose signature, in a line-of-sight visualization, is a circle of progressively larger diameter. Since the entire region is moving downward at the post-shock speed, the net result is the triangular signature seen in the figure. The behavior was dramatically different for strong shocks (Fig. 19): in this case the combustion did not appear to proceed as a spherical flame front, and it was difficult to precisely pinpoint the progress of the reaction. A much clearer understanding came from numerical simulations of the flow by Niklaus Adams' group [35] who showed that a deflagration-to-detonation transition (DDT) occurs at high M.

The other important conclusion came from a comparison of the time history of the main macroscopic properties between the non-reactive and reactive cases: at low M, the bubble dimensions appeared to be unaffected by the chemical reaction while at the high M the dimensions are measurably larger during the combustion event and then relax and tend towards their non-reactive counterparts.

4 Shock-Accelerated Vortex Rings

The SBI is an ideal configuration to study the interaction of a shock wave with a density non-homogeneity (in both the chemically non-reactive and reactive cases), due to its simple, well-defined geometry. But, as discussed in the previous section, the necessity of a soap film to prepare the initial condition prevents the use of state-of-the-art diagnostic techniques like PLIF and PIV. This limitation led us to the development of a new experiment where a "simple, well-defined" geometry could be generated without soap.

The choice fell on a vortex ring to be generated by firing an open-ended "mini shock tube" into the main shock tube as shown in Fig. 20. The mini tube's driven section (2.2 cm ID) is surrounded by a "sleeve" connected to a vacuum pump. A gas heavier than the ambient gas in the main shock tube is introduced into the mini tube through a port immediately above the mini tube's diaphragm and the excess gas is suctioned out through the annulus. By careful selection of the driver and driven gases and the ratio of the driver length to the diameter, a "clean" vortex ring can be released in an upward motion into the main shock tube, with minimal wake effects.

This initial condition presents a more complicated geometry (a torus) than a spherical bubble. The inhomogeneity also contains a full vorticity field before interaction with the accelerating shock. But the absence of soap is a major improvement with regard to the diagnostics that can be used.

At the time of this writing, the first experiments are being carried out. Examples of PLIF images of a shocked vortex ring are in Fig. 21. An argon vortex ring is ejected into a nitrogen atmosphere in the main shock tube. A $M = 1.75$ shock wave strikes the ring and sets it in a downward motion. PLIF is performed at 20,000 fps. The shock

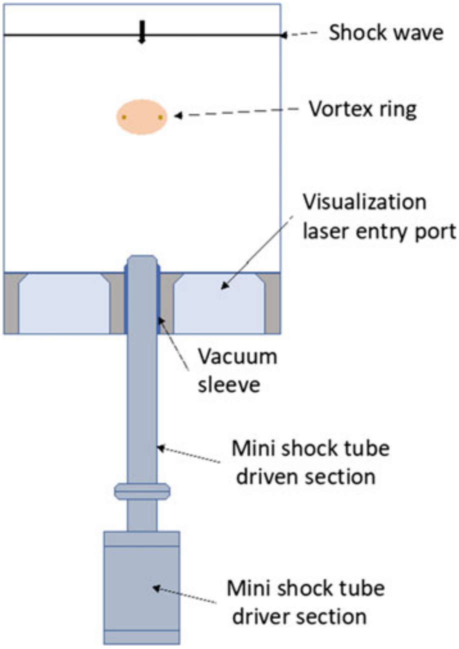

Fig. 20 Schematic of the "mini shock tube" used to generate a vortex ring and release it in an upward motion into the main shock tube

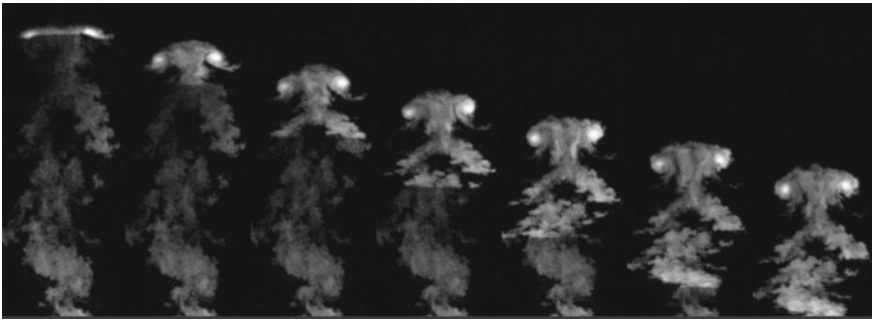

Fig. 21 Sequence of high-speed PLIF images. Ar vortex ring in N_2 accelerated by a $M = 1.75$ shock wave. Imaging at 20,000 fps. The shock location corresponds to the line of sharp contrast within each image

wave location is clearly visible as the line of sharp contrast between the shocked and unshocked regions (the higher PLIF signal being due to the higher number densities in the shocked regions).

The experimental results will be analyzed in much the same way as those from the RMI and SBI experiments, applying integral, statistical, and spectral approaches. The findings will be presented in a forthcoming journal article.

5 Conclusions

This was a very brief review of 25 years of work at WiSTL. Shock-inhomogeneity interactions were studied in a broad variety of geometries and physical conditions, deploying progressively more sophisticated diagnostic techniques. A lot was learned, directly from the experiments, and from comparisons against models and ever more detailed computer simulations.

But the most important achievement of all the activities described above has been the education of all the graduate and undergraduate students who have worked in the WiSTL. To all of them, the author expresses his heartfelt gratitude and admiration for their brilliant careers.

The author thanks the US-DOE/NNSA and the NSF for their financial support for all the work described here.

References

1. Anderson MH et al. https://doi.org/10.1007/s001930000067
2. Richtmyer RD. https://doi.org/10.1002/cpa.3160130207
3. Meshkov EE. https://doi.org/10.1007/BF01015969
4. Andronov VA et al (1976) Turbulent mixing at contact surface accelerated by shock waves. Sov Phys JETP 44(2):424
5. Müller E et al. https://doi.org/10.1086/169657
6. Urzay J. https://doi.org/10.1146/annurev-fluid-122316-045217
7. Smalyuk VA et al.https://doi.org/10.1063/1.4872026
8. Zhou Y. https://doi.org/10.1016/j.physrep.2017.07.005
9. Zhou Y. https://doi.org/10.1016/j.physrep.2017.07.008
10. Puranik PB et al. https://doi.org/10.1007/s00193-004-0231-8
11. Motl BJ et al. https://doi.org/10.13182/FST07-A1640
12. Jones MA, Jacobs JW. https://doi.org/10.1063/1.869416
13. Motl B et al.https://doi.org/10.1063/1.3280364
14. Weber C et al. https://doi.org/10.1007/s00193-012-0367-x
15. Weber C et al. https://doi.org/10.1063/1.4733447
16. Weber C et al. https://doi.org/10.1017/jfm.2014.188
17. Dimotakis PE. https://doi.org/10.1017/S0022112099007946
18. Reese D et al. https://doi.org/10.1007/s00348-014-1823-4
19. Reese D et al. https://doi.org/10.1017/jfm.2018.419
20. Noble CD et al. https://doi.org/10.1115/1.4048344
21. Noble CD et al. https://doi.org/10.1016/j.physd.2020.132519
22. Ranjan D et al. https://doi.org/10.1103/PhysRevLett.94.184507
23. Ranjan D et al. https://doi.org/10.1103/PhysRevLett.98.024502
24. Ranjan D et al. https://doi.org/10.1063/1.2840198

25. Niederhaus JHJ et al. https://doi.org/10.1017/S0022112007008749
26. Niederhaus JHJ et al. https://doi.org/10.1088/0031-8949/2008/T132/014019
27. Ranjan D et al.https://doi.org/10.1088/0031-8949/2008/T132/014020
28. Klein RI et al. https://doi.org/10.1086/345340
29. Zabusky NJ, Cheng SM. https://doi.org/10.1017/S0022112097008045
30. Peng G et al. https://doi.org/10.1063/1.1621628
31. Haehn N et al. http://iopscience.iop.org/1402-4896/2010/T142/014067
32. Markstein GH. https://doi.org/10.1016/S0082-0784(57)80054-X
33. Markstein GH. https://doi.org/10.1016/B978-1-4831-9659-6.50007-X
34. Haehn N et al. https://doi.org/10.1016/j.combustflame.2011.10.015
35. Diegelman F et al. https://doi.org/10.1016/j.combustflame.2016.09.014

Flow Formation Around a Body in the Area of Interference of Two Blast Waves

Irina V. Krassovskaya

1 Blast Wave Simulation in a Shock Tube

The study of blast wave interaction with a body is largely motivated by the need to understand complex unsteady gasdynamic phenomena. Much more complex processes arise when a body is in the area of interference of two blast waves moving in different directions. Flow interference for cases of overtaking interaction of two successive blast waves (double explosion) and head-on interaction of two blast waves propagating in opposite directions has been thoroughly investigated [1–5]. A body in the region of blast wave interference is subject to multiple impacts from shock waves moving in different directions. The flow field around the body may include various types of non-stationary interactions, such as shock reflection, shock refraction, shock-shock collisions and viscous-inviscid interactions. The results of experimental simulation of flow patterns forming around a body for cases of overtaking and head-on interference are presented below.

The experiments were performed in a double-diaphragm shock tube of the rectangular cross-section 150 × 50 mm^2. The high pressure chambers with the length $x_1 = 0.099$ m and $x_2 = 0.085$ m were used. The total length of the tube was 12 m. The working gases were CO_2 and N_2. In Fig. 1 the (x, t)-diagram of the flow at consecutive rupture of the two membranes is shown. The head of the rarefaction wave reaches the shock wave front, and that results in the formation of the blast wave profile behind the shock front. Then the second diaphragm opens and the second blast wave forms. When the two successive blast waves have merged, the system of gasdynamic discontinuities consisting of the final shock wave, the contact discontinuity and the rarefaction wave is formed.

I. V. Krassovskaya (✉)
Ioffe Institute, 26 Polytechnicheskaya, St Petersburg 194021, Russia
e-mail: i.kras@mail.ioffe.ru

© The Author(s), under exclusive license to Springer Nature Switzerland AG 2022

K. Takayama and O. Igra (eds.), *Frontiers of Shock Wave Research*,
https://doi.org/10.1007/978-3-030-90735-8_5

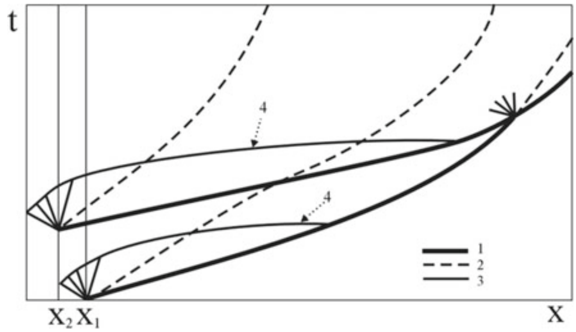

Fig. 1 (x, t)-diagram of the flow in double-diaphragm shock tube. 1—shock wave fronts; 2 —contact discontinuities; 3—fan of rarefaction waves; 4 —head of the rarefaction fans

2 Interaction of Two Successive Blast Waves with a Straight Wedge

Depending on whether the two blast waves merge before they have reached the wedge or while they propagate along the wedge surface, we can speak of two kinds of interaction. In the first case, the system of three discontinuities formed after the merging of two initial blast waves interacts with a wedge. The second kind of interaction is more complex. Two initial blast waves merge when propagating along the wedge surface. In the course of non-stationary interaction over the wedge multiple shock/shock and shock/solid surface interactions occur. In Fig. 2 the schematic illustration of the flow field structure at t = 0 for both kinds of interaction is shown. Here I_1, I_2 are initial blast waves, I, C and Rw are the resulting blast wave, the contact surface and the rarefaction wave, respectively. They are formed after the merging I_1 and I_2. Line Pm indicates the plane where the merger takes place.

For all experiments, the initial conditions in the high-pressure chambers and in the channel remained unchanged while the angle of wedge varied. The experiment was conducted for wedges with the angles $\beta = 48.5°, 30°, 15°$. Two weak blast waves were generated in CO_2. The results of the experiments are presented as shadow images in a time sequence.

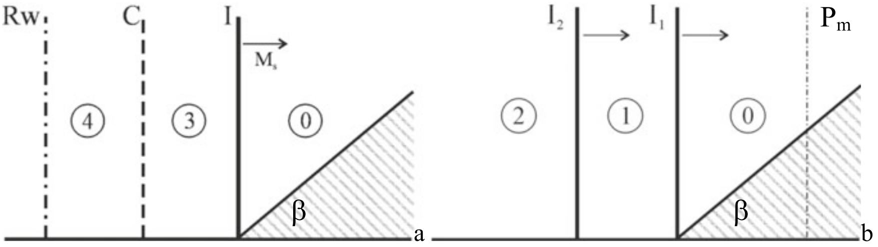

Fig. 2 Scheme of the flow in the initial time of interaction: **a** —blast wave collision occurs ahead of the wedge; **b** —blast wave collision occurs over the wedge surface

The first series of experiments were done for the case when the two initial blast waves merge before reaching the wedge (Fig. 2a). The experiments were carried out for the wedges with $\beta = 30°$ and 15°. The density ratio $\Gamma = \rho_i/\rho_j$ on the front of the resulting merged wave I is $\Gamma_{30} = 3.05$, on the front of contact discontinuity the parameter has the value of $\Gamma_{43} = 1.04$. The flow behind the resulting shock wave I is supersonic. In Figs. 3 and 4, the flow patterns are given for $\beta = 30°$ and 15°, respectively. Reflection of the resulting shock wave I over the wedge is MR for both wedges. The flow is self-similar and is determined only by Γ_{30} and β. The process of interaction of the planar contact surface with the curvilinear bow shock is non-stationary. Under the given conditions, regular refraction occurs, and the configuration with two (transmitted and reflected) shock waves and new contact surface forms. The reflected shock wave is very weak and thus cannot be seen in the shadow images presented. Figures 3 and 4 demonstrate different behaviors of the deflected contact surface. We can see that for the wedge with $\beta = 30°$ the deflected

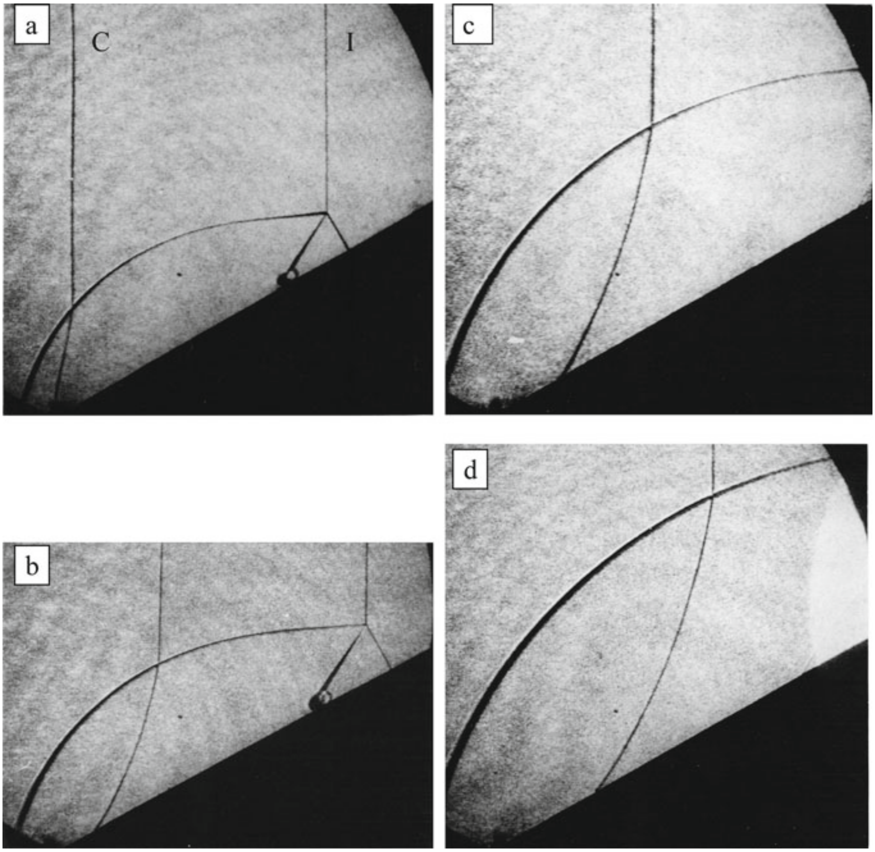

Fig. 3 Interaction of the merged shock wave and contact discontinuity with a wedge $\beta = 30°$

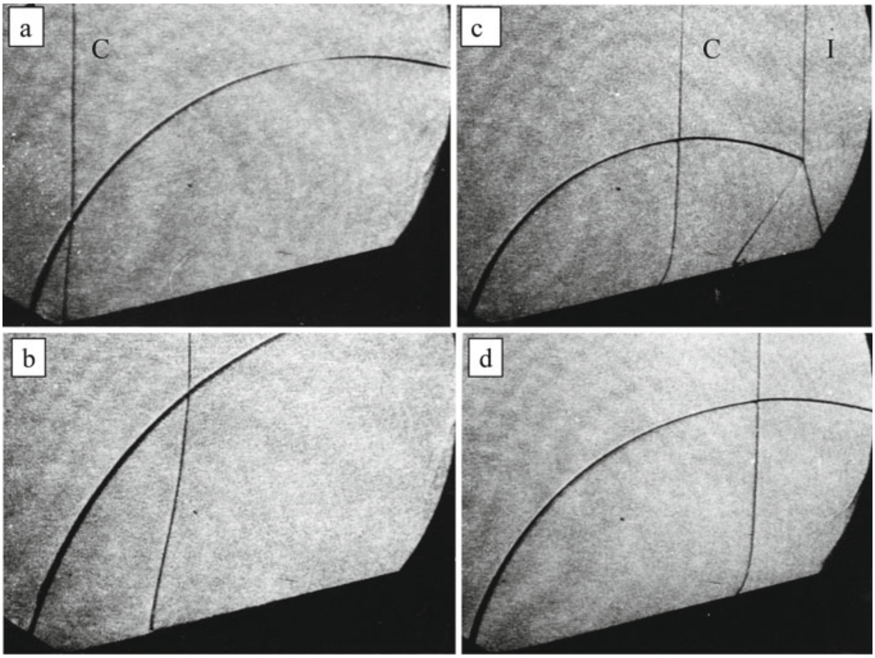

Fig. 4 Interaction of the merged shock wave and contact discontinuity with a wedge $\beta = 15°$

contact surface is curved along the entire length (Fig. 3), whereas for the wedge with $\beta = 15°$, it is curved near the wall only (Fig. 4).

The second type of interaction, where two initial blast waves merge while propagating along the wedge (Fig. 2b), is characterized by the multiple different shock wave interactions. This experiment was carried out for the wedges with $\beta = 48.5°$, 30° and 15°. The density ratios on the fronts of the initial blast waves were Γ_{10} =2.6, Γ_{21} = 1.26; the flow behind the first blast wave is subsonic. In the course of non-stationary process a lot of shock-on-shock, shock-by-shock collisions, shock reflections and shock refractions occur. The types of configuration change continuously.

In Fig. 5 the shadow images for wedge with $\beta = 48.5°$ are given. The stage until the merging the initial shock waves is characterized by the reflection of the first shock wave I_1, the flow formation over the wedge and the interaction of the second incident shock wave I_2 with the bow shock and its reflection from the wedge surface. For the given wedge, all shock interactions are regular (Fig. 5a, b). Figure 5c, d demonstrates the flow which forms when the merged shock wave reflects over the wedge. The contact surface interacts with the bow shock and then touches the wedge surface. It should be noted that the contact discontinuity does not reflect from the wedge. The contact discontinuities that can be seen in Fig. 5c, d result from the previous shock interactions.

Data analysis suggests that most complex shock wave configuration occurs in the case when the first incident shock wave reflects over the wedge as MR. In Fig. 6

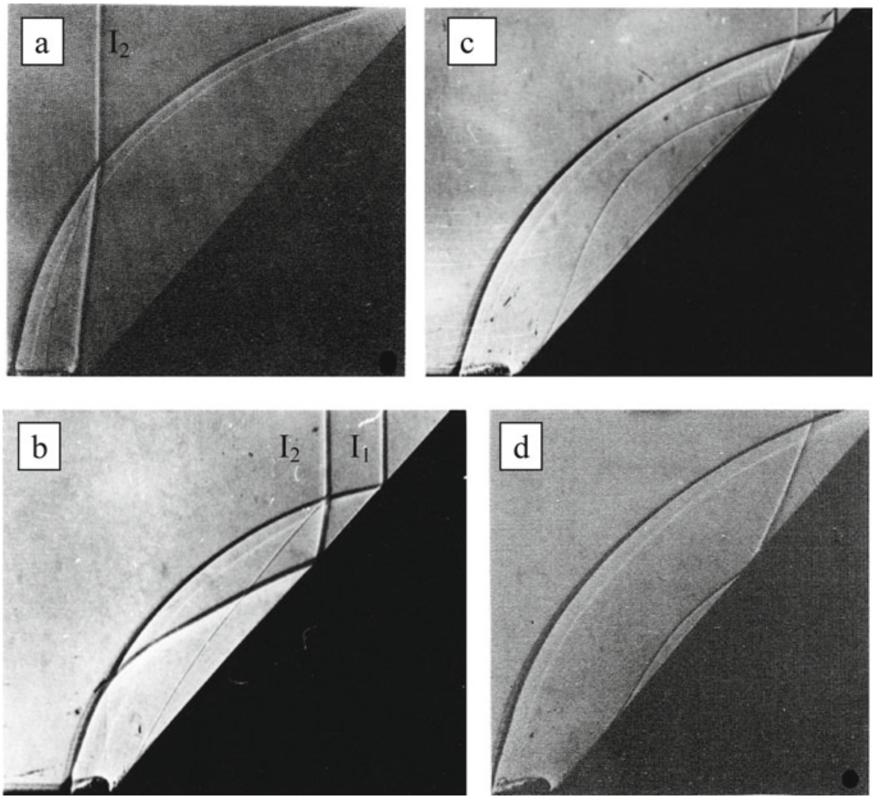

Fig. 5 Interaction of the successive shock waves with the wedge $\beta = 48.5°$

evolution of the interaction patterns is demonstrated in more detail for the wedge with $\beta = 30°$. At first, the incident shock wave I_1 reflects from the wedge, resulting in the formation of a Mach reflection configuration. When the second incident shock wave meets the bow shock, regular collision of the shock waves of unequal strength occurs. The four-shock configuration consists of two incident, two reflected shocks and a slipstream between them arises. (The slip surface is not seen on the shadow image, Fig. 6a). In the course of propagation of the second incident shock I_2 along the wedge (Fig. 6a–c), the conditions of interaction change. The transmitted shock wave $\tilde{I}_2$ reflects from the horizontal and then from the inclined wedge surface (that is from the concave double wedge). As a result, transitioned regular reflection configuration TRR (a two-shock configuration with additional shock) occurs (Fig. 6b). The next instant, this system of shock waves comes to the slip surface of the first MR.

Refraction of the transmitted shock $\tilde{I}_2$ on the slip surface changes the condition of its reflection from the wedge. A new RR configuration forms (Fig. 6c). It should be noted that the geometry and distribution of the parameters of this configuration differ from the corresponding characteristics of the two-shock configuration shown

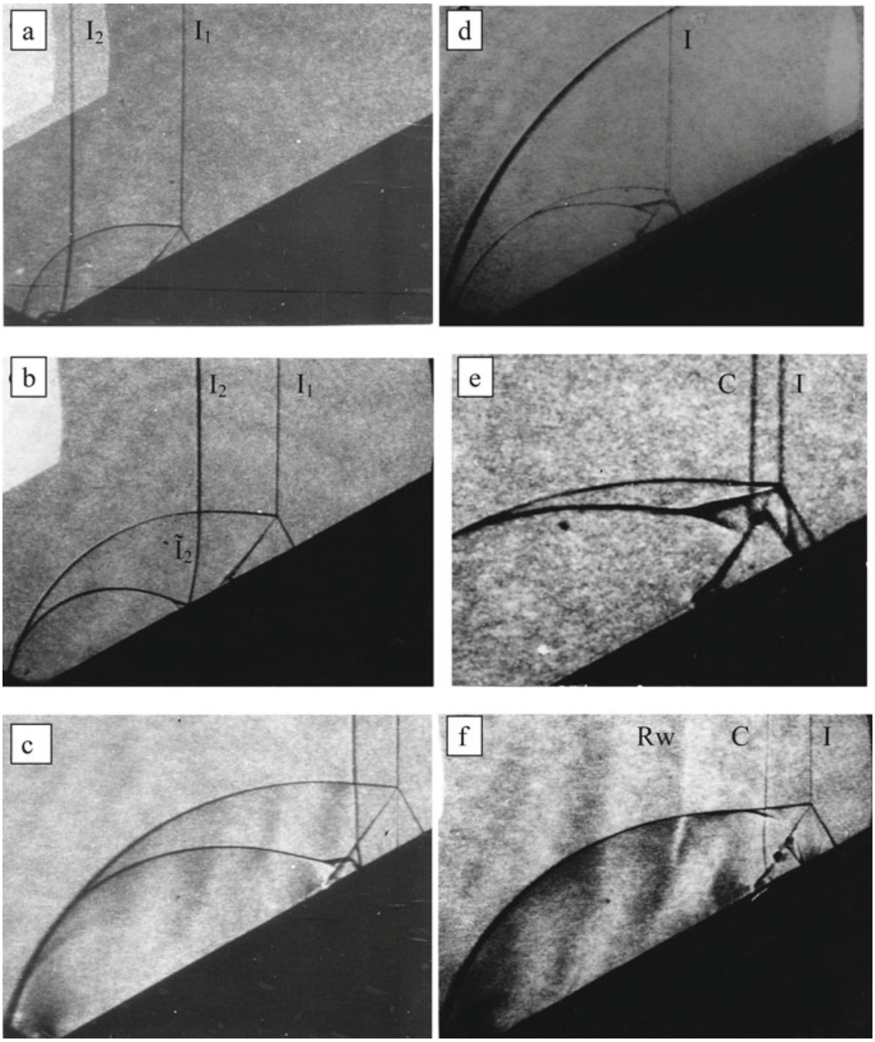

Fig. 6 Interaction of the successive shock waves with the wedge β = 30°

in Fig. 6b. Over time, the second incident shock I_2 and its reflection configuration overtake the Mach reflection of the first incident shock I_1. The merging of I_1 and I_2 results in the final shock wave I, contact surface C and rarefaction wave Rw. All described shock wave interactions result in the formation of a new MR configuration and a system consisting of several contact discontinuities (Fig. 6e, f).

The flow patterns for β = 15° are given in Fig. 7. The shadow image (Fig. 7a) demonstrates the moment when both incident shock waves interact with the wedge. Following the collision with the bow shock, non-stationary reflection of the second shock wave $\tilde{I}_2$ from the solid surface takes place. In this case, we can expect the

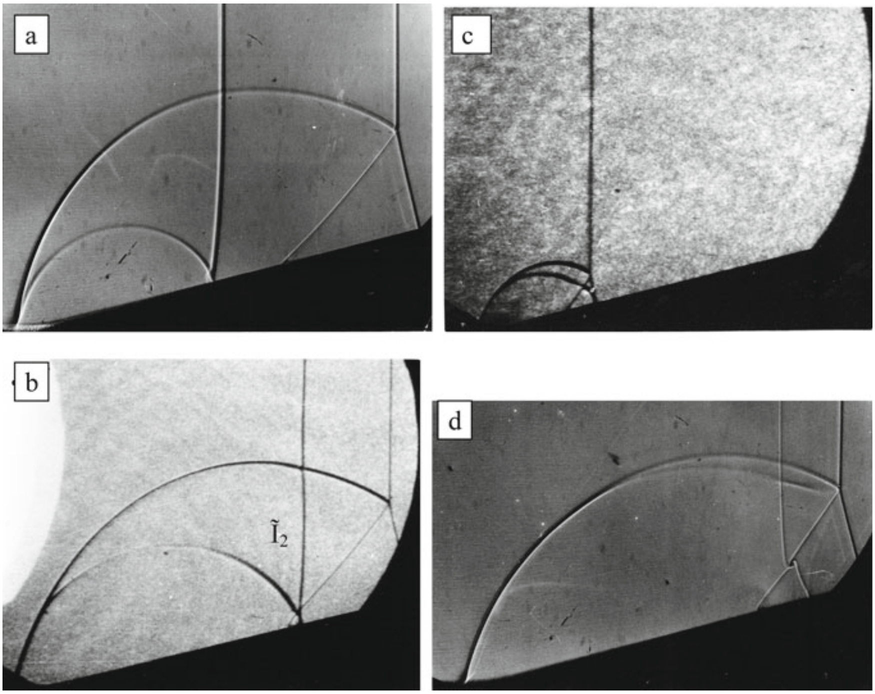

Fig. 7 Interaction of the successive shock waves with the wedge β = 15°

transition from regular reflection to Mach reflection. The results of the measurements of pressure in the fixed point on the wedge surface confirms this suggestion. These data will be presented below. Figure 7c, d demonstrate the flow pattern which forms after the merging of the two incident blast waves.

As the experimental results showed, the problem of interaction of slip discontinuities with each other requires more detailed consideration. Figure 8 presents an enlarged image of a fragment of Fig. 7d. The structure is composed of four discontinuities with no intersection point. We see a small vortex area instead. Indeed, two slip discontinuities positioned at an angle to each other cannot intersect at a point: otherwise the condition of the flow parallelism will not be observed. The pattern shown in Fig. 8 features four contact discontinuities that originated in the course of four different processes. A similar situation can be seen in Fig. 6f that features a structure composed of five contact discontinuities.

Analysis of the shadow images shows that the non-stationary stage of the interaction process features very complex configurations, leading to the formation of a new system of gasdynamic discontinuities. As a result, the conditions of loading on the wedge surface change continuously.

The pressure in the fixed point of the wedge surface at various time instants are presented in Fig. 9a for β = 48.5° and Fig. 9b for β = 15°. In these figures the dimensionless pressure P is defined as p/p_0, where p_0 is the pressure of the quiescent

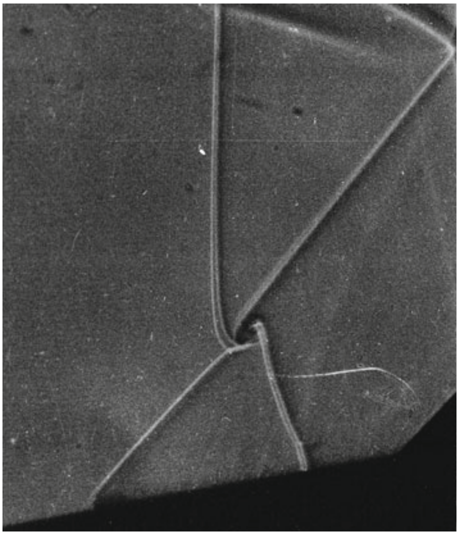

Fig. 8 Contact discontinuities structure

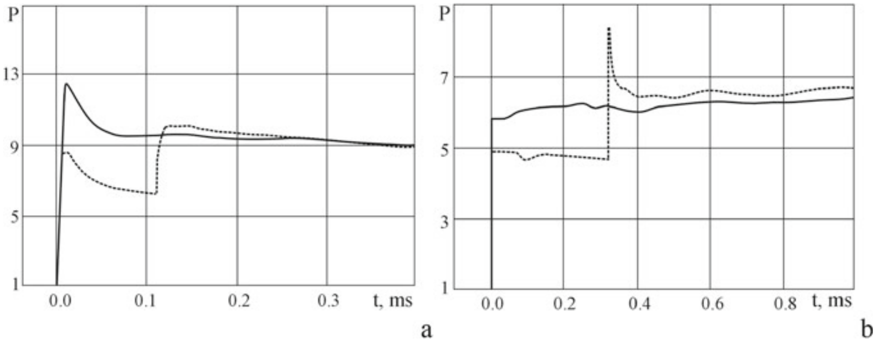

Fig. 9 Presure history for the fixed point on the wedge surface, **a**—$\beta = 48.5°$, **b**—$\beta = 15°$

gas. In both figures the solid lines correspond to the pressure histories for the kind of interaction when two incident shock waves merge before they reach the wedge nose. The dashed lines present the pressure histories for the case when incident shock waves reflect from the wedge separately. Reflection of the second shock wave from the wedge with $\beta = 15°$ (Fig. 9b) features a pressure profile with strong gradient immediately behind the front. For the wedge with $\beta = 48.5°$, pressure behind the second shock wave remains constant for some time. Both results match the shock wave patterns in Fig. 5b and Fig. 7a. Under given conditions, the maximum pressure on the wall of the wedge with $\beta = 15°$ is achieved after the second incident wave, and for the wedge with $\beta = 48.5,°$ it is registered after the merged wave.

3 Flow Around the Cylinder in the Area of the Interference of the Two Blast Waves

The flow interference of two blast waves moving in opposite directions is simulated by the flow occurring in a shock tube at normal reflection of the shock wave from the end of the tube. The distribution of the parameters behind its front is similar to the parameters behind the blast wave of the point explosion. The incident shock wave Mach numbers were $M = 1.2 \div 6$. The duration of the flow in the working section was up to $6 \div 10$ μs. The problem of diffraction of a single blast wave over a cylinder was studied by authors [6, 7]. Here we show the result of the experimental study of the dynamics of the flow over a cylinder which is subject to impact from both incident and reflected shock waves. In Fig. 10, schematic patterns of the flow over a cylinder are given for two time instants.

The incident shock wave impacts the cylinder which is in a quiescent gas. The reflected shock wave interacts with the flow formed around the cylinder. In Figs. 11, 12, 13 and 14, the shadow images illustrate both stages of the process. The incident shock Mach number at $t = 0$ (the time instant when the shock front impacts the cylinder) $M_s = 2.9$. The pressure ratio Ps and the Mach number behind the shock front are $Ps = 9.3$ and $M = 1.52$, respectively. The cylinder diameters $D = 12$ mm and $D = 30$ mm were used. The dimensionless time $\ddot{t}$, is defined as $\ddot{t} = t \cdot D/V_s$, where V_s is the gas velocity behind the incident shock wave.

The first stage of the process is the flow formation around the cylinder as it interacts with the incident shock wave. By the time $\ddot{t} = 1.9$, the parameters at the rear critical point are determined basically by the reflection of the diffracted portion of the incident shock front (Fig. 11b). The formation of the shock system behind the cylinder results from the reverse flows as well as interactions of the reflected shock waves with vortices and with boundary layers (Fig. 11b, c and 12).

The process of formation of the wake flow and the tail shocks continues until $\ddot{t} = 12 \div 15$ (Fig. 11c). The typical supersonic flow around a cylinder is observed at this time instant.

When the oncoming flow becomes subsonic, the flow structure around the cylinder changes considerably. This stage of the process is illustrated by Fig. 11d–f. The detachment of the bow shock increases very rapidly. Finally, the bow shock degenerates into a planar decay shock wave moving upstream. The geometry of the wake changes: the diameter of the wake throat increases. The position of the separation point and the angle of the shock emanating from the separation point change.

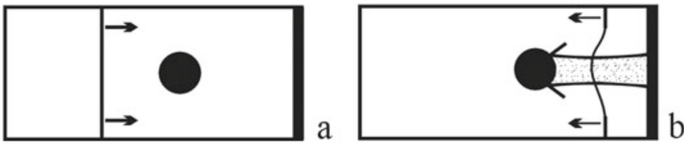

Fig. 10 Schemes of the flow over a cylinder

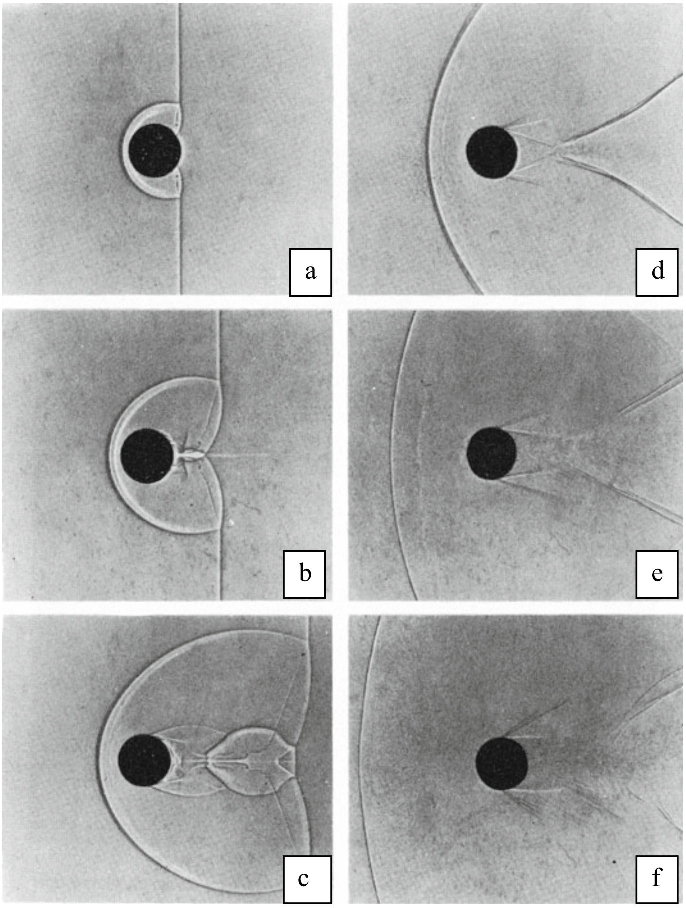

Fig. 11 Evolution of the flow at the interaction between a blast wave and a cylinder D = 12 mm. Time instants are $\ddot{t} = 1.0, 1.9, 3.7, 12.7, 37.3, 54.4$

The reflected shock wave appears in our range of sight at $\ddot{t} = 325$. In this time instant the Mach number of the oncoming flow is $M \approx 0.5$. Change in the flow structure in the course of propagation of the reflected shock wave is presented in Fig. 13. As shown in Fig. 13a, the shock wave front is curved due to the interaction with the wake. The central part of the reflected shock is accelerated, and at the distance $1 \div 1.5$ D becomes invisible. The flow from the marginal parts of the reflected wave to the center forms a vortex flow. At the given strength of the reflected wave, the jet impacts the cylinder. As a result, a stagnation shock propagating from left to right occurs (Fig. 13c–f). The conditions at the separation point change: the separation angle increases, and the strength of the shock at the separation point intensifies.

The shadow images presented in Fig. 13d–f show the process of diffraction of a shock wave over a cylinder. It is worth noting that the reflected wave moves in

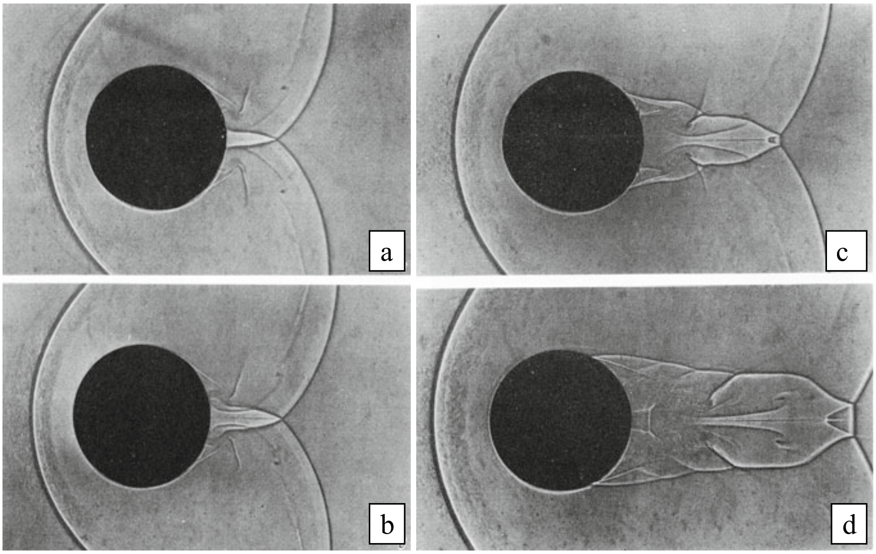

Fig. 12 Initial stage of the flow development behind the cylinder at the interation with the blast wave. D = 30 mm. Time instants are ť = 1.7, 1.9, 2.3, 2.9

the counterflow. Interaction of two flows moving in the opposite directions leads to the formation of new stagnation areas as well as local shocks in the mid-section plane. Experimental pictures obtained for the cylinder with D = 30 mm are presented in Fig. 14. Figure 14a demonstrates the flow structure where two separation points are in the mid-section. Figure 14b shows a later stage of the diffraction process. At some point the parts of the reflected wave meet (Fig. 13e, f), and the integrity of the reflected front is restored. At the distance equal approximately to 4D, the shock becomes planar.

As demonstrated by the experimental data obtained, the dynamics of the shock structure for cases of interaction of a cylinder with incident and with reflected shock waves differ significantly. These results, in our opinion, may be of both fundamental and practical significance. It is obvious that the phenomenon requires further in-depth study.

The author is grateful to her former colleagues M. K. Beryozkina and M. P. Syshchikova, who participated in the presented research.

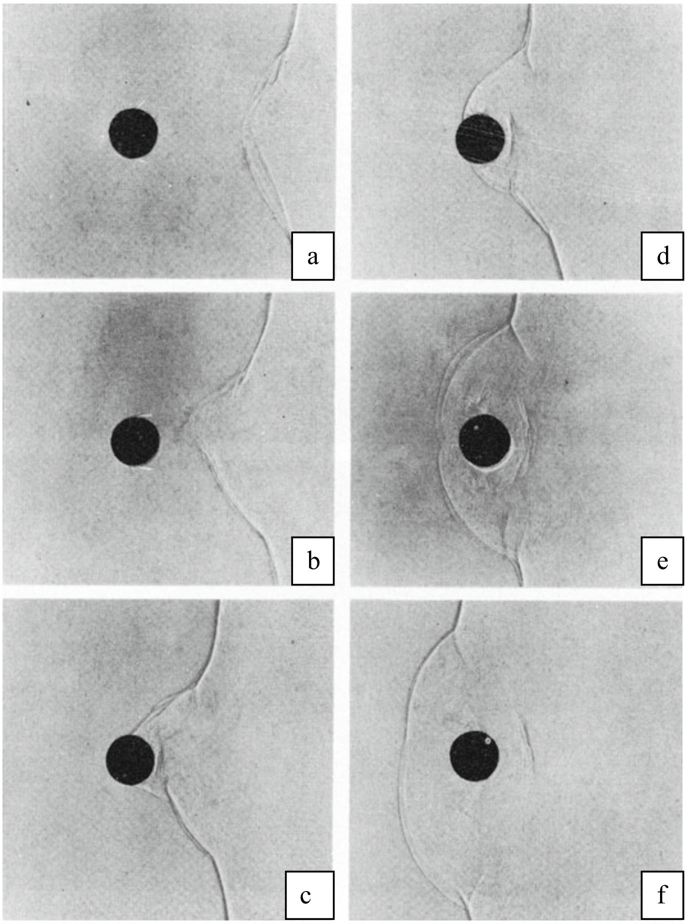

Fig. 13 Dynamics of the flow around the cylinder at the interaction with the reflected shock wave. D = 12 mm. Time instants are $\ddot{t}$ = 326.6, 327.0, 328.5, 329.0, 330.0, 330.6

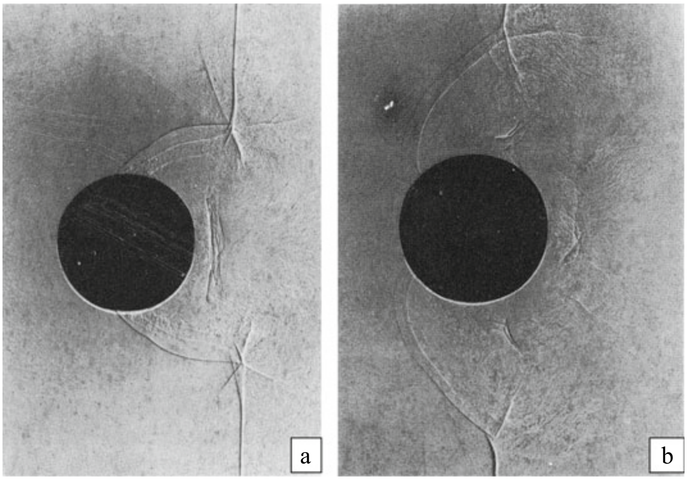

Fig. 14 Interaction of the reflected shock wave with a cylinder. Initial stage. D = 30 mm

References

1. Andriankin EI, Myagkov NN (1981) Double explosion in the perfect gas. Prikl Mekh Tekh Fiz 4:119–125
2. Andriankin EI, Myagkov NN (1983) Propagation of shock waves after a double explosion in the gas with counterpressure. Prikl Mekh Tekh Fiz 5:98–103
3. Andrushchenko VA, Murashkin IV (2013) Investigation of shock wave processes at an early stage of the interaction of two explosions in the nonuniform atmosphere. Estestv Tekh Nauki 6:25–27
4. Andrushchenko VA, Murashkin IV, Shevelev YuD (2015) Numerical investigation of o the problem on multiple explosions in the presence of an underlying surface. In: Proceedings of the 19th international conference on computational mechanics and modern application packages. Alushta, Russia, pp 362–364
5. Krassovskaya IV, Syschikova MP (1985) Some properties of the flow arising at head-on collision of two blast waves. Comb Expl Shock Waves 5:113–116
6. Ofengeim DKh, Drikakis D (1997) Simulation of blast wave propagation over a cylinder. Shock Waves 7:305–317
7. Beryozkina MK, Ofengeim DKh, Syshchikova MP (1995) Investigation of flow formation around a cylinder and in the wake behind it at diffraction of strong shock waves. In: Abstracts of the 20th international shock wave symposium. Pasadena, California, pp 141–142

Interaction of Small Scale Blast Waves with a Sphere, Cones, and an Ellipsoid

Kazuyoshi Takayama and Koji Tamai

1 Introduction

In dusty gas shock tube flow studies, dust particles are traditionally assumed to be spherical and their drag force is estimated based on the drag coefficient in steady flows. However, in reality upon shock wave loading on spherical particles, shock wave reflection and diffraction induce unsteady effects. In the past a few measurement of unsteady drag forces on bodies of various configurations were conducted.

Igra and Takayama [5] discussed unsteady drag forces on spheres in shock tube flows. Shock tube experiments of spheres were carried out by Britan et al. [3], Rodriguez et al. [7], and Bredin and Skews [2]. We proposed to directly measure drag forces acting on a sphere impinged by a shock wave of Ms = 1.20 [10]. In this experiment, we installed an accelerometer in an 80 mm diameter aluminum sphere, suspended the sphere in a vertical 300 × 300 mm cross sectional shock tube and monitored the evolution of the acceleration of the sphere. The force so far measured was compared with a result of a careful numerical simulation solving the Navier–Stokes equations.

Tamai [9] generated small scale blast waves exploding small amounts of explosives in a controlled fashion and also developed a shock tube, named as a blast wave simulator, which could simulate the small scale blast wave loading. These small scale blast waves were loaded onto axially-symmetric bodies having various configurations and the evolution of drag forces acting on these models was measured.

The two cone models were tested; a 40° apex angle and 80 mm base diameter cone, 60° apex angle and 60 mm diameter cones whose bases are combined, and a 60 mm minor diameter and 90 mm major diameter ellipsoid. The measured results were compared with numerical simulations solving the Euler equations.

K. Takayama (✉)
Institute of Fluid Science, Tohoku University, Sendai, Japan

K. Tamai
Central Glass Co. Ltd, Matsuzaka, Japan

© The Author(s), under exclusive license to Springer Nature Switzerland AG 2022

K. Takayama and O. Igra (eds.), *Frontiers of Shock Wave Research*,
https://doi.org/10.1007/978-3-030-90735-8_6

2 Experiment

Blast wave experiments have usually been conducted in open fields on a large scale. Therefore, such projects are not easily controlled. If explosion tests could be conducted on a laboratory scale, accurate data acquisition would be possible and the agreement between experiments and numerical predictions would be closer. To accomplish such an ambitious task, we at first started measuring the evolution of drag forces acting on bodies with various configurations upon its loading by blast waves.

Small Scale Explosion

Small scale blast waves were generated by igniting a 100 mg weight of PETN (Pentaerythritol Tetranitrate). The PETN had a dimension of a 5.4 mm in o.d. and 10 mm in length and was connected to an igniter. The igniter was a 10 mg weight silver azide pellet (AgN_3) glued on the edge of a 0.6 mm o.d. polished quartz optical fiber and inserted into a 1.2 mm i.d. hole drilled on the PETN surface.

To detonate the igniter, a Q-switched Nd:YAG laser beam of 20 mJ in energy and 7 ns in pulse width was transmitted through the optical fiber and the igniter was exploded in a time delay of less than 100 ns [6]. The PETN was instantaneously detonated.

As diverging blast waves were stable, thus after propagating about 100 mm from the explosion center, a uniformly spherical blast wave was obtained. Experiments were conducted inside a 1.8 m diameter test chamber which was part of the two-stage gas gun of the Shock Wave Research Center (SWRC) of the Institute of Fluid Science in the Tohoku University.

Figure 1 shows the time variation of overpressure across the blast wave, measured at stand-off distance of 100 mm using a pressure transducer (Kistler Model 603B). Two measured data shown by cross and circle were compared with appropriate numerical result (solid line). The ordinate denotes overpressure in kPa and the abscissa denotes the elapsed time in μs.

The simulation was done by solving one-dimensional Euler equations. The PETN explosion was replaced by a rupture of a 3 mm o.d. imaginary sphere containing pressurized air at 2.3 GPa and at room temperature. The total energy of the pressurized sphere was equivalent to that of 100 mg PETEN. The PETN has energy of 6.8 J/mg but about 30% of the PETN energy was consumed in a shock wave formation.

Figure 2 schematically shows the experimental setup. The tested model was suspended by a 1.2 mm o.d. stainless steel wire and placed100 mm below the PETN. The PETN pellet was positioned parallel to the suspension wire at 5 mm to the side. The force acting on the model was measured by an accelerometer (Endevco Piezoelectric accelerometer 2250A-10, sensitivity of $1.02 v/m/s^2$, and resonant frequency

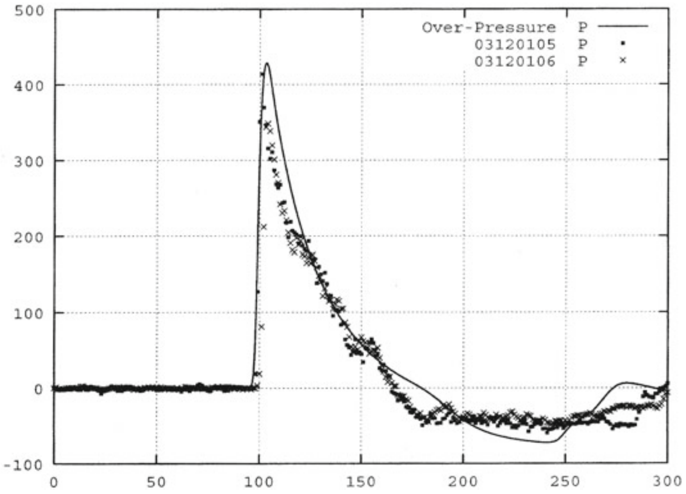

Fig. 1 Pressure history of a blast wave generated by the explosion of 100 mg PETN

Fig. 2 Experimental setup of a blast wave test

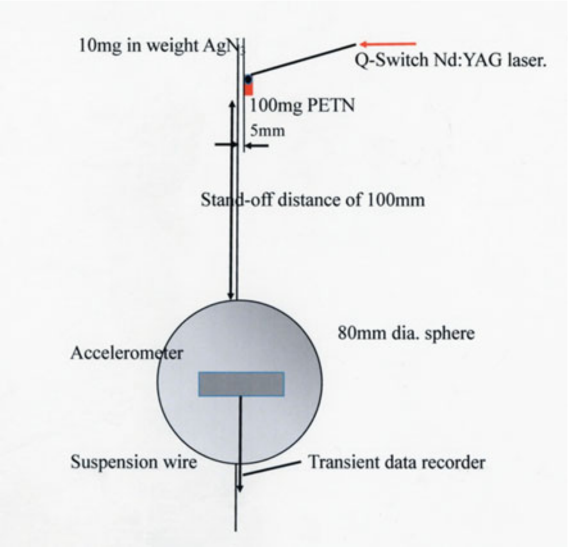

of 80 kHz) installed inside individual test models. For the given model weight, the force was readily estimated from the measured acceleration.

However, the acceleration was affected by the eigen-frequency of the model and suspension wire.

To eliminate the eigen-frequency from the measured data, we conducted a preparatory experiments impacting the test model, the accelerometer, and the suspension wire with an impact hammer (PCB 086C03) of known frequency characteristics. In eliminating the eigen-frequency from the measured data, the time variation of forces acting on the test model is readily obtained.

Prior to the blast wave tests, calibrations were conducted on individual test models. The details of the data deduction were reported in Tanno et al. [10] and in Tamai [9].

Blast Wave Simulator

A blast wave simulator is a shock tube which has a very short high-pressure chamber so as to generate a shock wave having an overpressure profile similar to that behind a blast wave. The shock tube is a vertical 300 × 300 mm shock tube, Tanno et al. [10], but its high-pressure channel is 200 mm long and 300 mm i.d., and has a 300 mm i.d. and 200 mm long double diaphragm section. A shallow cone of 116 mm height and 290 mm o. d. is attached at the end of the high pressure chamber. Figure 3a shows the blast wave simulator. Test models are suspended by a stainless steel wire along the shock tube center line. The wire is fixed underneath the diaphragm section so tightly as to eliminate the noises created at the moment of the diaphragm rupture. Figure 3b shows the test model.

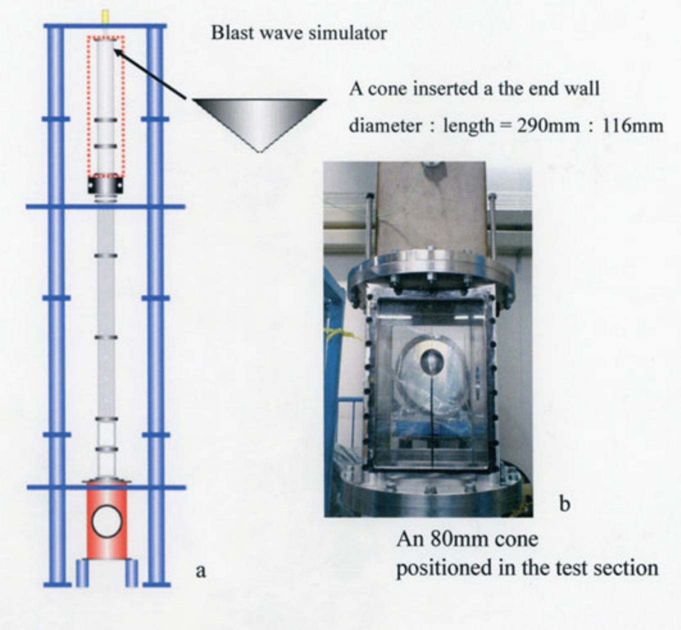

Fig. 3 The blast wave generator: **a** shock tube; **b** test model placed in the test section

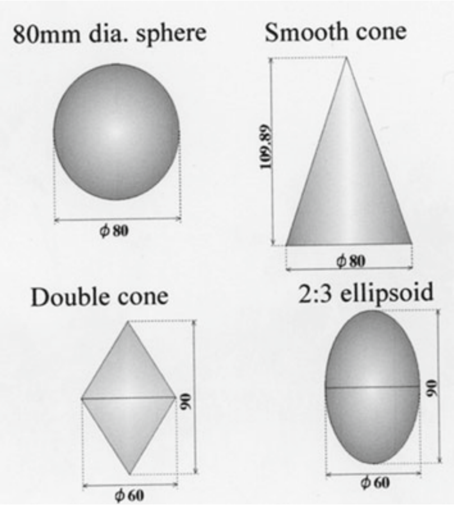

Fig. 4 Test models: **a** an 80 mm diameter sphere; **b** a 40° apex angle cone; **c** 60°apex angle double cones; and **d** a 60 mm minor diameter and 90 mm major diameter ellipsoid

Test Models

Test models are suspended by a 1.2 mm o.d. stainless steel wire and positioned in the test section as seen in Fig. 3b.

Figure 4a shows an 80 mm o.d. sphere weighing 684 g; in Fig. 4b a cone of 40°apex angle, the 80 mm base diameter, and weighing 471 g; in Fig. 4c two 60° apex angles, 60 mm base diameter cones connected upside down in a diamond shape weighing 226 g; in Fig. 4d a 60 mm minor diameter and 90 mm major diameter ellipsoid weighing 442 g. Drag forces were obtained through the process firstly eliminating the eigen-frequency out of the measured acceleration data and secondly by dividing the processed data by the weight of models.

Numerical Simulation

Tamai [9] simulated the interaction of the test models with small scale blast waves solving the Euler equations in axial symmetry co-ordinates using the GRP/MBT Scheme [1].

3 Results and Discussion

An 80 mm Sphere

Figure 5a shows the acceleration of an 80 mm diameter sphere impinged by the blast wave shown in Fig. 1. The ordinate shows acceleration in m/s^2 and the abscissa shows time in μs. The red solid line shows the control of the Q-switched Nd:YAG laser. A Q-switched beam was irradiated at 400 μs and instantaneously the PETN was ignited. The black solid line shows the acceleration of the sphere with the elapse of time. The blast wave propagated along the stand-off distance of 100 mm and impinged the sphere later. When the blast wave impinged the model, the shock wave Mach number is estimated to have been about Ms = 1.21 ± 0.02. However, as the suspension wire was only 5 mm distant from the PETN the precursory stress waves induced by the explosion propagated along the suspension wire. The stress waves and reflected waves appear in Fig. 5, whereas in the blast wave simulator, the precursory waves generated at the diaphragm ruptures were stopped from propagating through the suspension wire.

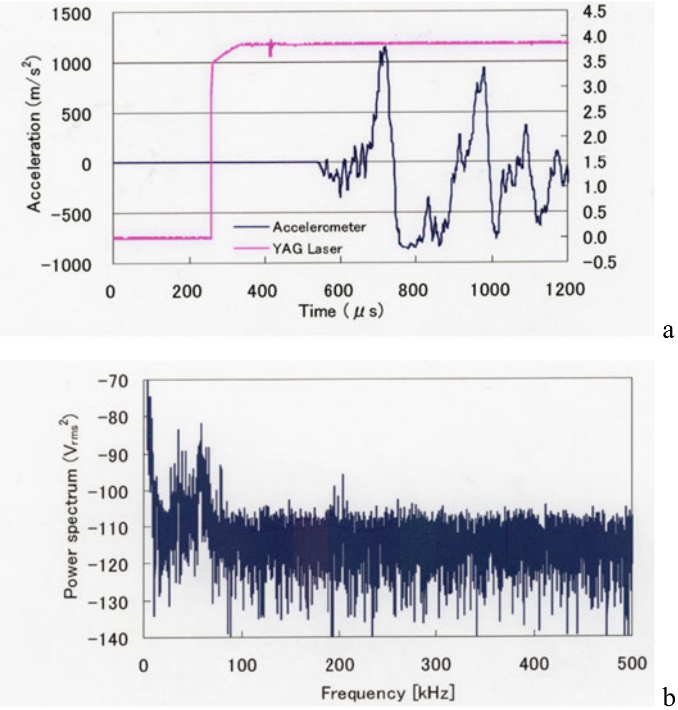

Fig. 5 Result of blast wave loading on an 80 mm diameter sphere: **a** time variation of an acceleration; **b** power spectra of **a**

Applying the Fourier transformation to measured acceleration data, we obtained the power spectra shown in Fig. 5b, from which we could determine the eigen-frequency of the model and the suspension wire. In the present series of experiments, we conducted the preparatory experiments and obtained the eigen-frequencies of individual test models.

We impacted the test model by an impact hammer, the impact characteristics of which were known. Then, from the impact response, we successfully estimated the eigen-frequency of the model. Then eliminating the contribution of the eigen-frequency out of the measured signals and dividing the acceleration by the model weight, we estimated unsteady drag forces. However, the signal seen in Fig. 5a was so distorted that we did not use it for comparison with the numerical simulation.

In Fig. 6, unsteady drag forces acting on an 80 mm o.d. sphere measured by the blast wave simulator were compared with numerical simulations. The ordinate shows the force in N and the abscissa shows the elapsed time in μs. The solid line and shaded line show a numerical simulation and a result obtained by the blast wave simulator. The agreement between the numerical simulation and the experiments was fairly good.

Drag forces increased and became a maximum at the position where the reflected shock wave on the frontal surface transited from Mach reflection to regular reflection, that is, the local inclination angle of the sphere is the critical transition angle [4]. Drag forces remained high for a relatively wide area in the vicinity of the critical transition angle and started to decrease when the transmitting shock wave propagated along the rear surface of the sphere. The propagation of the transmitting shock wave along the spherical rear surface was much more complex than that along conical rear surface.

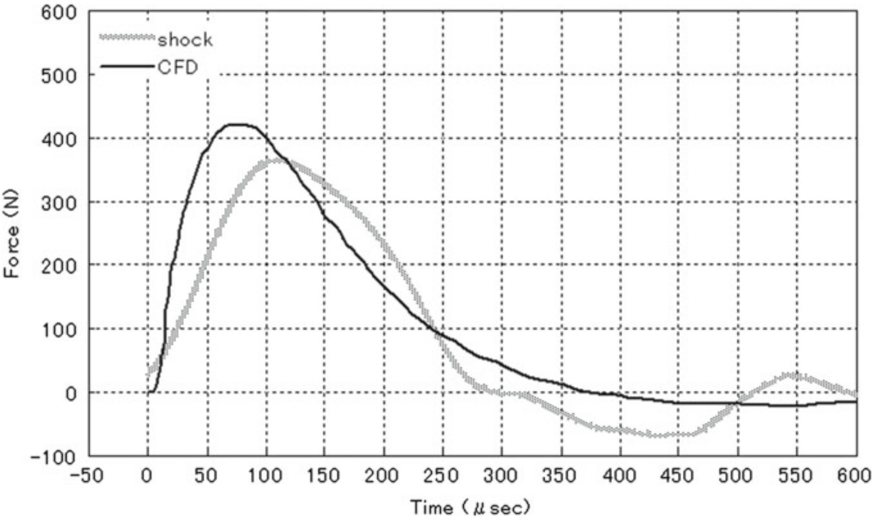

Fig. 6 Unsteady drag force acting on an 80 mm o.d. sphere

A shock wave diffracting along a cylindrical rear surface would converge into a line, whereas a shock wave diffracting along the spherical rear surface was an implosion into the rear stagnation point. The integration of pressures over the entire surface resulted in the drag force. Hence, the drag force could be negative when the pressure at the rear stagnation became very high.

This trend was also found in the numerical simulation reported by Tanno [10].

40° Apex Angle Cone

We loaded, in a small scale blast wave experiment, a shock wave at Ms = 1.20 onto a 40° apex angle and 80 mm base diameter cone. The measured drag forces were compared with the numerical results in Fig. 7. The solid line shows the numerical result, a broken line shows the result of small scale blast wave loading, and a shaded line shows that of shock wave loading. The value of maximum drag force measured by the small scale blast wave loading was higher than that measured in the blast wave simulator. The maximum drag force appearing in the blast wave simulator appeared slightly earlier in the small scale blast wave loading than in the blast wave simulator. However, taking the slight difference of in the shock wave Mach numbers between the two experiments into consideration; such a difference was negligibly small. Hence the blast wave simulator was found to be a very useful facility.

As the reflection of the incident shock wave of Ms = 1.20 from the cone remained a regular reflection, the pressure on the cone was constant. Then the pressure behind the diffracting shock wave at the edge was constant. Hence the resulting drag force

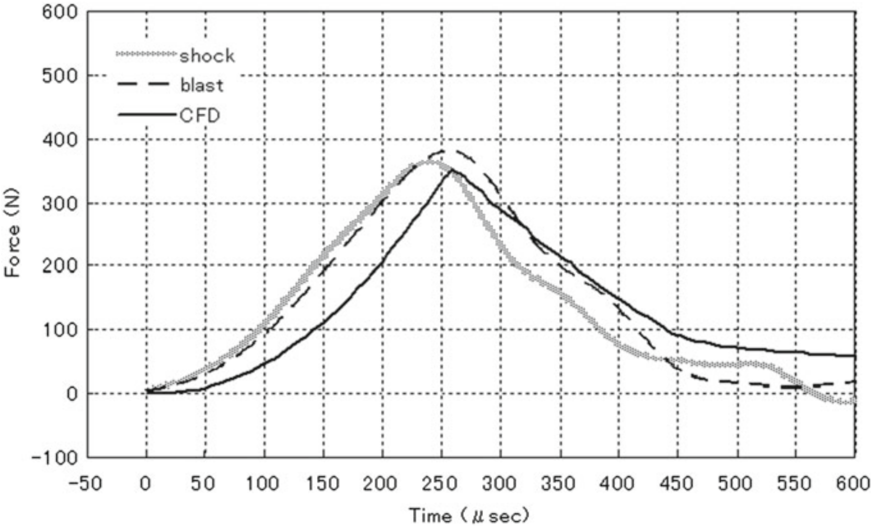

Fig. 7 Unsteady drag force acting on a 40° apex angle cone

decreased monotonously with the elapse of time. The diffracting shock wave did not focus.

The numerical results agreed well with the experimental results. However, it is an open question as to what would occur if such a simple model like a cone was impacted obliquely by a planar shock wave. Then the resulting drag forces of obliquely impinged cone would become much more complex.

60° Apex Angle Cones Combined in Diamond Shape

We loaded a small scale blast wave and a shock wave at Ms = 1.20 onto a 60° apex angle and a 60 mm base diameter cone combined into a diamond shape. In Fig. 8, we compared measured drag forces with the numerical simulation. The ordinate shows drag forces in N and the abscissa shows the elapsed time in μs. The solid line shows the numerical result, a broken line and a shaded line shows results of the small scale blast wave loading and the blast wave simulator, respectively. The measured drag forces increased and decreased monotonously and agreed well with those of the numerical results. However, values of measured maximum drag forces were 10–20% higher than the CFD results.

The reflected shock wave over the frontal cone surface was regular reflection so that the pressure remained constant and the pressure behind the diffracting shock wave at the 120° corner also remained constant. Hence, the drag force monotonously increased along the frontal conical surface and decreased monotonously along the

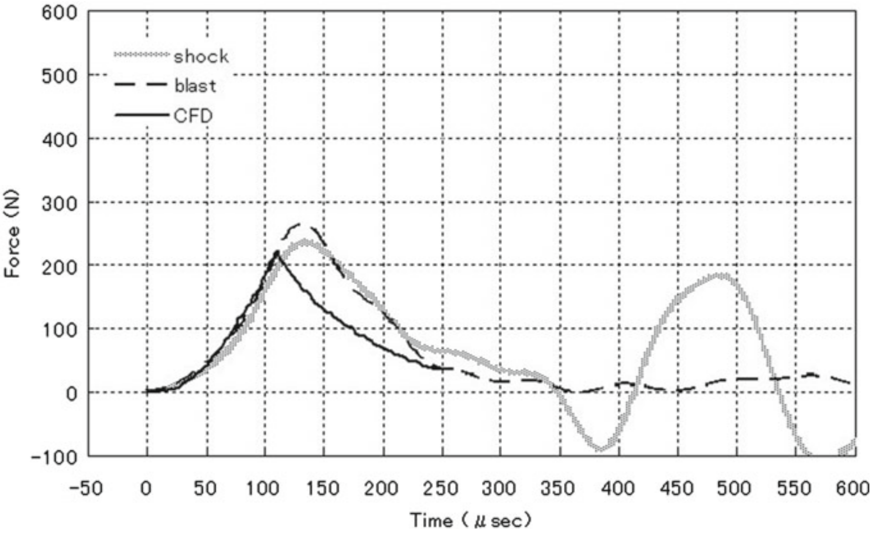

Fig. 8 Unsteady drag force acting on 60° apex angle cones combined in diamond shape

rear cone surface. The diameter of the 40° apex angle cone was 80 mm and the maximum drag force was about 365 N, while the diameter of the 60° apex angle cone was 60 mm and the maximum drag force was about 207 N. In the scatter of the experimental conditions, the ratio of the maximum drag forces acting on two cones was 1.76 whereas the ratio of cross sections of the two cones was 1.78. Hence the maximum drag force is proportional to the cone's cross section.

In the blast simulator experiment, we noticed the presence of a secondary fluctuation of the drag force but ignored such a fluctuation.

A 60 mm Minor Diameter and 90 mm Major Diameter Ellipsoid

We loaded a small scale blast wave and a shock wave in a blast wave simulator at Ms = 1.20 on a 60 mm minor diameter and 90 mm major diameter ellipsoid and compared the measured results with an appropriate numerical simulation, see in Fig. 9.

The ordinate shows the drag forces in N and the abscissa shows the elapsed time in µs. The solid line shows the result of the numerical simulation, marked CFD and a broken line and a shaded line show results of the blast wave loading and the blast wave simulator, respectively.

Along the frontal surface, the reflected shock wave transited from regular to Mach reflection at the critical transition angle and then the pressure was a maximum [4].

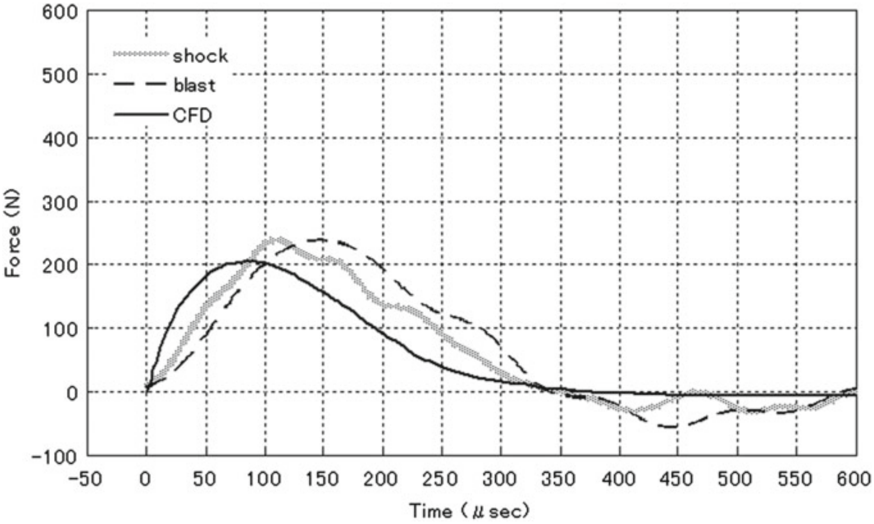

Fig. 9 Unsteady drag force acting on a 60 mm minor diameter and 90 mm major diameter ellipsoid for Ms = 1.20 and comparison with CFD

Hence, drag forces were high in the vicinity of the critical transition angle. A similar trend appeared over the 80 mm diameter spheres as seen in Fig. 6. Trends of drag force profiles measured in the small scale blast wave loading and in the blast wave simulator agreed well and as to the region where the drag forces remained high continued over about 100 μs, whereas the numerical drag force profile appeared slightly earlier and the value of maximum drag force was low. This would be attributable to the lower estimation of shock wave Mach number Ms = 1.20. It should be Ms = 1.22 in numerical simulation.

Measured drag force profiles showed the appearance of negative drag force. The numerical simulation also showed a slight sign of negative drag force. The pattern of drag force profiles is very similar to the shock/sphere interaction. In the case of shock wave loading on cones, we found a correlation that the maximum drag force varied proportional to the projected area of cones. A similar correlation seems to exist in the sphere and ellipsoid. Hence this correlation would be expanded universally to all the models.

4 Concluding Remarks

This is a project of applying shock tube technology to conduct a reliable small scale blast wave test.

By exploding a 100 mg PETN pellet, we safely and accurately generated blast waves that were on a laboratory scale. The characteristics of the blast waves were so reproducible that we measured directly drag forces of a sphere, cones, and an ellipsoid exposed to the blast waves. To support the project, we constructed a blast wave by modifying a vertical 300 × 300 mm shock tube. The details of the vertical shock tube are described in Takayama [8].

This report is a simple introductory work using small blast wave loading. At the moment, an effort is directed to uniaxial force measurement but the present performance should be refined to expand to multi-axial force measurement.

References

1. Ben-Artzi A, Falcovitz J (2003) Generalized Riemann problems in computational fluid dynamics. Cambridge University Press, London
2. Bredin M, Skews B (2001) The measurement of drag in unsteady compressible flow. In: proceeding 23rd international symposium on shock waves. Arlington, pp 463–471
3. Britan A, Elpherin T, Igra O, Jiang P (1995) Acceleration of a sphere behind planar shock waves. Exp Fluids 20:84–90
4. Heilig W (1982) High speed interferometric study of unsteady shock wave processes. In: proceeding 15th international congress on high speed photography and photonics
5. Igra O, Takayama K (1993) Shock tube study of the drag coefficient of a sphere in a non-stationary flow. Proc R Soc Lond Ser A 442:231–246

6. Mizukaki N (2001) Study of quantitative visualization of shock wave phenomena. Ph.D. Thesis, graduate school of engineering, faculty of engineering, Tohoku University
7. Rodriguez G, Grandeboueuf P, Khelifi M, Haas JF (1995) Drag coefficient measurement of sphere in a vertical shock tube and numerical simulation. In: proceeding 20th international symposium on shock waves, vol. 3. Marseille, pp 43–48
8. Takayama K (2019) Visualization of shock wave phenomena. Springer-Verlag, Heidelberg
9. Tamai K (2004) Study of developments of a small blast wave test facility and a blast wave simulator. Ph.D. Thesis, graduate school of engineering, faculty of engineering, Tohoku University
10. Tanno H, Itoh K, Saito T, Abe A, Takayama K (2003) Interaction of a shock with a sphere suspended in a vertical shock tube. Shock Waves 13:191–200

Mach Waves Occurring Over a Backward Facing Edge in Supersonic Flow

V. Sridhar, F. Seiler, R. Hruschka, H. Kleine, S. Gai, and J. Srulijes

1 Introduction

Flows over and in cavities often present in high-speed flows can lead to unsteady fluid oscillations. These fluid oscillations typically cause unwanted drag increase, structural noise and vibrations, which can exert severe damage to the structure of the vehicle. This topic is therefore important to current investigations in aerodynamics and in acoustics. Despite the apparent simplicity of the basic flow configuration, the flow inside the cavity is rather complex because of its inherent unsteadiness, and some aspects of modeling it have not yet been fully clarified. Numerous investigations have been conducted on this subject, most recently a study on the influence of the length-to-depth ratio L/D of the cavity on the flow behavior [21].

At supersonic speeds, the cavity flow produces waves which can lead to large pressure gradients, which are mainly represented by the so-called Mach waves. For a better understanding of these fundamental processes, schlieren visualizations of cavity flows have been performed in a blow-down wind tunnel at flow Mach numbers 2 and 3. The measured angles and speeds of the Mach waves are compared with an analytical model established recently for the Mach wave dynamics emitted from supersonic shear layers [9, 12]. It should be added that this model was developed for planar flows, however all previous experimental verifications were conducted for axisymmetric flows, where the shear layer thickness was small compared to the diameter of the jet, which justified the application of a two-dimensional planar theory.

V. Sridhar · H. Kleine (✉) · S. Gai
University of New South Wales (UNSW), Australian Defence Force Academy, Canberra, ACT 2600, Australia
e-mail: h.kleine@adfa.edu.au

F. Seiler
Karlsruhe Institute of Technology (KIT), 76131 Karlsruhe, Germany

R. Hruschka · J. Srulijes
French-German Research Institute of Saint-Louis (ISL), 68301 Saint-Louis, France

© The Author(s), under exclusive license to Springer Nature Switzerland AG 2022

K. Takayama and O. Igra (eds.), *Frontiers of Shock Wave Research*,
https://doi.org/10.1007/978-3-030-90735-8_7

The current study, to the best of the authors' knowledge, is the first application of this theory to a truly planar flow configuration.

The experiments have been performed with schlieren visualizations of the cavity flow in the blow-down wind tunnel at UNSW Canberra at flow Mach numbers $M_i = 2$ and 3 (index i = wind tunnel flow), and the investigations described here were made for cavities with L/D = 8. From the experiments, the angles of the Mach waves and their movement downstream, in particular their velocities, are determined. As noted above, these experimental data are compared to the theory of Oertel sen et al. [9, 12]. In addition to the experiments, CFD-calculations were performed at ISL Saint-Louis to be visually compared with the experimentally taken Mach wave patterns and with the prediction of the theory of Oertel sen et al. [12].

2 Cavity Investigations at UNSW Canberra

Wind Tunnel Setup and Operation

Experiments were carried out with a planar two-dimensional cavity model at freestream flow Mach numbers of $M_i = 2$ and 3 in the supersonic blow-down wind tunnel facility at UNSW Canberra, see Fig. 1. The dimensions of the tunnel test section are 155 mm in height and 90 mm in width, and the diameter of the field of view is 140 mm. The tunnel is run with dried compressed air, and the 30 m^3 reservoir can provide a flow time of up to 25 s with a useful test flow time of up to approximately 20 s after the initial transient start-up. The flow Mach number is constant within a percentage variation of ±0.05% during the steady flow time.

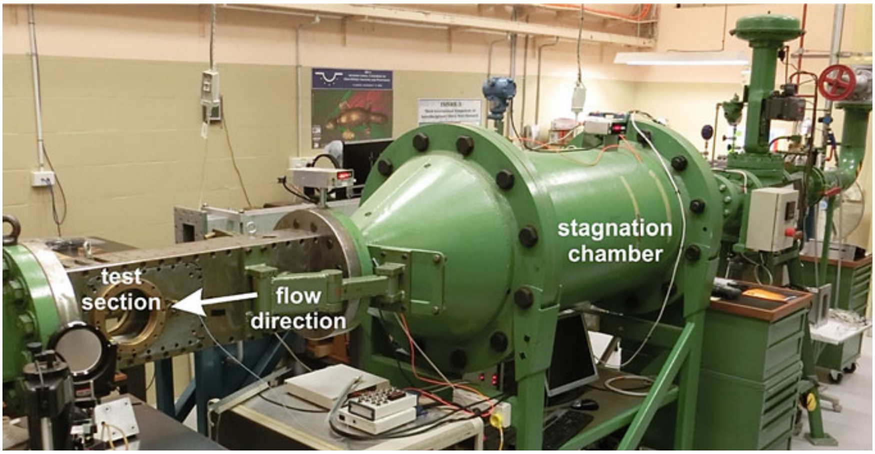

Fig. 1 Blow-down wind tunnel at UNSW Canberra

Typical absolute stagnation pressures in the plenum chamber upstream of the nozzle are 200 kPa for $M_i = 2$ and 300 kPa for $M_i = 3$. The planar nozzles are fixed and have to be exchanged if the Mach number is to be varied. For each Mach number, the uniformity of the flow in the test section was verified prior to a test series with the help of a traversable Pitot probe. Other pressure measurements and visualizations confirmed that the chosen nozzles delivered the design flow Mach numbers and that the relations for quasi-one-dimensional nozzle flow were appropriate to determine the free stream flow values. The static pressure in the test section was measured in each test, and the visualizations were only conducted when the pressure had reached the nominal steady state value.

The flow velocity u_i in the free stream is optically measured by streak records of the movement of the window boundary layers [20]. It agrees, within ±5 m/s, with the value predicted by assuming an isentropic expansion of the flow from known, measured conditions in the stagnation chamber of the wind tunnel. The free stream flow Mach number M_i is independently verified by pressure measurements and flow visualization. From those measurements, one can obtain the speed of sound a_i of the free stream and thus the free stream temperature T_i. Typically one finds that the measured value for T_i corresponds within less than three degrees to the value predicted by an isentropic expansion through the given nozzle. The temperature T_a in the cavity is assumed to be equal to the stagnation temperature of the flow (290 K in this case) irrespective of the Mach number, according to a widely accepted modification of the original equations describing the oscillations in the cavity [2]. This provides the following flow data with index (a) = cavity, index (i) = wind tunnel flow:

(1) $M_i = 2$: $u_i = 509$ m/s, $T_i = 161$ K, $T_a = 290$ K, $a_a/a_i = 1.34$;
(2) $M_i = 3$: $u_i = 612$ m/s, $T_i = 104$ K, $T_a = 290$ K, $a_a/a_i = 1.67$;

Cavity Geometry

The cavity is part of a splitter plate that spans the whole width of the tunnel (i.e. 90 mm), see Fig. 2a. It starts 184 ± 0.04 mm downstream of the front edge of the plate. This distance is also known as "fetch". Some experiments were also performed with a shorter fetch (33.6 ± 0.04 mm) to obtain an estimate for the influence of the boundary layer thickness on the flow behavior and type of boundary layer. The leading edge of the splitter plate is sharp to have an attached oblique shock on the lower side and an as-small-as-possible disturbance on the top side. The length, L, and depth, D, dimensions of the two cavities are, with L/D = 8:

(1) fetch = 184 mm ± 0.04 mm: L = 32 mm, D = 4 mm ± 0.04 mm (long fetch),
(2) fetch = 33.6 mm ± 0.04 mm: L = 40 mm, D = 5 mm ± 0.04 mm (short fetch).

The two cases consider different thicknesses and different types of the boundary layer arriving at the leading edge. The Reynolds number Re given below is determined with the free stream properties and the fetch as characteristic length.

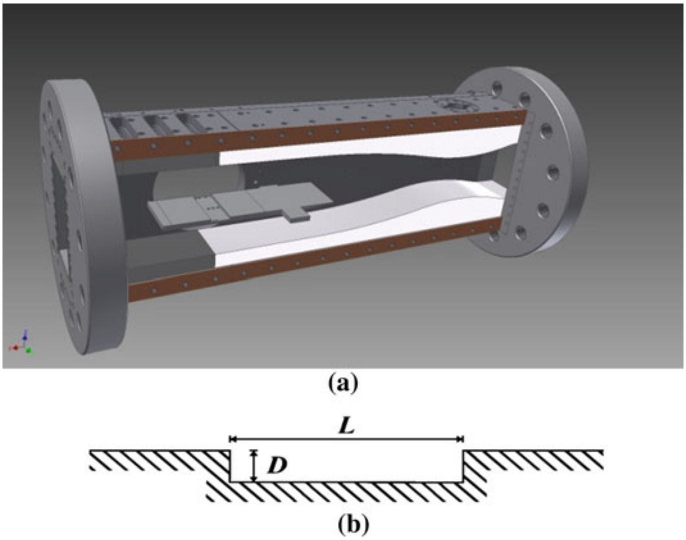

Fig. 2 Splitter plate with cavity **a** installation in the test section (sidewalls removed for clarity), flow from right to left, **b** basic cavity nomenclature and dimensions

(1) fetch = 184 mm: the boundary layer thickness at the cavity leading edge is around 3 mm. The boundary layer is fully turbulent with Re = 4.7 million for $M_i = 2$; Re = 4.3 million for $M_i = 3$.

(2) fetch = 33.6 mm: the boundary layer thickness is approximately 1 mm with laminar/ transitional behaviour and Re = 0.86 million for $M_i = 2$; Re = 0.78 million for $M_i = 3$.

Schlieren Method

Time-resolved flow visualisations were conducted with a high-speed camera and a Z-type schlieren setup, see e.g. Merzkirch [6] or Settles [16] for an overview of such visualization systems. Depending on how light source and schlieren cutoff are shaped, a monochrome schlieren system can, in a two-dimensional planar flow, detect either the magnitude of the density gradient in x- or y- direction or its overall magnitude irrespective of its direction. In the first two cases, the light source has the shape of a narrow slit, and the schlieren cutoff is a straight knife edge, while in the latter (known as “omnidirectional” schlieren system) both light source and cutoff have a circular shape. In the case of the omnidirectional schlieren system, it is necessary to correct the effects of astigmatism [3].

The two concave mirrors in the setup have a focal length of 2.624 m. The camera used in the present tests is a Shimadzu HPV-1 which can capture 102 frames at a constant resolution of 312 × 260 pixels with frame rates up to 10^6 frames per

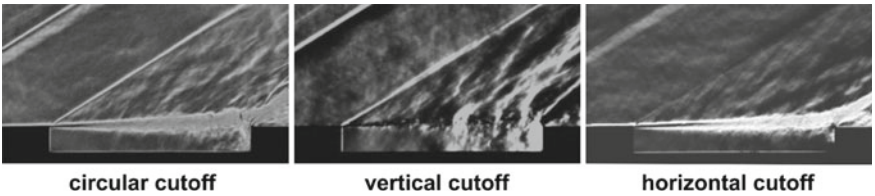

Fig. 3 Mach number 2 flow over the cavity visualized with different schlieren techniques

second (fps) and a minimum exposure time of 0.25 μs. Typical frame rates in the tests reported here are 250,000 and 500,000 fps. The image magnification in the tests conducted ranges from 0.41 to 0.57. The light source is a powerful photographic flash light (Metz 45CT4) that provides sufficient illumination for recording times up to 1 ms [19, 23]. The visualization is started by manual trigger once the flow in the tunnel is fully established.

Each visualization technique displays different features of the flow field in and above the cavity, see Fig. 3, where each visualization is taken with a different version of the schlieren technique (different cutoffs). These images were obtained for a cavity configuration with the shorter fetch distance of 33.6 mm from the splitter plate front edge to the cavity leading edge. For the tests described further below, primarily the vertical cutoff is used as the main features of interest are generating density gradients in flow direction in which a vertical cutoff schlieren setup has the highest sensitivity.

Cavity Schlieren Visualizations

Representative image series for flow Mach numbers $M_i = 2$ and $M_i = 3$ are shown in Fig. 4a, b for the first case described in Sect. "Cavity Geometry" with a fetch of 184 mm, i.e. for a fully turbulent boundary layer at the beginning of the shear layer

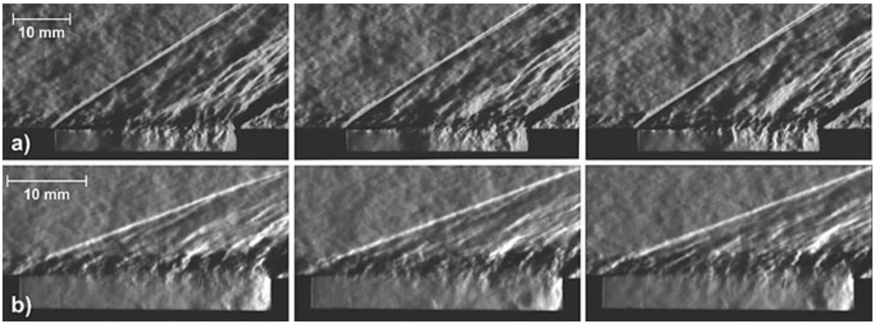

Fig. 4 Schlieren frames with fetch = 184 mm, turbulent boundary layer, frames are $\Delta t = 8$ μs apart: frame rate 250 kfps, **a** $M_i = 2$ and **b** $M_i = 3$

over the cavity. In both series, a weak oblique shock, called Mach line, emanating from the leading edge is most visible as a result of the separating boundary layer. For Mach number $M_i = 2$, the angle of this weak shock is theoretically predicted as 30.0°, and for Mach number $M_i = 3$ this angle becomes 19.5°. The calculated values are verified by measuring the angles on the visualizations of Fig. 4 with an accuracy of ± 1° which indicates that the design Mach numbers 2 and 3 are, indeed, established in the free stream.

Both series in Fig. 4 show the flow being macroscopically stationary, especially when looking at the cavity leading edge Mach line. The incoming plate boundary layer, with a thickness of about 3 mm, separates at the cavity leading edge forming from there a shear layer from which pressure waves are emitted to the inside and the outside of the cavity as clearly visible in Fig. 4. The angles of the waves appear slightly steeper than the angles of the leading edge Mach lines. This fact suggests that these pressure waves are the well-known Mach waves, which are triggered by structures in the shear layer as they move more slowly than the flow in the wind tunnel. This observation was already reported by Sridhar et al. [22, 23] and will be further explored in this work.

The second case noted in Sect. "Cavity Geometry" is done with short fetch of 33.6 mm and a laminar/transitional boundary layer at the leading edge of the cavity. The Mach waves are more noticeable, Fig. 5, than for a turbulent incoming boundary layer as it is seen on Fig. 4. It seems that the Mach waves in Fig. 5 are formed slightly further downstream from the separation edge, as compared to the cases with a turbulent boundary layer. The images also give the impression that the Mach waves here develop more regularly in time and space than in the case of a boundary layer that is turbulent at the cavity leading edge.

On the basis of visualizations such as Figs. 4 and 5, a schematic of the supersonic flow over the cavity can be established, showing in Fig. 6 how outward and inward of the cavity waves exist that run downstream. According to this it is reasonable to assume that the separation of the boundary layer at the leading corner of the cavity develops into a series of pressure waves, steepened as Mach waves which arise from macroscopic structures moving inside the shear layer. In the literature (e.g. [25, 26]), instabilities are often held responsible for this. Realistically, however, these are vortex structures which form a downstream-moving vortex train. The schematic given in Fig. 6 is derived from this idea. This drawing is supported by the detailed investigations of Oertel sen. et al. [9–12] on the Mach waves released from the shear

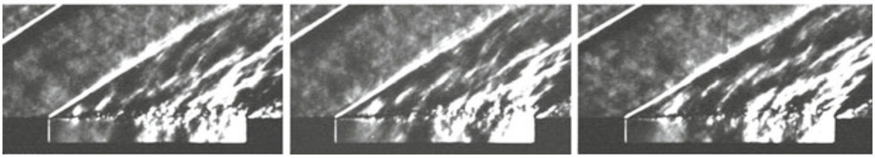

Fig. 5 Schlieren frames with fetch = 33.6 mm, laminar/transitional boundary layer, frames are $\Delta t = 8\ \mu s$ apart; frame rate is 1 Mfps, $M_i = 2$

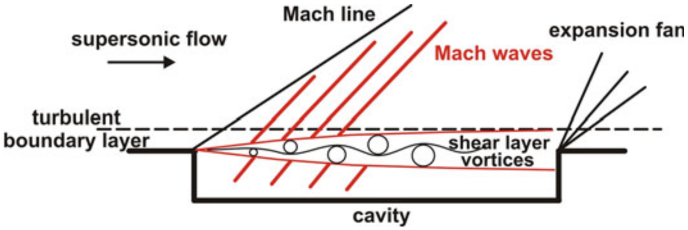

Fig. 6 Schematic of the flow pattern with shear layer, Mach line at leading edge, Mach waves and expansion fan at trailing edge

layer at supersonic jets. Other authors, e.g. [5, 13–15] also suggest that it is reasonable to associate the large turbulent structures being represented by vortices which move downstream in the jet mixing layer.

When looking at Figs. 4 and 5, the Mach waves appear clearly visible in the flow above the cavity. They are regularly arranged which is particularly evident. Within the cavity, the Mach waves are visibly smeared. This is mainly caused by the fact that the region inside the cavity is confined by the cavity bottom wall. As a result, the Mach waves occurring inside the cavity are reflected at the bottom of the cavity and cannot be well identified.

3 Similarity Between Jet and Cavity Shear Layer

Jet-Produced Mach Waves

In supersonic flows there exists a similarity between the shear layer separating the internal jet flow from the outer environment and the shear layer over a cavity. A differential interferometry visualization of a supersonic jet at Mach number 2.2 is shown in Fig. 7, taken by Oertel [8]. Mach waves are present inside the jet and outside. The angle of each of the two Mach wave families is represented by a red line.

Oertel’s idea is that the shear layer is divided into two vortex trains which move at two different velocities, namely inside the jet in the direction of the supersonic jet with a high velocity w’ and outside the jet towards the periphery with a lower velocity w”, as depicted schematically in Fig. 8. The different velocities in the two vortex trains are indicated by the dissimilar distances between the vortices in the schematic diagram of Fig. 8. In this example, the w’-vortices are three times faster than the w”- vortices. For simplicity, the vortices here have a round shape, but this does not have to be the case in general. As described above, the vortices draw associated Mach waves, both moving downstream at the same speeds. The w’- Mach waves are associated with the w’-vortices, and the same applies to the w”- Mach waves and the w”-vortices. Consequently, the w’-Mach waves in the surrounding are fast

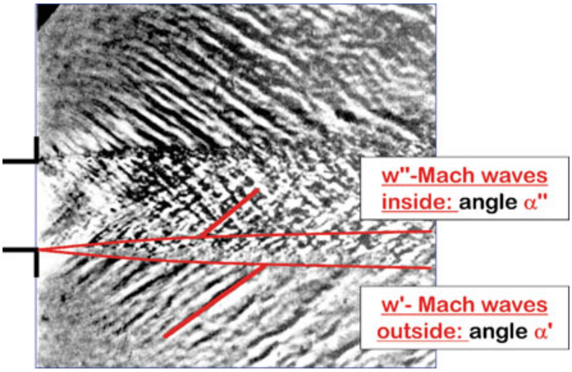

Fig. 7 Differential interferometry picture of a free jet at $M_i = 2.2$ [8]

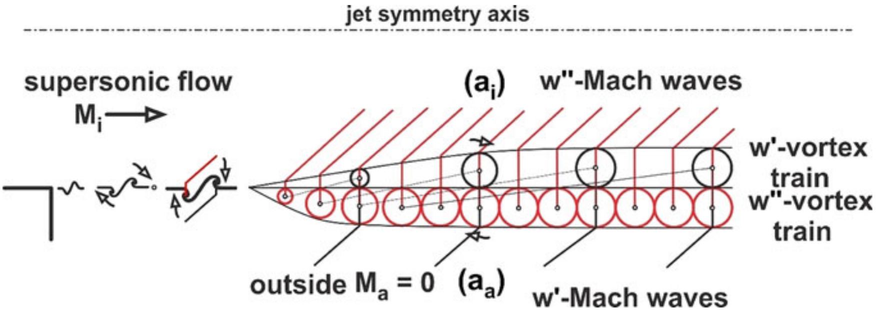

Fig. 8 Two vortex trains inside the jet shear layer. Example with $w'/w'' = 3$, $a_a = a_i$, $M_i = 2$

running and are linked with the w'-vortex train. The slower w"-Mach waves in the jet flow are produced by the w"-vortex train outside. A detailed description of these gasdynamic processes is given in Oertel sen et al. [9, 12].

In Oertel sen et al. [12] the existing work in the area of supersonic jet noise generation is described extensively which is why a repetition is omitted here. In the mentioned publication it is outlined that numerical results, partially obtained by large-eddy simulations, mostly describe the formation of Mach waves outside of supersonic free jets. Some of these results are compared with the theory of Oertel sen et al. [12], and they are mostly in proper accordance. Similarly, comparisons with experimental data also show a satisfactory match, see also Oertel sen et al. [9]. Classical models are also addressed in Oertel sen et al. [12], e.g. Tam [24, 26], but have difficulties in correctly describing angles and speeds of Mach waves from supersonic shear layers.

Cavity-Produced Mach Waves

In supersonic flow, the shear layer of a free jet and the one above a cavity are similar in their behavior. As each emit Mach waves to the inside as well as to the outside. Therefore, it is expected that Oertel's theory can also be used to explain the dynamics of Mach wave emission by the cavity shear layer. A schematic drawing similar to that in Fig. 8 is given in Fig. 9 with the two vortex trains moving downstream inside the cavity shear layer.

Comparing the jet flow field (Fig. 7) with that of the cavity (Fig. 4) one can see that the flow inside the jet (i) is represented by the flow “outside the cavity”, also denoted by (i). Analogously, the area outside the jet (a) corresponds to the area “within the cavity”, hereafter referred to as (a). One important difference is the fact that the (a)-region in the case of the cavity is confined by the cavity floor while it is unconfined in the case of the jet flow seen in Fig. 7. The resulting feedback from the cavity walls affects the w’-Mach waves within the cavity, which cannot be well identified due to reflections at the bottom of the cavity, see Figs. 4 and 5. Furthermore, three-dimensional flow effects along the width of the cavity of 90 mm lead to distortions of the schlieren light beam so that wave fronts become less clearly visible within the cavity. As a result, a measurement of the w’-waves from the available visual records would have a large error range, and therefore an evaluation and a comparison with the theory is omitted.

Furthermore, when approaching the trailing edge of the cavity, the shear layer itself partially interacts with this trailing edge and can no longer be considered as a free shear layer in this region. It can therefore be expected that the two-vortex-train model will not be applicable once the influence of the trailing edge modifies the shear layer. It should also be noted that the shear layer thickness is small compared to the extent of the free stream flow, but it is of a similar order of magnitude as the cavity depth. As mentioned in Sect. “Cavity Investigations at UNSW Canberra”, the influence of the thickness of the shear layer was investigated with two different fetches, 184 mm and 33.6 mm, to determine the influence of incoming boundary layer thickness and its type on the formation of Mach waves: either turbulent for the long fetch and laminar/transitional for the short fetch arrangement.

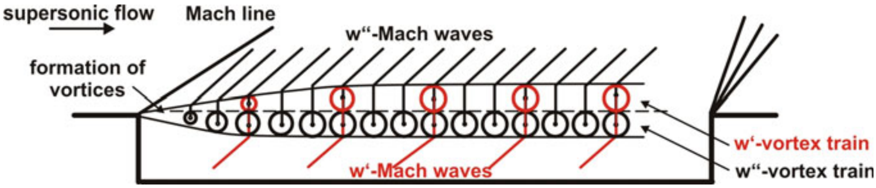

Fig. 9 Two vortex trains inside the cavity shear layer. Same example as given in Fig. 8 with w’/w” = 3, $a_a = a_i$, $M_i = 2$

Oertel's Theory

The two-vortex-train shear layer model given in Fig. 9 shows that the w"-Mach waves over the cavity are formed by the w"-vortex train that faces into the cavity. Similarly, the w'-vortex train generates the w'-Mach waves inside the cavity. It follows that the Mach waves have their origin deep inside the shear layer. This can be seen in an enlargement of the shear layer topology, given in Fig. 10, which shows that the w"-Mach waves outside the cavity begin deep down in the shear layer as is predicted by the theory of Oertel sen et al. [12]. One w"-Mach wave of the many waves to be seen, is displayed by a red line for viewing in Fig. 10.

The schematic of Fig. 9 shows the case for w'/w" = 3, $a_a = a_i$, as for Fig. 8, which means that the w'-vortices propagate in this example three times faster than the w"-vortices and therefore pass them at a constant rate. A (schematic) snapshot of a w'-vortex just passing a w"-vortex is given in Fig. 11 at the moment when the w'-vortex is just seen in front of the w"-vortex, which is here drawn as the tail. All vortex pairs forming the two vortex trains must have the following properties, which are the assumptions of the two-train vortex model established in the theory of Oertel sen et al. [9, 12]:

- two stable vortex trains exist: the w'- train and the w"- train,
- the w'- train produces the cavity w'-Mach waves inside the cavity,
- the w"- train produces the w"-Mach waves outside the cavity, and
- for stability reasons, that is, in order to have long lasting vortices, the pressures at both vortex crests must be the same, i.e., the relative Mach numbers must be equal at the outside and inside facing bulges (see Fig. 12), from the point of view of the shear layer.

The two passing vortices are again given in Fig. 12. The vortices transport gas through their rotation, which constitutes an entrainment process already mentioned by Lau and Fisher [4]. This means that the w'-vortices transport gas from outside the cavity (i) into the sheared mixing layer and the w"-vortices do the same with gas

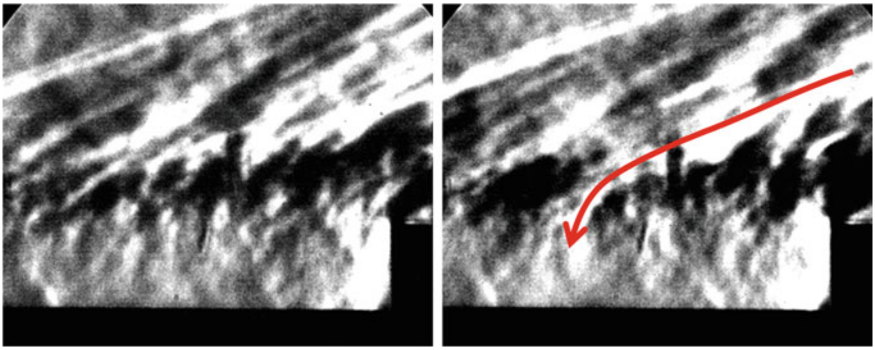

Fig. 10 Enlarged shear layer pattern near the trailing edge of the cavity (flow Mach number 3)

Fig. 11 Configuration of two vortices passing each other and instantly forming a front vortex and a tail vortex

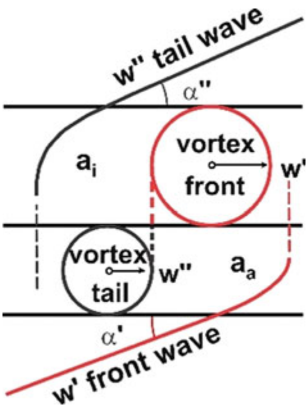

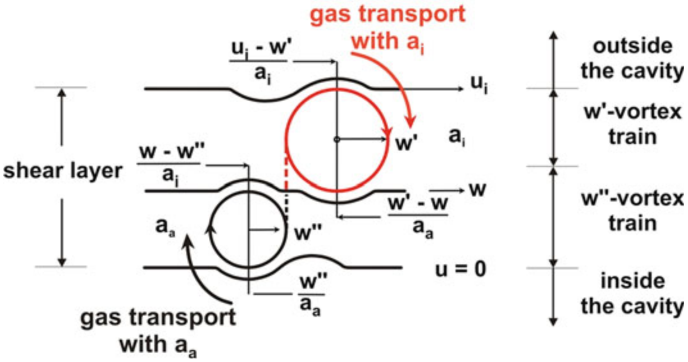

Fig. 12 Vortex stability considerations related to relative Mach numbers

from inside the cavity (a). This gas exchange is the basis for the estimate that the w'-layer is practically formed by gas having the speed of sound a_i as present in the free stream wind tunnel flow. The w''-layer has the sound speed a_a as it is fed by the cavity gas. The entrainment processes induced by the vortices are schematically drawn in Fig. 12 and are extensively described in Oertel sen et al. [9, 12]. As a result of this gas transport into the mixing layer it is obvious that the sound speeds in the two zones, i.e., the gas temperatures, remain practically constant.

The vortices act as crests with troughs arranged in-between as shown schematically in Fig. 12. Within the quasi-steady point of view seen from the vortices moving with w' and w'', the pressure at the crests must be considered. If the pressures at both sides of the crests are the same and lower than the pressure outside of the shear layer, the pressure balance tends to increase the amplitude of the vortices and makes the downstream movement of the vortex sheets stable. In the opposite case of an overpressure, the vortices disappear. These conditions define the limits of the existence of the Mach waves, see Oertel sen et al. [11]. For equal gas pressures and temperatures on each side of the vortices (considered at the bulges) it follows from gasdynamic considerations that the Mach numbers on both sides also have to be equal.

From this, one can find the Mach number equalities (1) and (3) and, under the condition of no gas slippage between the two vortex trains, the relation for the speed at the w-plane separating the vortex trains, Eq. (2):

$$\mathrm{w}' - \text{vortex}: \ \frac{\mathrm{u_i} - \mathrm{w}'}{\mathrm{a_i}} \ \text{and} \ \frac{\mathrm{w}' - \mathrm{w}}{\mathrm{a_a}} \tag{1}$$

$$\text{in between}: \ \mathrm{w} = \frac{1}{2}\left(\mathrm{w}' + \mathrm{w}''\right) \tag{2}$$

$$\mathrm{w}'' - \text{vortex}: \ \frac{\mathrm{w} - \mathrm{w}''}{\mathrm{a_i}} \ \text{and} \ \frac{\mathrm{w}''}{\mathrm{a_a}} \tag{3}$$

As a solution of this set of three Mach number equations the following relations can be derived, Oertel sen et al. [11, 12]:

$$\frac{\mathrm{w}}{\mathrm{a_a}} = \frac{\mathrm{M_i}}{1 + \mathrm{a_a}/\mathrm{a_i}} \tag{4}$$

$$\frac{\mathrm{w}'}{\mathrm{a_a}} = \frac{\mathrm{M_i} + (\mathrm{w}/\mathrm{a_a})}{1 + \mathrm{a_a}/\mathrm{a_i}} \tag{5}$$

$$\frac{\mathrm{w}''}{\mathrm{a_a}} = \frac{\mathrm{M_i} - (\mathrm{w}/\mathrm{a_a})}{1 + \mathrm{a_a}/\mathrm{a_i}} \tag{6}$$

The relative Mach number Eqs. (5) and (6) represent the Mach numbers of the w'- and the w"-vortices moving inside the shear layer in supersonic flow when Mach waves are present. Both are very similar, but not identical, to the classical "convective Mach number model" proposed for compressible shear layers with only one vortex street inside the shear layer, see e.g. Papamoschou and Bunyajitradulya [13]. The convection Mach number is usually denoted as $\mathrm{M_c}$ and equals the Mach number definition in Eq. (4) which is also specified by, e.g. Bailly and Fujii [1]. Formula (4) alone usually describes the propagation velocity of simple vortex structures in subsonic mixing layers. Nonetheless, there also can exist w-vortices in supersonic shear layers producing w-Mach waves, if the overtaking process which periodically forms vortex pairs, briefly fails and a single w-vortex is temporarily formed, emitting w-Mach waves to the outside and to the inside of the cavity.

It should be added here that the term "Mach waves" taken from the literature is not entirely correct. These are shock waves, which at a distance of a few centimetres from the jet have almost the strength of the bow waves of small-calibre projectiles at the same distance from the trajectory [7]. Nevertheless, the angles of the jet emitted shock waves can be approximated with the known Mach angle relation, sin (angle) = 1/Mach number, as follows:

$$\sin \alpha' = a_a/w' \tag{7}$$

$$\sin \alpha'' = a_i/(u_i - w'') \tag{8}$$

$$\frac{u_i - w''}{a_i} = \frac{M_i + (a_a/a_i)(w/a_a)}{1 + a_a/a_a} \tag{9}$$

Using these formulas, the w’- and w”-velocities as well as the Mach wave angles α’, α” can be calculated. The flow velocity u_i and the speeds of sound a_i and a_a are typically input parameters. As indicated earlier, in this study only w” and α” were compared with experiments due to the physical constraints of the cavity influenced w’ and α’. An uncertainty analysis of the theory has shown that variations of the input parameters only mildly affect the predictions for w’, w”, α’ and α”. If, for example, in the case of $M_i = 2$, the speed of sound ratio a_a/a_i varies between 1.29 and 1.41 as a result of a ± 10 K uncertainty in the temperatures T_a and T_i, w” and α” vary by only ± 12 m/s and ± 1.3°, which is within the range of uncertainty for the measurements of the values from experimental records, as outlined in the following section.

By means of the ratio of the sound speeds, a_a/a_i from Sect. “Wind Tunnel Setup and Operation”, the Mach wave velocities w’ and w” are determined with Eqs. (4)–(6), and their angles α’, α” with Eqs. (7)–(9). For the present tests, this results in:

$$M_i = 2,\ w' = 416\ \text{m/s},\ w'' = 167\ \text{m/s},\ a' = 55.2°,\ a'' = 48.1°;$$
$$M_i = 3,\ w' = 526\ \text{m/s},\ w'' = 239\ \text{m/s},\ a' = 40.4°,\ a'' = 33.2°.$$

4 Comparison with Oertel’s Theory

Long Fetch with Turbulent Plate Boundary Layer

Mach wave angle α”

The experimental setup has an essentially two-dimensional geometry. Along this two-dimensional geometry different individual Mach waves are generated. The schlieren light beam traverses the flow perpendicularly to the flow direction, therefore these different individual Mach waves are simultaneously visualized by the line-of-sight schlieren technique. Many of these waves therefore appear to be partly unclear and slightly smeared. Nevertheless, individual Mach waves can be identified as bright lines against the dark background. These Mach waves grow out of the shear layer as straight waves.

The derivations in Sect. “Oertel’s Theory” allow one to calculate the angle α” with the theory from Oertel sen et al. [9, 12]. For a Mach number $M_i = 2$ wind tunnel flow with $a_a/a_i = 1.34$ one obtains α” = 48.1° which was calculated and specified

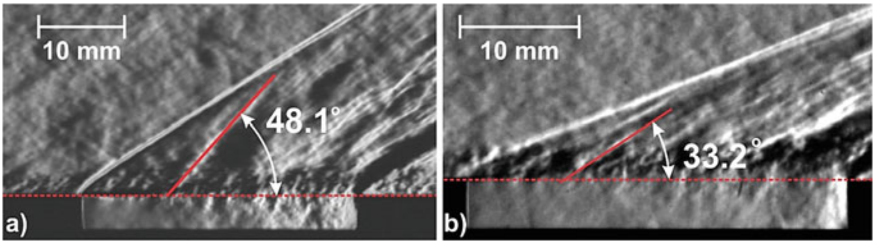

Fig. 13 Comparison of Mach wave angles with theoretical prediction, long fetch = 184 mm with incoming turbulent boundary layer of thickness 3 mm. (left) $M_i = 2$, (right) $M_i = 3$

in Sect. "Oertel's Theory". This calculated Mach wave angle is drawn in Fig. 13a as a red line on a representatively selected Mach wave for comparison with the Mach waves visible on the schlieren pictures. Within the accuracy of measurement (± 1°), the angle of the visualized Mach waves and the angle of the calculation agree well. For flow Mach number $M_i = 3$ ($a_a/a_i = 1.67$), the calculation gives $\alpha'' = 33.2°$ (see Sect. "Oertel's Theory" Again the comparison of the Mach wave visualizations and calculation (red line in Fig. 13b) indicates a good agreement between experiment and theory.

This good match of measured and theoretically predicted Mach wave angles is found only in the first half of the length of the cavity. In the second half of the cavity, the Mach waves are more and more affected by the deflection of the flow at the rear end of the cavity, as mentioned earlier. In this part of the flow, the conditions of the theory are no longer applicable.

Mach wave velocity w"

If a Mach wave is well visible in the flow above the cavity, its propagation can be tracked, and one can determine its propagation speed w". This is depicted in Fig. 14a, giving the displacement Δs, which with the known time increment (the four frames shown in Fig. 14a are 4 µs apart), gives $w''_{exp} = \Delta s/\Delta t = 163 \pm 10$ m/s. The subscript (exp) indicates that this value was found from experimental visualization records. The theoretical prediction using Eq. (6) gives $w''_{th} = 167$ m/s, which again is close to the experimental value. This optical evaluation method was reproducibly tested with other frames of the same test and with tests repeated under identical initial conditions. The test-to-test deviations constitute the indicated uncertainty of ± 10 m/s. This method can be applied within the error margin mentioned for optically well recognizable and easy-to-track Mach waves as illustrated in Fig. 14a. The consistently good correspondence between experimental and theoretically predicted values can be seen as confirmation of the applicability of the analytical two train theory.

Such Mach waves can also be visualized and their propagation speed can be quantified by using a streak technique. A similar approach was already used by Oertel sen et al. [9]. In the present study, the streak records were digitally generated from full-frame visualizations, in the same fashion as described in Sridhar et al. [20]. This method can be used advantageously when Mach waves emitted to the free

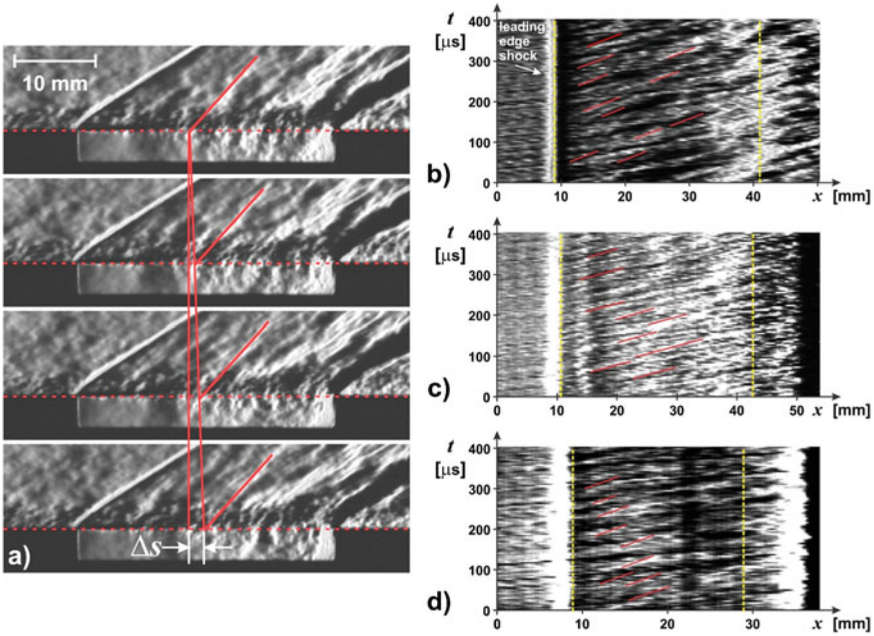

Fig. 14 Evaluation of well visible Mach waves, long fetch = 184 mm, turbulent boundary layer; time interval between shown frames: 4 µs. **a** tracking the path of a Mach wave at flow Mach number $M_i = 2$, **b** digital streak schlieren record for $M_i = 2$, **c** digital streak schlieren record for $M_i = 3$, **d** digital streak schlieren record for $M_i = 2$ and L/D = 5 in addition for comparison

stream are not as well visible as the one shown in Fig. 14a. Most of them generally have a limited lifetime because of multiple interactions with other wave elements of the flow and/or failure in the vortex train formation [12]. The benefit of this approach is that in addition to well observable waves one can detect wave structures that are present in the flow but not dominant enough to produce readily observable traces on regular visualizations such as those shown in Fig. 14a.

The corresponding results are given in Fig. 14b for $M_i = 2$ (same experiment as shown in Fig. 14a) and Fig. 13c for $M_i = 3$. With this technique, individually selected wave fronts can be identified in the resulting x-t diagram, indicated by several red lines in Fig. 17b–d. From the gradient of these path-time traces, Δs/Δt, their speed (subscript exp-streak) is determined. The digital streak schlieren record in Fig. 14b is obtained 10 pixels or 1.6 mm above the surface of the flat plate, and the record in Fig. 14c is for a line 10 pixels or 1.7 mm above the surface (the imaging factors of both visualizations are different). The dashed yellow vertical lines indicate the leading and the trailing edges of the cavity, respectively.

One can, for $M_i = 2$, identify with the streak technique many traces that correspond to waves with a speed of $w''_{\text{exp-streak}} = 166$ m/s ± 10 m/s, which agrees well with the above theoretical result for w”. The indicated scatter of the velocity values is primarily a result of the inherent uncertainty of the measurement of the line slope, which is a consequence of the limited spatial resolution of the visualization. As before, these waves exist only for a limited time, which indicates the presence of various wave interaction processes in the flow above the cavity. An important reason for this is the following [12], as already described in Sect. 3: the w'-vortices move faster than the w''-vortices and regularly form vortex pairs, as they pass each other during their movement downstream. In cases where the overtaking process fails, a single w-vortex is occasionally formed. Short-term weak w-waves arise with their angle being larger than the angles of the w''- and w'-Mach waves. For $M_i = 3$ one finds $w''_{\text{exp-streak}} = 246$ m/s ± 10 m/s (Fig. 14c) which again compares well with the values predicted by Oertel's theory, namely $w''_{\text{th}} = 239$ m/s.

The investigation described by Sridhar et al. [20] generated a large number of visualizations of cavity flows with different length-to-depth ratios ($3 \leq L/D \leq 8$). In the current study, L/D should not be a relevant parameter, as long as the character of the flow is not changed due to a too short length of the cavity and the flow pattern remains that of an open cavity. This was confirmed by evaluating the outer flow for different values of L/D in the same way as in Fig. 14b, c. Figure 14d is a representative result for $L/D = 5$ (streak traces obtained 10 pixel or 1.2 mm above the surface of the flat plate) and $M_i = 2$. The streak record yields $w''_{\text{exp-streak}} = 161$ m/s ± 10 m/s which is again close to the value predicted by Oertel's theory. From these streak evaluations of Fig. 14b–d it is observably confirmed that the processes in the second half of the cavity change, and it is obvious on the streak records that the pattern of emitted Mach waves vanishes when the trailing edge of the cavity is approached. Figure 14a clearly confirms this fact.

Short Fetch with Laminar/Transitional Plate Boundary Layer

Mach wave angle α''

In the case of a boundary layer arriving in laminar/transitional state at the leading edge of the cavity, as specified in Sect. "Cavity Geometry" with a thickness of 1 mm, the vortices and thus the resulting Mach waves visibly detach at a regular fixed time interval. This is obvious from the constant distance between the waves when viewing Fig. 15, best illustrated in the picture on the left-hand side. With turbulent incoming boundary layer, in contrast, the Mach waves do not appear to be as temporally constant and regularly formed, as is seen from Fig. 13. They look more smeared, arguably caused by the boundary-layer-induced turbulence acting on the formation of vortices and Mach waves.

The Mach waves in the laminar/transitional boundary layer case seen in Fig. 15 appear to be broad, which probably arises from the fact that in the transverse direction of the schlieren light path several Mach waves grow side-by-side out of the shear layer with a small angle variation so that the angle of one single Mach wave cannot be exactly determined. Nonetheless, there are only small differences between the visualized Mach waves and the analytical theory.

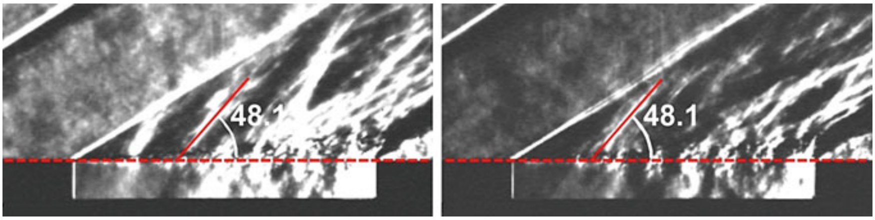

Fig. 15 Comparison of Mach wave angles with theoretical prediction, short fetch = 33.6 mm with incoming laminar/transitional boundary layer thickness of 1 mm, $M_i = 2$

Comparing the shapes and appearance of the Mach waves in Fig. 13 (turbulent incoming boundary layer) and 15 (laminar/transitional incoming boundary layer), the visualizations indicate that neither the thickness of the incoming boundary layer nor its type visibly influence the angle of the Mach waves. This outcome is reported by Sridhar et al. [22] too, showing that the formation of the Mach waves is essentially identical for both fetch lengths and therefore not visibly dependent on the boundary layer thickness nor its type, i.e. whether the boundary layer is turbulent or laminar.

From visualizations taken for a laminar/transitional incoming boundary layer, like Figs. 5 and 15, a rough estimate of the Mach waves' frequency yields a range between $\nu \approx 20$ to 40 kHz, using the mean distance between the Mach waves visible, their wavelength, and from Sect. "Oertel's Theory" for $M_i = 2$ their theoretical velocity w" = 167 m/s. The uncertainty in determining the average distance is approximately 30% which is the main contributor to the width of the specified frequency range. Counting the emerging Mach waves directly behind the cavity leading edge in high-speed sequences such as those shown in Fig. 15, the formation frequency of the Mach waves is of the same order of magnitude as stated above. Sridhar et al. [18, 19] examined the frequency spectrum with the same wind tunnel and cavity data. They identified several resonant frequencies (modes) in the computations and measurements, i.e. several peaks in the range from nearly zero to 40 kHz which indicates that the emission occurs in a wide frequency range. As already reported in Sect. "Long Fetch with Turbulent Plate Boundary Layer", due to the two-dimensional experimental geometry, different individual Mach waves are simultaneously generated and visualized by the line-of-sight schlieren technique. This can lead a wide mix of different frequencies being present for the emission of Mach waves rather than a defined frequency.

Mach wave velocity w"

Finally, for case with laminar/transitional boundary layer, see Sect. "Cavity Schlieren Visualizations", the w"-velocity was again determined by path-time evaluations from representative image series (Fig. 16). Tracing the paths of selected, well-visible Mach waves yields $w''_{exp} = \Delta s/\Delta t = 167 \pm 20$ m/s (left) and 153 ± 20 m/s (right). The agreement with the theoretically calculated speed value of $w''_{th} = 167$ m/s, Eq. (6), is again very good in the context of the measurement uncertainty. Streak records such as the ones shown in Fig. 14b, c confirm the given experimental results for w''_{exp}.

Table 1 Measured and theoretical Mach wave velocities

Mach number M_i	Fetch/boundary layer type	Experiment w" (m/s)	Theory Eq. (6) w" (m/s)
2	184 mm/turbulent	163 ± 20 166 ± 25 177 ± 20 169 ± 20 173 ± 20	167
3	184 mm/turbulent	246 ± 25	239
2	33.6 mm/laminar/transitional	167 ± 20 153 ± 20	167

Remarks The evaluation of the angles of the Mach waves and their velocities show comparable results for the turbulent incoming boundary layer case (long fetch) as well as for the laminar/transitional one (short fetch), if one considers measurement inaccuracies. This conclusion is an important indication that the thickness and type of the boundary layer at the separation edge of the cavity hardly play any role in the formation of the Mach waves. Nevertheless, the experiments with short fetch, when the boundary layer is laminar/transitional at the leading edge, show the Mach waves more regularly distributed above the cavity than with long fetch. As well, the angles of the Mach waves and their velocities are unaffected by the nature and thickness of the boundary layer. These outcomes provide a confirmation that the theory with two vortex trains running downstream at different speeds inside the shear layer is adequate. Table 1 lists a number of experimentally evaluated velocities of the Mach waves and the related theoretical values. Included in the listing are the velocities taken from Figs. 14 and 16, as well as further evaluation results from other tests run under the same conditions.

5 Existence of Mach Waves

The cavity flows seen in Figs. 4 and 5 undoubtedly emit Mach waves. Nonetheless, there are supersonic shear layers that do not emit Mach waves. Oertel sen et al. [10] describe in detail the stability criteria and at which flow conditions Mach waves occur and where not. For this reason, it is interesting to investigate whether at the given wind tunnel conditions, $M_i = 2$ and 3, Mach waves may exist. Following Oertel sen et al. [10] Mach waves are only lasting if the following two conditions are met:

(1) w'-Mach waves can only emerge if $w' > a_a$, see Eq. (10a), and
(2) w"-Mach waves exist if $(u_i - w'')_> a_i$, see Eq. (10b).

The two mentioned limitations indicate for the w'- and w"-vortices the need to move supersonically relative to the speeds of sound inside, a_a, as well as outside,

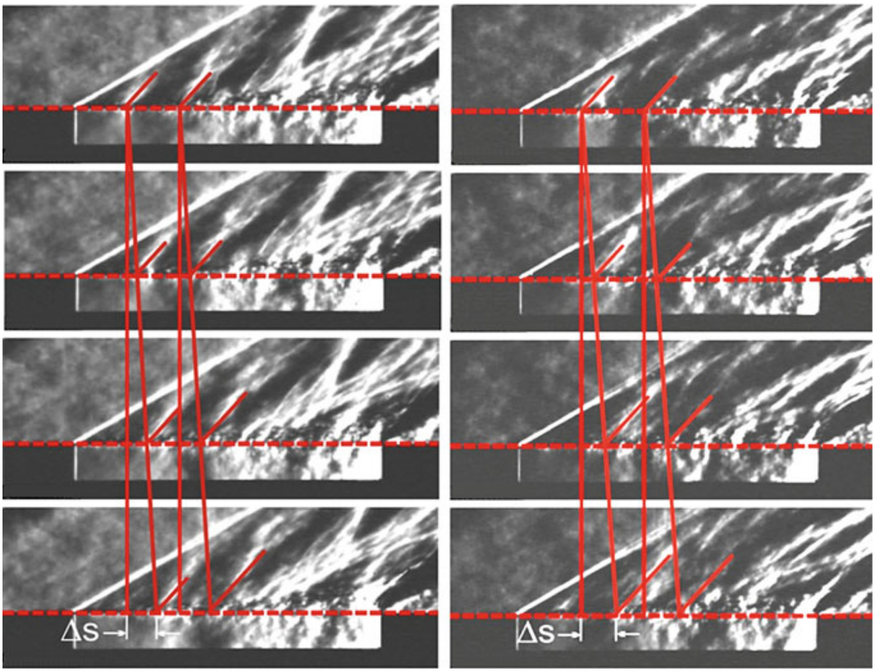

Fig. 16 Path of well visible Mach waves, $M_i = 2$: time between shown frames 8 μs (left), 10 μs (right), short fetch = 33.6 mm, laminar/transitional boundary layer thickness = 1 mm

Fig. 17 Mach wave stability field

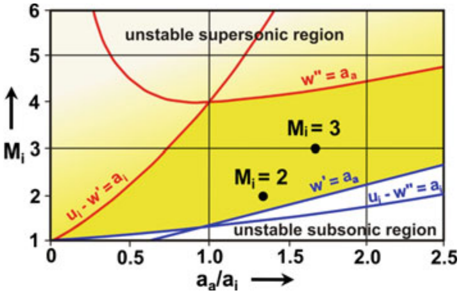

a_i, of the cavity. From Eqs. (4)–(6), the resulting inequalities, (10a) and (10b), are deduced for the w'- and w"-waves depending on M_i:

$$\mathrm{w}' > \mathrm{a_a} : M_i > \frac{(1 + a_a/a_i)^2}{2 + a_a/a_i} \tag{10a}$$

$$\mathrm{u_i} - \mathrm{w}'' > \mathrm{a_i} : M_i > \frac{(1 + a_a/a_i)^2}{1 + 2\,(a_a/a_i)} \tag{10b}$$

Two other limits restrict the existence of Mach waves. Each vortex represents a hump as illustrated in Fig. 12, protruding from the flow cross-section. It can only persist if the static pressure in the wind tunnel flow as well as in the cavity is below the pressure value at the vortex peripheries. This pressure effect tends to increase the amplitude of the vortex chains, i.e. the shear layer behaves stable. This only happens at relative subsonic Mach numbers with:

(1) $w'' < a_a$, Eq. (11a) and;
(2) $(u_i - w') < a_i$, Eq. (11b).

In a supersonic flow with $w'' > a_a$ and $(u_i - w') > a_i$, as each of the vortices form a bulge, the flow is forced to evade this obstacle, and this leads to a localized pressure increase. Typically a compression occurs and the w'- and the w''-vortices may disappear. The regularity of the vortices as a postulate of the current theory cannot be maintained—it only exists at relative subsonic Mach numbers at which the vortices can exist and last:

$$u_i - w' < a_i : \qquad M_i < (k + a_a/a_i)^2 \tag{11a}$$

$$w'' < a_a : \qquad M_i < \frac{a_i}{a_a}(1 + a_a/a_i)^2 \tag{11b}$$

The four limits (10a, b) and (11a, b) are shown in the diagram of Fig. 17 as border lines forming the dark yellow region in which only stable Mach waves can be present. The four limitations are characterized as follows:

> (First & second limitations): Below the limiting lines with $w' = a_a$ and $u_i - w'' = a_i$ absolutely no Mach waves can occur. We call this region the "unstable subsonic region" which is seen in Fig. 17 with a white background. Both restrictions are severe and strong conditions.
>
> (Third & fourth limitations): The transition to the region above the boundary lines $w'' = a_a$ and $u_i - w' = a_i$, which is called the "unstable supersonic region", is smooth (light yellow region in Fig. 17). In this area, the Mach waves can exist only for short times.

The cavity flow experimentally shows generated Mach waves, and this observation is confirmed by the two plotted data dots in the stability diagram in Fig. 17. These dots are placed above both borderlines, the $w' = a_a$ curve and the $u_i - w'' = a_i$ curve, in the dark yellow region which represents the range fully permissible for Mach wave emission.

6 Comparison with CFD-Calculations

Computational fluid dynamics (CFD) simulations were conducted at a Mach number $M_i = 2$ and at $a_a/a_i = 1.34$. The simulated flow conditions corresponded to those in the measurements. The cavity geometry was identical to the wind tunnel experiment, i.e. with L/D = 8 and a distance between leading edge and cavity of 33.6 mm, thus reproducing the short-fetched experimental setup. In order to limit computational cost, the width of the cavity in the simulation was reduced to a value of 20 mm with periodic lateral boundary conditions. This corresponds to a numerical model of a cavity of infinite width, hence wall effects present in the real wind tunnel measurement are not modelled. It was verified that the simulated width was at least an order of magnitude larger than the largest observed eddy structures in the cavity. This assures that eddies are not spatially constrained, hence results are not compromised by the limited lateral extent of the simulation domain.

The detached eddy simulation (DES) method [17] was employed. This hybrid simulation technique solves the boundary layer flow in Reynolds-averaging Navier–Stokes (RANS) mode and switches to large-eddy-simulation (LES) mode in flow regions several cell sizes away from walls, which is inside the cavity and also in the free shear layer above. This modelling allows eddies responsible for Mach wave formation to develop and evolve exclusively in the LES region. As opposed to the experiment, there are neither vortices nor Mach waves modelled as long as the boundary layer is attached to the wall plate ahead of the cavity. This compromise is necessary to limit the computational expense of the numerical simulation.

To minimize the numerical dissipation while maintaining solver stability, the pressure-based finite-volume solver ANSYS Fluent V. 15 was used in combination with a bounded central differencing scheme. The RANS regions of the flow as well as the non-resolved sub-grid scale turbulence were modelled by the k-ω-turbulence closure. A numerical time step of 10^{-7} s proved sufficiently small to ensure results independent from this parameter. The structured grid consisted of 32.2 million hexahedral cells. 200 cells were distributed evenly across the domain width, while 800 were distributed in stream-wise direction and 140 normal to the cavity floor, respectively. The cavity itself was discretized with 122 cells in floor-normal, 400 in lengthwise and 200 in span-wise direction. The flat-plate and cavity walls were modeled as adiabatic. The simulations were run until the eddy structures were fully developed, and the time averaged values of shear layer thickness and forces on the cavity walls no longer changed. To assure solution independence from grid resolution, a grid with 68 million cells was used in an additional simulation. The difference in average pressure on the cavity rear wall obtained with the two grids amounted to 4.5%, which shows that the doubling of cells only leads to small differences in the results. For the calculations shown here the smaller grid (32.2 million cells) was used.

An instant picture of the flow field solution is shown in Fig. 18a. The resolved cavity vortices are colored to indicate local pressure and are shown along with the density gradient in the central plane in the form of numerical schlieren. The Mach waves emitted by the shear layer are clearly observable and their angles agree well with the theoretical prediction of Eq. (8) that provided a value for $\alpha'' = 48.1°$ (see Sect. "Oertel's Theory" which is inserted as a red line for comparison. The pressure fluctuations in the cavity exceed 20%, with peak values observed towards the cavity rear wall.

The calculations were also used to determine the value of the speed of sound inside the cavity. The result for $M_i = 2$, shown in Fig. 18b, indicates that, indeed, the average speed of sound inside the cavity of 342.5 m/s is close to the previously

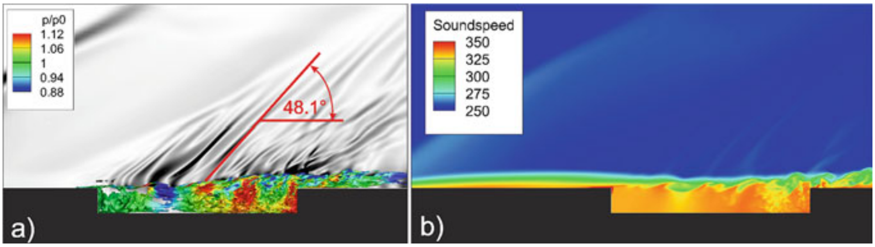

Fig. 18 Simulation results for Mach number $M_i = 2$, **a** pressure distribution inside the cavity and numerical schlieren display of the flow above the shear layer, **b** numerically determined distribution of the sound speed (in m/s)

assumed value of 341 m/s. Similarly, additional CFD calculations for the higher Mach number $M_i = 3$ confirmed the assumption made on the basis of the results in Heller et al. [2], namely that the average temperature inside the cavity corresponds to the stagnation temperature.

The convective velocities of the Mach wave structures seen in Fig. 18a in downstream direction were determined by tracking them over time at eight different locations in the central plane of the flow field. The average value observed was 192 m/s, with a standard deviation of 43 m/s. The theory of Oertel sen et al. (e.g. [12]) provides a value of 167 m/s, which lies within the standard deviation of the CFD simulation result.

7 Summary and Conclusions

The investigations reported herein concentrate on so-called open cavities having a length-to-depth ratio $L/D < 10$ in order to obtain fundamental predictions on the acoustic noise emitted to the environment, and forces acting on structures, where such cavities occur. Wind tunnel experiments at UNSW Canberra were conducted to investigate the flow over such a cavity, and schlieren flow visualizations revealed the creation of unsteady Mach waves above and inside the cavity. The wind tunnel tests were run at Mach numbers 2 and 3 with two cavity configurations: with a long fetch of 184 mm from the tip of a splitter plate downstream to the leading edge of the cavity, and a short fetch of 33.6 mm. The fetch was varied to obtain an estimate of the influence of the incoming boundary layer thickness and type on the behaviour of the shear layer on the topology of the Mach waves emitted. For the long fetch the incoming boundary layer was fully turbulent. In the case of the short fetch, a laminar/transitional boundary layer was generated. It was found that there were no obvious differences in the formation of the Mach waves when either the fetch or the boundary layer type was varied. Mach waves were formed each time, they remained stable and with the same appearance. A small difference, however, is that with laminar/transitional incoming boundary layer, the Mach waves appear to be emitted more regularly in time.

These observations were compared with a theory developed by Oertel [9, 12] which describes the Mach wave dynamics of supersonic jets based on the fact that vortices are formed inside the shear layer which propagate within two zones at different speeds, called w' and w''. It follows from the theory that these vortical structures are the sources of the Mach waves emitted to the jet's inside and to the outside environment. This two-vortex-street model, applied to supersonic shear layers in free jet applications, has been extensively tested with experimental data. These validations have all been positive, indicating that this model can be used to predict the angles of the Mach waves and their propagation behavior. The application to Mach waves emitted from a cavity reported here is another validation case. The tests at UNSW Canberra showed that Mach wave angles and Mach wave speeds obtained in the experiments agree, within the measurement accuracy, with the predictions from theory mentioned.

CFD simulations of the cavity flow with Mach number $M_i = 2$ were performed at ISL Saint-Louis as another independent means to determine the Mach wave angles and to compare the results with the theoretical predictions of Oertel sen et al. [9, 12]. The three-dimensionality of the flow field leads to a relatively large spread in observed Mach wave angles and velocities, with average values showing good agreement between schlieren experiment (Sect. "Schlieren Method"), numerical simulation (Sect. 6) and theory (Sect. "Oertel's Theory"). The consistency of experimental, numerical and theoretical results can be seen as a confirmation of the process stipulated in the theory, namely that Mach waves are produced by the vortical structures moving in the shear layer over the cavity. One can conclude that the analytical formulas derived are capable of correctly describing the occurrence of these Mach waves, and this outcome indicates that the recently published theory can be applied with good accuracy to the Mach wave dynamics which occur in/above a supersonic cavity flow.

References

1. Bailly C, Fujii K (2016) High-speed jet noise. Mech Eng Rev 3(1)
2. Heller HH, Holmes DG, Covert EE (1971) Flow-induced pressure oscillations in shallow cavities. J Sound Vib 18(4):547–553
3. Kleine H (2001) Flow visualization. In: Ben Dor G, Igra O, Elperin T (eds) Handbook of shock waves, vol 1, Chapter 5.1. Academic Press, Boston, pp 683–740
4. Lau JC, Fisher MJ (1975) The vortex-street of turbulent jets part 1. J Fluid Mech Part 2 67:299–337
5. Lele SK, Mendez S, Ryu J, Nichols J, Shoeybi M, Moin P (2010) Sources of high-speed jet noise: analysis of LES data and modeling. Procedia Eng 6C:84–93
6. Merzkirch W (1987) Flow visualization, 2nd edn. Academic Press, Orlando
7. Oertel H (1977) Interferometrische untersuchungen des lärms von überschallstrahlen (Interferometric studies of the noise of supersonic jets). Report DLR-FB 77–16

8. Oertel H (1978) Kinematik der machwellen in der umgebung von überschallstrahlen (kinematic of mach waves surrounding supersonic jets). ISL Report R 112/78
9. Oertel sen H, Seiler F, Srulijes J (2013) Visualization of Mach waves produced by a supersonic jet and theoretical explanations. J Vis 16(4):303–312
10. Oertel sen H, Seiler F, Srulijes J (2015) The limits of Mach wave emission from supersonic jets. ISSW30, vol 1. Springer, pp 287–292. ISBN 978–3–319–46211–0, ISBN 978–3–319–46213–4 (eBook). https://doi.org/10.1007/978-3-319-46213-4
11. Oertel sen H, Seiler F, Srulijes J (2015) The formation of Mach waves from supersonic jets with outer coflowing. ISSW30, vol 1. Springer, pp 281–286. ISBN 978–3–319–46211–0, ISBN 978–3–319–46213–4 (eBook). https://doi.org/10.1007/978-3-319-46213-4
12. Oertel sen H, Seiler F, Srulijes J, Hruschka R (2016) Mach waves produced in the supersonic jet mixing layer by shock/vortex interaction. Shock Waves J 26(3):231–240
13. Papamoschou D, Bunyajitradulya A (1997) Evolution of large eddies in compressible shear layers. Phys Fluids 9(3):756–765
14. Papamoschou D, Debiasi M (1999) Noise measurements in supersonic jets treated with the Machwave elimination method. AIAA J 37(2):154–160
15. Rossmann T, Mungal MG, Hanson RK (2002) Character of Mach wave radiation and convection velocity estimation in supersonic shear layers. AIAA 2002–2571
16. Settles GS (2001) Schlieren and shadowgraph techniques. Springer, New York
17. Spalart PR (2001) Young person's guide to detached eddy simulation grids. NASA Report CR2001 211032
18. Sridhar V, Gai SL, Kleine H (2012) A numerical investigation of supersonic cavity flow At Mach 2, In: 18th Australasian fluid mechanics conference, Launceston, Australia
19. Sridhar V (2014) Computational and experimental investigation of supersonic two-dimensional and axi-symmetric shallow open cavities. Thesis, The University of New South Wales, Canberra, Australia
20. Sridhar V, Kleine H, Gai SL (2015) Visualization of wave propagation within a supersonic two-dimensional cavity by digital streak schlieren. Exp Fluids 56(7):152
21. Sridhar V, Gai SL, Kleine H (2016) Oscillatory characteristics of shallow open cavities in supersonic flow. AIAA J 54(11):3495–3508
22. Sridhar V, Seiler F, Kleine H, Gai SL, Srulijes J (2018) Mach waves emitted from the shear layer over a cavity in supersonic flow. In: 18th International Symposium on Flow Visualization ISFV18, Swiss Federal Institute of Technology (ETH) Zürich, Switzerland, Permanent Link. https://doi.org/10.3929/ethz-b-000279183
23. Sridhar V, Seiler F, Kleine H, Gai SL, Hruschka R, Srulijes J (2019) Mach waves over a cavity in supersonic flow. In: 32th International Symposium on Shock Waves (ISSW32), National University of Singapore, Singapore, Permanent Link. http://rpsonline.com.sg/rps2prod/ISSW32/e-proceedings/html/0065.xml
24. Tam CKW (1971) Directional acoustic radiation from a supersonic jet generated by shear layer instability. J Fluid Mech 46:757–768
25. Tam CKW (1995) Supersonic jet noise. Annual Rev Fluid Mech 27(544):17–43
26. Tam CKW (2009) Mach wave radiation from high-speed jets. AIAA J 47(10):2440–2448

Medical Application of Miniaturized Underwater Shock Wave Focusing

Hiroaki Yamamoto and Kazuyoshi Takayama

1 Introduction

Underwater shock waves are generated upon irradiation of Q-switched laser beams in water through an optical fiber. When a shock wave is generated at one of the focal points inside a truncated ellipsoidal reflector, we can focus the reflected shock wave at the second focal point outside the reflector. We have already applied this method to minimally invasive therapeutic devices.

Medical applications of underwater shock waves have been developed, regardless of their nonsense terminology, such as electrohydraulic [1], electromagnetic [2–11], an array of piezo-electric elements [12, 13] and micro explosive [14].

In the series of our study, we firstly optimized the shape of the optical fiber tip to improve features of shock wave generation and to elongate the durability of the optical fiber. Secondly our effort was to optimize efficiency of shock wave focusing. Eventually through trial and error we found optimal shape of the optical fiber tip.

2 Underwater Shock Wave Generation Method

Laser Induced Micro Shock Waves in Water

To generate the shock waves, we irradiated Q-switched Holmium Yttrium Garnet (Ho: YAG) laser (SLR-HO-EOQ, wavelength of 2.1 μm, Sparkling Photon Inc.,

---

H. Yamamoto (✉)
Department of Cardiovascular Medicine, Graduate School of Medicine, Tohoku University, 2-1Seiryo-machi, Aoba-ku, Sendai-shi, Miyagi-ken 980-8574, Japan
e-mail: yamahiro@cardio.med.tohoku.ac.jp

K. Takayama
Tohoku University, Sendai-shi, Japan

© The Author(s), under exclusive license to Springer Nature Switzerland AG 2022

K. Takayama and O. Igra (eds.), *Frontiers of Shock Wave Research*,
https://doi.org/10.1007/978-3-030-90735-8_8

Tokyo, Japan) at pulse width of 100 ns and pulse energy of from 18 to 39 mJ into water. The pulse laser beam was transmitted through 0.4 mm core-diameter low-OH content quartz optical fiber (FIP400440480, Polymicro Technologies, USA).

Configuration of Fiber Tip

We have eventually learned that optical fiber tip having hyperboloidal or spherical sharp-pointed laser exit end with roughened surface are effective for generating more intense shock wave rather than polished flat end [15–17]. However, we knew that two weaknesses prevented from the satisfactory achievements. Firstly, the exit end could be easily broken due to strong absorption of laser energy at the abrasive surface [16, 17]. Once the tip was damaged, the resulting jaggedly shaped surface, although this irregularity is minute, would have diffused laser beams or caused a slight migration of the spot of shock wave generation. Especially when shock waves are focused using a truncated ellipsoidal reflector, such damages of optical fiber tip would result in deviation of focus points, or we would no longer expect sharp peak pressure.

Secondary, laser absorption would occur both inside and outside of the fiber end [17]. Shock waves would be generated in a spatially and temporally superimposed fashion when the distance between the absorption points inside and outside the fiber tip is remarkably close [17], nevertheless such an energy loss cannot be neglected. Thus, in generating shock waves by means Q-switched laser through optical fibers, we decisively need sufficiently long durability.

Figure 1 shows schematic diagram of a cross section of the optical fiber tip. To prevent laser beam focusing inside the exit end and resultant optical breakdown of quartz, we shaped the exit end into circular truncated conical shape. Unlike spherical or aspherical lens, a laser beam is converged into the outside of the exit end by an internal reflection on the lateral side surface of the cone. The taper angle of the cone is less than critical taper angle αc so that laser beam incident on the lateral side of cone is totally reflected.

Furthermore, the cone surface was polished to a mirror gloss with 1 μm polishing film to prevent laser absorption inside micro cracks and diffused reflection on roughened surface. Accordingly, it is considered that laser beam is focused into water near the top edge of fiber with minimal energy loss.

The critical taper angle α_c is predicted to range from 31.0° to 34.2° in the following equations:

$$\theta_c = \sin^{-1}\left(\frac{n_w}{n_{qtz}}\right) = \frac{\pi}{2} - \frac{\alpha_c}{2} - \theta_t \tag{1}$$

$$\alpha_c = \pi - 2\left(\theta_t + \sin^{-1}\frac{n_w}{n_{qtz}}\right) \tag{2}$$

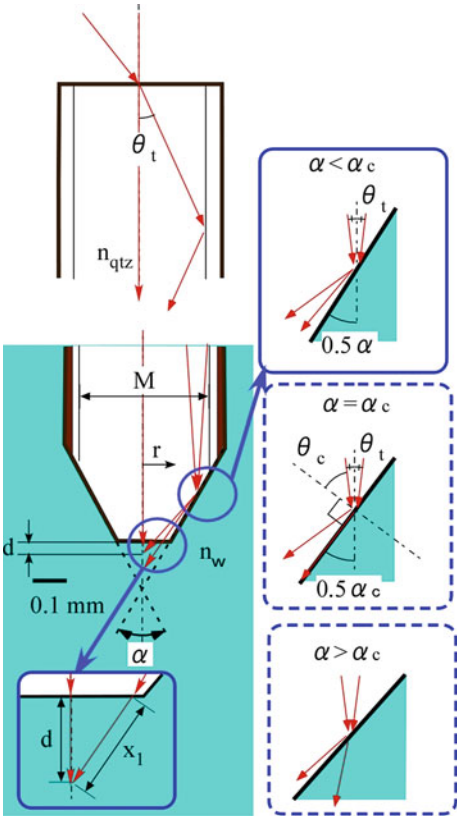

Fig. 1 Schematic diagram of fiber tip

$$\theta_t = \sin^{-1}\left(\frac{NA}{n_{qtz}}\right) \tag{3}$$

Here θ_c, θ_t, NA, n_{qtz} and n_w denotes the critical angle on the lateral side of cone, the deviation angle of laser incident direction from the center axis of the fiber, the numerical aperture of fiber (0.22 ± 0.02), the refractive index of fiber core (1.437) and water (1.301 at 20 °C) respectively.

Energy Distribution of Laser Beam

Energy distribution of laser beam along the center axis of the fiber tip is estimated by ray trace method as follows. On the lateral surface of the fiber tip, the laser beam is incident from the left at angle of

$$\frac{\pi}{2} - \left(\frac{\alpha}{2} \pm \theta_i\right), \theta_i \leq \theta_t \tag{4}$$

Here distributions of θ_i have a normal distribution whose average and standard deviation are 0.11 (1/2NA) and 0.1, respectively.

The reflectance of the incident laser beam Rs is.

$$R_s = \left(\frac{n_{qtz}\cos\left(\frac{\pi}{2} - \frac{\alpha}{2}\right) - n_w \cos\left(\sin^{-1}\frac{n_{qtz}}{n_w}\sin\left(\frac{\pi}{2} - \frac{\alpha}{2}\right)\right)}{n_{qtz}\cos\left(\frac{\pi}{2} - \frac{\alpha}{2}\right) + n_w \cos\left(\sin^{-1}\frac{n_{qtz}}{n_w}\sin\left(\frac{\pi}{2} - \frac{\alpha}{2}\right)\right)} \right)^2 \tag{5}$$

The total reflection condition is given by the following equation according to Snell's law:

$$\frac{n_{qtz}}{n_w}\left(\sin\left(-\frac{\alpha}{2} + \cos^{-1}\left(\frac{NA}{n_{qtz}}\right)\right)\right) > 1 \tag{6}$$

Total reflection beam which radiated from fiber tip concentrates on the center axis of the fiber tip. The distance between the fiber tip and the point at which laser beam intersects the center axis of the fiber tip is represented by.

$$d = \frac{r - h\tan\frac{\alpha}{2}}{\tan\left(\sin^{-1}\left(\frac{n_{qtz}}{n_w}\sin(\alpha + \theta_i)\right)\right)},\ 0 \le r \le \frac{D}{2} \tag{7}$$

Here r is the radial distance from the center axis of the optical fiber, and D is core diameter of fiber.

On the assumption that Gaussian beam emits from the laser, the energy flux at r is given by the following equation:

$$E(r) = EP(r)\pi dr^2 / \int_0^{0.5D} P(r)\pi r^2 dr \tag{8}$$

Here, E = const. and P(r) is probability density function described as

$$P(r) = \frac{1}{\sqrt{2\pi\sigma^2}} exp\left(-\frac{(r - 0.5D)^2}{2\sigma}\right) \tag{9}$$

Here σ is the standard deviation and $\sigma = 0.1$.

Energy loss of Ho: YAG ($\lambda = 2.1$ µm) laser in water is estimated by

$$E(l) = E(0)\exp(-\mu_a l) \tag{10}$$

Here, l is optical path length and μ_a is absorption coefficient of 0.8.

By Eqs. (5), (7), (8), (9) and (10), energy distribution along the center axis of the fiber tip can be expressed as

$$E(d) = \int_0^{0.5D} E(r) R_s \exp(-\mu_a x_1) dr + E(0)(1 - R_s)\exp(-\mu_a d) \qquad (11)$$

Pressure Measurement

Figure 2 shows a schematic diagram of the experimental set-up. The tip of optical fiber was set on the center axis of truncated ellipsoidal brass cavity using precisely locating device within a tolerance of 50 μm. When a pulse laser beam is irradiated, a micro shock wave is generated at F1 and propagates radially. Then it reflects at the cavity wall and converges on the F2. The relative position between the reflector and the optical fiber (F) was varied using accurate positioning stage. When a peak pressure of focused shock wave becomes a maximum, it is determined that the position of shock wave source agrees with the inner focus of a reflector. The distance between the fiber tip and the open end of a reflector was defined as Cf.

Spatial distribution of shock wave pressure was measured by PVDF needle hydrophone with 0.5 mm sensitive diameter and 35 ns rise time (Müller-Platte Needle Probe, Dr. Müller Instruments, Oberursel, Germany) fixed on a XYZ positioning stage. The signals are stored in a digital transient memory (DS-5534, Iwatsu electric co., ltd.) with sampling rate of 2GS/s.

The test section is composed of a stainless-steel chamber (100 mm inside diameter, 100 mm depth) and an acryl window (140 mm × 140 mm × 25 mm), filled with pure water (Milli-Q water, degassed in a vacuum chamber prior to use).

Fig. 2 Schematic diagram of underwater micro shock wave focusing

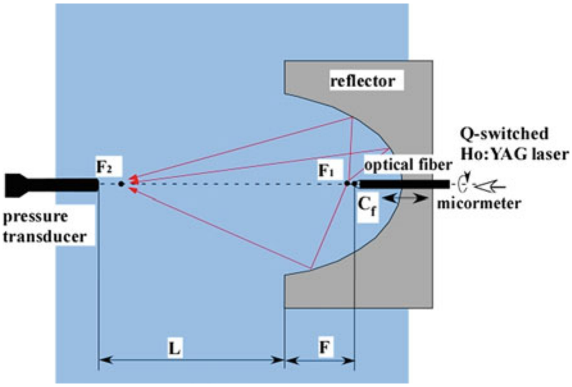

Visualization

Figure 3 shows a schematic diagram of the experimental set-up. Shock waves are visualized by shadowgraph. The image in the test section was taken with the high-speed camera (HPV-X, Shimadzu corp., Kyoto, Japan). The inter-frame time, exposure time and image resolution were 100 ns, 50 ns and 400 × 250 pixels, respectively.

Fig. 3 Optical set-up

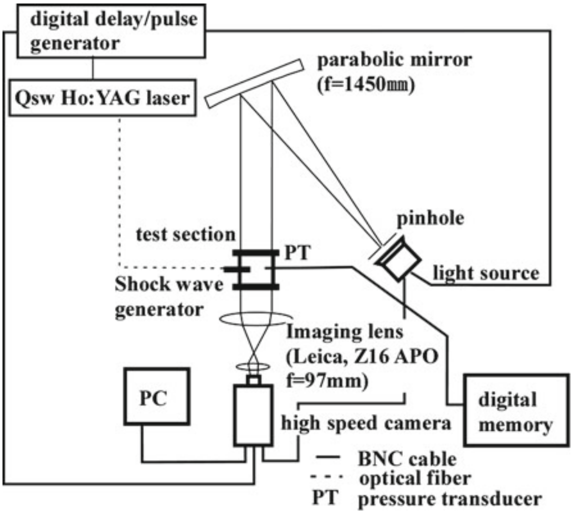

Fig. 4 Schematic diagram of the underwater shock wave from the fiber tip. ΔD: degree of deviation of shock front from spherical shape; blue line: shock front; dashed line: a sphere centered at Cs; Cs: originating point of shock wave; d: distance between Cs and fiber tip

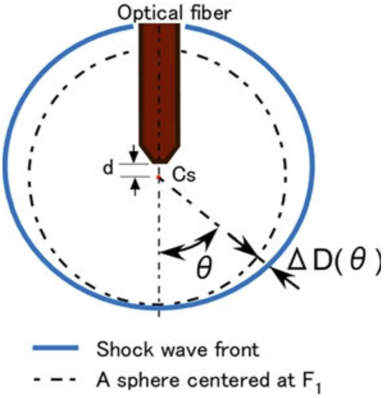

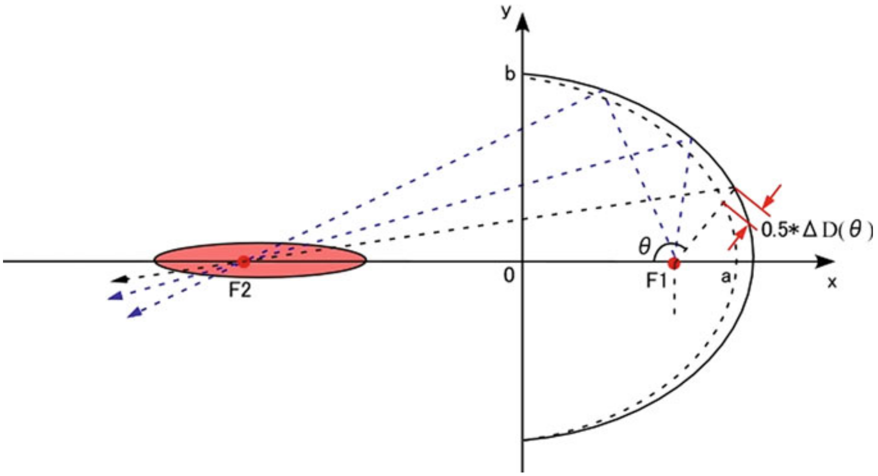

Fig. 5 Schematic diagram of reflection surface correcting method

Modification of the Shock Wave Reflector

Figure 4 shows a schematic diagram of the underwater shock wave generated from the optical fiber. To reveal variations in shock wave front's geometry between the flat and tapered fiber output shapes, we have defined ΔD as degree of deviation of shock front from a sphere shape centered at F1 [6]. ΔD was measured on digital images using PC software (Image J [18, 19]).

Furthermore, based on the measured degree of deviation of shock front from sphere (ΔD) by digital image analysis, coordinate data of the reflection surface was corrected as shown in Fig. 5.

3 Results and Discussion

Laser Beam Focus

Figure 6 shows laser energy distribution along the beam axis where α and E is 18.6° and 25.8 J, respectively. It is shown that laser beam by the internal reflection is focused between 0.24 mm and 0.41 mm away from fiber tip. On the other hand, intensity of direct laser beam is less than 20% of the focused laser beam.

Figure 7 shows relationship between maximum overpressure and F. Shock waves were reflected/converged by a truncated ellipsoidal cavity made of brass (ellipticity: 1.50, minor axis: 3.5 mm, opening size: 6.58 mm, F1: 2.12 mm). When the fiber tip is shifted by 2.40 mm from the open end of the reflector (0.28 mm from F1),

Fig. 6 Laser energy distribution along the beam axis

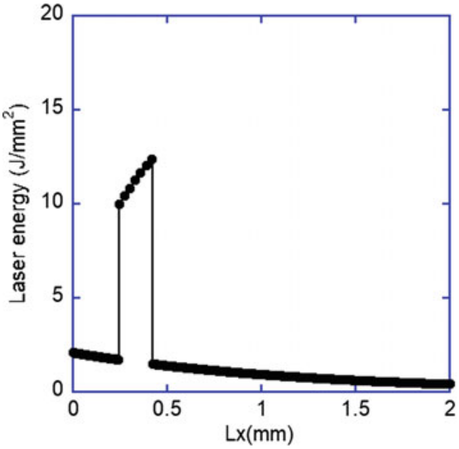

Fig. 7 Relationship between max. overpressure and F

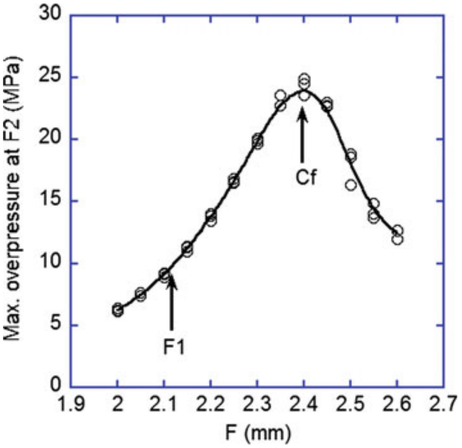

reflected/converged shock wave at F2 has the largest intensity. Accordingly, the position of the shock wave source (Cs) is estimated to be 0.28 mm.

According to the model of the moving breakdown in liquids [20], when the peak power of a laser pulse exceeds the threshold power required for optical breakdown in the medium, plasma is created at the positions along the axis of the incoming beam, and it grows toward the incident laser beam. Due to shielding effect of plasma, trailing edge of laser pulse is absorbed on the side oriented toward the incident laser beam. Consequently, plasma has a right cone-shape with a base of higher energy density. Since the high-energy density leads to high pressure inside the plasma resulting in high shock peak pressure in the liquid surrounding the plasma, Cs is positioned at bottom end of laser beam focus.

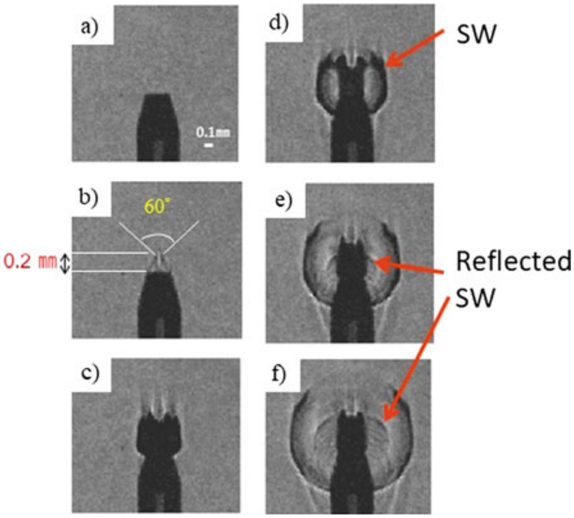

Fig. 8 Sequential propagation of the underwater SW

Generation of Laser Induced Shock Wave

Figure 8 shows example of typical events induced by irradiation of a 17 mJ laser pulse of 100 ns duration into the distilled water through optical fiber. The taper angle of fiber tip is 30°. Laser beam propagating in the periphery of fiber reflects on the lateral side of fiber tip and converges on water along the axis of the fiber at an angle of 60°.

A cavitation bubble appears dark on image after 0.1 μs from laser irradiation (Fig. 8c). Because the pulse duration of incident laser beam is longer than the lifetime of plasma, the bubble wall is vaporized by a tail of laser pulse transmitting through the bubble and the bubble wall extends toward the laser irradiation direction.

The shock wave is visible around the expanding bubble after 0.2 μs from laser irradiation. The collision of shock wave with the fiber tip result in reflection wave around the tip and transmitted wave inside fiber (Fig. 8d). The transmitted wave propagates through the quartz fiber trailing conical wave in the surrounding water because the sound speed of the fiber is 10 times faster than that of water (Fig. 8e, f).

Geometry of Shock Wave Front.

Figure 9 shows degrees of deviation of shock wave front from sphere centered at Cs by image processing. Based on approximate curves of the degrees of deviation (ΔD), reflecting surface was corrected.

Figure 10 shows pressure distributions on the central axis of reflector under three conditions. In the condition “A”, the reflecting face is modified, whereas the fiber

Fig. 9 Degrees of deviation of shock wave front from sphere centered at Cs

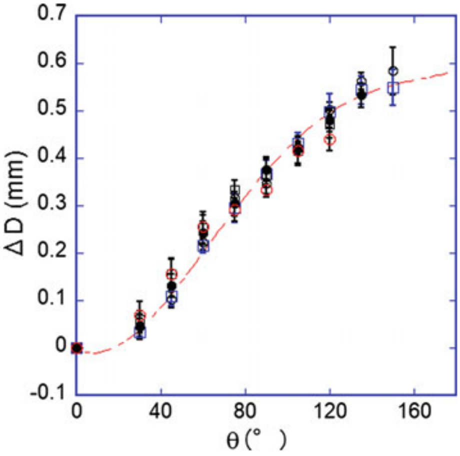

Fig. 10 Pressure distributions on the central axis of reflector; A: modified reflector and the fiber tip is located on F1; B: ellipsoid reflector and the origination

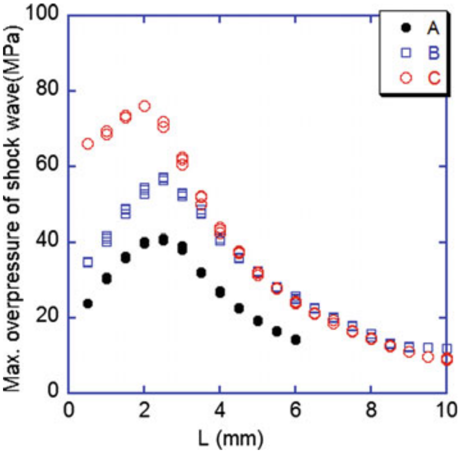

tip is locating on F1. In the condition "B", the reflecting face is ellipsoid (ellipticity: 1.50, minor axis: 2.0 mm, opening size: 3.60 mm, F1: 3.54 mm), and the origination point of SW is located on F1. In the condition "C", the reflecting face is modified, and the origination point of SW is located on F1.

Comparing the effects of reflector modification (A) with the values of fiber positioning (B), the later effect is larger. Furthermore, combination of reflector modification and fiber positioning is obviously effective in generation of intense focused shock wave.

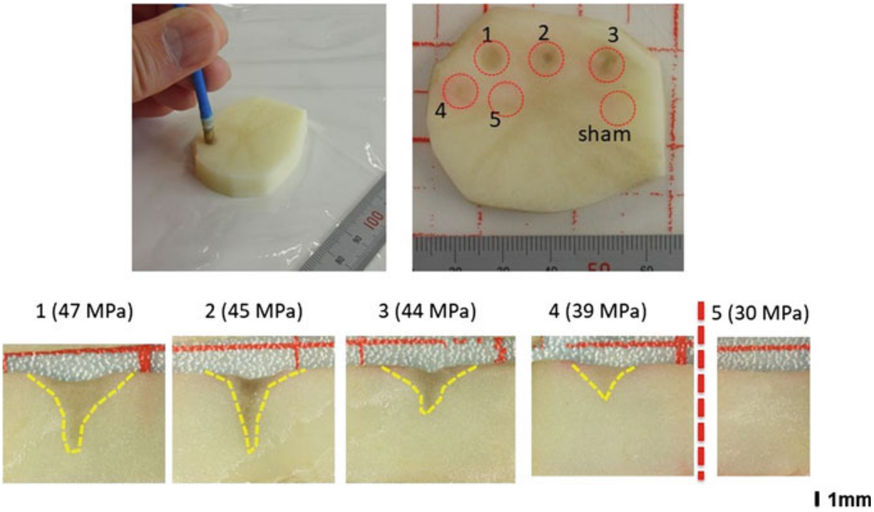

Fig. 11 A slab of potato exposed by 180 shock waves at maximum overpressure varying from 30 to 47 MPa

Threshold of Cell Injury Induced by Focused Shock Wave.

We examined threshold of cell injury induced by the focused shock wave using the reflector of the condition “C”. Cell injuries were recognized using enzymatic browning of fresh potato [21]. Figure 11 shows a cross section of a slab of potato exposed by 180 shock waves at maximum overpressure varying from 30 to 47 MPa. The shock wave-induced damaged regions were clearly dark colored. It is also clear that the damaged region extends beyond focus point.

Taking medical application of this system into considering, it is important to control the degree of ablation. Figure 12 shows relationship between the depth of damaged area and the maximum overpressure. No damage was observed less than 30 MPa, however between 39 and 47 MPa, a positive correlation is observed between the depth of damaged area and the overpressure. The relationship between shock wave intensity and lesion depth is comparable to a porcine cardiac muscle [22, 23].

4 Summary

1. Degrees of deviation of shock front from a spherical shape centered at the laser focus were measured based on high-speed shadowgraph images.
2. Performance of the shock wave generator was successfully improved by optimization of the shape of a reflecting surface and the fixing position of optical fiber.

Fig. 12 Relationship between depth of damaged area and maximum overpressure at F2

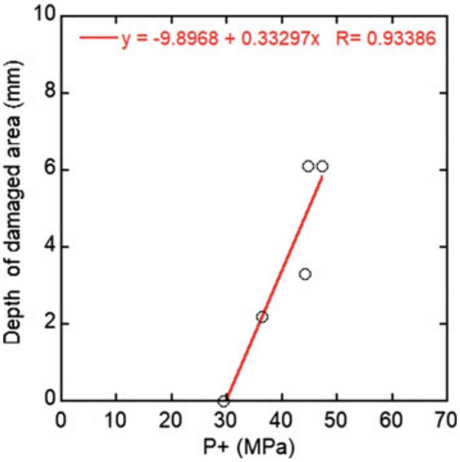

Acknowledgements This work was supported by the A-STEP (Adaptable & Seamless Technology Transfer Program through Target-driven R&D) of JST. We are grateful to Mr. M. Kaneda of Sparkling Photon Inc., Mr. S. Hayasaka, Kazuo Katsurashima and Prof. Hiroaki Shimokawa of Tohoku University Hospital, Hitachi Maxell, Ltd., Funakoshi Co., Ltd. and FLTec Co., Ltd. for manufacturing of experimental facility, as well as to Mr. N. Tokuoka and Mr. I. Kaneko of Shimadzu Corp., Dr. Y. Hamate and Mr. H. Sonobe of Nobby Tec. Ltd. for visualization experiments.

References

1. Rieber F (1947) Shock wave generator. United States patent US2559227 A, 24 May 1947, Int ClA61N7/02, G10K15/06, A61H23/00
2. Wilbert DM, Reichenberger H, Noske B, Riedmiller H, Alken P, Hohenfellner R (1987) New generation shock wave lithotripsy. J Urol 138:563–565
3. Zhong P, Smith N, Simmons NW, Sankin G (2011) Anew acoustic lens design for electromagnetic shock wave lithotripters. Am Int Phys Conf Proc 1359:42–47
4. Mancicni JG, Neisius A, Smith N, Sankin G, Astroza GM, Lipkin ME, Simmons WN, Preminger GM, Zhong P (2013) Assessment of a modified acoustic lens for electromagnetic shock wave lithotripters in a swine model. J Urol 190:1096–1101
5. Neisius A, Smith NB, Sankin G, Kuntz NJ, Madden JF, Fovargue DE, Mitran S, Lipkin ME, Simmons WN, Preminger GM, Zhong P (2014) Improving the lens design and performance of a contemporary electro, magnetic shock wave lithotripter. Proc Natl Acad Sci USA 111:E1167–E1175
6. Wess OJ, Marlinghaus EH, Katona J (1990) A new design of an optimal acoustic source for extracorporeal lithotripsy. In: Burhenne J (ed), Biliary lithotripsy II: adapted from the proceedings of the second international inter-disciplinary symposium on biliary lithotripsy, Year Book Medical Publishers, Chicago, pp 211–214, 24–26 Apr 1989
7. Köhrmann KU, Rasswiller JJ, Manning M, Mohr G, Henkel TO, Jünemann KL, Alken P (1995) The clinical introduction of a third-generation lithotripter: modulith SL 20. J Urol 153:1379–1383

8. Wess O (2012) Physics and technique of shock wave lithotripsy (SWL). In: Talati J, Tiselius HG, Albala DM, Ye Z (eds) Urolithiasis. Basic science and clinical practice. Springer Verlag, London, pp 301–311. https://doi.org/10.1007/978-1-4471-4387-1_38
9. Standenraus J (1991) Erzeugung und Ausbreitung freifeldfokussierter Hochenergiedruckimpulse in Wasser. Dissertation, University of Stuttgart, Stuttgart, p 173 (in German)
10. Eisenmenger W, Du X, Tang C, Zhao S, Wang Y, Rong F, Dai D, Guan M, Qi A (2002) The first clinical results of wide-focus and low-pressure ESWL. Ultrasound Med Biol 28:769–774
11. Loske AM (2007) Shock wave physics for urologist. Centro de Física Aplicada y Technología Avanzada, UNAM, Querétaro, México
12. Dreyer T, Krauss W, Bauer E, Riedlinger RE (2000) Investigations of compact self focusing transducers using stacked piezoelectric elements for strong sound pulses in therapy. In: Schmeider SC, Levy M, McAvoy BR (eds) Proceeding of the IEEE ultrasonics symposium;22–25 October 2000; San Juan, Puerto Rico. New York: Institute of Electrical and Electronic Engineers, vol 2, pp 1239–1242. https://doi.org/10.1109/ULTSYM.2000.921547
13. Loske AM, Fernández F (2010) The development of tandem extracorporeal shock wave lithotripsy. In: Loske AM (ed) New trends in shock wave applications to medicine and biotechnology. Research Signpost, Kerala, pp 137–149
14. Kuwahara M, Kambe S, Orikasa K, Takayama K (1987) Extracorporeal stone disintegration using chemical explosive pellets as an energy source of underwater shock waves. J Urol 135:814–817
15. Hosseini SHR, Takayama K (2004) Study of micro shock waves and cavitation generated by Ho: YAG laser beam for medical application. In: Behnia M, Lin W, McBain GD (eds) Proceedings of the 15th Australasian fluid mechanics conference, University of Sydney, Sydney, Australia, 13–17 Dec 2003
16. Nakahara M, Nagayama K (1999) Water shock wave emanated from the roughened end surface of an optical fiber by pulse laser input. J Mater Process Technol 85:30–33
17. Nose H, Maeda H, Yamamoto N, Nakahara M (2004) Effect of optical fiber output surface on laser induced shock wave and its application. Japanese J Appl Phys 43:6145–6151
18. Rasband WS, ImageJ US (2012) National Institutes of Health, Bethesda, Maryland, USA. http://imagej.nih.gov/ij/
19. Schneider CA, Rasband WS, Eliceiri KW (2012) NIH Image to ImageJ: 25 years of image analysis. Nat Methods 9:671–675
20. Vogel A, Nahen K, Theisen D, Noack J (1996) Plasma formation in water by picosecond and nanosecond nd: yag laser pulses—part i: optical breakdown at threshold and superthreshold irradiance. IEEE J Sel Top Quantum Electron 2(4):847–860
21. Sunka P, Babicky V, Clupek M, Benes J, Pouckova P (2004) Localized damage of tissues induced by focused shock waves. IEEE Trans Plasma Sci 32(4):1609–1613
22. Hasebe Y, Yamamoto Y, Fukuda K, Nishimiya K, Hanawa K, Shindo T, Kondo M, Nakano M, Wakayama Y, Takayama K, Shimokawa H (2015) Development of a novel shock wave catheter ablation system−the first feasibility study in pigs. PLoS ONE 10(1):e0116017. https://doi.org/10.1371/journal.pone.0116017
23. Hirano M, Yamamoto H, Hasebe Y, Fukuda K, Morosawa S, Amamizu H, Ohyama K, Uzuka H, Takayama K, Shimokawa H (2018) Development of a novel shock wave catheter ablation system—A validation study in pigs in vivo. Europace 20:1856–1865. https://doi.org/10.1093/europace/eux244

Experimental Demonstration on High-Speed Gas Gun Driven by a Gaseous Detonation

Shinichi Maeda and Tetsuro Obara

1 Introduction

In our research group, a detonation-driven high-speed gas gun has been constructed by applying a gaseous detonation (hereinafter referred to simply as detonation), which is an explosive gaseous combustion accompanying a strong shock wave, as the driving source of the high-speed gas gun to launch a projectile at supersonic to hypersonic speeds. Detonation [1, 2] is the combustion wave propagating in a gaseous combustible mixture at hypersonic speed (generally, the Mach number is about 5 to 7). The strong shock wave at the front adiabatically compresses the mixture to induce combustion, and the expanding burnt gas supports the propagation of shock wave, and these propagate like that the self-sustained shock wave supported by the chemical reaction. Unlike usual diffusive combustion waves (deflagration waves), the combustion occurs behind the strong shock wave, so that the pressure of burned gas rises several tens times the initial pressure and the burned gas temperature is higher than that of the deflagrative combustion. Focusing on the feature that such high enthalpy gas with high pressure can be generated comparatively easily, the researches aiming at engineering application of detonation have been carried out, for example; combustion processes of internal combustion engines (major concepts are known as pulsed detonation engines [3] and rotating detonation engines [4]) and thermal spraying guns [5]. The driving sources with high enthalpy gas which drive shock tubes and shock tunnels are also known as the possible application of detonation [6]. Our research group has also devoted efforts to the development of pulse detonation engines [7, 8] and detonation-driven shock tunnels [9].

Presles and Bauer [10] proposed the application of detonation to high-speed gas guns as “Detonation products gun”. Figure 1 shows the schematic diagram of the

---

S. Maeda (✉) · T. Obara
Graduate School of Science and Engineering, Saitama University, 255 Shimo-Okubo, Sakura-ku, Saitama-shi, Saitama 338-8570, Japan
e-mail: shinichi_maeda@mech.saitama-u.ac.jp

© The Author(s), under exclusive license to Springer Nature Switzerland AG 2022
K. Takayama and O. Igra (eds.), *Frontiers of Shock Wave Research*,
https://doi.org/10.1007/978-3-030-90735-8_9

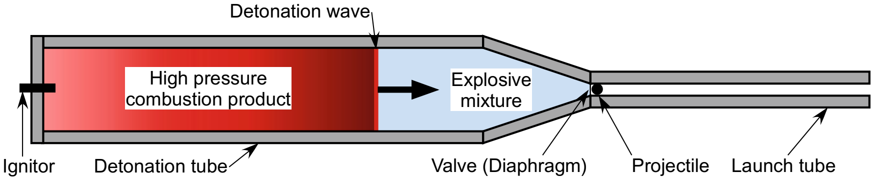

Fig. 1 Schematic of a single-stage detonation-driven high-speed gas gun

detonation-driven high-speed gas gun, which is the focus of this study. Detonation waves initiated near the closed end in the straight tube (hereafter called detonation tube) play a role like the piston (called reactive piston in [10]) which compresses the combustible mixture filled with the certain initial pressure by the strong shock wave and raises the temperature (speed of sound) by combustion while propagating in the right direction of Fig. 1 in the detonation tube. The launch tube is connected in the downstream of the detonation tube, and after the detonation wave reaches the entrance of the launch tube, the valve is opened (or the diaphragm is ruptured), and the burnt gas accelerates the projectile. Presles and Bauer [10] considered only the simple theoretical model to estimate the performance of such the gas gun, however, compared with the single-stage gas gun using gunpowder or compressed gas, it could avoid inconveniences and problems in handling gunpowder, and considering the thermodynamic state of burned gas behind the detonation wave, it was comparatively easy to obtain the wide range of projectile velocity exceeding 1500 m/s. The small number of experimental studies had been conducted for the single-stage gas guns [11, 12] such as Fig. 1 and for the two-stage light gas guns [13] in which detonation was used to drive free pistons.

In this study, experiments have been conducted with the aim of constructing the laboratory-scale compact high-speed gas gun that can achieve launching speed of 1–3 km/s with the relatively small projectile (about 5–10 mm in diameter) using the detonation tube filled with the combustible mixture at less than 10 atm of filling pressure. This velocity range is usually achieved with single-stage gas guns using gunpowder or compressed gas or small two-stage light gas guns. The motivation of this study was to use the gas gun for observation [14, 15] of a shock-induced combustion and detonation wave formed around a high-speed projectile launched in a combustible mixture. Therefore, the projectile velocity of Mach 4 (approximately 1.4 km/s) or more is generally required in order to induce the combustion behind the shock wave formed around the projectile, and the projectile velocity of Mach 7 (approximately 2.5 km/s, which is order of propagation velocity of Chapman-Jouguet (C-J) detonation) or more is required in order to form the detonation wave around the projectile. This range of projectile velocity covers to some extent the range required for aerodynamic studies around supersonic to hypersonic flying vehicles. The detonation-driven high-speed gas gun is attractive in that it can avoid inconvenience in handling gunpowder, and it is easy to obtain a high projectile velocity at a filling pressure much lower than that of conventional single-stage light-gas gun driven by a compressed gas (as a matter of course, it is necessary to pay close attention to handling combustible mixtures). In this paper, the result of experimental research on the detonation-driven high-speed gas gun [16, 17] which our research group have carried out is described.

2 Experimental Setup and Conditions

A schematic diagram of the detonation-driven high-speed gas gun constructed in this study is shown in Fig. 2. Figure 2(a) shows the single-stage gas gun simply consisting of two straight tubes. The detonation tube and the launch tube were connected through the tapered tube with a 30° of converging angle. The detonation tube was a simple stainless-steel tube of 50 mm inner diameter, and the experiment was carried out under three types of length: 2180, 3020, and 4280 mm length. The detonation tube was initially filled with the combustible mixture, and the detonation was initiated by the ignition unit (composed of four automotive spark plugs) installed at the left end. Stoichiometric hydrogen–oxygen mixture or stoichiometric hydrogen–oxygen mixture diluted with helium at a volume ratio of 10–60% were used as the combustible mixtures. The hydrogen, oxygen, and helium gases were filled respectively in the detonation tube at the given partial pressure just before the experiment, and the mixture was ignited after about 15 min at rest for diffusive mixing. The launch tube was a stainless-steel tube of 5 mm inner diameter and 1040 mm length, or 10 mm inner diameter and 1510 mm length. The detonation tube and the launch

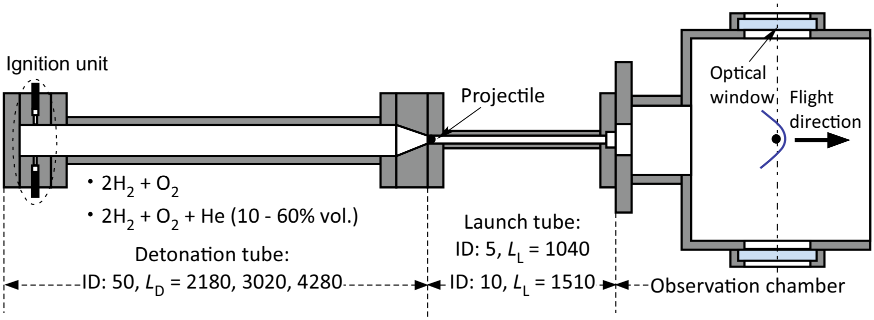

(a) Single-stage gun

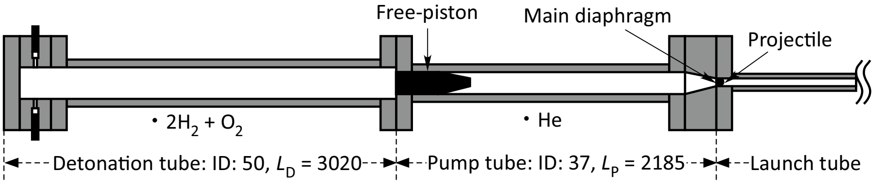

(b) Two-stage gun

Fig. 2 Schematic of the detonation-driven high-speed gas gun (unit of length: [mm])

tube were initially separated by a PET diaphragm. The projectile was a high-density polyethylene sphere of 4.76 mm (about 52 mg) or 9.53 mm (about 426 mg) diameter depending on the inner diameter of launch tube. In this study, the sabot for holding the projectile was not used, and the projectile was directly installed at the upstream end of the launch tube in advance.

Figure 2(b) shows the two-stage light gas gun, in which the pump tube for compressing the light gas (helium) is connected between the detonation tube (length 3020 mm) and the launch tube. The pump tube was 37 mm in inner diameter and 2185 mm in length, and the free piston made of aluminum (about 290 g) or polycarbonate (about 130 g) was initially installed in the upstream end. The experimental setup was basically the same as that of the single-stage gas gun except that the pump tube was added. The main diaphragm installed between the pump tube and the launch tube was also the PET diaphragms as well as other sections, and the diaphragms were overlapped to increase the rupture pressure of the main diaphragm.

The launch tube was initially evacuated to less than 2 kPa in both configurations of the single-stage gas gun and the two-stage light gas gun. In the downstream of the gas gun, there was the observation chamber for measuring the projectile speed, and it was measured by time of flight when the projectile passed through the two diode lasers placed at a certain distance apart and by direct observation of the projectile using the high-speed camera (nac image technology, ULTRA Cam HS-106E) from the optical windows.

3 Experimental Results

Single-Stage Gas Gun (Effect of Length of the Detonation Tube)

Figure 3 shows the projectile velocity with the launch tube diameter of 5 mm and the detonation tube length of $L_{\mathrm{D}} = 2180$ mm and 4280 mm against the initial pressure of the detonation tube. The open symbols are the experimental results. The observation chamber, where the projectile velocity was measured, was filled with an atmosphere of 50 kPa, and the distance from the launch tube exit to the laser lines for measurement was 265 mm. Therefore, the projectile velocity in Fig. 3 includes slight deceleration by the drag in the atmosphere. The closed symbols with solid lines are the calculated values of the ideal velocity of a single-stage light-gas gun [18] of the same shape as the experimental equipment in this study. The closed triangle and circle symbols are the ideal projectile velocities of the single-stage light-gas gun calculated when compressed gas of hydrogen or helium is filled in the detonation tube at the initial pressure of the horizontal axis, respectively. The time and effort involved in conducting the detonation-driven experiments are almost the same as for the single-stage light-gas guns driven by compressed gas (detonation initiation is not very difficult for fuel-oxygen mixtures at initial pressures above atmospheric pressure). For

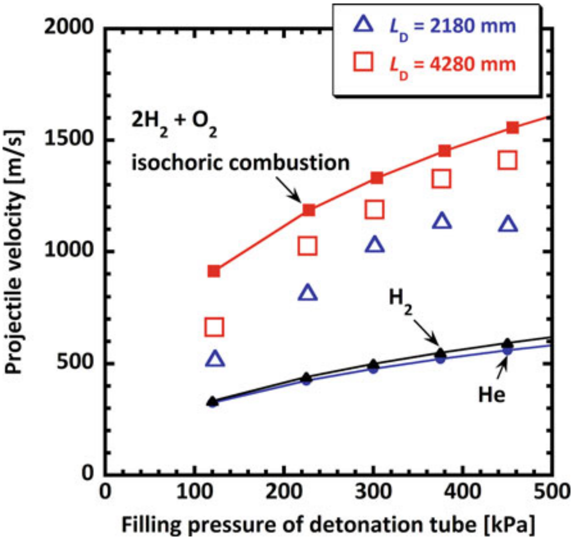

Fig. 3 Projectile velocities obtained experimentally by using the different lengths of the detonation tubes, L_D (Open symbols). Closed symbols with solid lines are theoretical values in the single-stage light gas gun using the given driver gases (hydrogen or helium) [17]

the given initial pressure in Fig. 3, the experimental results of detonation-driven case show to increase the projectile velocity by a factor of two to three compared to the ideal projectile velocity for the compressed-gas-driven case. Although the maximum projectile velocity obtained in this experiment was about 1400 m/s, the initial pressure of about 5 MPa was required to obtain the same velocity with the ideal single-stage light-gas gun driven by hydrogen or helium. In Fig. 3, the calculated projectile velocity (closed square symbol with solid line) is shown when the ideal single-stage light-gas gun was driven by the burned gas after constant volume combustion of the same combustible mixture, as the direct comparison with the experimental result. The state after constant volume combustion at the given initial condition was calculated using chemical equilibrium calculation software NASA CEA [19]. In the case of detonation, the ideal performance of the detonation-driven high-speed gas gun needs further study because it does not take into account the gasdynamic process such as the generation of the non-uniform thermodynamic state distribution of burned gas in the detonation tube, the existence of flow velocity induced by the detonation wave, and the reflection of the detonation wave at the entrance of the launch tube. Therefore, although the experimental results cannot be explained quantitatively by assuming the constant volume combustion model, the calculated values in Fig. 3 seem to roughly represent the ideal performance of the high-speed gas gun driven by the burned gas.

In the experimental results of Fig. 3, focusing on the effect of detonation tube length, L_D, when the L_D was doubled, the projectile velocity increased 1.1–1.3 times for the same initial pressure. Figure 4 shows the pressure histories at the launch tube inlet measured under the several conditions in Fig. 3. For the three conditions of initial pressure (120, 225, 450 kPa), the pressure histories of detonation tube length of 2180 mm (black line) and 4280 mm (red line) are shown. The piezoelectric pressure transducer used for the measurement was recessed-mounted through the small hole

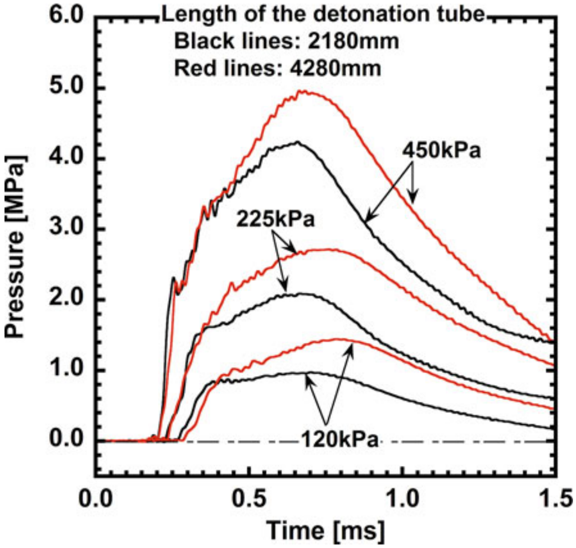

Fig. 4 Pressure histories at the inlet of the launch tube [16]

(inner diameter 2 mm and length 43 mm) in the inner wall of launch tube. Therefore, though the pressure was supposed to rise sharply by the arrival of burnt gas, the measurement result did not seem to follow the instantaneous pressure rise. However, as the qualitative tendency, it was found that the longer the detonation tube was, the longer the inlet pressure of the launch tube was maintained higher value.

Figure 5 schematically shows the factors of this tendency. The state on the C-J detonation wave propagating through the detonation tube depends only on the initial pressure among the experimental parameters of this study, and is not affected by the detonation tube length. However, the distribution of state behind the detonation wave depends on the detonation tube length. The state in a simple detonation tube with a closed end and a constant cross section was theoretically formulated when one-dimensional propagation of steady detonation waves was assumed [20]. Figure 5(a) schematically shows the pressure distribution at the time when the C-J detonation wave reaches the entrance of the launch tube. A self-similar decelerated rarefaction wave (so called Taylor wave) exists behind the detonation front to satisfy the boundary condition (flow velocity is zero) at the closed end. The head of rarefaction wave coincides with the detonation front, and the tail of rarefaction wave exists at the middle position between the closed end and the detonation front. The burned gas has the flow velocity in the same direction as the propagation of the detonation wave in the Taylor wave, and the flow velocity becomes zero and the thermodynamic state becomes spatially uniform in the region between the tail of the Taylor wave and the closed tube end (so called plateau region). Therefore, the longer the detonation tube, the longer the region of the Taylor wave becomes, and the spatial gradient of the pressure becomes more gradual. Then, Fig. 5(b) schematically shows the pressure distribution when the C-J detonation wave is reflected at the entrance of the launch tube and the reflected shock wave begins to propagate upstream of the detonation

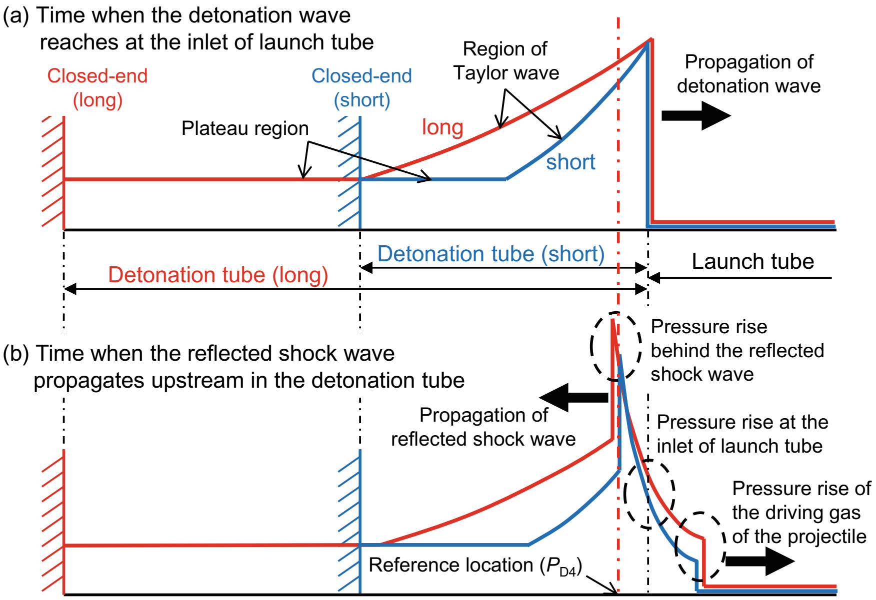

Fig. 5 Schematic of the pressure distribution inside the gas gun [16]

tube (this time corresponds to the start of acceleration of the projectile). The pressure behind the reflected shock wave becomes the driving pressure of the projectile. Since the reflected shock wave propagates back in the Taylor wave, the pressure behind the reflected shock wave becomes higher in the longer detonation tube because the pressure in the Taylor wave region becomes higher as the detonation tube is longer in the certain cross-section (reference location in Fig. 5(b)) near the inlet of the launch tube. This resulted in that the duration of the high pressure at the entrance of the launch tube was lengthened, and the projectile speed became to rise. It can be said that this is the one of features of the detonation-driven high-speed gas gun which applied the gas-dynamic process accompanied with the propagation of the detonation.

Single-Stage Gas Gun (Effect of Composition of Combustible Mixture)

The effect of helium dilution was investigated in the expectation that the thermodynamic state of burned gas after detonation was changed to the state more suitable for driving the projectile. Figure 6 shows the projectile velocity when the dilution ratio of helium was changed from 0% (no dilution) to 60% while the initial pressure of the detonation tube was maintained at 450 kPa. The symbol connected by the

Fig. 6 Effect of dilution rate of helium gas on projectile velocity while total filling pressure of mixtures were constant at 450 kPa [17]

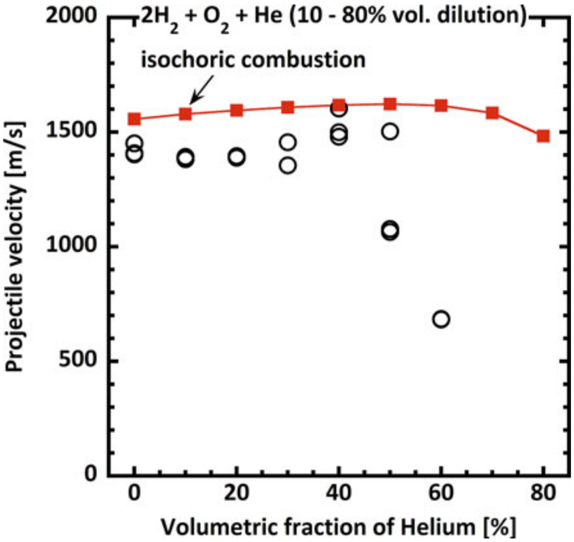

solid line is a calculated value assuming constant volume combustion as in Fig. 3. The calculated results show that the projectile velocity is almost independent of the dilution ratio of helium. This is because, as shown in Fig. 7, helium dilution has a positive effect for increasing the projectile velocity by increasing the sound velocity of burned gas, but has a negative effect for it by increasing the specific heat ratio of burned gas. When the dilution ratio exceeds 60%, the theoretical projectile velocity begins to decrease because the pressure after constant volume combustion begins

Fig. 7 Effect of dilution rate of helium gas on thermodynamic properties of combustion products by assuming isochoric combustion, while total filling pressure of mixtures are constant at 450 kPa. Each value is normalized by values of non-dilution; p_{CV} = 4.59 MPa, a_{CV} = 1590 m/s and γ_{CV} = 1.21 [17]

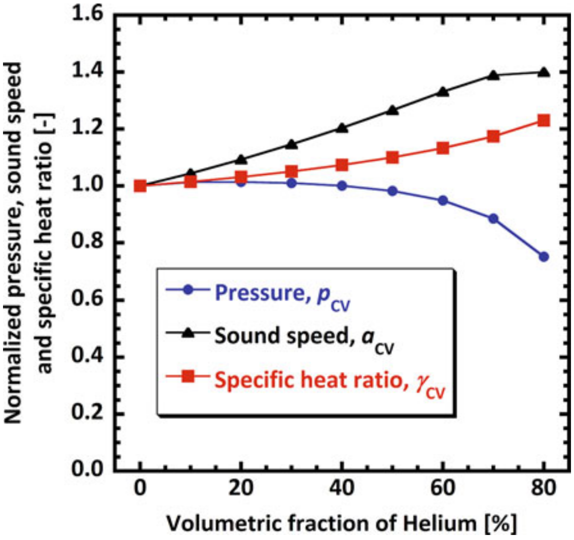

to decrease significantly. The experimental results show that the projectile velocity remains almost constant up to about 40% dilution ratio. Therefore, the theoretical calculation of single-stage light-gas gun assuming constant volume combustion can be the basis to explain the experimental result at least qualitatively. However, when the dilution ratio was more than 50%, the experimental projectile velocity rapidly decreased because the detonation initiation became unstable by lowering the reactivity of combustible mixture. In other words, when the dilution ratio was less than 40%, the projectile velocity was maintained even if the amount of energy released by combustion was reduced, and it means that the energy efficiency of the gas gun can be improved by the helium dilution.

In the sense of changing the thermodynamic state of burned gas to the more suitable state, it is also considered to increase the equivalence ratio of hydrogen–oxygen mixture. In this case, the experiment did not carry out for the safety reason, because unreacted hydrogen would remain. Then, this paper shows results of theoretical calculation of single-stage light-gas gun assuming constant volume combustion in Fig. 8. As the equivalence ratio increases, the sound speed of burned gas increases and the specific heat ratio also increases, but the change of the specific heat ratio is slight. However, since the pressure of the burned gas greatly decreases with the increase in the equivalence ratio, the projectile velocity of the slightly rich mixture is the highest as a result. From the results so far, the theoretical calculation well shows the qualitative tendency of the experimental results, and it is considered that the possibility of significantly increasing the experimental projectile velocity by increasing the equivalence ratio is low.

Fig. 8 Effect of equivalence ratio of hydrogen–oxygen mixture on thermodynamic properties of combustion products and projectile velocity by assuming isochoric combustion, while filling pressure of mixtures are constant at 480 kPa. Thermodynamic properties are normalized by values of stoichiometric mixture; $p_{CV} = 4.85$ MPa, $a_{CV} = 1536$ m/s and $\gamma_{CV} = 1.13$

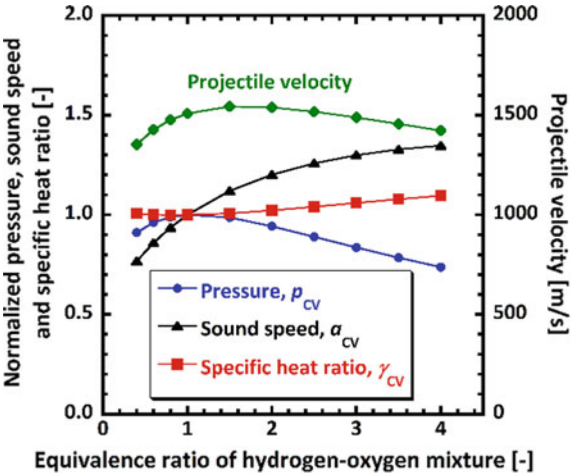

Single-Stage Gas Gun (Effect of the Projectile Diameter)

Figure 9 shows the projectile velocity for the detonation tube length of 3020 mm against the initial pressure of the detonation tube. The open symbols are experimental results obtained with the two types (inner diameter and length, L_L) of launch tubes. Deceleration of the free-flight projectile in the observation chamber was negligible because it was evacuated as well as the launch tube. Repeated experiments at the same condition were performed under the all conditions. The closed symbols connected by solid lines are the results of theoretical calculation of a single-stage light-gas gun assuming constant volume combustion, as in the case of Figs. 3 and 6. As can be seen from Fig. 9, the reproducibility of the projectile velocities under the same conditions was good as that of a conventional single-stage light-gas gun. Additionally, the tendency of projectile velocity for the change of initial pressure was clear, and the required projectile velocity could be obtained with good accuracy. The maximum projectile speed obtained in the present study was about 1400–1500 m/s for the 4.76 mm diameter projectile and about 1300 m/s for the 9.53 mm diameter projectile. It is a future work of this study to investigate whether there is the technique which can increase the projectile velocity without increasing the initial pressure of the detonation tube using the same launch tube. The pressure behind the reflected shock wave propagating in the Taylor wave shown schematically in Fig. 5 rapidly decays with time from the maximum pressure at the reflection. It is considered that how to maintain the pressure high behind the reflected shock wave is important for the increase of the projectile velocity, as it was understood from the present result that the projectile velocity increased by lengthening the detonation tube.

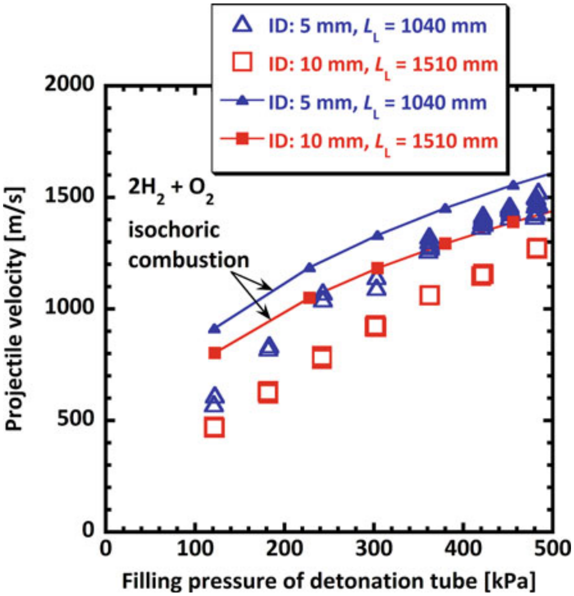

Fig. 9 Projectile velocities obtained experimentally by using the different diameters and lengths of the launch tubes (Open symbols). Closed symbols with solid lines are theoretical values in the single-stage light gas gun using the given driver gases

Two-Stage Light Gas Gun

The typical way to obtain the projectile velocity exceeding the single-stage gas gun using the same driving source (detonation tube in this study) as the single-stage gas gun is to make the two-stage light gas gun. In this case, the principle of the gas gun is essentially the same as that of a two-stage light gas gun driven by gunpowder or compressed gas. However, as in the case of the single-stage gas gun, it has the advantage that the detonation tube with the comparatively low initial pressure can provide sufficient inertia to the free piston for compressing the light gas.

The typical pressure histories measured in the two-stage light gas gun is shown in Fig. 10. In the figure, PD3 and PD5 are pressure histories in the detonation tube, which were measured at 1500 mm and 2500 mm from the ignition end, respectively. PP2 and PL1 were measured at the end of pump tube and at the inlet of launch tube, respectively, across the main diagram in Fig. 2. The first pressure peaks of PD3 and PD5 detected the detonation wave propagating downstream. When the detonation wave reached the inlet of pump tube and reflected off the base of free piston, it started to be driven and the PP2 gradually started to rise. In the compression process of the light gas, the reflected shock wave traveled back and forth between the rear surface of free piston and the ignition end of detonation tube, and there were multiple pressure rises in PD3 and PD5. In this condition, the main diaphragm ruptured at the time when PP2 reached about 10 MPa, and the rapid rise of PL1 drove the projectile to the velocity of about 2 km/s.

Figure 11 shows the projectile velocity obtained under the current operating conditions. Conditions 1 through 5 were for the inner diameter of launch tube of 5 mm, and conditions 6 and 7 were for the inner diameter of launch tube of 10 mm, and the

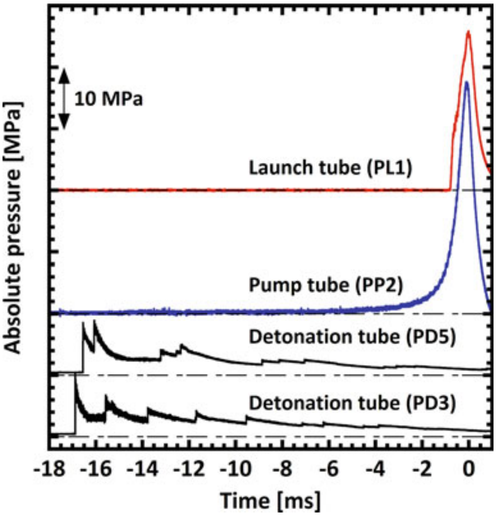

Fig. 10 Typical pressure histories in the detonation tube (PD3 and PD5), pump tube (PP2) and launch tube (PL1) during the operation of the two-stage gun driven by the hydrogen–oxygen detonation. Detonation tube: $2H_2 + O_2$, 452 kPa, Pump tube: He, 102 kPa, Main diaphragm thickness: 125 μm, Projectile velocity: 1920 m/s [17]

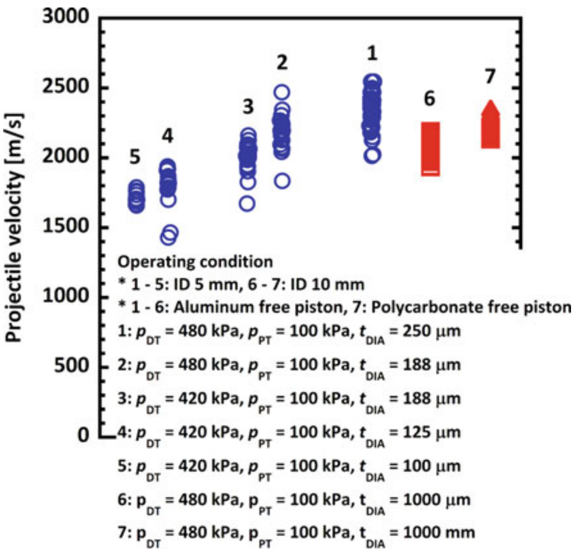

Fig. 11 Projectile velocities in the two-stage light-gas gun experiments. ID: inner diameter of the launch tube, p_{DT}: initial pressure of the detonation tube, p_{PT}: initial pressure of the pump tube, t_{DIA}: main diaphragm thickness

total data was about 285 shots. Deceleration in the measurement section was negligible because the observation chamber was evacuated as well as the launch tube. The horizontal axis does not show the physical parameter, but the difference of operating conditions described in the figure. As can be seen from the figure, the reproducibility of the projectile velocity under the same operation condition was not so good as compared with the single-stage gas gun, but the inner diameter of the launching tube of 5 mm covered from the maximum projectile velocity (about 1.4 km/s) obtained by the single-stage gas gun to about 2.5 km/s. Comparing conditions 6 and 7 with the 10 mm inner diameter launch tube, the projectile velocity was slightly higher with the lighter polycarbonate free piston, obtaining the maximum velocity of about 2.2 km/s.

4 Conclusions

In this study, the high-speed gas gun using the gaseous detonation initiated in a hydrogen–oxygen mixture was constructed. The single-stage gas gun and the two-stage light gas gun using the same detonation tube as the driving source were used to cover the range of projectile velocity from 500 m/s to 2500 m/s. It goes without saying that the handling of combustible mixtures requires extreme care, but we believe that the ability to achieve supersonic to hypersonic projectile velocity under operational conditions with the initial pressure of a few atmospheres is attractive. In particular, the characteristics of the detonation-driven high-speed gas gun can be well demonstrated by the single-stage gas gun, and we would like to develop it as one of the detonation applications.

References

1. Fickett W, Davis WC (1979) Detonation, theory and experiment. Dover Publications
2. Lee JHS (2008) The detonation phenomenon. Cambridge University Press
3. Roy GD, Frolov SM, Borisov AA, Netzer DW (2004) Pulse detonation propulsion: challenges, current status, and future perspective. Prog Energy Combust Sci 30(6):545–672
4. Lu FK, Braun EM (2014) Rotating detonation wave propulsion: experimental challenges, modeling, and engine concepts. J Propul Power 30(5):1125–1142
5. Endo T, Obayashi R, Tajiri T, Kimura K, Morohashi Y, Johzaki T, Matsuoka K, Hanafusa T, Mizunari S (2016) Thermal spray using a high-frequency pulse detonation combustor operated in the liquid-purge mode. J Therm Spray Technol 25(3):494–508
6. Olivier H, Zonglin J, Yu HR, Lu FK (2002) Detonation-driven shock tubes and tunnels. Prog Astronaut Aeronaut 198:135–203
7. Sakurai T, Minagawa T, Yoshihashi T, Obara T, Ohyagi S (2004) A study for development of hydrogen-fueled pulse detonation engines. Sci Technol Energetic Mater 65(4):125–133
8. Sakurai T, Ooko A, Yoshihashi T, Obara T, Ohyagi S (2005) Investigation of the purge process on the multi-cycle operations of a pulse detonation engine. Trans Japan Soc Aeronaut Space Sci 48(160):78–85
9. Kim T-H, Obara T, Yoshikawa M, Ohyagi S (2006) experimental study on a flow field behind backward-facing step using detonation-driven shock tunnel. Shock Waves 15(1):1–12
10. Presles HN, Bauer P (1983) Detonation products gun. Rev Sci Instrum 54(11):1511–1512
11. Verreault J, Batchelor P, Higgins AJ (2009) Development of a detonation-driven gas gun capable of 3 km/s projectile velocity. In: 27th international symposium on shock waves
12. Li J, Chen H, Zhang S, Zhang X, Yu H (2016) A gasdynamic gun driven by gaseous detonation. Rev Scient Instrum 87(1):015112
13. Chang X, Shimomura K, Taki S (1996) Development and performance examination of a two-stage detonation light gas gun. Trans Japan Society Mech Eng Series B (in Japanese) 62(599):2819–2825
14. Maeda S, Kanno S, Yoshiki I, Obara T (2017) Time-resolved schlieren observations of shock-induced combustion around a high-speed spherical projectile. Sci Technol Energetic Mater 78(1):19–26
15. Maeda S, Yoshiki I, Kanno S, Tomita K, Obara T (2017) Occurrence conditions for unsteady combustions in shock-induced combustions around spherical projectiles. Trans Japan Soc Mech Eng (in Japanese) 83(852):17–00019
16. Maeda S, Kanno S, Koto R, Obara T (2015) Experiment of projectile acceleration using a gaseous detonation driven gas gun. Trans Japan Soc Mech Eng (in Japanese) 81(822):14–00332
17. Maeda S, Kanno S, Yoshiki I, Obara T (2016) Experimental study on acceleration of projectile by a gaseous detonation-driven gas gun using a light gas. Sci Technol Energetic Mater 77(4):79–85
18. Seigel AE (1965) The theory of high speed guns. AGARDograph 91
19. McBride BJ, Gordon S (1996) Computer program for calculation of complex chemical equilibrium compositions and applications. Technical Report NASA RP-1311, Lewis Research Center
20. Endo T, Fujiwara T (2002) A simplified analysis on a pulse detonation engine model. Trans Japan Soc Aeronaut Space Sci 44(146):217–222

Shock Interactions with Solid Objects; from Simple to Complex Geometries

Charles E. Needham

A shock wave, in a gas, forms when energy is locally deposited more rapidly than it can be dissipated at the speed of sound in the surrounding medium. When this occurs, the surrounding medium is compressed and heated, resulting in a higher than ambient sound speed in the compressed gas. The leading edge of the compressed gas expands at the local speed of sound. This super-sonic front is a shock wave. The shock wave is characterized by a near instantaneous rise in pressure (P), density (ρ), temperature (T) and material velocity (u), as well as sound speed (C_s). There are conservation equations that relate the shock front properties and the ambient gas properties. These equations are called the Rankine-Hugoniot (R-H) relations and apply to any shock front.

The R-H relations use the ratio of specific heats of the gas (γ), which for ambient sea level air, has a value of 1.4. For shock waves with peak overpressures less than about 20 bars, the value of γ remains at 1.4. If the shock front pressure is above ~ 20 bars, the value of γ changes due to excitation of molecular vibration, rotation and ionization. For most examples in this chapter, the value of gamma is assumed to be 1.4 unless otherwise expressly stated.

1 Planar Shock Reflection

The simplest interaction of a shock wave with a solid object is the reflection from a planar surface oriented perpendicular to the direction of motion of the shock wave. Upon striking the solid surface, the velocity of the gas behind the shock front is suddenly brought to zero and the kinetic energy ($q = 1/2\rho u^2$) is converted to internal energy(heat). The R-H relations show the reflected overpressure (ΔP_r) is given by:

C. E. Needham (✉)
Needham Consulting, LLC., Albuquerque, NM, USA

© The Author(s), under exclusive license to Springer Nature Switzerland AG 2022

K. Takayama and O. Igra (eds.), *Frontiers of Shock Wave Research*,
https://doi.org/10.1007/978-3-030-90735-8_10

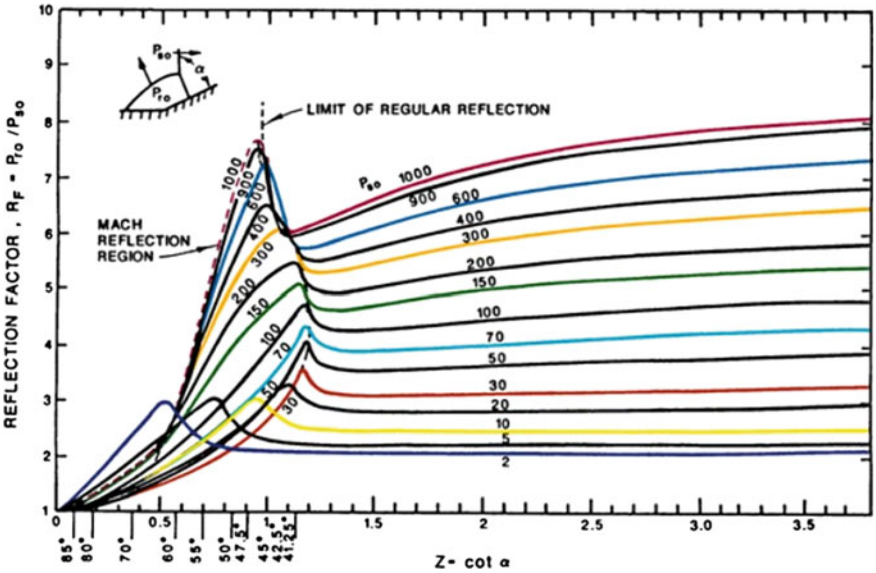

Fig. 1 Reflection factor as a function of the cotangent of the angle between the shock velocity vector and the surface. Labeled overpressures are in PSI

$$\Delta P_r = 2\Delta P_i + (\gamma + 1)q$$

Where ΔP_i is the incident overpressure and ΔP_r is the reflected overpressure.

The reflection factor is the ratio of the overpressure of the incident shock to that of the reflected shock. The reflection becomes significantly more complicated when the incident shock is no longer perpendicular to the plane. Figure 1 shows the reflection factor as a function of the cotangent of the angle between the incident shock and the reflecting plane. For large cotangent, the reflection factor approaches the R-H reflection factor for a perpendicular reflection. As the cotangent approaches zero, the plane's surface is parallel to the shock propagation vector and there is no reflection; the reflection factor is 1.

2 Mach Reflection

For values of the cotangent between 0 and 1.3, the reflection is dominated by the formation of a Mach reflection. A Mach reflection forms when the reflected shock catches the incident shock and the point at which they join rises above the planar surface. Note, from the plot, that the maximum reflection factor for many incident pressure levels can be greater than the perpendicular value when the angle is between 40 and 50°. (For a detailed description of Mach reflection, refer to Ben-Dor "Shock Wave Reflection Phenomena", Springer, 2007).

To further the understanding of the Mach reflection phenomena, an international symposium was founded in 1981. The Mach Reflection Symposium convened approximately yearly for over 20 years. The symposium invited investigators, from around the world, who were actively working on Mach reflection phenomena. The attendees included mathematicians, experimentalists, and numerical analysts from academia, industry and governments. It was at these meetings that many of us became familiar with Dr. Sakurai's work.

3 Rectangular Block Interaction

A slightly more complex structure is a two-dimensional rectangular block. Figures 2 and 3 are from the Ernst Mach institute in Freiburg, Germany. A 1.4 bar, square wave shock is incident on the front face of the block. In the example shown in Fig. 2, the incident overpressure without a block is the light grey curve near the top of the plot. The black and red waveforms are the overpressure as a function of time at the

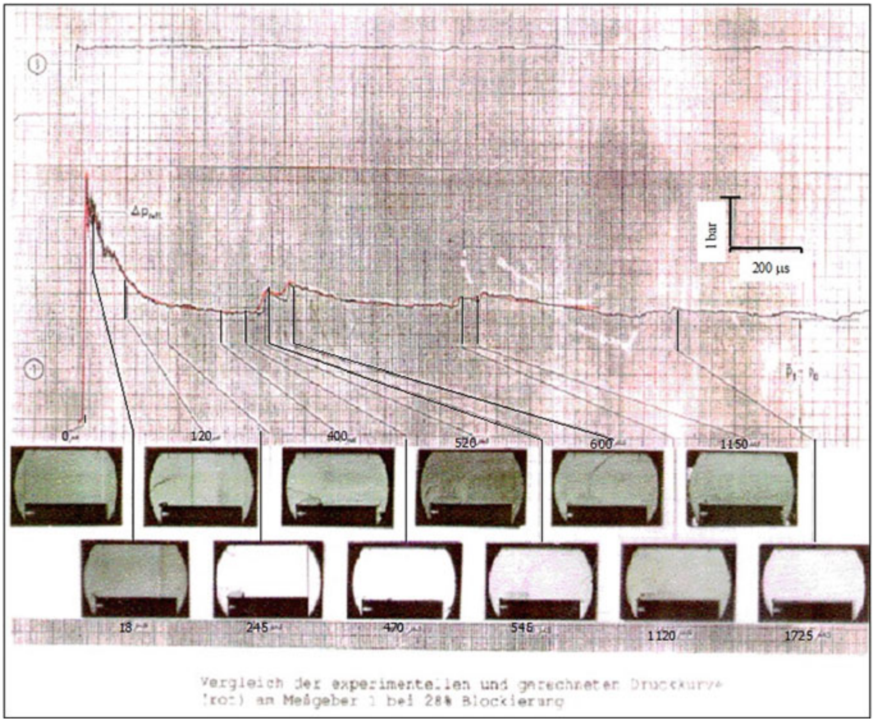

Fig. 2 Experimental and calculated overpressure waveform at the leading edge of a rectangular block. The sequence of photos below the waveform shows the shock configuration at a number of times following the initial interaction

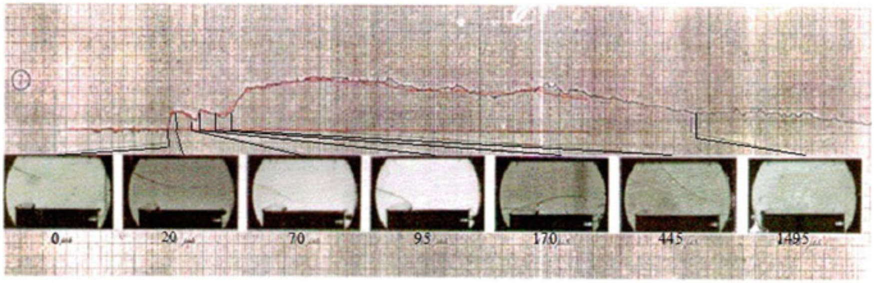

Vergleich der experimentellen und gerechneten Druckkurve
(rot) am Meßgeber 7 bei 28% Blockierung

Fig. 3 Experimental overpressure waveform compared with the numerical result on the downstream end of a rectangular block. The sequence of photos below the waveform shows the shock configuration at a number of times following the initial interaction

center of the leading surface of the block. The red curve shows the results of a two-dimensional hydrodynamic calculation conducted at the Ernst Mach Institute by Dr. Werner Heilig. From the photographs below the waveform, the shock configuration at a number of times is joined to the appropriate time in the waveform.

Starting at the far left, the photo sequence is as follows: The shock reaches the leading edge of the block, the shock has reflected from the front face of the block and continues over the upper surface. A vortex is just forming near the upper corner of the block. The overpressure drops from the reflected pressure to the stagnation pressure as the shock progresses over the block. The vortex is shed from the leading edge and trails the shock front near the upper surface. The shock reflected from the front surface travels upward and strikes the upper surface of the shock tube and reflects back to the block. The double shock arriving near a time of 600 µsec is the shock reflected from the roof of the shock tube and its reflection from the floor of the tube. The double shock arriving near a time of 1150 µsec is a second reflection from the tube surfaces. The numerical calculation (in red) is nearly an overlay of the experimental waveform.

In Fig. 3 the block is reversed in the shock tube so the pressure gauge is on the downstream end of the block. As in Fig. 2, the experimental waveform is plotted (in black) with the calculated waveform (in red). The pressure and time scales are the same as in Fig. 2. The time is measured relative to the arrival of the shock at the gauge in the center of the downstream end of the block. The first arrival is the shock that has turned the upper rear corner and traveled down the rear of the block. The second shock arrival is the reflection of the first shock from the floor of the shock tube. A vortex forms when the shock turns the upper corner (diffracts) and trails the leading shock. The reflection of the leading shock interacts with the vortex just as the shock reflected from the roof of the shock tube arrives at the gauge position. The overall effect of the vortex interaction is to diffuse the incoming shocks and produce a gradual rise in pressure (a compressive wave) at the back of the block. Note that the overpressure on the downstream end of the block remains below the free stream overpressure for the entire time of the experiment.

4 Shock Interaction with a Baffle System

In order to examine the behavior of shocks propagating through openings and interacting with vortices, a series of careful experiments were conducted at the Ernst Mach Institute in Freiburg, Germany. A Mach 1.31 shock was photographed as it propagated through a series of baffles. Dr. Heinz Reichenbach of EMI, graciously gave me a set of shadowgrams from these experiments when I visited his laboratory. These very detailed photographs were also used to evaluate the accuracy of first principles code calculations for this very complex flow.

Figure 4 is taken at a time of 117.3 μsec after the shock struck the first baffle. At this time the incident shock has just reached the second baffle. The shock is about to reflect from the side wall of the first "room". A pair of strong vortices have formed at the edges of the opening and propagated downstream. The shear velocity between the flow through the opening and the edge of the vortex induces Kelvin–Helmholtz instabilities which get wrapped into the vortices.

At a time of 174.3 μsec, (Fig. 5) the vortices have expanded and the incident shock has reached the center of the second "room". The side wall reflected shock in the first "room" has reached about half way to the opening in the first baffle. A pair of Mach shocks have formed near the opening in the first baffle. The vortices have grown and continue to entrain the increasingly K-H unstable gas. Secondary vortices are beginning to form along the shear layer in the vortex.

The weakened shock reaches the third baffle at a time of 234.3 μsec. (Fig. 6) A pair of vortices is shed from the second baffle. In the first room, the wall reflected

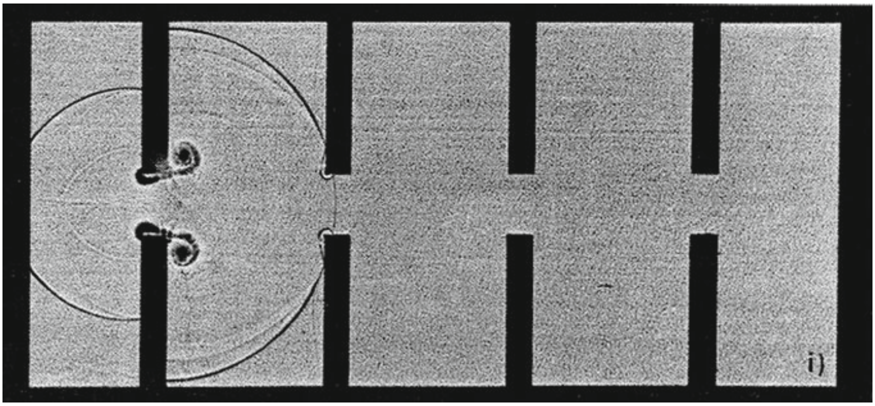

Fig. 4 Shock and vortex configuration at a time of 117.3 μsec after the shock arrived at the first baffle

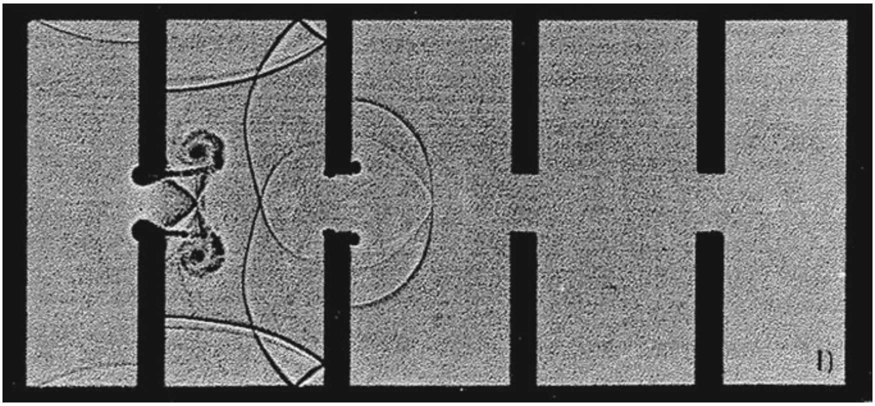

Fig. 5 Shock and vortex configuration at a time of 174.3 μsec after the shock arrived at the first baffle

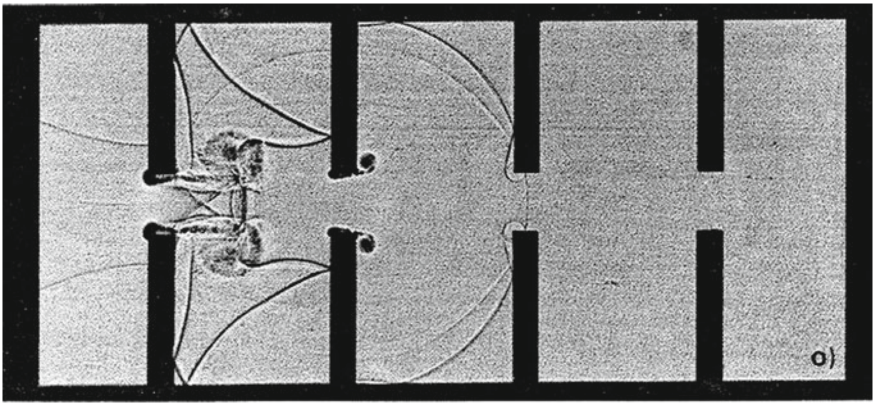

Fig. 6 Shock and vortex configuration at a time of 234.3 μsec after the shock arrived at the first baffle

shock has reached the vortex. The rotating vortex first displaces the shock front. The interaction of the shock with the K-H unstable gas diffuses the shock front and it becomes a compression wave within the vortex. Note how the shock front is curved by the rotational velocity of the vortex, prior to the shock front diffusing. The shock reflected from the second baffle has reflected from the downstream side of the first baffle. In the region of the first opening, this shock is diffused as it interacts with the K-H unstable gas.

By the time that the weakened shock has reached the fourth baffle (Fig. 7), the vortex from the second baffle opening has grown to nearly half the distance to the third baffle. Note that secondary vortices have been generated within the primary vortices. These secondary vortices are generated by shear velocities within the primary vortex.

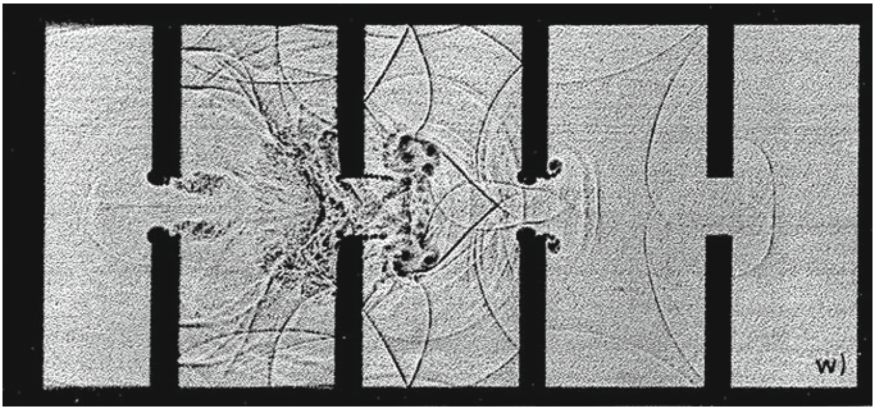

Fig. 7 Shock and vortex configuration at a time of 354.3 μsec after the shock arrived at the first baffle

The shock interactions with the vortices have diffused the shocks and perturbed the vortices. The vortices between the first and second baffle have degenerated into a region of instability, causing the shocks to diffuse as they continue to reverberate. Vortices have formed at both the leading and trailing sides of the third baffle. The vortices at the trailing edge have just started to be shed from the third baffle.

5 Blast Wave Formation

A blast wave is a category of shock waves in which the shock front parameters begin to decay immediately behind the shock front. Each of the blast wave parameters decays at a different rate and has a different positive duration. The overpressure and density fall below ambient values and the velocity changes sign at the end of the positive phase. Figure 8 is a cartoon of the behavior of a given parameter for a blast wave. In general, the decay behind the front is exponential.

Fig. 8 Cartoon of a blast wave parameter as a function of range at a fixed time

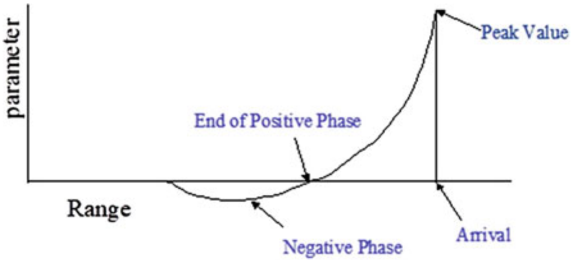

When a blast wave reflects from a structure, the reflected wave front moves into a region of lower and decaying pressure, density and velocity. The load on a structure caused by a blast wave is therefore very different from that of a square wave shock.

6 Blast Wave Interaction with a Realistic Structure

In the previous sections, the basic mechanisms for shock interaction with a structure have been demonstrated. These include: reflection, diffraction, vortex formation and vortex shedding. The mechanisms for a blast wave interaction are similar, with the addition of the effects of the decay and the negative phase. The rate of decay behind the shock front in a blast wave is directly related to the rate of decay of the shock front parameters as a function of distance. For example, the shock front overpressure in a blast wave which has a small positive phase duration will decay more rapidly than for a blast wave with a longer positive phase. When blast waves load a structure, the size of the structure relative to the positive phase of the blast wave must be considered.

The positive duration for a one kilogram explosive charge will have only 10% of the duration for a 1000 kg charge of the same explosive at the same pressure level. The induced loads on a structure cannot be considered uniform because the peak values change as they traverse the structure. As an example, a 1 kg charge of TNT detonated 2 m from a plane surface will generate a blast wave with an incident overpressure of ~ 200 kPa (29 PSI) at the nearest point (Fig. 9). However, at a point 3 m from that point in the plane (3.6 m from the charge), the peak incident overpressure is reduced to ~ 50 kPa (7.25 PSI). This factor of 4 reduction in incident overpressure leads to a reduction in reflected pressure of a factor of 5.5 in only a 20% increase in distance from the charge.

Structure response is a function of a combination of peak overpressure and impulse. Following a blast wave striking the front wall of a building, three effects are seen that impact the loads on the building. First, the peak overpressure jumps from the incident to the reflected value. Second, a vortex forms at each edge of the wall (top and sides). Third, a rarefaction wave is initiated at each edge and travels, at the local sound speed, toward the center of the wall. If there are openings in the wall, a vortex will form at each edge of the opening and a rarefaction wave will also be initiated.

The vortex has two effects on the loads. The rotational flow enhances the dynamic pressure parallel to the side walls and roof while lowering the overpressure in the region of the vortex. Also, the vortex overpressure is lower than in the blast wave and can be below ambient, thus causing the internal pressure to load the side walls outward and the roof upward.

The rarefaction wave(s) changes the impulse load on the wall. Points near an edge of the wall see a sudden reduction in the pressure load, whereas points further from the edge are exposed to higher overpressure for a greater duration and thus greater impulse.

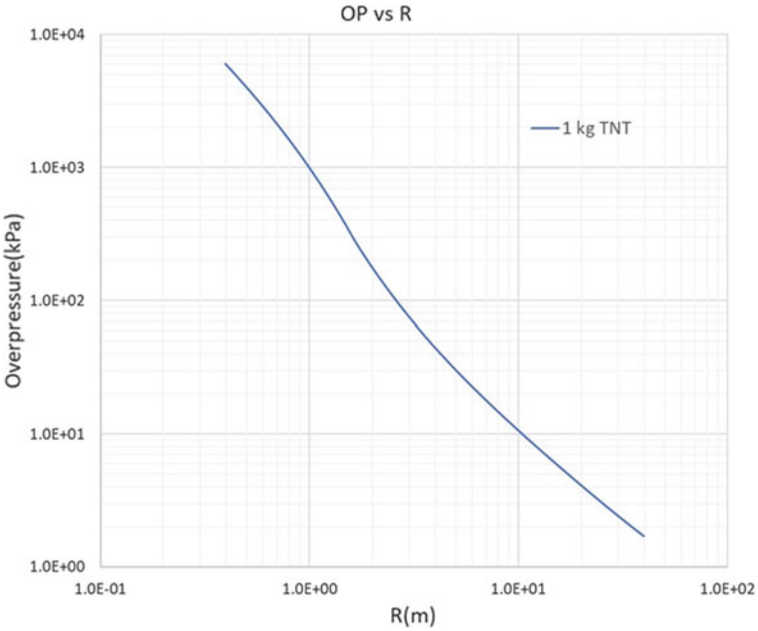

Fig. 9 Overpressure as a function of radius for a spherical 1 kg TNT charge

To illustrate these effects, refer to the results of a high-fidelity three-dimensional hydrodynamic calculation of the structure loads on a four-story building resulting from a ground level detonation 7.6 m in front of the building. Each story is approximately 3 m in height. Figure 10 is an interior view of one half of the building at a time of 12 ms. following the detonation and the incident shock has not yet reached the top outer corner of the front face of the building. In this figure, red indicates a low pressure with yellow, green, blue and violet indicating higher pressure levels. On the ground floor, the blast wave has entered the windows and loaded the ceiling about half way through the building. The vortices have reduced the pressure near the window openings.

On the second floor the shock front has reached about one third of the way through the building. The enhanced pressure on the ceiling of the ground floor results in an upward force with no counterforce from above. The same loading sequence, to a lesser degree, is seen on the second and third floors. Most buildings are not designed to take upward loading on the floor, consequently (in the experiment), the blast first lifted the floor, then slammed it downward breaking the supports and collapsing the floor.

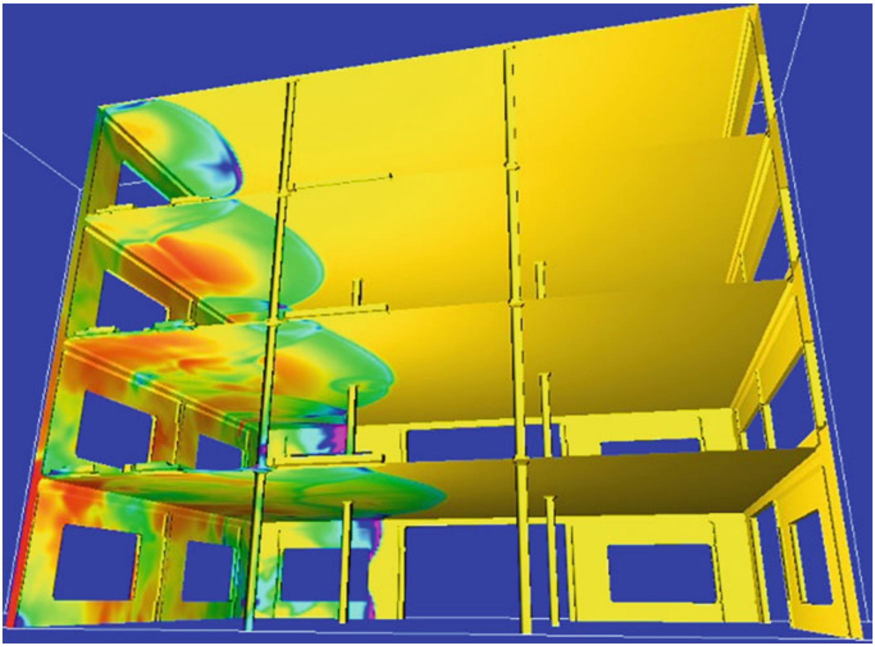

Fig. 10 Overpressure distribution on a 4 story building at a time of 12 ms. after a detonation at ground level 7.6 m in front of the left wall. Only one half of the building is shown. Red indicates low pressure with increasing pressure shown in yellow, green, blue and violet

7 Finite Duration Effects

In addition to limiting the overpressure impulse, the finite duration of a blast wave produces some interesting structural responses. Remember that overpressure is a scalar, i.e., it acts equally in all directions. This means that when a blast wave strikes a structure, the acceleration of the air and the structure are dependent on their areal density. For example, when a blast wave strikes a glass window, the glass density is approximately 2000 times that of the air. The air is accelerated away from the point of reflection at 2000 times that of the glass. Thus, by the time the glass has moved 1 cm., the blast wave is more than 20 m away.

In an experiment with a building and a charge similar to that shown in Fig. 10, some of the windows were glazed rather than open. The glass windows were approximately 6 mm thick and were loaded by a 3 bar blast wave. The glass was immediately shattered by the blast wave and accelerated into the interior of the structure. By the time the glass had moved a few centimeters, the negative phase had arrived and the glass fragments were pulled out of the building and landed on the ground in front of the loaded wall.

8 Effect of Structure Response

In another experiment, the British government built a scaled version of the buildings in a downtown major city. The buildings were made of concrete and were heavily instrumented with pressure gauges. They were subjected to a blast wave with the scaled equivalent of a nuclear detonation. When the experimental results were presented, the experiment was severely criticized because, it was thought, the building response and corresponding loss of energy would have reduced the severity of the blast as it progressed through the city. The experiment was, therefore, not realistic.

The experiment was repeated, but this time the buildings were constructed of light metal frames and mirror glass. The same instrumentation was placed on all buildings and they were subjected to the same blast level as for the concrete structures. Figure 11 is a comparison of the gauge records from four different buildings within the model city. The red curves are from the concrete city and the blue curves are from the mirror glass city.

The conclusion after examining all the records was that there was no discernable difference in arrival time as the blast wave progressed through the city; which means there was no discernable change in the shock front overpressure or the positive duration. The waveforms were within experimental variations. When the impulses were compared, the mirror glass impulses had the same number of measurements

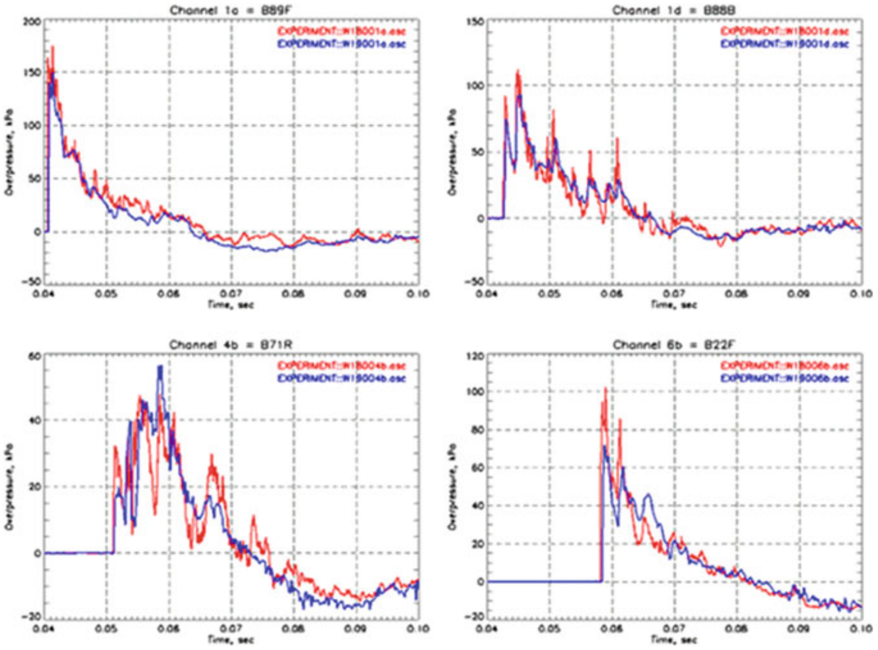

Fig. 11 Pressure waveform comparisons for concrete and mirror glass structures

greater than the concrete experiment as there were below the concrete results and the variations were only several percent.

The overall conclusion from the British experiments was that the structure response occurred so late in time after the blast wave struck that it had no discernable effect. This also demonstrates that, although all the glass was pulverized, (with the exception of 2 small panes) the energy needed to cause the damage was a very small fraction of the blast wave energy.

An experiment with a similar theme was conducted in the Ernst Mach Institute shock tube. A two-dimensional model of a house with a pitched roof and a window opening was constructed out of steel. The model was subjected to a shock with a Mach number ~ 1.4. The shadowgrams, taken at a sequence of times, clearly showed the interaction of the shock wave with the structure. Again, the results were criticized because the structure was non-responding.

A new model with the same dimensions was constructed out of Balsa wood and loaded with the same shock level. Much to the surprise of the experimenters, there was no discernable difference between the shadowgrams from the two experiments. During the entire time of the structure load, the Balsa wood model had no measurable motion.

The explanation is that the density of the Balsa wood is nearly three orders of magnitude greater than that of the air in the shock. The shock waves moved a meter in the same time that the Balsa model moved a millimeter.

With this experimental evidence, most "structures" can be treated as non-responding during the entire time of the blast wave interaction. Numerical calculations with the assumption of non-responding structures provide highly accurate structure loads.

9 A Complex Structure Load Example

In the previous sections, the loads on two-dimensional and three-dimensional structures have been demonstrated. The same phenomena occur when the structures become more complex. The incident shock is reflected from the upstream side of the structure, vortices form and rarefaction waves advance at the local speed of sound from every edge. The shock is diffracted around corners and reduced pressures are observed on the downstream regions of the structure. Mach reflections occur at the appropriate angles and the peak overpressure rises accordingly. The following is an example of the shock interaction with a very complex set of structures.

A military vehicle carrying 5 personnel, struck a buried mine with its right front tire. Applied Research Associates was contracted by the United States government to make detailed calculations of the blast loading on the vehicle and on the personnel in and on the vehicle. The results of the loads on personnel were to be corelated with their injuries. All personnel survived the explosion and were able to describe their positions in the vehicle at the time of the detonation. A finely zoned three-dimensional hydrodynamic calculation was conducted which included the vehicle (with the right front door partially open, it was hot that day) and the personnel in their positions.

The numerical method used in the example of Figs. 2 and 3 has been shown to be capable of accurately defining the pressure loads on structures and was employed for this situation. Figure 12 shows the outline of the vehicle which was modeled in detail from digital design drawings. Personnel were then located in their positions in and on the vehicle. The vehicle and its occupants were treated as non-responding. In the calculation, several thousand numerical gauges monitored the overpressure loads as a function of time on the surfaces of the vehicle and the personnel. Figure 12 highlights the maximum overpressure loads on the personnel. The vehicle is made nearly transparent to make the occupants more visible.

Details, such as the passenger door was partially open and the passenger's foot was outside the cabin at the time of the detonation, were included in the calculation. That foot received a load of more than 3 bars. The back of the passenger on the right side of the rear of the vehicle received more than 2 bars overpressure on his back while the passenger on the left side of the rear of the vehicle received only about half a bar. The two interior passengers, away from the open door, received less than a half bar.

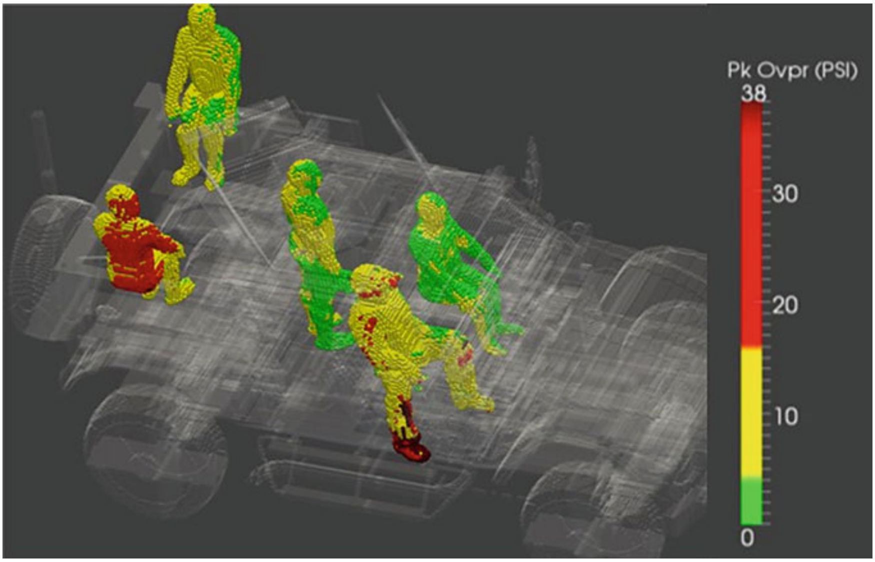

Fig. 12 Pressure loading on a complex target

10 Summary

Examples of shock interactions with structures have been given. Structures ranged from a flat plane to a rectangular block to multiple planes with openings (a system of baffles). A building, consisting of a number of planes with openings demonstrated the complexity of the interaction of a blast wave with a realistic structure.

The treatment of most structures as non-responding has been justified through comparisons between experiments and numerical calculations. The shock geometry generated by the interaction with a structure is insignificantly different whether the structure is made of concrete, steel, mirror glass or Balsa wood.

Vortices are formed when a shock wave encounters the edge of a structure or an opening in a structure. The vortex is characterized by a rotational velocity and an unstable slip stream. The shear velocities and the density gradients across the slip stream induce Kelvin Helmholtz instabilities which take the form of smaller vortices within the primary vortex. These ever-decreasing sized vortices have the effect of converting kinetic energy into internal energy (pressure). The effect of these vortices on shock waves is first to deflect them in the rotating velocity field and diffuse them as they pass through the instabilities.

Modern hydrodynamic codes and high performance computer systems provide the means of accurately representing the loads resulting from shock (or blast) waves interacting with simple and/or very complex structures.

Experimental Study of Generation and Mitigation of Weak Shock Waves Induced in Intake and Exhaust Pipe Lines of Automobile Engines

Noriaki Sekine

1 Introduction

In the advent of the widespread of hybrid automobiles, it would be worthwhile to review the generation of exhaust pipe line noises of automobile engines and their reduction. It is emphasized that exhaust gases released from the engine cylinders propagating along exhaust gas pipe lines eventually coalesced into weak shock waves and hence the mitigation of exhaust gas noises is discussed based, in principle, on compressive gas dynamic. Therefore, this chapter, so far as the author knows, would contribute to the research frontier of one of successful industrial applications of the shock wave research [1–5, 7–10].

Firstly, for the sake of readers, it is explained that the exhaust gas pipe line with particular combination of engine throttle angles, high pressure exhaust gases coalesced into weak shock waves in propagating along the exhaust gas pipe line and eventually became trains of unpleasant noises. Secondly in order to efficiently mitigate unpleasant exhaust gas noise using silences and mufflers, it is demonstrated that conventional approaches of shock wave dynamics are useful. Lastly weak shock waves appear even in turbocharger air induction systems.

N. Sekine (✉)
SUBARU TECHNO Co Ltd, Gunma, Ota, Japan
e-mail: sekine.noriaki@stc.subaru.co.jp

© The Author(s), under exclusive license to Springer Nature Switzerland AG 2022

K. Takayama and O. Igra (eds.), *Frontiers of Shock Wave Research*,
https://doi.org/10.1007/978-3-030-90735-8_11

2 Presence of the Shock Waves in Exhaust Gas Pipe Lines [1–3]

Characteristics of Unpleasant Noises in Exhaust Gas Pipe Lines

Recently drivers prefer to drive high performance automobiles having high power and hence low back pressure exhaust systems. At high speed running of these engines, we hear loud jarring noises. These unpleasant noises are generated at full load and free load firings and mortaring with the throttle angle at idling state. The unpleasant noises are not observed in systems equipped with turbochargers.

Figure 1 shows measured sound levels in the ordinate (unite in 10 dB) by varying the engine speed in the abscissa (1000 rpm). Dashed line designates noise levels and increases with the engine speed, whereas a solid line designates randomly increasing unpleasant exhaust sound levels.

Applying the frequency transformation to the measured results in Fig. 1, Fig. 2 shows the power spectrum of the pressure levels in the ordinate (unite in 10 dB) against the sound frequency in the abscissa (in kHz). Dashed and solid lines designate the pleasant and unpleasant sound levels cases in Fig. 1, respectively. For noise

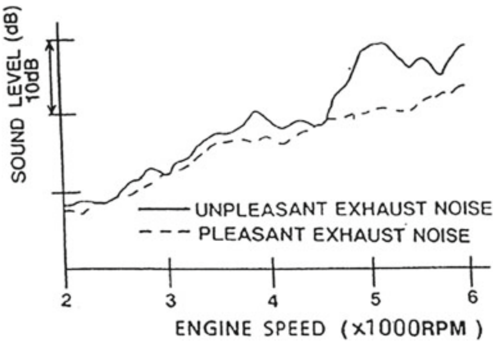

Fig. 1 Sound level of unpleasant exhaust noise

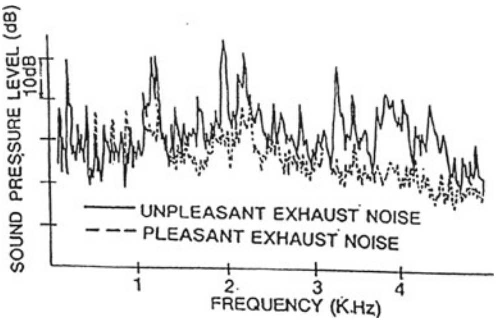

Fig. 2 Spectrum of unpleasant exhaust noise

frequency under 1 kHz, the noise levels of pleasant and unpleasant noise levels are nearly identical but over 1 kHz, unpleasant noise level is consistently higher.

Pressure Measurements

We installed pressure transducers, Kistler Model 6001, along exhaust gas pipe line systems connected to a water cooled 4-cycle 0.55-L gasoline engine and installed exhaust gas pressures. Figure 3 shows the engine and the exhaust gas pipe line system. The test conditions are both full load and free load firing conditions and with motoring with wide open throttle. Simultaneously we measured exhaust noises in monitoring engine rotational speed.

Figure 4 shows pressure variations measured at the engine (1), along the exhaust pipe positioned at (2), (3), and (4), and at the exit of the muffler (5) in the presence and the absence of unpleasant noises. The ordinates show pressures in display of 500 kPa scale positioned at (1), in display of 50 kPa scale at (2) and (3), in the display of 20 kPa scale at (4), and in the display of 5 kPa scale in (5). The measurement at the (5) was performed using a microphone positioned at 45° oblique position. The abscissa shows time sequence in 5 ms scale. The upper parts of the individual pressure display show the pressure variations monitoring with the idling throttle angle, in which the unpleasant noise is generated. The lower parts show the pressure variations motoring wide a throttle in which the unpleasant noise is not generated. The trains of high pressures released from the engine cylinder (1) attenuate quickly with propagation but the pressure profile at the peak is steepened with the propagation.

We then repeated the measurement with the identical condition with one conducted in the upper part of Fig. 4 but removing the muffler. The pressure was measured at the position of (5) facing 45° obliquely to the exhaust pipe. It is immediately noticed that the pressure profile measured at (5) had repetition of discontinuously steep rise, which indicates the presence of shock waves (Fig. 5).

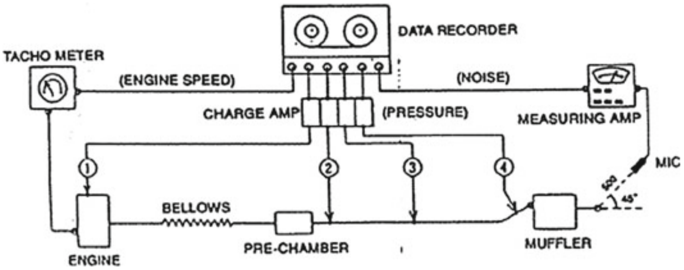

Fig. 3 Measurement set up of engine exhaust pressure and noise

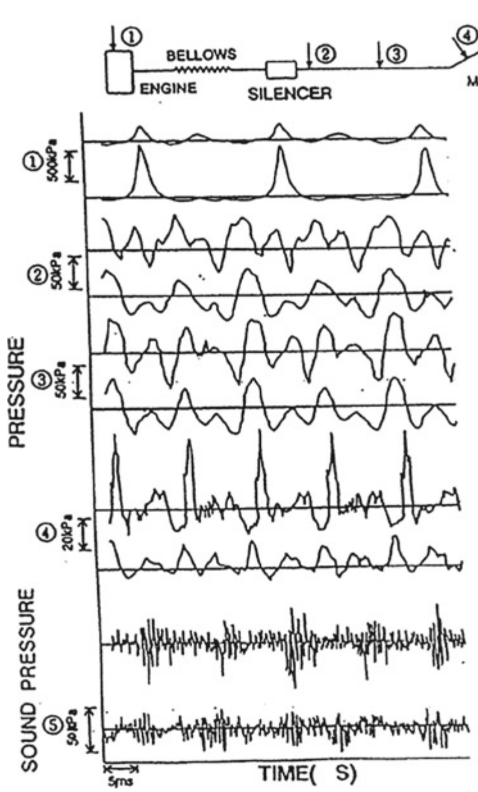

Fig. 4 Pressure variations in the exhaust system

Optical Flow Visualization

It would be straightforward if the coalescence of high-pressure exhaust gas into weak shock wave. We then performed an analogue experiments applying double exposure holographic interferometry [1–5] and a high speed imaging using an Ima-Com high-speed camera (Model 675, John Hadland, Co Ltd.) [6].

We conducted an analogue experiment firing a commercial water cooled 4-cycle 0.55-L gasoline engine connecting it to a 30 mm i.d. straight exhaust gas pipe line system shown in Fig. 6. The pipe line was connected to a two-dimensional test section having a 30 × 40 mm entry section and a 90 × 140 mm observation section, which was installed in a 30 mm wide × 300 mm i.d. circular test section. Figure 6 also shows a double exposure holographic interferometric optical arrangement in the Institute of Fluid Science, Tohoku University [1–3]. The source light was a double pulse holographic ruby laser and was split into an object beam OB and a reference beam RB. The optical arrangement of the OB was identical with that of conventional shadowgraph. The light path lengths of both OB and RB were set identical with each other and the RB was superimposed on a holo-film.

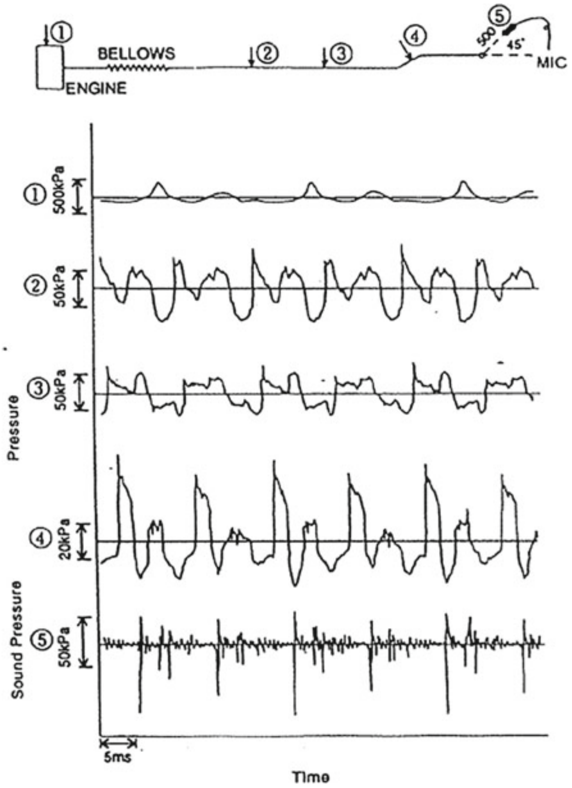

Fig. 5 Pressure variations in the straight pipe

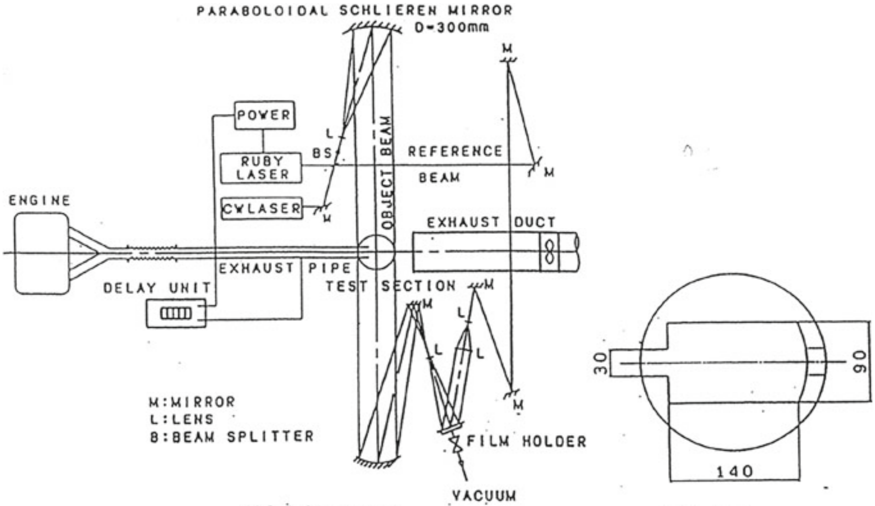

(a) Optical Arrangement (b) Test Section

Fig. 6 Optical arrangement of flow visualization

The prototype engine was operated at 5,500 rpm. The combustion product gases had high-pressure and high-temperature, presumably at 330–340 K, released into the straight tube. Hence the exhaust gas eventually built up weak shock wave while propagating in the test section as already observed in Fig. 5.

The source light was exposed, for the first time, at a no flow condition and was synchronized, for the second time, with the engine operation. The phase change so far generated in the flow field formed density contours as fringe distributions.

Streak Recording

We replaced the light source with a continuous Nd:YAG laser and recorded shadowgraph images viewed through a 1 mm wide slit positioned along the center line of the test section by ImaCom high speed camera. Thus, the sequentially arranged slit images were recorded.

Figure 7a, b show the result and its sketch, respectively. The abscissa shows the distance of 30.6 cm between two markers and the ordinate shows time sequence in msec. In Fig. 7b, oblique lines visible on the right-hand side shows compression

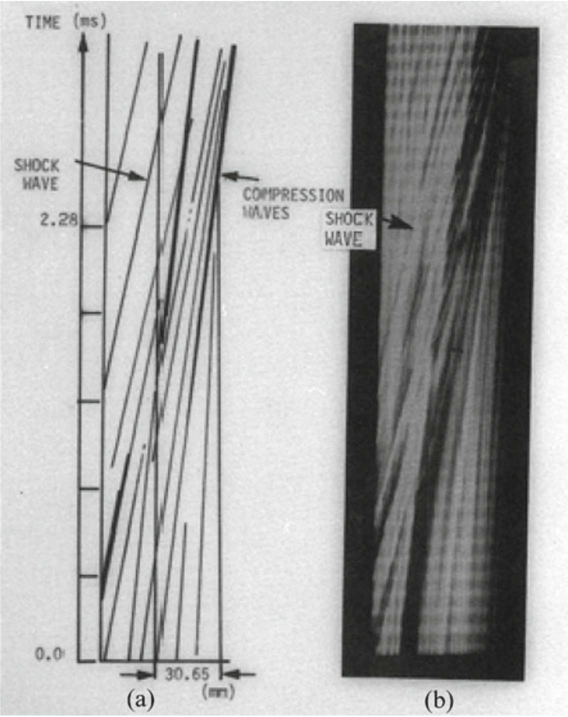

(a) (b)

Fig. 7 The presence of shock waves in exhaust gases

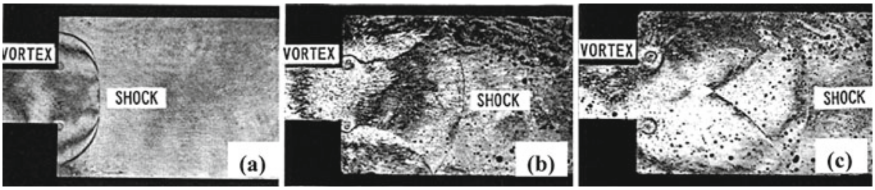

Fig. 8 Sequential interferograms. Weak shock generation from engine exhaust gas

waves running at sonic speed coalescing, with time sequence, into a train of weak shock waves. Lines with steeper angles show the trajectories of flying debris.

Sequential Observations of Weak Shock Waves in the Test Section

Figure 8a, b and c shows sequential observation of a weak shock wave generated running the 0.55-L engine shown in Fig. 6. The engine was running at 6,800 rpm, 5.900 rpm, and 6,500 rpm, respectively.

The ratio of specific heats γ of the mixture of combustion product gas, water vapor, and air was estimated to be $\gamma = 1.35$. The shock Mach number Ms, so far estimated was Ms = 1.1. The engine running in these speed ranges could reproduce wave interaction inside a confined space. and the debris and water vapor deposited on the wall hardly affected the wave motions. In analogue experiments the engine speeds were slightly scattering. These results simulate the characteristics of propagation and mitigation of weak shock waves propagating inside silencers and mufflers.

Numerical Simulation

In order to study the interaction of weak shock waves with confined structures, the numerical prediction is useful. We numerically solved two-dimensional Euler Equations for Ms = 1.1 using a in house code made at the Institute of Fluid Science the structure of which was based on the TVD scheme [11].

The exhaust gas contains water vapor droplets and debris, so that it is, exactly speaking, a two-phase gas mixture. Although specific heats ratio of the exhaust gas mixture was so far estimated in this series of experiments $\gamma = 1.35$ and the gas temperature was about 330–340 K, in the present numerical simulation, the gas mixture is a diatomic gas of $\gamma = 1.40$ at 300 K.

Visualized results are compared with corresponding numerical results in Fig. 9a–h. Figure 9a shows an earlier stage of the shock wave diffracting at the entry corners. In the visualized results, water droplets and wet debris sticking on the sidewalls were

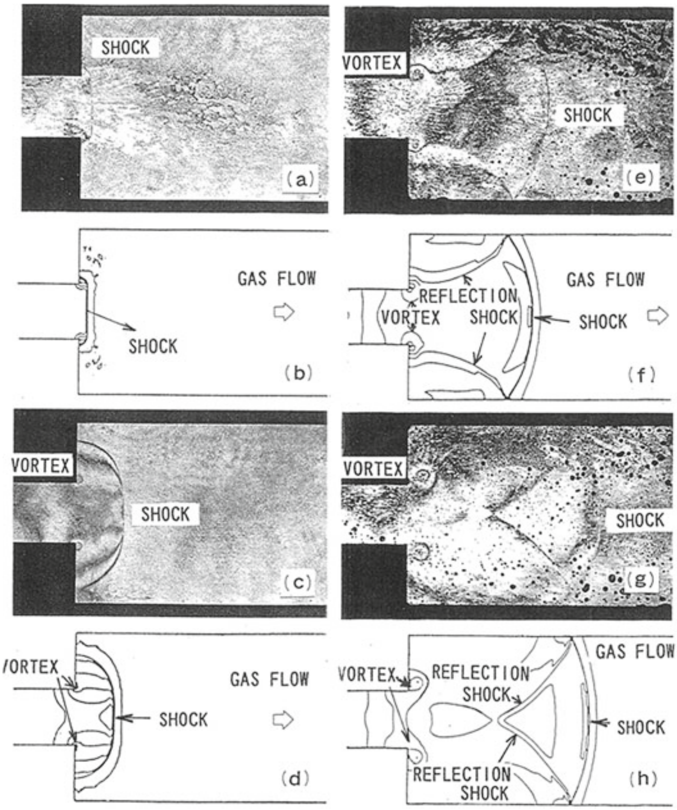

Fig. 9 Comparison between visualizations and numerical results

observed on the side walls, but these contaminations would not disturb the wave motion. Figure 9b shows the simulated density contour. The shock wave is so weak that distinct fringes are not observed.

In the elapse of time in Fig. 9c, d, the transmitting shock wave was diffracted and attenuated with its propagation. In Fig. 9e, f, the transmitting shock wave is reflected successively from the upper and lower walls. Their interactions promote their attenuation. It would be concluded that such interactions are fundamental mechanism of mitigating waves inside silencers and mufflers. As seen in Figs. 8 and 9, the waves so far observed are not acoustic waves but weak shock waves. The waves reflected from the upper and lower walls mutually interacted with each other and promoted their mitigation. Lastly in Fig. 9g, h, the distribution of visualized fringes and the simulated fringes agree fairly well, which implies that the present simulation, although it is based on the Euler Solver and assumed a diatomic gas, give finer information of wave mitigation in the exhaust gas pipe line systems more accurately than the conventional linear acoustic theory.

3 Characteristics of Weak Shock Waves in Silencers

Analogue Experiments of Weak Shock Waves in Smooth Wall Silencers

Figures 10 and 11 show experimental setups of analogue experiments. In order to generate weak shock waves and to observe their interaction with a model silencer, we used a shock tube equipped with a mode; silence. Figure 10 shows a shock tube: a 150 mm i.d. and 1550 mm long high- pressure chamber and a 60 × 150 mm cross section and 5560 mm long low-pressure channel. The test gas is air at ambient condition. Rupturing a Myler diaphragm at high pressurized nitrogen at 131 kPa, we obtained consistently shock waves of about Ms = 1.1–1.2. Using the double exposure holographic interferometer, we visualized sequentially weak shock wave propagation in this analogue silence.

We used two pressure transducers (Kistler Model 603 B): the first one was installed at the 400 mm interval as shown in and at 225 mm ahead of the entrance of the analogue silencer and the second one was installed at 285 mm from the exit of the silencer as shown in Fig. 11.

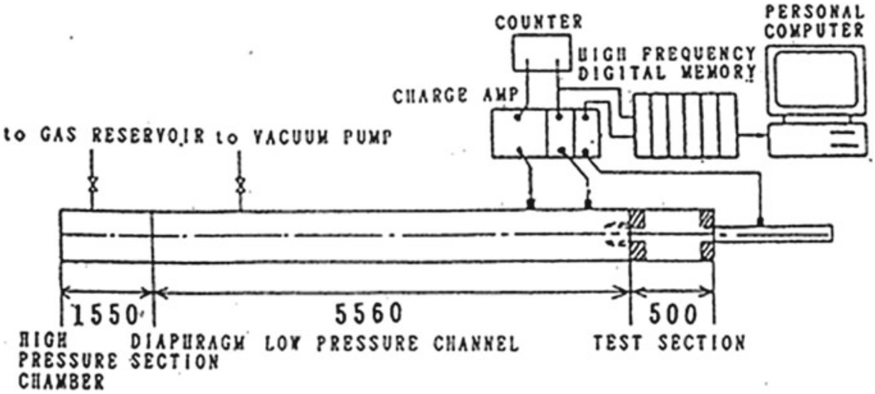

Fig. 10 The shock tube and analogical silencer

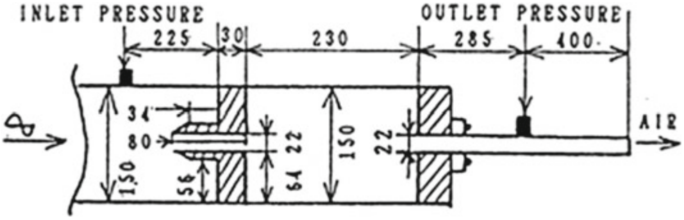

Fig. 11 Analogical silencer

An analogue silencer has flat upper and lower walls having 500 mm long and is long enough to accommodate a baffle plate, which enabled to form convert a double chamber silencer. The end wall has a high 22 mm exit which is the same size as the prototype exhaust pipe line.

Figure 12a–d, show sequential observations for Ms = 1.16; Fig. 12a was taken at the elapsed time of 370 μs after the shock wave arrival at the trigger position, Fig. 13b at 550 μs, Fig. 13c at 650 μs, and Fig. 13d at 800 μs.

The weak shock wave is diffracting at the entry corner and attenuate in Fig. 12a. The transmitting shock wave was reflected from the upper and lower walls as seen in Fig. 12b, c. Twin vortices appear at the upper and lower entrance corners, developing in the elapse of time.

The diffracting shock wave is reflected from the upper and lower walls. The reflected shock waves transit from regular to Mach reflections depending on the intersection angle with the wall. The transition procedure of the reflected shock wave also promotes the attenuation.

In Fig. 12d, upon arrival at the end wall of the silencer, the transmitting shock wave was reflected from the end wall. Then, the transmitting shock wave interacts with the resulting reflected shock wave forming a complex wave interaction, which,

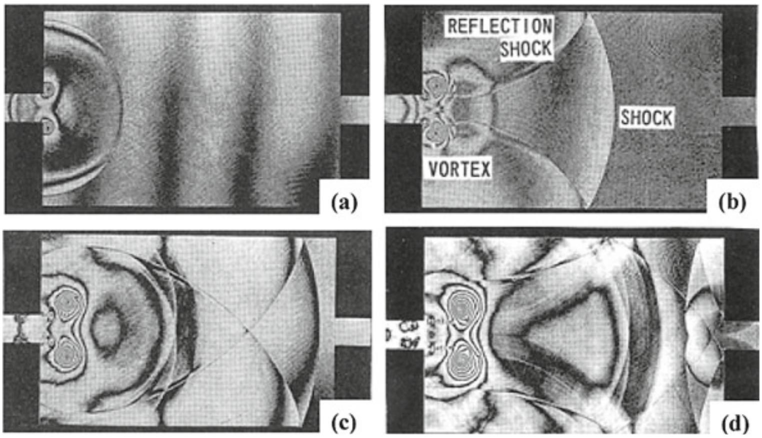

Fig. 12 A single-chamber silencer: weak shock waves propagating at Ms = 1.16 in air

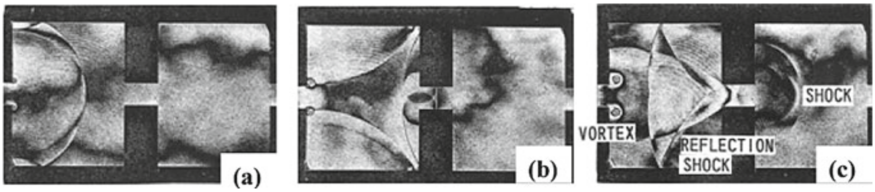

Fig. 13 Double-chamber type: weak shock waves propagation, at Ms = 1.13 in air

in short, progressively mitigate waves promoting to suppress exhaust gas noises in a silencer.

We inserted a baffle plate in the middle of the analogue silence forming a double chamber silencer. Figure 13a–c show sequential observations of the mitigation of Ms = 1.13 shock wave propagating along the double chamber silencer. Figure 13a was taken at the elapsed time of 500 μs after the shock wave arrival at the trigger position, Fig. 13b 600 μs, Fig. 13c 750 μs. If comparing the transmitting shock wave in Fig. 13c with that in Fig. 12c, we can readily speculate that the double chamber efficiently attenuates the waves in the single chamber silencer.

Analogue Experiments of Weak Shock Waves in a Roughened Wall Silencer

An analogue silencer with smooth walls can mitigate weak shock wave mitigation by means of wave interaction. Then we will examine the effect of wall conditions. Figure 14a–d show sequential interferograms of Ms = 1.41 shock wave propagating inside an analogue silencer with a roughened wall surface.

We roughened the upper and lower walls of the smooth wall silencer. The roughness comprises of 1.0 mm thick and 3.0 mm wide and 7.0 mm long steel plates separated 1.5 mm interval as seen in Fig. 14a–d, which is, in short, a wall with equally-spaced arrayed grooves.

The sequential observations are performed in Fig. 14a at the elapsed time of 600 μs after the shock wave arrival at the trigger position, in Fig. 14b at 740 μs, in Fig. 14c at 880 μs, and in Fig. 14d at 950 μs.

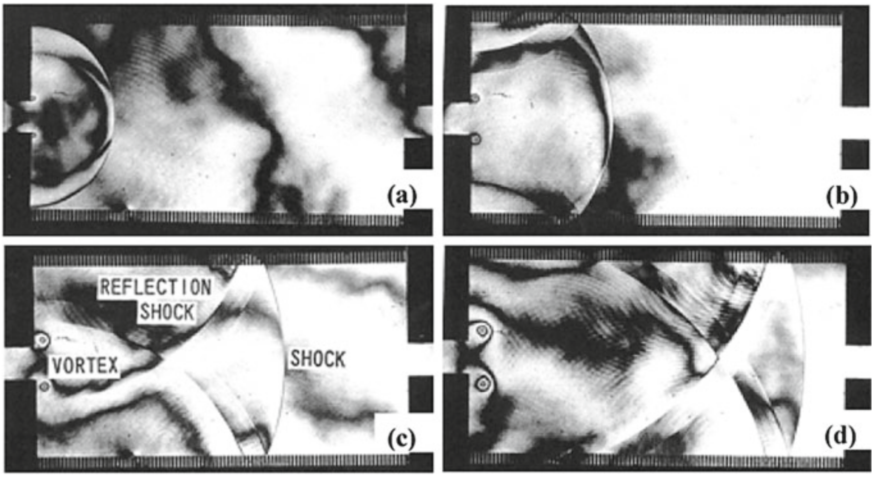

Fig. 14 Mitigation of weak shock waves in a silencer of roughened surface

In propagating along the roughened wall, the foot of transmitting shock wave is partially reflected from the 1.0 mm wide solid wall and is diffracted at the 1.5 mm wide opening. Such a reflection and a resulting expansion wave were very faintly observed in Fig. 14. The interaction of these wavelets effectively contributes to the mitigation of the weak shock wave suppressing the exhaust gas noise.

Encouraged by these observations, we will discuss to optimize the shape of silencers and mufflers based on shock tube analogy.

Characteristics of Silencer Shape

We measured the resulting pressures at the exit in the system shown in Fig. 11. Figure 15 summarizes results.

The silencer characteristic is evaluated in terms of the pressure loss, in other word, the pressure reduction rate and the pressure-frequency correlation. In this subsection, we will discuss these items from tests performed in various analogue silencers having different structures as shown in Fig. 15. The ordinates show pressure in 10 kPa, and the abscissa show elapsed time in msec. The types of analogue silencers are shown

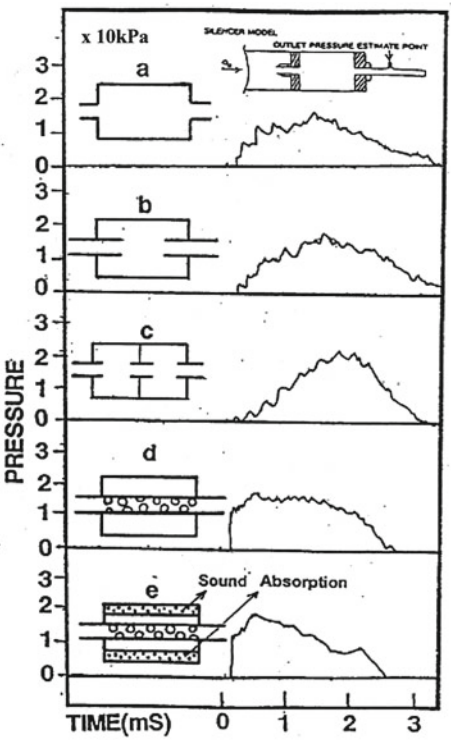

Fig. 15 Pressure variation of silence

as following: a single chamber silencer in the absence of exhaust pipe insertions at frontal and end walls, simple expansion type silence, in Fig. 15a; a single chamber in the presence of exhaust pipe insertions at the frontal and end walls in Fig. 15b; double chamber in the presence of exhaust pipe insertions in Fig. 15c: a single chamber with a straight through perforated exhaust pipe insertion, named a perforated resonator type, in Fig. 15d; and a single chamber with a similar resonator made of open cell aluminum sponge in Fig. 15e. Time variations of pressures measured by the second pressure transducer of these analogue silences are summarized in Fig. 15.

The double chamber silence shows the most favorable pressure loss in Fig. 15a, whereas the vales of peak pressures at the silencer exit is mitigated the most favorably in the double chamber silencer in Fig. 15b. The peak pressure variations are well reduced in perforated resonators in Fig. 15d, e and appear to be smoother than any other analogue simulators. The resonator composed of open cell aluminum sponge shown in Fig. 15e diminished the over pressure very well and after the elapsed time of 2.5 ms the exhaust gas noises were nearly suppressed. In Fig. 16, let's define R as the pressure reduction rate as a ratio of the outlet pressure Pm to the measure pressure Pr in front of the entry of the analogue silencer, as R = Pm/Pr.

Fig. 16 Definition of R (= Pm/Pr)

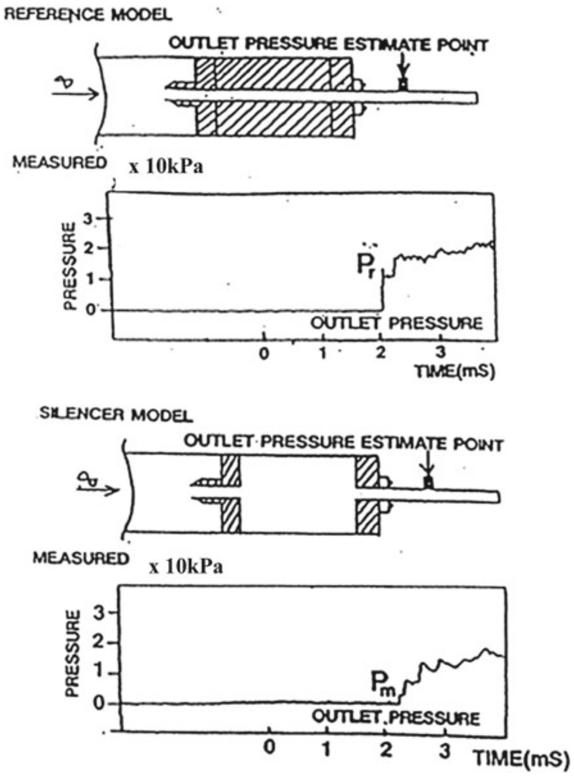

Let m and n be defined as the ratios of the silencer diameter D to the exhaust pipe diameter d and the silencer length L, m = D/d and n = D/L, respectively. In Fig. 17 the components of the double chamber silencer are sketched. The symbol a show a staggered distance of the exit pipe from the central axis. In Table 1 “a” denotes the staggered distance a = a/D.

Table 1 Shape factor of the silencer contribution from individual components to the pressure reduction R evaluated at the exit pipe in % and sketch of these silencer components Table 1 indicates that the contributions the individual influential components to the pressure reduction. The expansion ratio is the most influential and the chamber number is found to be secondary effective.

We then numerically discuss the contribution of n to R solving the two-dimensional Navire-Stokes Equations for Ms = 1.1 shock wave propagating along a straight tube connected to both single chambers connected to a muffler. Results are summarized in Figs. 18 and 19.

The pressure reduction rate A = Pw/Po is evaluated along the exhaust pile length of 1500 mm in front of the muffler. Pw and Po in Fig. 18a, b show the peak pressure

Fig. 17 Each factor symbol

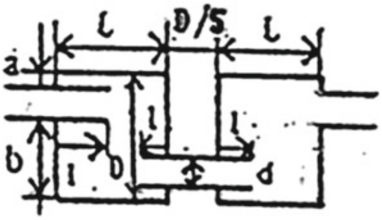

Table 1 Shape factor of silencer

Factor symbol	D/d (m)	Inserted (I)	Staggered (a)	Number of chamber
R%	76%	3%	5%	16%

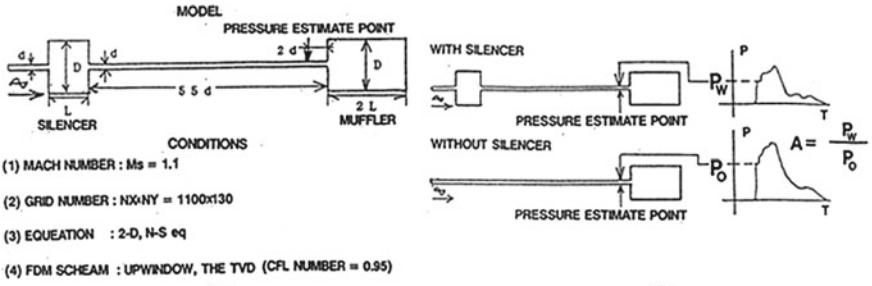

(a) (b)

Fig. 18 **a** Numerical model, **b** Definition of pressure reduction rate

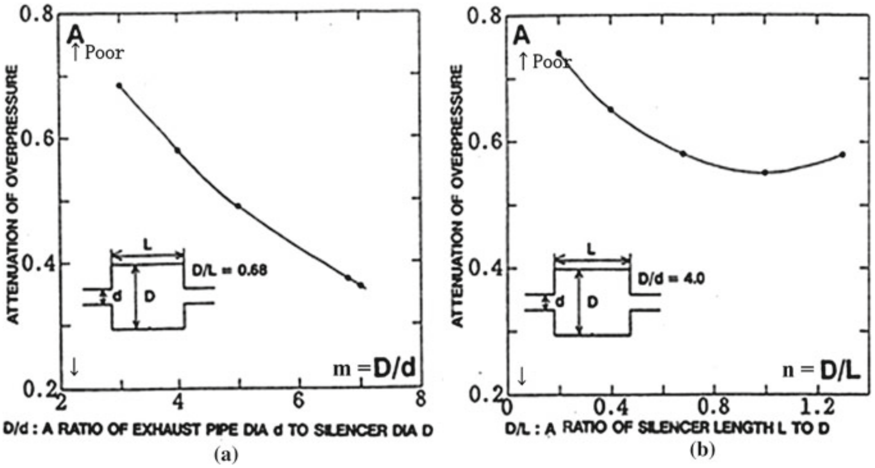

Fig. 19 (**a**), (**b**) Numerical results. **a** m **b** n

at the wave fronts measured in the presence of the silencer and in the absence of the silencer, respectively.

The pressure reduction rate A varies depending on the variation of m and n using the SUBARU prototype silencer for small car. In Fig. 19a, the ordinate denotes A and the abscissa denotes m where n = 0.68. In Fig. 19b, the ordinate denotes A and the abscissa denotes n, where m = 4.0. Data points are collected from the simulated results and solid curves designate the interpolated ones.

In Fig. 19a, the larger m is, the smaller the pressure reduction rate A becomes. In Fig. 19b the A is optimized at n is about 1.0. This implies that the silencer geometry can be optimized. It is noticed that we can hardly optimize the silencer geometry by trusting the existing acoustic approaches.

We applied the Fourier transformation to the time variation of pressure numerically obtained and evaluated the frequency correlation of exhaust gas noises. The results are summarized in Fig. 20 for four types of the silencers already shown in Fig. 15.

In Fig. 20a–d show the summary. The fourth case summarizes perforated tubes shown in Fig. 16d, e.

The ordinates denote the insertion loss in dB and the abscissa denotes frequency in Hz. Note that the ordinates denote the loss so that the plus sign indicates the increase of loss toward the negative direction.

Unpleasant exhaust noises are mostly caused by the presence of shock waves, which are suppressed typically in the frequency ranges between 1–3 kHz in the two chamber silencer seen in Fig. 20c. The insertion loss increases in the frequency range of 3–5 kHz and the loss in the frequency ranges between 1–3 kHz are presumably caused by flow induced noises.

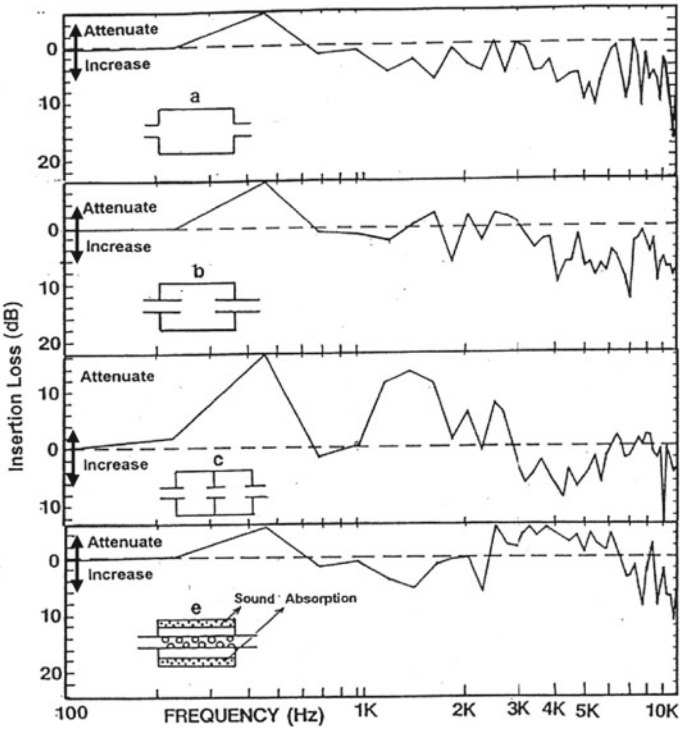

Fig. 20 Insertion loss of various silencers

4 Applications of Shock Wave Characteristic to Exhaust and Intake Systems

Application to a Prototype Engine for Small Cars [4, 5, 7, 9, 10]

Let's apply the previous results to exhaust and intake systems of a 0.66-litter prototype engine used for a small car. In Fig. 21a, b, a single chamber silencer and a double chamber silencer are shown, respectively.

In the first and second displays in Fig. 21a, the no-flow picture of a single chamber silencer and its simulated density contours for Ms = 1.5 are compared, respectively. The third display in Fig. 21a shows the simulated pressure variation. The ordinate of the third display shows the pressure measured at the position (1) of the first display normalized by the pressure measured at the position (2). The abscissa shows the elapsed time in μ-sec. The discontinuous pressure rise corresponds to the transmitting shock wave and its following reflections.

The results of a double chamber silencer are shown in the three displays shown in Fig. 21b: no-flow picture; numerical density contours; and time variation of measured

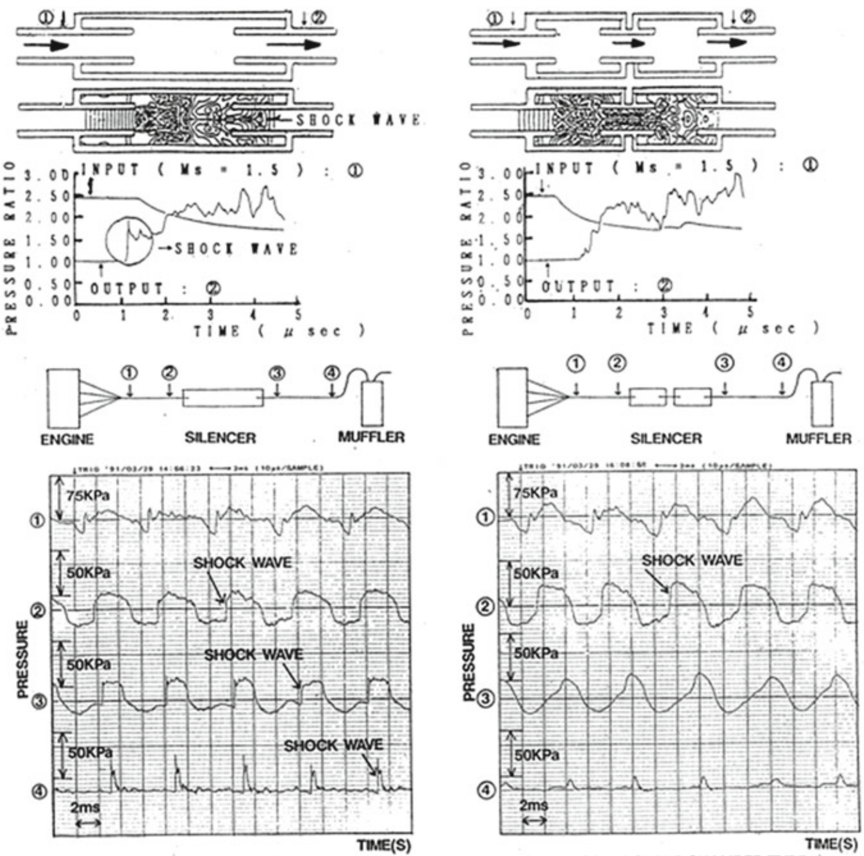

(a) A SINGLE CHAMBER TYPE

(b) A DOUBLE CHAMBER TYPE

Fig. 21 Characteristics of engine exhaust gas pipe line noise, **a** a single chamber silencer, **b** a double chamber silencer

pressures, respectively. In the third display of Fig. 21b, we can notice the transmitting shock wave is attenuated.

The fourth displays in Fig. 21a, b schematically explain the positions of pressure measurements along the exhaust gas pipe lines. The fifth displays show the variation of the measured pressures at the individual positions. The ordinates denote pressures in kPa and the abscissae denote time in second. Pressures measured in the position (4) in a single chamber in Fig. 21a silencer show discontinuous pressure rises appearing repeatedly. These indicated attenuated shock waves are sources unpleasant noises, whereas those in the double chamber as measured at (4) in Fig. 21b, the pressure profiles are no longer discontinuous, and their values are significantly reduced.

Hence, we convinced that the silencer structure decisively affects the mitigation of exhaust gas pipe line noises. Then the result was applied to the engine design for SUBARU small cars. We installed them to the commercial cars.

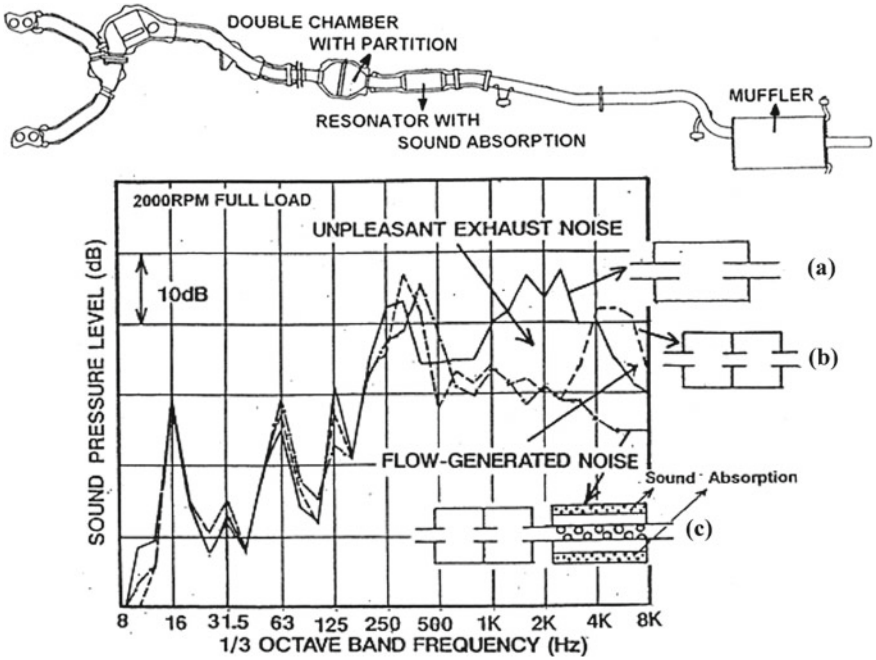

Fig. 22 Exhaust gas pipe line system installed in a prototype engine (upper) and the spectra of exhaust sound pressure levels for three types of silencer (lower)

Figure 22(upper) shows exhaust gas pipe line system installed in a water cooled 2.0-litter horizontal 4-cylinder, 4-cycle gasoline engine having multi-point-fuel-injection. The gas temperature measured at the exit of silencer was 500 K and noise was also measured there.

Figure 22(lower) shows spectra of sound pressure levels measured at the exit of silencer. The frequency band of the noise ranges from approximately 1/3octave band 1–4 kHz was observed for three silencer types; (a) a single chamber silencer with the inserted exhaust pipe; (b) a double chamber silencer with the inserted exhaust pipe; and (c) a combination of the double chamber silencer shown in (b) and the single chamber silencer with a pipe and silencer wall coated with sound absorption layer as shown in Fig. 20d. The ordinate denotes the sound pressure level in dB and the abscissa denotes 1/3 octave band frequency in Hz. Sounds of their level with 1/3 octave band frequency corresponds unpleasant noises induced by shock wave.

In Fig. 22(lower), it is readily seen that the type (a) silencer fails to suppress 1/3 octave band sound levels whereas the type (b) silencer suppresses them but promotes flow induced noises. However, the type (c) silencer reduces shock wave induced noises and flow induced noises as well. Hence the type (c) silencer has been successfully adopted in the design of practical exhaust gas pipe systems. SUBARU vehicles Model IMPRESSA 92MY, LEGACY 93MY, FORESTER 94MY have been equipped with these exhaust gas pipe systems.

Application to Passenger Cars Exhaust Pipe Line Systems [8–10]

Pressure Measurement

We tested a prototype water cooled 2.0-L horizonta1 4-cylinder, 4 cycle gasoline having multi-point-fuel-injection. Connecting it to an electrical dynamometer through a transmission, we measured the exhaust gas pressure in firing condition under full load at engine speed of 2,000 rpm. An exhaust pipe front (EPF) connected to a catalytic converter. Figure 23a, b show sketches of two prototype engines named 93MY-EPF (a) and 89MY-EPF (b), respectively. Figure 24a shows results of pressure measurements along the 93MY-EPF connected to the silencer in firing condition under full load at engine speed of 2,000 rpm. Figure 24b shows the position of the pressure measurement along EPF and the silencer using the pressure transducer of Kistler 603 B. The exhaust gas temperature at the exit of the muffler was 600 K.

Figure 24a shows time variations of pressures measured at individual ports from (1) to (7) shown in Fig. 24b. Ordinates denote pressure in kPa and the abscissa designate the elapse of time in sec. The arrow scale shows 5 ms. When the exhaust

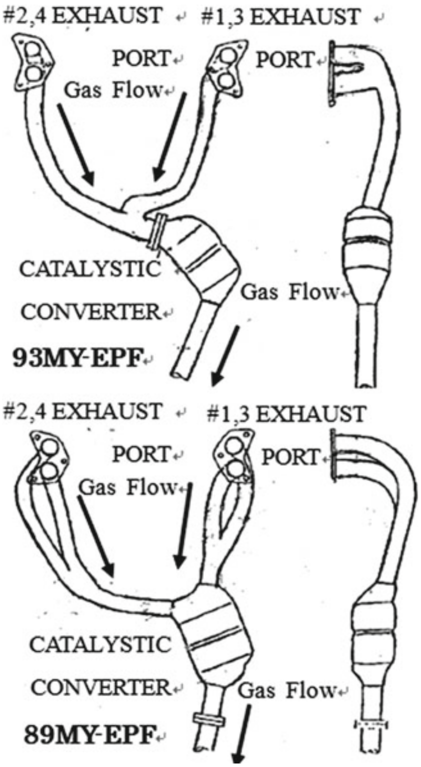

Fig. 23 94MY-EPF (**a**), 89MY-EPF(**b**)

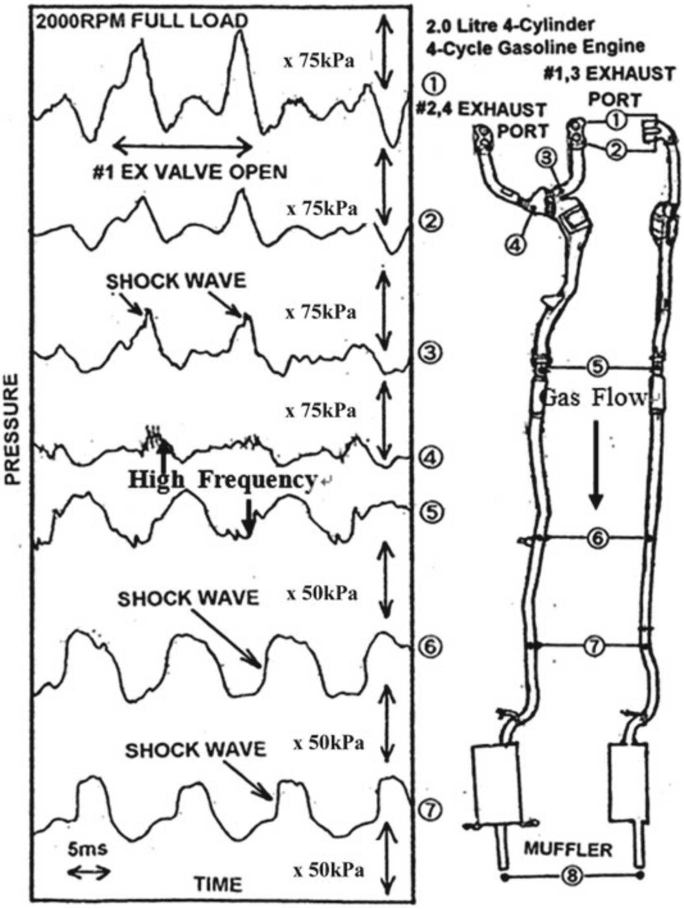

Fig. 24 Pressure measurement (**a**), 93MY-EPF system (**b**)

valve is open, we can observe high exhaust peak pressures in (1) and (2) which coalesce into shock wave as seen in (3).

Shock Tube Analogy of Shock Wave Propagation Inside the Exhaust Pipe Line Systems

In order to study the shock wave propagation in EPF, we visualized shock wave propagation along an EPF simulator by using double exposure holographic interferometry. Figure 25 shows the schematic diagram of the experiment. The test section has a 30 mm wide two-dimensional EPF shape sandwiched with acrylic plates. Oblique and horizontal 280 mm long and a 30 × 30 mm cross sectional exhaust ports are connected to the test section as seen in Fig. 25. To simulate the high-pressure exhaust

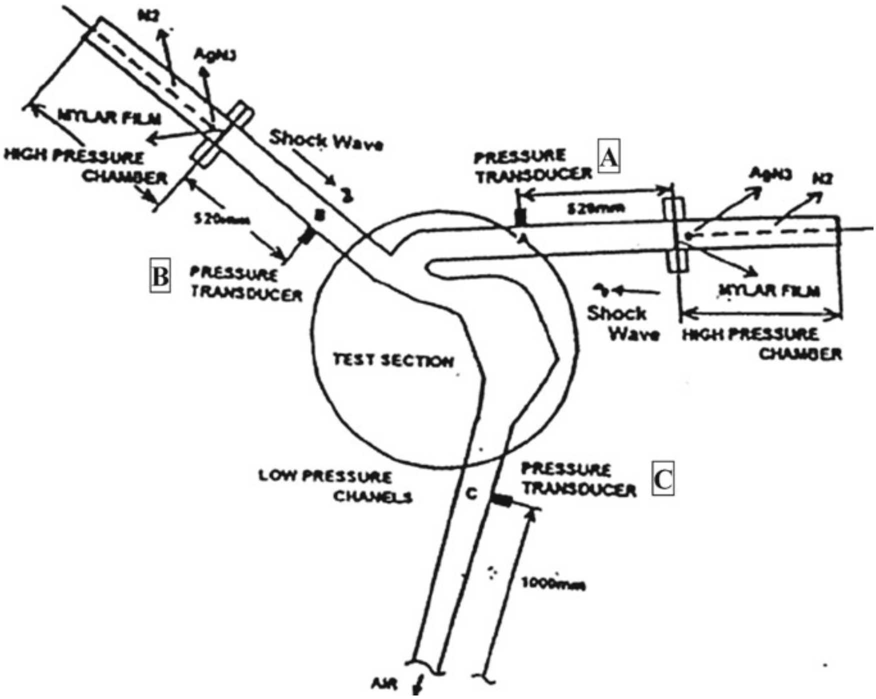

Fig. 25 Shock tube analogy of shock wave propagation in an EPF simulator

gas supply, we connected to the exhaust ports two 550 mm long shock tube high-pressure chambers containing the pressurize nitrogen. Each high-pressure chamber is separated by a 9 μm thick Mylar diaphragm from the exhaust port. A tiny explosive of 10 mg silver azide pellet, AgN_3, is glued at the thin optical fiber tip and is attached on the diaphragm. The explosive is detonated upon the irradiating the Q-swiched Nd:YAG beam and spontaneously rupture the diaphragm. Hence the shock wave so far created inside the exhaust port is in the range of $Ms = 1.1$ and is precisely controllable.

Figure 26 shows schematic diagram of shock tube operation and control of double exposure holographic interferometry. The optical setup so far used is identical to that we already explained in Fig. 6.

Visualized results are shown in Fig. 27a, b for 93MY-EPF and 89MY-EPF, respectively. The fringes thus visualized in the shock tube analogy indicate the presence of pressure waves. Presumably similar wave interactions would appear in the prototype silencers and the catalytic converters. At the corner fringe concentrations exist, which would correspond the presence of noises. These shock tube analogies would explain the process of exhaust noises generation in the exhaust pipe line system.

We measured pressures at the positions $\boxed{A}$, $\boxed{B}$, and $\boxed{C}$ as seen in Fig. 25. The measured pressure levels are summarized in Fig. 28.

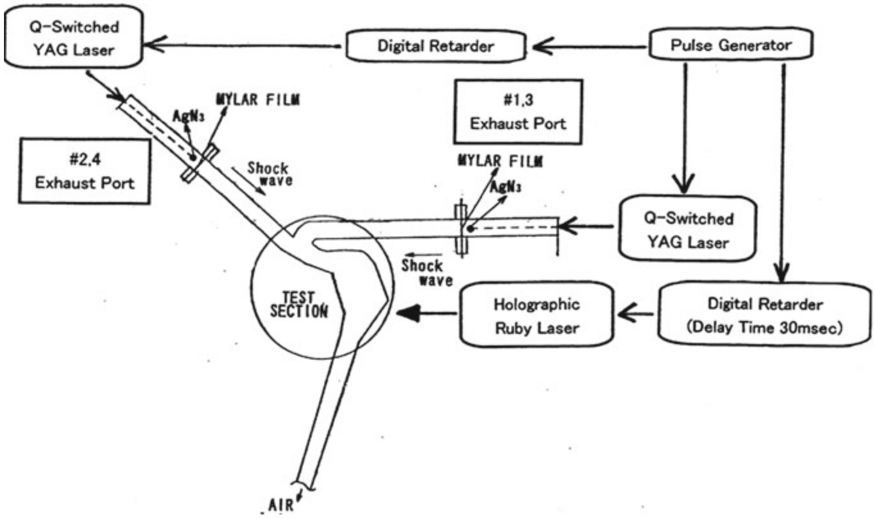

Fig. 26 Schematic diagram of the shock tube operation and optical visualization

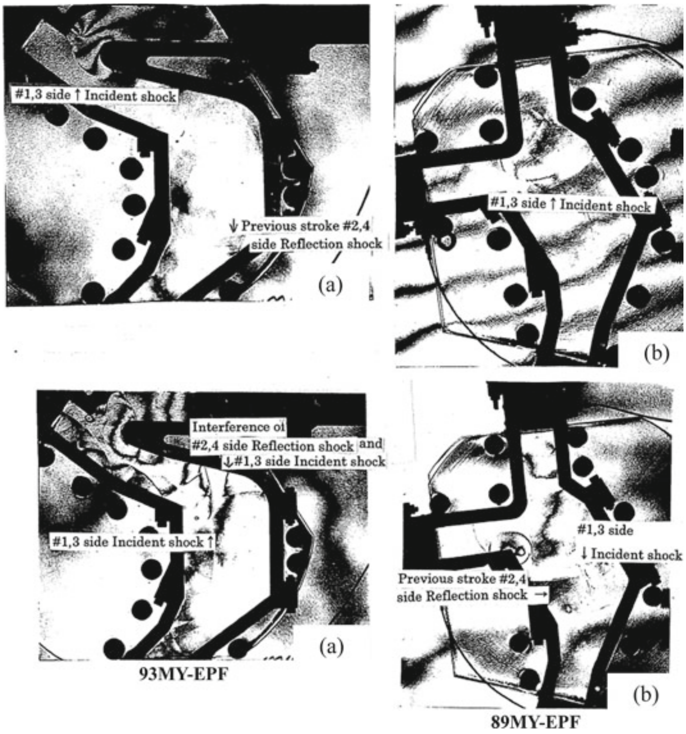

Fig. 27 Result of visualization 93MY-EPF (**a**), 89MY-EPF (**b**)

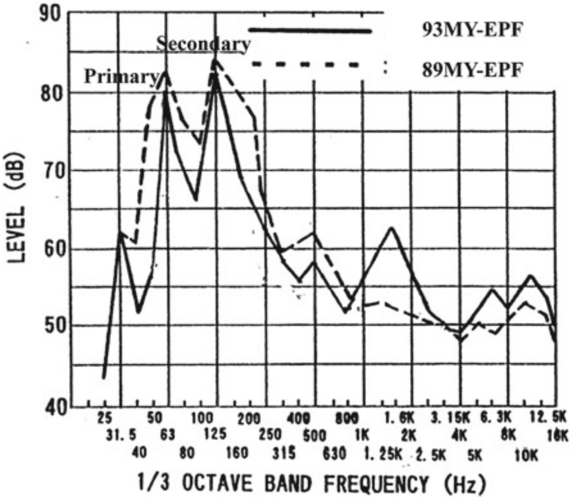

Fig. 28 Comparison of EPF pressure frequency characteristics between 93 and 89 MY

The ordinate denotes pressure level in dB and the abscissa denotes 1/3 octave band frequency in Hz. Solid line designates 93MY-EPF and dash line designates 89MY-EPF.

In Fig. 28 the shock tube analogy reproduces similar trends as observed in prototype engine tests. It is concluded that shock wave induced unpleasant noises induced should be suppressed by the silencers located close to the EPF. Updated models of SUBARU engines are designed based on this concept.

Characteristics of Weak Shock Waves Occurring in Intake System [10]

In engines equipped with turbocharger, depending on operational conditions the excess pressures are created, which not only damage the turbocharger but also induce unpleasant noises. To prevent such a damage, a safety valve is equipped releasing the excess pressure into open air.

Upon our pressure measurement, it is revealed that when the safety valve is operated we observed the presence of a weak shock wave of about Ms = 1.06. We, for the first time, monitored the weak shock wave in intake systems. To prevent the unpleasant noises in the intake system we installed a silencer mitigating shock waves and enlarge the diameter of intake systems. The updated design concept is applied to mass production engines of recent cars.

5 Summary

1. It was proven that exhaust gases released from exhaust gas pipe lines of automobile engines coalesced into weak shock wave and caused unpleasant engine noises. Hence their reduction should be discussed from the point of view of shock wave dynamics.
2. Shock tubes are used to simulate the propagation of weak shock waves in exhaust gas pipe lines and successfully applied to determine an optimum shape of silencer. The results are used to design prototype automobile engines.
3. Weak shock waves appear not only in exhaust gas pipe line but also air intake systems.
4. This project is indeed one of the successful industrial application of shock wave research.

Acknowledgements The author would like to express his gratitude to Kazuyoshi Takayama, Emeritus Professor of Tohoku University for his guidance throughout the course of the present project and also to Dr. Osamu Onodera, Institute of Fluid Science, Tohoku University for his assistance in conducting the experiments.

References

1. Sekine N, Matsumura S, Takayama K, Onodera O, Ito K (1987) Induction and propagation of shock waves in the exhaust pipe of an internal combustion engine. JSME 53–498. B-527 (Japanese)
2. Sekine N, Matsumura S, Takayama K, Onodera O, Ito K (1989) Shock wave development and propagation in automobile exhaust systems. SAE Paper 880082
3. Sekine N, Matsumura S, Aoki K, Takayama K (1988) Generation and propagation of shock waves in the exhaust pipe of a 4cycle automobile engine. In: 17th ISSW AIP conference proceedings 208, pp 671–676
4. Sekine N, Onodera O, Takayama K (1992) Effect of shock waves on silencer characteristics in exhaust gas flows of automobile engines. In: 19th ISSW conference proceedings
5. Sekine N, Kudo I, Onodera O, Takayama K (1994) Study of silencer characteristics in a gas flows with shock wave (1st report: Propagation of shock wave in the silencer). JSME.60–573, B-527 (Japanese)
6. Takayama K (1983) Application of holographic interferometry to shock wave research. Proc SPIE 398:174–180
7. Sekine N, Kudo I, Onodera O, Takayama K (1994) Study of silencer characteristics in a gas flows with shock wave (2nd report: Pressure characteristics of the silencer). JSME 60–575. B-527 (Japanese)
8. Sekine N, Onodera O, Takayama K (1993) Characteristics of shock waves on exhaust system in exhaust gas flows of automobile engines. In: 20th ISSW conference proceedings
9. Sekine N, Onodera O, Takayama K (1995) Study of silencer characteristics for shock waves in exhaust gas flows. In: 7th research conference of the institute of fluid science. Tohoku Univ, [71] (Japanese)

10. Sekine N, Ninomiya Y (2014) Overview of intake and exhaust noise. In-house (SUBARU) report PJ34–14–0003 (Japanese)
11. Harten A (1983) High resolution schemes for hyperbolic conservation lows. J Comput Phys 49:357–393

Equation of State for Water Based on the Shock Hugoniot Data

Kunihito Nagayama

1 Thermodynamic Formulation

Introduction

Water is important in our daily life, and it has been studied extensively including high-pressure phase diagram [1]. One of the complexities brought to the interpretation of the shock data is the shock Hugoniot compression curve seems tangent or invade into the ice VII phase even at relatively low pressures.

Shock Hugoniot data for water have been measured precisely by several authors, and among them the equation of state of Rice-Walsh type has been proposed [2, 3].

We have measured the shock Hugoniot compression curve for water by using the high-pressure gas gun with the optical sensitive method of detecting the shock front up to around 1 GPa pressure region [4, 5], i.e., the lowest segment of the Hugoniot curve as shown by Rybakov [1]. This is the pressure region Hugoniot seems contact with ice boundary.

We have found that the shock Hugoniot in this region is given by

$$u_s = A + Bu_p, \tag{1}$$

where us, and up denote the shock velocity and the particle velocity, respectively [4, 5]. And, A, and B denote the empirical coefficients, whose values are found to be equal to the following.

$$A = 1.45\ [\text{km/s}], \tag{2}$$

K. Nagayama (✉)
Kyushu University, Fukuoka, Japan

© The Author(s), under exclusive license to Springer Nature Switzerland AG 2022

K. Takayama and O. Igra (eds.), *Frontiers of Shock Wave Research*,
https://doi.org/10.1007/978-3-030-90735-8_12

$$B = 1.99 \tag{3}$$

Shock Hugoniot is given by Eq. (1), then the internal energy or the shock pressure as a function of η is written by

$$\varepsilon_H = \varepsilon_0 + \frac{1}{2}\frac{A^2\eta^2}{(1 - B\eta)^2}, \tag{4}$$

$$p_H = \frac{\rho_0 A^2 \eta}{(1 - B\eta)^2}, \tag{5}$$

where η is defined as the degree of compression

$$\eta \equiv 1 - \frac{v}{v_0} \tag{6}$$

where v denotes the specific volume, and 0 is the suffix corresponding to the initial state.

In this report, the equation of state for water has been studied based on the above shock data and shock Hugoniot functions.

Polynomial Expansion of Thermodynamic Variables

The present theory is formulated by extending the thermodynamic expansion formula published firstly by Bethe [6] and Zel'dovich and Raizer [7]. The expansion itself can be used for any medium with arbitrary equation of state. The increase in the shock pressure and that in the internal energy are thermodynamically expanded in terms of the volume change and the entropy change up to the fourth order of volume change. They are given by the equations,

$$\begin{aligned}\Delta p = {} & \left(\frac{\partial p}{\partial v}\right)_{S_0} \Delta v + \frac{1}{2}\left(\frac{\partial^2 p}{\partial v^2}\right)_{S_0} \Delta v^2 + \frac{1}{6}\left(\frac{\partial^3 p}{\partial v^3}\right)_{S_0} \Delta v^3 \\ & + \frac{1}{24}\left(\frac{\partial^4 p}{\partial v^4}\right)_{S_0} \Delta v^4 + \left(\frac{\partial p}{\partial S}\right)_{v_0} \Delta S + \left(\frac{\partial^2 p}{\partial S \partial v}\right)_{S_0} \Delta S \Delta v\end{aligned} \tag{7}$$

$$\begin{aligned}\Delta \varepsilon = {} & \left(\frac{\partial \varepsilon}{\partial v}\right)_{S_0} \Delta v + \frac{1}{2}\left(\frac{\partial^2 \varepsilon}{\partial v^2}\right)_{S_0} \Delta v^2 + \frac{1}{6}\left(\frac{\partial^3 \varepsilon}{\partial v^3}\right)_{S_0} \Delta v^3 \\ & + \frac{1}{24}\left(\frac{\partial^4 \varepsilon}{\partial v^4}\right)_{S_0} \Delta v^4 + \left(\frac{\partial \varepsilon}{\partial S}\right)_{v_0} \Delta S + \left(\frac{\partial^2 \varepsilon}{\partial S \partial v}\right)_{S_0} \Delta S \Delta v\end{aligned} \tag{8}$$

Polynomial expansion up to fifth order of volume change is not very difficult, but I decided the expansion up to fourth. One of the reasons of this decision is the difference in the order depends on what you choose for the variables. In the discussion of shock Hugoniot, the difference appears in the pressure and energy expression due to the Rankine-Hugoniot relationship. Advantage of choosing internal energy is that one does not need to define higher order derivatives of the Grüneisen parameter.

Rewriting the last several terms, we obtain

$$\begin{aligned}\Delta p = &\left(\frac{\partial p}{\partial v}\right)_{S_0}\Delta v + \frac{v_0^2}{2}\left(\frac{\partial^2 p}{\partial v^2}\right)_{S_0}\Delta v^2 + \frac{v_0^3}{6}\left(\frac{\partial^3 p}{\partial v^3}\right)_{S_0}\Delta v^3 \\ &+ \frac{v_0^4}{24}\left(\frac{\partial^4 p}{\partial v^4}\right)_{S_0}\Delta v^4 + \frac{\gamma_0}{v_0}T_0\Delta S + \left(\frac{\partial}{\partial v}\left[\frac{\gamma}{v}T\right]\right)_{S_0}\Delta S\Delta v,\end{aligned} \tag{9}$$

$$\begin{aligned}\Delta \varepsilon = &-p_0\Delta v - \frac{1}{2}\left(\frac{\partial p}{\partial v}\right)_{S_0}\Delta v^2 - \frac{1}{6}\left(\frac{\partial^2 p}{\partial v^2}\right)_{S_0}\Delta v^3 \\ &- \frac{1}{24}\left(\frac{\partial^3 p}{\partial v^3}\right)_{S_0}\Delta v^4 + T_0\Delta S - \frac{\gamma_0}{v_0}T_0\Delta S\Delta v,\end{aligned} \tag{10}$$

where we have used the following formula.

$$\left(\frac{\partial p}{\partial S}\right)_{v_0} = \left(\frac{\partial p}{\partial \varepsilon}\right)_{v_0}\left(\frac{\partial \varepsilon}{\partial S}\right)_{v_0} = \frac{\gamma_0}{v_0}T_0 \tag{11}$$

$$\left(\frac{\partial^2 p}{\partial S\partial v}\right)_{S_0} = \left(\frac{\partial}{\partial v}\left[\frac{\gamma}{v}T\right]\right)_{S_0} \tag{12}$$

We define the decrement in three variables by

$$\begin{aligned}\Delta p &\equiv p - p_0 > 0 \\ \Delta v &\equiv v - v_0 < 0 \\ \Delta S &\equiv S - S_0 > 0\end{aligned} \tag{13}$$

Since we consider the compression wave, variables have the sign shown in Eq. (13), where we have used the formula in Eq. (10).

$$\left(\frac{\partial \varepsilon}{\partial v}\right)_{S_0} = -p_0 \tag{14}$$

We also show the expansion in terms of the non-dimensional variable η.

$$\Delta p = \left(\frac{\partial p}{\partial \eta}\right)_{S_0}\eta + \frac{1}{2}\left(\frac{\partial^2 p}{\partial \eta^2}\right)_{S_0}\eta^2 + \frac{1}{6}\left(\frac{\partial^3 p}{\partial \eta^3}\right)_{S_0}\eta^3$$

$$+\frac{1}{24}\left(\frac{\partial^4 p}{\partial\eta^4}\right)_{S_0}\eta^4+\frac{\gamma_0}{v_0}T_0\Delta S-v_0\left(\frac{\partial}{\partial v}\left[\frac{\gamma}{v}T\right]\right)_{S_0}\eta\Delta S \tag{15}$$

$$\Delta\varepsilon=+v_0p_0\eta+\frac{v_0}{2}\left(\frac{\partial p}{\partial\eta}\right)_{S_0}\eta^2+\frac{v_0}{6}\left(\frac{\partial^2 p}{\partial\eta^2}\right)_{S_0}\eta^3$$
$$+\frac{v_0}{24}\left(\frac{\partial^3 p}{\partial\eta^3}\right)_{S_0}\eta^4+T_0\Delta S+\gamma_0T_0\eta\Delta S \tag{16}$$

For later use, we will calculate the term appearing in the last in Eq. (15).

$$\begin{aligned}\left(\frac{\partial}{\partial v}\left[\frac{\gamma}{v}T\right]\right)_S&=\frac{\gamma}{v}\left(\frac{\partial T}{\partial v}\right)_S+\frac{T}{v}\left(\frac{d\gamma}{dv}\right)_S-\frac{\gamma T}{v^2}\\&=-\frac{T}{v^2}\left[\frac{v}{v_0}\left(\frac{d\gamma}{dv}\right)+\gamma^2+\gamma\right]\end{aligned} \tag{17}$$

Applying this to the initial state, we have

$$\left(\tfrac{\partial}{\partial v}\left[\tfrac{\gamma}{v}T\right]\right)_{S_0}=-\tfrac{T_0}{v_0^2}\left[\left(\tfrac{d\gamma}{d\eta}\right)_0+\gamma_0^2+\gamma_0\right] \tag{18}$$

It is noted that this expression contains the derivative of the Grüneisen parameter at the initial state, which is unknown at moment.

This formulation is based on the fact that the entropy change associated with shock compression in any medium is of the order of cube power of the change in volume. If Eq. (18) is inserted to Eq. (15), we have

$$\Delta p=\left(\frac{\partial p}{\partial\eta}\right)_{S_0}\eta+\frac{1}{2}\left(\frac{\partial^2 p}{\partial\eta^2}\right)_{S_0}\eta^2+\frac{1}{6}\left(\frac{\partial^3 p}{\partial\eta^3}\right)_{S_0}\eta^3$$
$$+\frac{1}{24}\left(\frac{\partial^4 p}{\partial\eta^4}\right)_{S_0}\eta^4+T_0\Delta S\left[\frac{\gamma_0}{v_0}+\frac{1}{v_0}\left[\left(\frac{d\gamma}{d\eta}\right)_0+\gamma_0^2+\gamma_0\right]\eta\right] \tag{19}$$

and,

$$\Delta\varepsilon=+v_0p_0\eta+\frac{v_0}{2}\left(\frac{\partial p}{\partial\eta}\right)_{S_0}\eta^2+\frac{v_0}{6}\left(\frac{\partial^2 p}{\partial\eta^2}\right)_{S_0}\eta^3$$
$$+\frac{v_0}{24}\left(\frac{\partial^3 p}{\partial\eta^3}\right)_{S_0}\eta^4+T_0\Delta S\left[1+\gamma_0\eta\right], \tag{20}$$

where we assumed that initial pressure p_0 is neglected compared with the shock pressure.

Hugoniot Expression by the Use of the Rankine-Hugoniot Relationship

Now we use the Rankine-Hugoniot relationship in order to apply the general expansion formula, (15) and (16) into shock Hugoniot function.

$$\varepsilon - \varepsilon_0 = \frac{p + p_0}{2}(v_0 - v) \tag{21}$$

or

$$\Delta\varepsilon = \frac{2p_0 + \Delta p}{2}(-\Delta v) = -p_0\Delta v - \frac{1}{2}\Delta p\Delta v = +v_0 p_0 \eta + \frac{v_0}{2}\eta\Delta p \tag{22}$$

Combining the Rankine-Hugoniot relationship, Eqs. (21) or (22), we will discuss the shock Hugoniot curve.

It is noticeable that maximum power of volume change used in the polynomial expression of shock pressure, Eq. (19) or of internal energy, Eq. (20) is different due to the existence of η in Eq. (22). This is the reason why we will formulate the equation of state in terms of the internal energy and not of pressure, as explained earlier. Thereafter, we will discuss the shock Hugoniot using the internal energy equation, which we could retain terms up to the fourth order of volume change.

If Eq. (19) is inserted to Eq. (22), we obtain

$$\begin{aligned}\Delta\varepsilon_H &= +v_0 p_0 \eta + \frac{v_0}{2}\eta\Delta p \\ &= v_0 p_0 \eta + \frac{v_0 \eta^2}{2}\left[\left(\frac{\partial p}{\partial \eta}\right)_{S_0} + \frac{1}{2}\left(\frac{\partial^2 p}{\partial \eta^2}\right)_{S_0}\eta + \frac{1}{6}\left(\frac{\partial^3 p}{\partial \eta^3}\right)_{S_0}\eta^2\right] + \frac{\gamma_0 \eta}{2}T_0 \Delta S,\end{aligned} \tag{23}$$

where only the terms of up to the fourth order in η are retained. To do so, the pressure change, Eq. (19) of only up to the third order terms is necessary as explained earlier.

If we compare Eq. (23) with Eq. (20),

$$\begin{aligned}\Delta\varepsilon = &+v_0 p_0 \eta + \frac{v_0}{2}\left(\frac{\partial p}{\partial \eta}\right)_{S_0}\eta^2 + \frac{v_0}{6}\left(\frac{\partial^2 p}{\partial \eta^2}\right)_{S_0}\eta^3 + \frac{v_0}{24}\left(\frac{\partial^3 p}{\partial \eta^3}\right)_{S_0}\eta^4 \\ &+ T_0 \Delta S\left[1 + \gamma_0 \eta\right]\end{aligned} \tag{24}$$

Two equations are equal up to the second order of volume change. This fact is called the second order contact between the shock Hugoniot and the isentrope centering the same initial state. In other words, the entropy change by shock compression is a tiny quantity in the order of third order of magnitude of the volume change [2, 3]. Or more specifically, the terms in Eq. (23) of the third order or smaller,

$$\Delta\varepsilon_{III} = \tfrac{v_0\eta}{2}\left[\tfrac{1}{2}\left(\tfrac{\partial^2 p}{\partial\eta^2}\right)_{S_0}\eta^2 + \tfrac{1}{6}\left(\tfrac{\partial^3 p}{\partial\eta^3}\right)_{S_0}\eta^3\right] + \tfrac{\gamma_0\eta}{2}T_0\Delta S \tag{25}$$

should be equal to the corresponding terms in Eq. (24), namely,

$$\Delta\varepsilon_{III} = \tfrac{v_0}{6}\left(\tfrac{\partial^2 p}{\partial\eta^2}\right)_{S_0}\eta^3 + \tfrac{v_0}{24}\left(\tfrac{\partial^3 p}{\partial\eta^3}\right)_{S_0}\eta^4 + T_0\Delta S[1+\gamma_0\eta] \tag{26}$$

In order for the third or higher order quantities in both equations to be equivalent, the assumption that the entropy change should be of the third order quantity. So, we write the entropy change as

$$\Delta \mathrm{S} = \frac{\mathrm{v}_0}{12\mathrm{T}_0}\left(\frac{\partial^2 \mathrm{p}}{\partial\eta^2}\right)_{\mathrm{S}_0}\eta^3 + \frac{\mathrm{a}_0}{\mathrm{T}_0}\eta^4, \tag{27}$$

where the first term in Eq. (27), the third order term is derived by the comparison of Eqs. (26) and (27) in the third order terms. One may determine the parameter a_0 to be consistent to both equations. If Eq. (27) is inserted into Eqs. (25), (26), we get

$$\Delta\varepsilon_{III} = \frac{v_0\eta}{2}\left[\frac{1}{2}\left(\frac{\partial^2 p}{\partial\eta^2}\right)_{S_0}\eta^2 + \frac{1}{6}\left(\frac{\partial^3 p}{\partial\eta^3}\right)_{S_0}\eta^3\right] + \frac{\gamma_0 v_0}{24}\left(\frac{\partial^2 p}{\partial\eta^2}\right)_{S_0}\eta^3 \tag{28}$$

$$\begin{aligned}\Delta\varepsilon_{III} &= \frac{v_0}{6}\left(\frac{\partial^2 p}{\partial\eta^2}\right)_{S_0}\eta^3 + \frac{v_0}{24}\left(\frac{\partial^3 p}{\partial\eta^3}\right)_{S_0}\eta^4 \\ &\quad + \left[\frac{v_0}{12}\left(\frac{\partial^2 p}{\partial\eta^2}\right)_{S_0}\eta^3 + a_0\eta^4\right][1+\gamma_0\eta]\end{aligned} \tag{29}$$

By comparing the above two equations, the third order term is apparently consistent. If we compare the fourth order terms, we obtain

$$\frac{v_0}{12}\left(\frac{\partial^3 p}{\partial\eta^3}\right)_{S_0} + \frac{\gamma_0 v_0}{24}\left(\frac{\partial^2 p}{\partial\eta^2}\right)_{S_0} = \frac{v_0}{24}\left(\frac{\partial^3 p}{\partial\eta^3}\right)_{S_0} + a_0 + \frac{\gamma_0 v_0}{12}\left(\frac{\partial^2 p}{\partial\eta^2}\right)_{S_0} \tag{30}$$

then we have

$$a_0 = \tfrac{v_0}{24}[\left(\tfrac{\partial^3 p}{\partial\eta^3}\right)_{S_0} - \gamma_0\left(\tfrac{\partial^2 p}{\partial\eta^2}\right)_{S_0}] \tag{31}$$

Finally, it is found that the entropy change by shock compression is given by the following formula.

$$T_0\Delta S = \tfrac{v_0}{12}\left(\tfrac{\partial^2 p}{\partial\eta^2}\right)_{S_0}\eta^3 + \tfrac{v_0}{24}\left[\left(\tfrac{\partial^3 p}{\partial\eta^3}\right)_{S_0} - \gamma_0\left(\tfrac{\partial^2 p}{\partial\eta^2}\right)_{S_0}\right]\eta^4 \tag{32}$$

Then it is possible to insert the entropy change into Eq. (20) and obtain the shock Hugoniot function for the shock energy as a function of volume change.

$$\begin{aligned}\Delta\varepsilon_H = &+v_0 p_0 \eta + \frac{v_0}{2}\left(\frac{\partial p}{\partial \eta}\right)_{S_0}\eta^2 + \frac{v_0}{6}\left(\frac{\partial^2 p}{\partial \eta^2}\right)_{S_0}\eta^3 + \frac{v_0}{24}\left(\frac{\partial^3 p}{\partial \eta^3}\right)_{S_0}\eta^4 \\ &+\left[1+\gamma_0\eta\right]\frac{v_0}{12}\left(\frac{\partial^2 p}{\partial \eta^2}\right)_{S_0}\eta^3 + \frac{v_0}{24}\left[\left(\frac{\partial^3 p}{\partial \eta^3}\right)_{S_0} - \gamma_0\left(\frac{\partial^2 p}{\partial \eta^2}\right)_{S_0}\right]\eta^4\end{aligned} \tag{33}$$

Note the third order term in Eq. (33) can be calculated as

$$\frac{v_0}{4}\left(\frac{\partial^2 p}{\partial \eta^2}\right)_{S_0}\eta^3 \tag{34}$$

Then the fourth order terms will be

$$\begin{aligned}&\frac{v_0}{24}\left(\frac{\partial^3 p}{\partial \eta^3}\right)_{S_0}\eta^4 + \frac{\gamma_0 v_0}{12}\left(\frac{\partial^2 p}{\partial \eta^2}\right)_{S_0}\eta^4 + \frac{v_0}{24}\left[\left(\frac{\partial^3 p}{\partial \eta^3}\right)_{S_0} - \gamma_0\left(\frac{\partial^2 p}{\partial \eta^2}\right)_{S_0}\right]\eta^4 \\ &= \frac{v_0}{12}\left[\left(\frac{\partial^3 p}{\partial \eta^3}\right)_{S_0} + \frac{\gamma_0}{2}\left(\frac{\partial^2 p}{\partial \eta^2}\right)_{S_0}\right]\eta^4\end{aligned} \tag{35}$$

Finally, Eq. (33) become

$$\begin{aligned}\Delta\varepsilon_H = &+v_0 p_0 \eta + \frac{v_0}{2}\left(\frac{\partial p}{\partial \eta}\right)_{S_0}\eta^2 + \frac{v_0}{4}\left(\frac{\partial^2 p}{\partial \eta^2}\right)_{S_0}\eta^3 \\ &+\frac{v_0}{12}\left[\left(\frac{\partial^3 p}{\partial \eta^3}\right)_{S_0} + \frac{\gamma_0}{2}\left(\frac{\partial^2 p}{\partial \eta^2}\right)_{S_0}\right]\eta^4\end{aligned} \tag{36}$$

Application of Linear Relationship Between Shock Velocity and Particle Velocity

Shock Hugoniot function given by Eq. (4) for the internal energy as a function of η can be rewritten by the polynomial expression in terms of the powers of η, then each term of each power can be compared with Eq. (36). The resultant formulas for each derivatives of η are given by

$$\left(\frac{\partial p}{\partial \eta}\right)_{S_0} = \rho_0 A^2 \tag{37}$$

$$\left(\frac{\partial^2 p}{\partial \eta^2}\right)_{S_0} = 4\rho_0 A^2 B \tag{38}$$

$$\left(\frac{\partial^3 p}{\partial \eta^3}\right)_{S_0} = (18B - 2\gamma_0)\rho_0 A^2 B \tag{39}$$

If these equations are inserted into Eq. (36), we have

$$\Delta\varepsilon_{\mathrm{H}} = \frac{\mathrm{A}^2}{2}\eta^2 + \mathrm{A}^2\mathrm{B}\eta^3 + \frac{3}{2}\mathrm{A}^2\mathrm{B}^2\eta^4, \tag{40}$$

An isentrope centering the same initial state are obtained using Eq. (16) and neglecting the entropy increase terms, then we have

$$\Delta\varepsilon_S = \frac{A^2}{2}\eta^2 + \frac{2}{3}A^2 B\eta^3 + \frac{18B - 2\gamma_0}{24}A^2 B\eta^4 \tag{41}$$

Difference between $\Delta\varepsilon_H$ and $\Delta\varepsilon_S$ denotes the entropy change due to shock compression, and is equal to the value calculated by Eq. (32).

As you noticed in deriving Eq. (23), pressure formula is used in the energy equation only up to the terms of third order. After that the pressure formulas are derived to the same order of terms. First, Eqs. (15) and (32) are combined.

$$\Delta p_H = \left(\frac{\partial p}{\partial \eta}\right)_{S_0}\eta + \frac{1}{2}\left(\frac{\partial^2 p}{\partial \eta^2}\right)_{S_0}\eta^2 + \frac{1}{6}\left(\frac{\partial^3 p}{\partial \eta^3}\right)_{S_0}\eta^3 + \frac{\gamma_0}{12}\left(\frac{\partial^2 p}{\partial \eta^2}\right)_{S_0}\eta^3 \tag{42}$$

By the similar power expansion in terms of η, we have from Eqs. (37)–(39),

$$\Delta p_H = \rho_0 A^2\eta + 2\rho_0 A^2 B\eta^2 + 3\rho_0 A^2 B^2\eta^3 \tag{43}$$

Similarly, an isentrope centering the same initial state is calculated by Eq. (15) as

$$\Delta p_S = \rho_0 A^2\eta + 2\rho_0 A^2 B\eta^2 + \frac{(18B - 2\gamma_0)\rho_0 A^2 B}{6}\eta^3 \tag{44}$$

The entropy increase by shock compression in Eq. (29) can then be calculated by the use of Eqs. (37)–(39) as

$$T_0\Delta S = \frac{1}{3}A^2 B\eta^3 + \frac{1}{4}\left[(3B - \gamma_0)A^2 B\right]\eta^4 \tag{45}$$

Figure 1 shows the calculated results for the internal energy as a function of the degree of compression. Isentropic energy increase and the entropy increase by shock compression were also calculated and shown in Fig. 1.

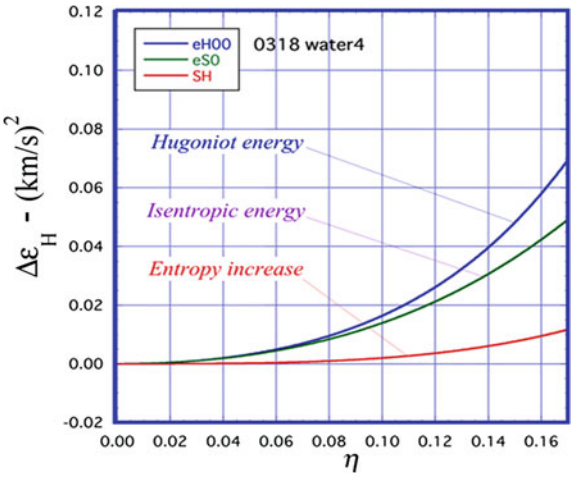

Fig. 1 Hugoniot energy versus η for water

2 Tait Equation as an Isentropic Compression Curve

We will apply the above results to the so-called Tait equation of state in a form of an isentrope [8, 9]

$$p(v, S) = \alpha(S)\left[\left(\frac{v}{v_0}\right)^{-n} - 1\right], \tag{46}$$

where the coefficient, α is assumed to be a function of entropy, whereas the coefficient *n* is assumed to be a constant.

Integration of Eq. (46) along an isentrope gives an expression of the internal energy as

$$\begin{aligned}\varepsilon(v, S) &= \varepsilon_0 - \int_{v_0}^{v} p(v, S)dv \\ &= \varepsilon_0 - \alpha(S)v_0\int_{1}^{v/v_0}\left[\left(\frac{v}{v_0}\right)^{-n} - 1\right]d\left(\frac{v}{v_0}\right) \\ &= \varepsilon_0 + \alpha(S)v_0\left[\frac{1}{n-1}\left(\frac{v}{v_0}\right)^{-n+1} + \left(\frac{v}{v_0}\right) - \frac{n}{n-1}\right]\end{aligned} \tag{47}$$

Expression of the shock Hugoniot using the Tait equation, Eq. (47) should be

$$\varepsilon_H(v) = \varepsilon_H(\eta) = \varepsilon_0 + \alpha(S_H)v_0\left[\frac{1}{n-1}\left(\frac{v}{v_0}\right)^{-n+1} + \left(\frac{v}{v_0}\right) - \frac{n}{n-1}\right] \tag{48}$$

It is therefore possible to estimate the increase in the entropy function, α(S) along the shock Hugoniot by comparing the shock energy, ε_H with the Tait energy calculated by Eq. (47). As expected, weak shock or isentropic approximation of Eq. (48) leads to the expansion starting at the square term of η, and this term compared with Eq. (41) gives the information on the coefficient, α(S_0).

$$\alpha(S_0) = \frac{\rho_0 A^2}{n} \tag{49}$$

Calculation of Tait isentrope has been made by putting the coefficient n as a parameter to adjust it to the isentropic energy. The result of calculation is shown in Fig. 2. Best fit to the isentrope calculated from the shock Hugoniot, Eq. (41) was obtained by the value of $n = 6.4$. As you see in Fig. 2, the agreement between two functions is satisfactory.

Figure 3 shows the result of calculation. As you see in Eq. (48), the increase in the ratio of the Hugoniot energy and the Tait energy should be the entropy function α(S). Figure 3 shows the result of calculation for α(S) along Hugoniot. One may notice that due to the slow increase in entropy along Hugoniot, α(S) along entropy is very steep. It is found in this analysis that the parameter n is somewhat larger than those reported previously.

Approximation of the function, α(S) by polynomial expression of η is very easily done and is given by

$$\alpha(S_H) = \alpha(\eta) = \alpha(S_0)\left[1.00 + 1.14\eta + 6.83\eta^2\right] \tag{50}$$

Fig. 2 Tait energy versus η for water

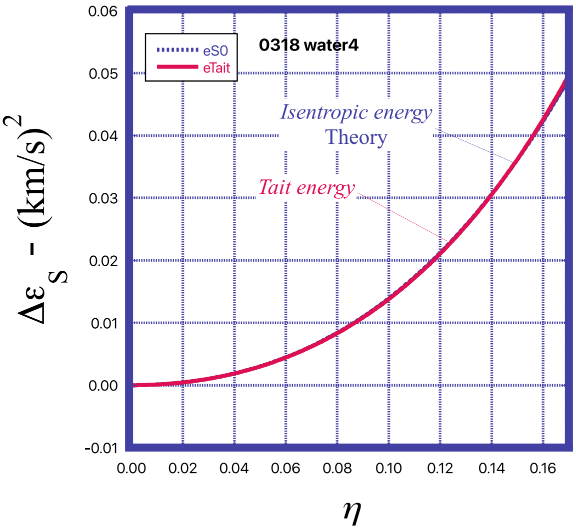

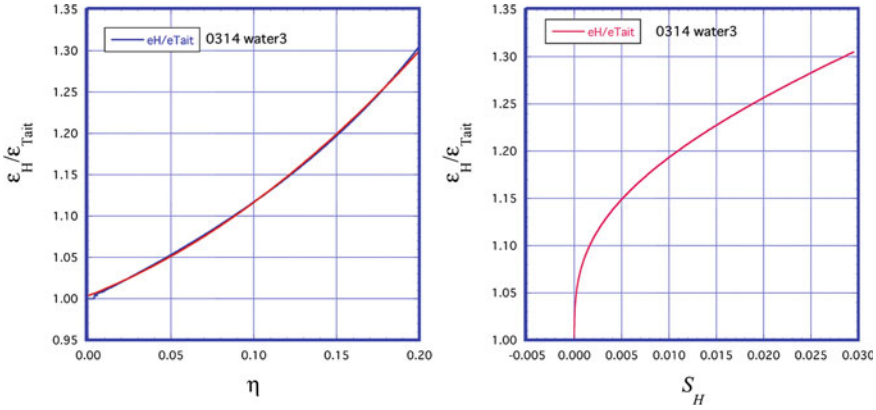

Fig. 3 Entropy function, α(S) in Tait equation versus η or versus S_H for water

Based on these analyses, one may safely use the Tait type equation for flow analysis including shock propagation.

3 Conclusion

It is my honor to present my recent research report on the occasion of 100 years of birth of Prof. Akira Sakurai.

Formulation of the equation of state has been done using polynomial expansion of thermodynamic variables together with shock Hugoniot data for water. Part of the ideas of this formulation stems from the fact that shock Hugoniot has second order contact with an isentrope centering the same initial state with Hugoniot. That means the shock Hugoniot itself contains sufficient information on the isentrope.

Using the available shock Hugoniot data, we will be successfully formulated the equation of state including the shock entropy as a function of shock strength. However, due to the order of expansion of variables limit the applicability of the method of application. Approximately, the pressure limit will be up to 0.5 GPa.

Even so, application of the results to the Tait-type equation of state, and information on an entropy function could be obtained.

References

1. Rybakov AP, Rybakov LA (1995) Polymorphism of shocked water. Eur J Mech B/Fluids 14:323–332
2. Walsh JM, Rice MH (1957) Dynamic compression of liquids from measurements on strong shock waves. J Chem Phys 26:815
3. Rice MH, Walsh JM (1957) Equation of state of water to 250 kilobars. J Chem Phys 26:824

4. Nagayama K, Mori Y, Shimada K (2002) Shock Hugoniot compression curve for water up to 1 GPa by using a compressed gas gun. J Appl Phys 91:476–482
5. Nagayama K, Mori Y, Motegi Y, Nakahara M (2006) Shock Hugoniot for biological materials. Shock Waves 15:267–275
6. Bethe H (1942) Theory of shock waves in a medium with arbitrary equation of state, original paper. In: Johnson JN, Cheret R (eds) Report, republished in a book, classic papers on shock compression science. Springer, London, pp 421–492
7. Zel'dovich YB, Raizer YP (1966) Physics of shock waves and high- temperature hydrodynamic phenomena. Academic Press, New York and London
8. Kirkwood JG, Bethe H (1942) The pressure wave produced by an underwater explosion; I, basic propagation theory, OSRD Report No. 588
9. Dymond JH, Malhorta R (1988) The tait equation: 100 years on. Int J Thermophys 9:6

General Solution of the 2D Navier–Stokes Equations and Its Application to Shock Wave Problems

Akira Sakurai and Susumu Kobayashi

1 Introduction

We are concerned with a general solution of the 2D Navier–Stokes equations of viscous, compressible flow in cylindrical coordinate system (r, θ). Although this kind of solution is needed for the investigation of various flows in angular flow region, not much is known especially of its general solution. Here we consider it in the form of power series expansion in r, whose coefficients are functions of θ only. It is found that these functions can be determined successively starting from its zeroth order solution, which is in fact an exact solution of the basic equations along a line $r = 0$ in (r, θ)-plane.

We utilize this solution to the investigation of viscous, compressible flow problems. In particular, in this paper, we use it for two problems in connection with the cause-study of the von Neumann paradox [1–3] appearing in phenomenon of Mach reflection in shock waves interaction. One is the determination of angles of three shocks, the other is the internal structure of triple point in Mach reflection, which is the problem of the flow in its *non-Rankine-Hugoniot zone* [4] (NRHZ). It is needed also to see the change in feature of shock wave reflection itself in rarefied gas flow as the zone is widened enough to influence the main flow field [5]. Furthermore, the present solution expressed in (x, y) system includes the fan-like flow which is expected to be utilized for the cause study on the appearance of jet near a black hole in space by adjusting the boundary condition on the surface around the black hole.

In the followings, first we present basic equations of continuity, momentum and energy for viscous, compressible fluid in (r, θ) coordinates system, which appear seldom in literature. Then we transform them to a form convenient for an r-power

---

A. Sakurai
Tokyo Denki University, 5 Senju-Asahi-cho, Adachi-ku, Tokyo 120-8551, Japan

S. Kobayashi (✉)
Saitama Institute of Technology, 1690 Fusaiji, Fukaya-shi, Saitama 369-0293, Japan
e-mail: kobayasi@sit.ac.jp

© The Author(s), under exclusive license to Springer Nature Switzerland AG 2022

K. Takayama and O. Igra (eds.), *Frontiers of Shock Wave Research*,
https://doi.org/10.1007/978-3-030-90735-8_13

expansion to derive equations for its coefficient-functions. They are ordinary differential equations and are integrated successively starting from its zeroth order solution which is an exact solution of the basic equations along $r = 0$. This first order solution is found to include a fan-like source flow from the origin in (x, y)-plane and to be utilized for the problem of determining the shock angles in Mach reflection, which is the subject of Sect. 3. Next in the 4th section we utilize the solution with more terms to see the feature of the flow field in the non-Rankine-Hugoniot zone appearing in Mach reflection and the result is compared with the one obtained numerically on the basis of Boltzmann-BGK equation [6].

2 The 2D Navier–Stokes Equations for Gas in Cylindrical Coordinate System

Let the velocity, the density, the pressure and the temperature be

$$\boldsymbol{V} = (V_r, V_\theta), \rho, p, T \tag{1}$$

where V_r, V_θ are respectively (r, θ) components of the velocity $\boldsymbol{V}$.

The 2D Navier–Stokes equations system for gas flow is composed of equations of continuity, momentum and energy. Here we have to express them in cylindrical coordinate and they are complicated because of the curvilinear coordinate system and the terms due to the flow of compressible gas.

First the continuity equation is simply given as,

$$\frac{\partial}{\partial r}(\rho V_r r) + \frac{\partial}{\partial \theta}(\rho V_\theta) = 0 \tag{2}$$

Equation of momentum for compressible fluid in Cartesian coordinate system is expressed in the familiar vector form:

$$\rho(\boldsymbol{v} \cdot \mathrm{grad})\boldsymbol{v} = -\mathrm{grad} p + \mu\left[\Delta \boldsymbol{v} + (1/3)\mathrm{grad}(\mathrm{div}\boldsymbol{v})\right],$$

where μ and $\boldsymbol{v}$ are the coefficient of viscosity (assumed constant) and the flow velocity in Cartesian coordinate system, respectively. Thus

$$\boldsymbol{v} = (u, v), u = V_r \cos\theta - V_\theta \sin\theta, v = V_r \sin\theta + V_\theta \cos\theta.$$

With some manipulation, this equation is transformed into cylindrical coordinate system as follows:

$$\rho\left(V_r \frac{\partial V_r}{\partial r} + \frac{V_\theta}{r}\frac{\partial V_r}{\partial \theta} - \frac{V_\theta^2}{r}\right)$$

$$= -\frac{\partial p}{\partial r} + \mu\left[\Delta V_r - \frac{V_r}{r^2} - \frac{2}{r^2}\frac{\partial V_\theta}{\partial \theta} + \frac{1}{3}\frac{\partial}{\partial r}\frac{1}{r}\left(\frac{\partial r V_r}{\partial r} + \frac{\partial V_\theta}{\partial \theta}\right)\right] \tag{3}$$

$$\rho\left(V_r\frac{\partial V_\theta}{\partial r} + \frac{V_\theta}{r}\frac{\partial V_\theta}{\partial \theta} + \frac{V_r V_\theta}{r}\right)$$
$$= -\frac{\partial p}{r\partial \theta} + \mu\left[\Delta V_\theta - \frac{V_\theta}{r^2} + \frac{2}{r^2}\frac{\partial V_r}{\partial \theta} + \frac{1}{3}\frac{1}{r}\frac{\partial}{\partial \theta}\frac{1}{r}\left(\frac{\partial r V_r}{\partial r} + \frac{\partial V_\theta}{\partial \theta}\right)\right], \tag{4}$$

where

$$\Delta \equiv \frac{\partial^2}{\partial r^2} + \frac{1}{r}\frac{\partial}{\partial r} + \frac{1}{r^2}\frac{\partial^2}{\partial \theta^2}.$$

Energy equation for compressible fluid is given by

$$\rho[(\boldsymbol{V}\cdot grad)E + p(\boldsymbol{V}\cdot grad)(1/\rho)] = \kappa\Delta T + \Phi,$$

where *E, K,* Φ are the internal energy per unit mass, the heat conductivity (assumed constant), and the dissipation function due to viscosity.

This equation is expressed in (r, θ) coordinates as follows,

$$\rho\left[\left(V_r\frac{\partial}{\partial r} + V_\theta\frac{\partial}{r\partial \theta}\right)E + p\left(V_r\frac{\partial}{\partial r} + V_\theta\frac{\partial}{r\partial \theta}\right)\frac{1}{\rho}\right] = \kappa\Delta T + \Phi, \tag{5}$$

with

$$\Phi = \mu\left\{2\left[\left(\frac{\partial V_r}{\partial r}\right)^2 + \left(\frac{\partial V_\theta}{r\partial \theta} + \frac{V_r}{r}\right)^2\right] + \left(\frac{\partial V_r}{r\partial \theta} + \frac{\partial V_\theta}{\partial r} - \frac{V_\theta}{r}\right)^2 \right.$$
$$\left. -\frac{2}{3}\left(\frac{\partial V_r}{\partial r} + \frac{\partial V_\theta}{r\partial \theta} + \frac{V_r}{r}\right)^2\right\}. \tag{6}$$

These equations are supplemented by thermal and caloric equations of state for a perfect gas:

$$p = \rho R T, \tag{7}$$

$$E = c_v T, \tag{8}$$

where R is the specific gas constant and c_v is the specific heat at constant volume (assumed constant).

For convenience, Eqs. (5) and (6) are rewritten as follows:

$$\rho r\left[\left(V_r r\frac{\partial}{\partial r}+V_\theta\frac{\partial}{\partial\theta}\right)E+p\left(V_r r\frac{\partial}{\partial r}+V_\theta\frac{\partial}{\partial\theta}\right)\frac{1}{\rho}\right]=\kappa r^2\Delta T+\Psi, \tag{5a}$$

$$\Psi=\mu\left\{2\left[\left(r\frac{\partial V_r}{\partial r}\right)^2+\left(\frac{\partial V_\theta}{\partial\theta}+V_r\right)^2\right]+\left(\frac{\partial V_r}{\partial\theta}+r\frac{\partial V_\theta}{\partial r}-V_\theta\right)^2\right.$$
$$\left.-\frac{2}{3}\left(r\frac{\partial V_r}{\partial r}+\frac{\partial V_\theta}{\partial\theta}+V_r\right)^2\right\}. \tag{6a}$$

We transform these to a form convenient for r-power expansion in non-dimensional expression. Let representative velocity, pressure and density respectively be U, p_0 and ρ_0 and use the temperature T_0 given by the perfect gas relation (7) by $p_0=\rho_0 RT_0$, the velocity of sound C_0, by $C_0=\sqrt{\gamma RT_0}$ (γ: specific heats ratio), Prandtl number σ given by $\sigma=c_p\mu/\kappa$ and representative length r_0 by $r_0=\mu/(\rho_0 C_0)$, where c_p is the specific heat at constant pressure (assumed constant). Making use of these relations, we represent the variables r, V_r, V_Θ, ρ, p, T, E, as well as the dissipation function Ψ and Laplacian Δ in dimensionless form by,

$$r/r_0\to r,\quad V_r/C_0\to V_r,\quad V_\theta/C_0\ \to V_\theta,\ \ \rho/\rho_0\ \to\rho\ ,\ p/p_0$$
$$\to p,\quad T/T_0\to T,\quad E/c_v T_0\to E,\ \Psi/\kappa T_0\to\Psi,\quad \Delta/r_0^2\to\Delta$$

The dimensionless internal energy E turns out to be identical with the dimensionless temperature T (see Eq. 14).

Thus the basic equations and relations Eqs. (2)–(8) are expressed as follows:

From Eq. (2):

$$\frac{\partial}{\partial r}(r\rho V_r)+\frac{\partial}{\partial\theta}(\rho V_\theta)=0. \tag{9}$$

From Eq. (3):

$$\frac{4}{3}r^2\frac{\partial^2 V_r}{\partial r^2}+\frac{1}{3}r\frac{\partial}{\partial r}\left(\frac{\partial V_\theta}{\partial\theta}+4V_r\right)+\frac{\partial^2 V_r}{\partial\theta^2}-\frac{4}{3}V_r-\frac{7}{3}\frac{\partial V_\theta}{\partial\theta}=rY_1,$$
$$Y_1\equiv\rho\left[V_r r\frac{\partial V_r}{\partial r}+V_\theta\left(\frac{\partial V_r}{\partial\theta}-V_\theta\right)\right]+\frac{r}{\gamma}\frac{\partial p}{\partial r}. \tag{10}$$

From Eq. (4):

$$r^2\frac{\partial^2 V_\theta}{\partial r^2}+r\frac{\partial}{\partial r}\left(\frac{1}{3}\frac{\partial V_r}{\partial\theta}+V_\theta\right)+\frac{4}{3}\frac{\partial^2 V_\theta}{\partial\theta^2}-V_\theta+\frac{7}{3}\frac{\partial V_r}{\partial\theta}=rY_2,$$
$$Y_2\equiv\rho\left[V_r r\frac{\partial V_\theta}{\partial r}+V_\theta\left(\frac{\partial V_\theta}{\partial\theta}+V_r\right)\right]+\frac{1}{\gamma}\frac{\partial p}{\partial\theta}. \tag{11}$$

From Eqs. (5a) and (6a), and by redefining $\Phi\equiv\sigma(\gamma-1)\Psi$,

$$r^2 \Delta T + \Phi = rZ,$$

$$\Phi = \sigma(\gamma - 1)\left\{2\left[\left(r\frac{\partial V_r}{\partial r}\right)^2 + \left(\frac{\partial V_\theta}{\partial \theta} + V_r\right)^2\right] + \left(\frac{\partial V_r}{\partial \theta} + r\frac{\partial V_\theta}{\partial r} - V_\theta\right)^2 \right.$$
$$\left. -\frac{2}{3}\left(r\frac{\partial V_r}{\partial r} + \frac{\partial V_\theta}{\partial \theta} + V_r\right)^2\right\}, \tag{12}$$

$$\begin{aligned} Z &\equiv \frac{\sigma}{\gamma}\rho\left[\left(V_r r\frac{\partial}{\partial r} + V_\theta\frac{\partial}{\partial \theta}\right)T + (\gamma - 1)p\left(V_r r\frac{\partial}{\partial r} + V_\theta\frac{\partial}{\partial \theta}\right)\frac{1}{\rho}\right] \\ &= \frac{\sigma}{\gamma}\left[\rho\left(V_r r\frac{\partial}{\partial r} + V_\theta\frac{\partial}{\partial \theta}\right)T - (\gamma - 1)T\left(V_r r\frac{\partial}{\partial r} + V_\theta\frac{\partial}{\partial \theta}\right)\rho\right]. \end{aligned}$$

From Eqs. (7) and (8):

$$p = \rho T, \tag{13}$$

$$E = T. \tag{14}$$

3 The *r*-power Expansion

We seek a solution of the system of equations consisting of Eqs. (9)–(14) in the form of an r-power expansion:

$$V_r = \sum_{n=0}^{\infty} r^n V_r^{(n)}\ ,\ V_\theta = \sum_{n=0}^{\infty} r^n V_\theta^{(n)},\ \rho = \sum_{n=0}^{\infty} r^n \rho^{(n)},\ p = \sum_{n=0}^{\infty} r^n p^{(n)}$$
$$T = \sum_{n=0}^{\infty} r^n T^{(n)}, \tag{15}$$

where $V_r^{(n)}$,$V_\theta^{(n)}$,$\rho^{(n)}$,$p^{(n)}$, $T^{(n)}(n = 0, 1, 2\ldots)$ are all assumed to be functions of θ only. Similarly, the functions Y_1, Y_2, and Z are expressed as power series with respect to r:

$$Y_1 = \sum_{n=0}^{\infty} r^n Y_1^{(n)},\ Y_2 = \sum_{n=0}^{\infty} r^n Y_2^{(n)},\ Z = \sum_{n=0}^{\infty} r^n Z^{(n)}, \tag{16}$$

where $Y_1^{(n)}$, $Y_2^{(n)}$, $Z^{(n)}$ are also assumed to be functions of θ only.

We substitute Eqs. (15), (16) to Eqs. (9)–(13) and comparing the same order terms of r, we have equations to determine $V_r^{(n)}(\theta), V_\theta^{(n)}(\theta), \rho^{(n)}(\theta), p^{(n)}(\theta)$, $T^{(n)}(\theta)$ $(n = 0, 1, 2, \ldots)$. From Eq. (9):

$$\begin{aligned}
&V_\theta^{(0)} D\rho^{(n)} + \rho^{(n)}[(n+1)V_r^{(0)} + DV_\theta^{(0)}] = X^{(n-1)}, \\
&X^{(-1)} = 0, \\
&X^{(n-1)} = -\textstyle\sum_{i=0}^{n-1}\{V_\theta^{(n-i)} D\rho^{(i)} + [(n+1)V_r^{(n-i)} + DV_\theta^{(n-i)}]\,\rho^{(i)}\}.
\end{aligned} \tag{17}$$

where D stands for the differential operator with respect to θ,

$$D \equiv d/d\theta.$$

From Eq. (10):

$$\begin{aligned}
&[3D^2 + 4(n^2-1)]V_r^{(n)} + (n-7)DV_\theta^{(n)} = 3Y_1^{(n-1)}, \\
&Y_1^{(-1)} = 0, \\
&Y_1^{(n-1)} = \sum_{i=0}^{n-1}\sum_{j=0}^{n-1-i} \rho^{(n-1-i-j)}\Big[jV_r^{(i)}V_r^{(j)} + V_\theta^{(i)}\Big(DV_r^{(j)} - V_\theta^{(j)}\Big)\Big] \\
&\qquad\qquad + \frac{n-1}{\gamma}p^{(n-1)} \quad (n \geq 1).
\end{aligned} \tag{18}$$

From Eq. (11):

$$\begin{aligned}
&(n+7)DV_r^{(n)} + [4D^2 + 3(n^2-1)]V_\theta^{(n)} = 3Y_2^{(n-1)}, \\
&Y_2^{(-1)} = 0, \\
&Y_2^{(n-1)} = \sum_{i=0}^{n-1}\sum_{j=0}^{n-1-i} \rho^{(n-1-i-j)}\Big[jV_r^{(i)}V_\theta^{(j)} + V_\theta^{(i)}\Big(DV_\theta^{(j)} + V_r^{(j)}\Big)\Big] \\
&\qquad\qquad + \frac{1}{\gamma}Dp^{(n-1)} \quad (n \geq 1).
\end{aligned} \tag{19}$$

From Eq. (12):

$$\begin{aligned}
&(D^2 + n^2)T^{(n)} = -\Phi^{(n)} + Z^{(n-1)} \\
&\Phi^{(n)} = \frac{1}{n!}\left[\frac{\partial^n}{\partial r^n}\Phi\right]_{r=0}, \\
&Z^{(-1)} = 0, \\
&Z^{(n-1)} = \frac{\sigma}{\gamma}\left[\sum_{i=0}^{n-1}\sum_{j=0}^{n-1-i} \rho^{(n-1-i-j)}\Big(jV_r^{(i)}T^{(j)} + V_\theta^{(i)}DT^{(j)}\Big)\right.
\end{aligned}$$

$$-(\gamma-1)\sum_{i=0}^{n-1}\sum_{j=0}^{n-1-i}T^{(n-1-i-j)}\Big(V_r^{(i)}j\rho^{(j)}+V_\theta^{(i)}D\rho^{(j)}\Big)\Bigg]. \tag{20}$$

From Eq. (13):

$$p^{(n)}=\sum_{i=0}^{n}\rho^{(i)}T^{(n-i)}. \tag{21}$$

4 Solutions of Eqs. (17)–(20)

In close look at Eqs. (17)–(20), we can see that these equations can be integrated successively starting from the zeroth order solution $V_r^{(0)}(\theta)$, $V_\theta^{(0)}(\theta)$ which are exact solution of the momentum equation of Eqs. (10), (11) or Eqs. (3), (4) of the original Navier–Stokes equations system at $r=0$. These can be seen in the following.

First, we rearrange Eqs. (18), (19) for $V_r^{(n)}(\theta)$, $V_\theta^{(n)}(\theta)$ as

$$\begin{bmatrix}3D^2+4(n^2-1) & (n-7)D\\ (n+7)D & 4D^2+3(n^2-1)\end{bmatrix}\begin{bmatrix}V_r^{(n)}\\ V_\theta^{(n)}\end{bmatrix}=3\begin{bmatrix}Y_1^{(n-1)}\\ Y_2^{(n-1)}\end{bmatrix}, \tag{22}$$

which is reduced to,

$$\Delta^{(n)}\begin{bmatrix}V_r^{(n)}\\ V_\theta^{(n)}\end{bmatrix}=3\begin{bmatrix}\Delta_1^{(n-1)}\\ \Delta_2^{(n-1)}\end{bmatrix},$$

where

$$\begin{aligned}\Delta^{(n)}&=\begin{vmatrix}3D^2+4(n^2-1) & (n-7)D\\ (n+7)D & 4D^2+3(n^2-1)\end{vmatrix}=12\big[D^2+(n+1)^2\big]\\ &\quad\big[D^2+(n-1)^2\big]\\ \Delta_1^{(n-1)}&=\begin{vmatrix}Y_1^{(n-1)} & (n-7)D\\ Y_2^{(n-1)} & 4D^2+3(n^2-1)\end{vmatrix}=\big[4D^2+3(n^2-1)\big]Y_1^{(n-1)},\\ &\quad-(n-7)DY_2^{(n-1)}\\ \Delta_2^{(n-1)}&=\begin{vmatrix}3D^2+4(n^2-1) & Y_1^{(n-1)}\\ (n+7)D & Y_2^{(n-1)}\end{vmatrix}=-(n+7)DY_1^{(n-1)}\\ &\quad+\big[3D^2+4(n^2-1)\big]Y_2^{(n-1)}\end{aligned}$$

from which we can have the solutions $V_r^{(n)}$, $V_\theta^{(n)}$. Since $\Delta^{(0)}$ and $\Delta^{(1)}$ are of singular nature with double roots unlike the case with $n > 1$, these two cases for $n = 0$ and 1 are exceptional and we have to deal them separately.

For $n = 0$, from Eqs. (18), (19),

$$Y_1^{(-1)} = Y_2^{(-1)} = 0,$$

and

$$\Delta^{(0)} = 12(D^2 + 1)^2,\ \Delta_1^{(-1)} = \Delta_2^{(-1)} = 0,$$

we therefore have

$$\begin{aligned} V_r^{(0)} &= -A^{(0)}\cos\big(\theta + \alpha^{(0)}\big) - B^{(0)}\big[(1/7)\sin\big(\theta + \beta^{(0)}\big) + \theta\cos\big(\theta + \beta^{(0)}\big)\big], \\ V_\theta^{(0)} &= A^{(0)}\sin\big(\theta + \alpha^{(0)}\big) + B^{(0)}\theta\sin\big(\theta + \beta^{(0)}\big), \end{aligned} \tag{23}$$

where $A^{(0)}$, $B^{(0)}$, $\alpha^{(0)}$, $\beta^{(0)}$ are integration constants.

From Eq. (17), we have the differential equation for $\rho^{(0)}$,

$$V_\theta^{(0)} D\rho^{(0)} + \rho^{(0)}[V_r^{(0)} + DV_\theta^{(0)}] = 0.$$

By substituting Eq. (23), we have the simple differential equation for $\rho^{(0)}$

$$\frac{\rho^{(0)\prime}}{\rho^{(0)}} = -\frac{6}{7}\frac{B^{(0)}\sin\big(\theta + \beta^{(0)}\big)}{A^{(0)}\sin\big(\theta + \alpha^{(0)}\big) + B^{(0)}\theta\sin\big(\theta + \beta^{(0)}\big)}, \tag{24}$$

from which the solution is given by

$$\rho^{(0)} = C^{(0)}\exp\left[-\frac{6}{7}\int^{\theta}\frac{B^{(0)}\sin\big(\theta + \beta^{(0)}\big)}{A^{(0)}\sin\big(\theta + \alpha^{(0)}\big) + B^{(0)}\theta\sin\big(\theta + \beta^{(0)}\big)}d\theta\right], \tag{25}$$

where $C^{(0)}$ is an integration constant. The equation for the temperature $T^{(0)}$ is derived from Eq. (20) for $n = 0$.

Since $Z^{(-1)} = 0$, we have

$$\begin{aligned} T^{(0)\prime\prime} = -\Phi^{(0)} &= -\sigma(\gamma - 1)\left[2/3\left(V_\theta^{(0)\prime} + V_r^{(0)}\right)^2\right] + \left[\left(V_r^{(0)\prime} + V_\theta^{(0)}\right)^2\right] \\ &= -\sigma(\gamma - 1)\frac{8}{49}B^{(0)^2}\big[7 + \cos\ 2\big(\theta + \beta^{(0)}\big)\big]. \end{aligned}$$

Thus we easily have the solution for $T^{(0)}$ as,

$$T^{(0)} = -\frac{4}{49}\sigma(\gamma - 1)B^{(0)2}\left[7\theta^2 - \frac{1}{2}\cos 2(\theta + \beta^{(0)})\right] + D^{(0)}\theta + E^{(0)}, \tag{26}$$

where $D^{(0)}$ and $E^{(0)}$ are integration constants, and from Eq. (21) $p^{(0)}$ is given by

$$p^{(0)} = \rho^{(0)}T^{(0)}. \tag{27}$$

For $n = 1$, the following relations hold.

$$\begin{aligned}
&Y_1^{(0)} = \rho^{(0)}V_\theta^{(0)}\left(DV_r^{(0)} - V_\theta^{(0)}\right),\\
&Y_2^{(0)} = \rho^{(0)}V_\theta^{(0)}\left(DV_\theta^{(0)} + V_r^{(0)}\right) + \frac{1}{\gamma}Dp^{(0)},\\
&\Delta^{(1)} = 12(D^2 + 4)D^2,\ \Delta_1^{(0)} = 4D^2Y_1^{(0)} + 6DY_2^{(0)},\ \ \Delta_2^{(0)} = -8DY_1^{(0)} + 3D^2Y_2^{(0)}.
\end{aligned} \tag{28}$$

Then we have $Y_1^{(0)}$ and $Y_2^{(0)}$ as functions of, θ and so $\Delta_1^{(0)}$ and $\Delta_2^{(0)}$ are determined. Thus we have,

$$\begin{aligned}
V_r^{(1)} &= A^{(1)}\cos 2(\theta + \alpha^{(1)}) + B_1^{(1)} + 3\Delta_1^{(0)}/\Delta^{(1)},\\
V_\theta^{(1)} &= -A^{(1)}\sin 2(\theta + \alpha^{(1)}) + B_2^{(1)} + 3\Delta_2^{(0)}/\Delta^{(1)}.
\end{aligned} \tag{29}$$

For $n > 1$, we have generally from Eq. (22),

$$\begin{aligned}
V_r^{(n)} &= -A^{(n)}\cos(n+1)(\theta + \alpha^{(n)}) - \frac{n-1}{n+1}B^{(n)}\cos(n-1)(\theta + \beta^{(n)})\\
&\quad + 3\Delta_1^{(n-1)}/\Delta^{(n)},\\
V_\theta^{(n)} &= A^{(n)}\sin(n+1)(\theta + \alpha^{(n)}) + B^{(n)}\sin(n-1)(\theta + \beta^{(n)}) + 3\Delta_2^{(n-1)}/\Delta^{(n)},
\end{aligned} \tag{30}$$

where $A^{(n)}$, $B^{(n)}$, $\alpha^{(n)}$, $\beta^{(n)}$ ($n = 0, 1, 2, \ldots$) are integration constants. $3\Delta_1^{(n-1)}/\Delta^{(n)}$ and $3\Delta_2^{(n-1)}/\Delta^{(n)}$ are the particular solutions of inhomogeneous equation Eq. (22), formally given as

$$\begin{aligned}
3\frac{\Delta_1^{(n-1)}}{\Delta^{(n)}} &= \frac{1}{16n}\int\Big\{(n+7)\big[\sin(n+1)\big(\theta - \theta'\big) - (n-7)\sin(n-1)\big(\theta - \theta'\big)\big]Y_1^{(n-1)}\big(\theta'\big)\\
&\quad + \big[(n-7)\cos(n+1)\big(\theta - \theta'\big) - \cos(n-1)\big(\theta - \theta'\big)\big]Y_2^{(n-1)}\big(\theta'\big)\Big\}d\theta'.\\
3\frac{\Delta_2^{(n-1)}}{\Delta^{(n)}} &= \frac{1}{16n}\int\Big\{(n+7)\big[\cos(n+1)\big(\theta - \theta'\big) - \cos(n-1)\big(\theta - \theta'\big)\big]Y_1^{(n-1)}\big(\theta'\big)\\
&\quad + \big[(n+7)\sin(n-1)\big(\theta - \theta'\big) - (n-7)\sin(n+1)\big(\theta - \theta'\big)\big]Y_2^{(n-1)}\big(\theta'\big)\Big\}d\theta'.
\end{aligned}$$

Unlike the velocity components $V_r^{(n)}$ and $V_\theta^{(n)}$, other variables $\rho^{(n)}$, $p^{(n)}$, $T^{(n)}$ are all systematically dealt for $n \geq 1$. We have from Eq. (17),

$$V_\theta^{(0)}\rho^{(n)'} + \rho^{(n)}[(n+1)V_r^{(0)} + V_\theta^{(0)'}] = X^{(n-1)}. \tag{31}$$

Since $V_\theta^{(0)}$, $V_r^{(0)}$ are known from Eq. (23) and $X^{(n\text{–}1)}$ is supposed to be known from preceding functions of the (n–1)-th order terms ($X^{(-1)} = 0$), we can solve it to have,

$$\rho^{(n)} = e^{-W_n}\left[\int_\theta e^{W_n} X^{(n-1)}/V_\theta^{(0)} d\theta' + C^{(n)}\right], \tag{32}$$

where functions W_n ($n = 0, 1, 2, \ldots$) are integrating factors given by

$$W_n \equiv \int \frac{(n+1)V_r^{(0)} + DV_\theta^{(0)}}{V_\theta^{(0)}} d\theta',$$

and $C^{(n)}$ ($n = 0, 1, 2, \ldots$) are integration constants.

To obtain the temperature, we use Eq. (20) and we have $T^{(n)}$ and $p^{(n)}$ for $n \geq 1$:

$$T^{(n)} = F^{(n)} \sin n(\theta + \gamma^{(n)}) + \frac{1}{D^2 + n^2}\left(-\Phi^{(n)} + Z^{(n-1)}\right) \tag{33}$$

$$p^{(n)} = \sum_{i=0}^{n} \rho^{(i)} T^{(n-i)} \tag{34}$$

where $F^{(n)}$, $\gamma^{(n)}$ ($n = 0, 1, 2, \ldots$) are integration constants.

5 The Zeroth-Order Solution and Its Use for the Determination of Shock Angles in Mach Reflection

Here we consider to utilize the zeroth order solution to the problem of determining the shock angles in Mach reflection whose configuration is illustrated in Fig. 1a, b. Incident, reflected, and Mach stem shock waves are respectively represented by I, R and m. The incident shock angle ω is defined by the angle made by the incident shock and the incoming flow direction (the x-axis). The shock anglesλ, ω' are respectively those between the direction of the incoming flow and the tangents of reflected shock R and Mach stem m at their intersection point $r = 0$. Here we express these shock curves in (r, θ) coordinates:

$\theta = \theta_{1,2}(r)$ respectively for m and R, and expand these as

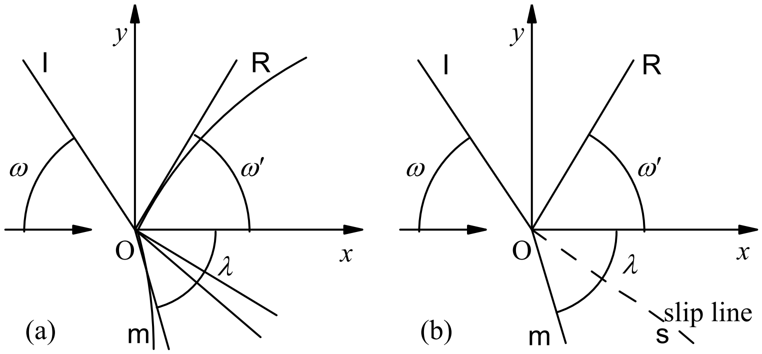

Fig. 1 **a** Configuration of Mach reflection. **b** Three-shock theory model

$\theta_{1,2}^{(n)} = \sum_{n=0}^{\infty} r^n \theta_{1,2}^{(n)}$ where
$\theta_{1,2}^{(n)} = (\partial^n \theta / \partial r^n) r = 0$, especially,
$\theta_1^{(0)} = -\lambda$,
$\theta_2^{(0)} = \omega$ to which we utilize the above zeroth order solution, while higher terms of $n > 0$ are related with the bending of shock lines determined successively by the higher order solutions.

This problem is related to resolve the ‘von Neumann paradox’ [1], which is explained symbolically in Fig. 2, where the ω' versus ω curves plotted in the reproduction of famous diagram by Harrison and Bleakney [6] given in Bleakney and Taub [3] are compared with the theoretical curves resulting from the three-shock theory by von Neumann [2]. Figure 2a is for the strong wave case of its inverse pressure ratio $\xi = 0.2$, while Fig. 2b is the weak case of $\xi = 0.9$. We can see that these curves agree well with experimental data in weak shock cases, whereas very poor agreement in stronger cases, which displays a paradoxical feature.

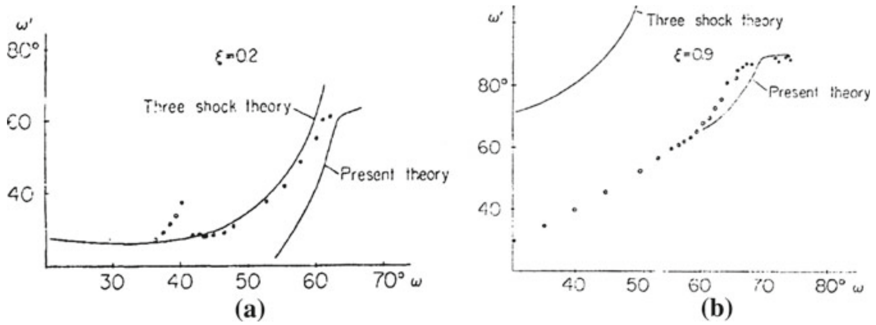

Fig. 2 ω' versus ω curves. **a** $\xi = 0.2$ (strong case). **b** $\xi = 0.9$ (weak case) compared with Harrison and Bleakney’s data [6]

There have been many contributions to resolve this situation, so many to refer only a few [4, 7–12] from its representatives. Most of these propose the postulation of inserting fan-like flow in the frame of original three-shock theory to result the resolution of the paradox. While these are essentially based on the perfect gas flow theory, some [4, 7, 9] consider it in viscous flow or kinetic model to have results consistent with experimental data. In the followings we show that the present zeroth order solution itself is a fan-like flow and its use is in fact the same as the one in viscous flow model. This fact can give a justification to the postulation of inserting fan-like flow proposed in most of these literatures above.

We are concerned here with the flow field between two shock waves R and m shown in Fig. 1, which is supposed to be almost uniform and parallel. So that the velocity component $V_\theta^{(0)}$ in Eq. (23) must vanish at a certain value of θ in between ($-\lambda$, ω') while the density gradient $\rho^{(0)'}$ must remain finite. This means that the numerator and the denominator of right-hand-side of Eq. (24) must vanish for the same value of θ (say, θ_0), thus we have $\alpha^{(0)} = \beta^{(0)}$. Then we have

$$\begin{aligned} V_r^{(0)} &= -\left(A^{(0)} + B^{(0)}\theta\right)\cos\left(\theta + \alpha^{(0)}\right) - B^{(0)}\left[(1/7)\sin\left(\theta + \alpha^{(0)}\right)\right], \\ V_\theta^{(0)} &= \left(A^{(0)} + B^{(0)}\theta\right)\sin\left(\theta + \alpha^{(0)}\right). \end{aligned} \tag{35}$$

For convenience, here the above relation is expressed in complex form $\boldsymbol{V}^{(0)} = V_r^{(0)} + iV_\theta^{(0)}$, then we have

$$\boldsymbol{V}^{(0)} = -A^{(0)}(1 + k\theta)e^{-i(\theta+\alpha^{(0)})} - B^{(0)}[(1/7)\sin(\theta + \alpha^{(0)})] \tag{36}$$

with

$$k = B^{(0)}/A^{(0)}.$$

Equation (25) for the density $\rho^{(0)}$ can now be integrated to give

$$\rho^{(0)} = c^{(0)}\exp\left[-\frac{6}{7}\int^\theta \frac{B^{(0)}}{A^{(0)} + B^{(0)}\theta}d\theta\right] = c^{(0)}\left(A^{(0)} + B^{(0)}\theta\right)^{-6/7} \tag{37}$$

and the temperature $T^{(0)}$ is given by Eq. (26).

These integration constants: $A^{(0)}$, $B^{(0)}$, $C^{(0)}$, $D^{(0)}$, $E^{(0)}$, and so far undetermined angles (ω',λ) and $\alpha^{(0)}$ altogether eight unknowns are determined by eight boundary conditions given by the shock wave values at $\theta = -\lambda$ for Mach stem shock m and at $\theta = \omega'$ for reflected shock R:

$$\boldsymbol{V}_{1,2} = (\ \boldsymbol{V}^{(0)})_{\theta=-\lambda,\omega'}, \quad \rho_{1,2},\ p_{1,2} = (\rho^{(0)},\ p^{(0)})_{\theta=-\lambda,\omega'} \tag{38}$$

where $\boldsymbol{V}_1 = (V_{1r}, V_{1\theta})$, $\boldsymbol{V}_2 = (V_{2r}, V_{2\theta})$ are respectively the velocities behind shock waves m and R with their r and θ components V_{1r}, $V_{1\theta}$; V_{2r}, $V_{2\theta}$ and their density and pressure values ρ_1, ρ_2; p_1, p_2. These shock values are given from the Rankine-Hugoniot conditions at R and m depending on the shock angles (ω',λ).

Now original three-shock theory [2] models the flow as illustrated in in Fig. 1b by two uniform flows $\boldsymbol{V}_1$, $\boldsymbol{V}_2$ separated by a slip flow line s in setting,

$$\theta_2 - \theta_1 = 0, \tag{39}$$

where θ_1, θ_2 are respectively the direction angles of $\boldsymbol{V}_1$, $\boldsymbol{V}_2$ from the x-axis (the incoming flow direction). Since this simple model caused the paradox, many authors [8, 10–13] proposed an alternative use of a fan-like flow in place of the slip flow line to resolve the 'paradox'. Here note that the flow represented by Eq. (35) above is a fan-like source flow from point O in (x, y)-plane and, in fact, we are utilizing it for the condition at the intersection point $r = 0$. Also it must be noted that the three-shock theory is in fact based on Euler's equation of perfect gas flow and uniform flow accompanied by the slip-flow is the natural and only solution of the Euler's equation to the three-shock model. On the other hand, the present fan-like flow setting is based on a solution of the Navier–Stokes equation which is consistent with the use of the viscous flow model for the flow field behind shock waves R and m in providing a foundation for the use of fan-like flow.

Let δ_1, δ_2 be the respective angles made by the velocity vectors $\boldsymbol{V}_1$, $\boldsymbol{V}_2$ with the corresponding shock waves m, R. Then we have

$$\delta_1 + \theta_1 = \lambda, \;\; \delta_2 + \theta_2 + \omega' = \pi, \tag{40}$$

so that

$$\begin{aligned} \frac{V_{1r}}{V_{1\theta}} &= \cot\delta_1 = \cot(\lambda - \theta_1) \\ \frac{V_{2r}}{V_{2\theta}} &= \cot\delta_2 = \cot(\pi - \theta_2 - \omega') = -\cot(\theta_2 + \omega') \end{aligned}$$

From Eq. (35),

$$\frac{V_r^{(0)}}{V_\theta^{(0)}} = -\cot(\theta + \alpha^{(0)}) - \frac{1}{7}\frac{B^{(0)}}{A^{(0)} + B^{(0)}\theta}$$

and the boundary conditions:

$$\frac{V_{1r}}{V_{1\theta}} = \left(\frac{V_r^{(0)}}{V_\theta^{(0)}}\right)_{\theta=-\lambda}, \;\; \frac{V_{2r}}{V_{2\theta}} = \left(\frac{V_r^{(0)}}{V_\theta^{(0)}}\right)_{\theta=\omega'},$$

we have

$$\cot(\lambda - \theta_1) = -\cot(-\lambda + \alpha^{(0)}) - \frac{1}{7}\frac{B^{(0)}}{A^{(0)} - B^{(0)}\lambda},$$
$$-\cot(\omega' + \theta_2) = -\cot(\omega' + \alpha^{(0)}) - \frac{1}{7}\frac{B^{(0)}}{A^{(0)} + B^{(0)}\omega'},$$

or

$$\left.\begin{aligned}\sin(\alpha^{(0)} - \theta_1) &= \sin(-\lambda + \alpha^{(0)})\sin(\lambda - \theta_1)\left(-\frac{1}{7}\frac{B^{(0)}}{A^{(0)} - B^{(0)}\lambda}\right), \\ \sin(\theta_2 - \alpha^{(0)}) &= \sin(\omega' + \alpha^{(0)})\sin(\omega' + \theta_2)\left(-\frac{1}{7}\frac{B^{(0)}}{A^{(0)} + B^{(0)}\omega'}\right).\end{aligned}\right\},$$

From which we have the spread of fan-like flow $\delta\theta \equiv \theta_2 - \theta_1$ as

$$\begin{aligned}\delta\theta &= \left(\alpha^{(0)} - \theta_1\right) + \left(\theta_2 - \alpha^{(0)}\right) \\ &= \sin^{-1}\left[\frac{-B^{(0)}}{7}\frac{\sin(-\lambda + \alpha^{(0)})\sin(\lambda - \theta_1)}{A^{(0)} - B^{(0)}\lambda}\right] \\ &\quad + \sin^{-1}\left[\frac{-B^{(0)}}{7}\frac{\sin(\omega' + \alpha^{(0)})\sin(\omega' + \theta_2)}{A^{(0)} + B^{(0)}\omega'}\right]\end{aligned} \tag{41}$$

Here we can see that $B^{(0)} = 0$ provides $\delta\theta = 0$ which is the slip flow, while non-zero $B^{(0)}$ provides the fan-like flow with divergence angle $\delta\theta$. For example, when $\delta\theta = 8.7 \times 10^{-3}$ rad (0.5°) and the incident shock Mach number is 1.10, $\omega' \approx 85$ deg for $\omega = 63$ deg, which is in good agreement with the experiment [14].

Actual procedure to determine ω' and λ is found to be the same as the ones appearing in our previous papers [9, 14] and we can utilize the results given in these papers. In Fig. 2, we can see that the present-theory curve agrees well with experimental data in weak shock case, while poor agreement in stronger case, which reflects the sharp bend of the shock curve near the intersection. It is seen that the present approach actually provides a kind of justification for the postulation in using viscous gas flow instead of perfect gas.

6 Internal Structure of Triple Point

Here we utilize the solution to investigate the flow-field inside the triple point appearing in Mach reflection, which is referred as non-Rankine-Hugoniot zone [4]. This problem is usually studied [13, 15] by computing the entire Mach reflection flow-field, but there is a difficulty: We have to have finer mesh locally near the triple point to see its internal structure but it is not easy to set the area beforehand because the area moves with advancing time step, although there are some contrivances to overcome it [16]. Here our approach is analytical and we can do it in steady flow to

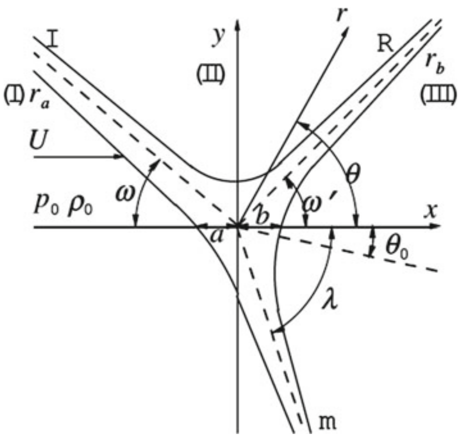

Fig. 3 Nomenclatures and boundaries of non-R-H zone

have a finite region set locally including the non-Rankine-Hugoniot zone in advance, so the scheme is free from the above difficulty.

In the followings, we first set the boundary for the non-R-H zone by two hyperbolas r_a, r_b as seen in Fig. 3 and investigate the flow field between these boundaries as the one[17, 18] for plane shock wave structure problem, which usually considers the problem in studying the solution of the Navier–Stokes equations system of one-dimensional viscous gas flow to satisfy the Rankine-Hugoniot shock condition for up- and down- stream in respective regions. Here we have to deal with a plane flow and no Rankine-Hugoniot relation is expected, so instead we use the 2D Navier–Stokes equations and use the zeroth order solution given in Sect. 5 at the downstream flow boundary r_b, while incoming uniform flow at the in-flow boundary r_a.

Setting of Boundaries

Figure 3 shows the nomenclature and the considered flow-field. The symbols I, R, and m designate the incident shock, reflected shock and Mach stem. The uniform flow U ahead of the incident shock flows parallel to the x-axis. The y-axis is defined perpendicular to the x-axis. The origin of (x, y)-coordinate system lies in the triple-point region. Since the shock thickness is finite, there is some yet harmless uncertainty in the location of the origin O. The region is divided by wave fronts into three regions (I), (II), and (III), and the edges of shock zone are approximated by hyperbolas, whose asymptotes meet the origin. Rigorously speaking, the asymptotes described here is a parallel line to the mathematical asymptote. Then we define the polar coordinate (r, θ). The edge of shock zone facing the uniform region (I) is $r = r_a(\theta)$, and that facing the region (III) is $r = r_b(\theta)$. We approximate these edges by hyperbolas whose asymptotes are parallel to the dashed line in Fig. 3. Let the three asymptotes in Fig. 3 be $\theta = \pi - \omega$, $\theta = \omega'$, and $\theta = 2\pi - \lambda$. These equations are expressed in (r,

θ)-coordinate as follows:

$$r_b : \quad r = b\left[\frac{-\sin\omega' \sin\lambda}{\sin(\theta - \omega')\sin(\theta + \lambda)}\right]^{1/2} \tag{42}$$

where a and b are the distances from the origin to the intersection of two hyperbolas with the x-axis ($a = r_a(\pi)$, $b = r_b(0)$).

Solution in Zone (II)

We use the solution given in Sect. 4 in the form of power series in r. In the present circumstances, we impose the condition that the solution must be single valued in the flow region inside the two boundaries, r_a, r_b so that we have $B^{(0)} = 0$ in Eq. (23), and thus

$$V_r^{(0)} = -A^{(0)}\cos\big(\theta + \alpha^{(0)}\big),\ \ V_\theta^{(0)} = A^{(0)}\sin\big(\theta + \alpha^{(0)}\big) \tag{43}$$

and $\rho^{(0)} = C^{(0)}$ from Eq. (25), $T^{(0)} = E^{(0)}$ from Eq. (26), and $p^{(0)} = \rho^{(0)}T^{(0)} = C^{(0)}E^{(0)}$ from Eq. (27). Making use of these, we can proceed to the second-order approximation. Since $Y_1^{(0)}$, $Y_2^{(0)} = 0$ from Eqs. (28), (43), and thus $\Delta_1^{(0)}$, $\Delta_2^{(0)} = 0$ from Eq. (28), we have

$$V_r^{(1)} = A^{(1)}\cos 2(\theta + \alpha^{(1)}) + B_1^{(1)},\ \ V_\theta^{(1)} = -A^{(1)}\sin 2(\theta + \alpha^{(1)}) + B_2^{(1)}$$

from Eq. (29). So that we have the velocity to the first order of r,

$$\begin{aligned} V_r &= V_r^{(0)} + rV_r^{(1)} = -A^{(0)}\cos\big(\theta + \alpha^{(0)}\big) + r\Big[A^{(1)}\cos 2(\theta + \alpha^{(1)}) + B_1^{(1)}\Big], \\ V_\theta &= V_\theta^{(0)} + rV_\theta^{(1)} = A^{(0)}\sin\big(\theta + \alpha^{(0)}\big) + r\Big[-A^{(1)}\sin 2(\theta + \alpha^{(1)}) + B_2^{(1)}\Big] \end{aligned} \tag{44}$$

which can be expressed in using complex velocity $\mathbf{V} = V_r + i\ V_\theta$,

$$\mathbf{V} = -\mathbf{A}^{(0)}e^{-i\theta} + r[\mathbf{A}^{(1)}e^{-2i\theta} + \mathbf{B}^{(1)}] \tag{45}$$

where we set

$$\mathbf{A}^{(0)} = A^{(0)}e^{-i\alpha^{(0)}},\ \ \mathbf{A}^{(1)} = A^{(1)}e^{-2i\alpha^{(1)}},\ \ \mathbf{B}^{(1)} = B_1^{(1)} + iB_2^{(1)}$$

The expression for $\rho^{(1)}$ can be derived from Eq. (32), where

$$W_1 = -\log\left|\sin\left(\theta + \alpha^{(0)}\right)\right|, \;\; X^{(0)} = -2C_0 B_1^{(1)}$$

Thus we have

$$\begin{aligned}\rho^{(1)} &= \sin\left(\theta + \alpha^{(0)}\right)\left[-\frac{2C_0 B_1^{(1)}}{A^{(0)}}\int \frac{d\theta}{\sin^2\left(\theta + \alpha^{(0)}\right)} + C^{(1)}\right] \\ &= \frac{2C_0 B_1^{(1)}}{A^{(0)}}\cos\left(\theta + \alpha^{(0)}\right) + C^{(1)}\sin\left(\theta + \alpha^{(0)}\right)\end{aligned}$$

Equation (33) with $\Phi^{(1)} = \mathrm{Z}^{(0)} = 0$ leads to

$$T^{(1)} = E^{(1)}\sin\left(\theta + \gamma^{(1)}\right)$$

where $E^{(1)}$ and $\gamma^{(1)}$ are the integration constants. Thus the density ρ, the pressure p, and the temperature T are expressed as

$$\begin{aligned}&\rho = \rho^{(0)} + r\rho^{(1)} = C^{(0)} + r[(2B_1^{(1)}C^{(0)}/A^{(0)})\cos(\theta + \alpha^{(0)}) + C^{(1)}\sin(\theta + \alpha^{(0)})], \\ &p = p^{(0)} + r(C^{(0)}T^{(1)} + \rho^{(1)}T^{(0)}) = C^{(0)}E^{(0)} + r(C^{(0)}T^{(1)} + \rho^{(1)}T^{(0)}), \\ &T = T^{(0)} + rT^{(1)} = E^{(0)} + rE^{(1)}\sin\left(\theta + \gamma^{(1)}\right),\end{aligned} \tag{46}$$

where $A^{(0)}, \alpha^{(0)}$; $A^{(1)}, \alpha^{(1)}$; $B_1^{(1)}$; $C^{(0)}, C^{(1)}$; $E^{(0)}, E^{(1)}, \gamma^{(1)}$ are integration constants to be determined by the boundary conditions at $r = r_a$, and $r = r_b$. To this, we express the uniform velocity to the zone (I) in a complex form:

$$\mathbf{V} = V_r + iV_\theta = Me^{-i\theta}, \;\; M \equiv U/C_0 \tag{47}$$

so that, along the parabola $r = r_a$, we have from Eqs. (45) to (47)

$$-\mathbf{A}^{(0)}e^{-i\theta} + r_a(\theta)[\mathbf{A}^{(1)}e^{-2i\theta} + \mathbf{B}^{(1)}] = Me^{-i\theta} \tag{48}$$

For the condition on the parabola $r = r_b$, we utilize the fan-like flow given by the solution (35) of Sect. 5 with its integration constants and angles λ, ω' determined to have, along $r = r_b$,

$$\begin{aligned}&-\mathsf{A}^{(0)}e^{-i\theta} + r_b(\theta)[\mathsf{A}^{(1)}e^{-2i\theta} + \mathsf{B}^{(1)}] = -(A^{(0)} + B^{(0)}\theta)e^{-i(\theta+\alpha^{(0)})} - B^{(0)}(1/7)\sin(\theta + \alpha^{(0)}) \equiv \breve{\mathsf{V}} \\ &\rho^{(0)} + r_b(\theta)\rho^{(1)} = \breve{C}^{(0)}(\breve{A}^{(0)} + \breve{B}^{(0)}\theta)^{-6/7} \equiv \breve{\rho}, \\ &p^{(0)} + r_a(\theta)p^{(1)} = \rho^{(0)}\{-4\sigma/49(\gamma-1)[7\theta^2 - (1/2)\cos(\theta + \alpha^{(0)})]B^{(0)^2} + D^{(0)}\theta + E^{(0)}\} \equiv \breve{p}\end{aligned} \tag{49}$$

Notice that the boundary value $(\breve{\mathbf{V}}, \breve{\rho}, \breve{p})$set on the parabola $r = r_b$, which is apart from the shock lines $\theta = -\lambda$, ω', corresponds to the situation in the plane shock wave structure problem in which boundaries are set apart the shock front.

Now obviously we cannot have any solution to satisfy Eqs. (48), (49) above completely, so we seek an approximate solution. Here we consider it for a small region near the origin of non-R-H zone. So we put, $\theta = \pi + \varphi$ in Eq. (48) and $\theta = -\alpha^{(0)} + \tilde{\phi}$, in Eq. (49), and expand these equations respectively in φ and $\tilde{\phi}$, to have from their expansion coefficients for the velocity,

$$\mathbf{A}^{(0)} + a(\mathbf{A}^{(1)} + \mathbf{B}^{(1)}) = -M$$

$$-i\mathbf{A}^{(0)} + s(\mathbf{A}^{(1)} + \mathbf{B}^{(1)}) - 2ia\mathbf{A}^{(1)} = iM$$

$$-\mathbf{A}^{(0)} e^{i\alpha^{(0)}} + \hat{r}_b(\mathbf{A}^{(1)} e^{2i\alpha^{(0)}} + \mathbf{B}^{(1)}) = (\breve{\mathbf{V}})_{r=r_b, \theta=-\alpha^{(0)}} = -A^{(0)}(1 - k\alpha^{(0)})$$

where we put $r_a'(\pi) = s$, $\quad r_b(-\alpha^{(0)}) = \hat{r}_b$. From these above we can determine $\mathbf{A}^{(0)}$, $\mathbf{A}^{(1)}$, $\mathbf{B}^{(1)}$ as,

$$\mathbf{A}^{(0)} = -a\frac{\overset{\rightharpoonup}{z} - z}{\Delta} S - M, \quad \mathbf{A}^{(1)} = -\frac{z}{\Delta} S, \quad \mathbf{B}^{(1)} = \frac{\bar{z}}{\Delta} S, \tag{50}$$

where

$$z = s + ia; \quad w = a + \hat{r}_b e^{i\alpha^{(0)}}; \quad \Delta = \overline{zw} - zw; \quad S = -M - A^{(0)}(1 - k\alpha^{(0)})e^{-i\alpha^{(0)}}$$

In the same manner, we can determine the constants $C^{(0)}$, $C^{(1)}$ for ρ, and $E^{(0)}$, $E^{(1)}$, $\gamma^{(1)}$ for p, T. For example $C^{(0)}$, $C^{(1)}$ for the density ρ are determined from equations given by conditions (48), (49) for ρ at $\phi = \tilde{\phi} = 0$.

Streamline and Density Distribution Along It

Streamline

Let $r = r\ (\theta, \theta_a)$ be a streamline through a point $r(\theta_a)$ on r_a, then

$$\frac{1}{r}\frac{dr}{d\theta} = \frac{V_r}{V_\theta} \text{ with } r = r(\theta_a, \theta_a) = r_a(\theta_a) \tag{51}$$

Here we use $V_r = V_r^{(0)} + rV_r^{(1)}$, $\quad V_\theta = V_\theta^{(0)} + r\ V_\theta^{(1)}$, and expand the right-hand-side term in the power of r to have an approximation and use Eq. (44) to have:

$$\begin{aligned}\frac{1}{r}\frac{dr}{d\theta} &= \left(\frac{V_r}{V_\theta}\right)_{r=0} + r\left[\frac{\partial}{\partial r}\left(\frac{V_r}{V_\theta}\right)\right]_{r=0} = \frac{V_r^{(0)}}{V_\theta^{(0)}} + r\frac{(V_r^{(1)}V_\theta^{(0)} - V_\theta^{(1)}V_r^{(0)}}{V_\theta^{(0)^2}} \\ &= -\cot\varphi + r\frac{L_1\sin\varphi + L_2\cos\varphi}{A^{(0)}\sin^2\varphi}\end{aligned} \tag{52}$$

where

$\phi = \theta + \alpha^{(0)}$, $L_1 = A^{(1)}\cos 2(\alpha^{(1)} - \alpha^{(0)}) + B_1^{(1)}$, $L_2 = A^{(1)}\sin 2(\alpha^{(1)} - \alpha^{(0)}) + B_2^{(1)}$.

By putting $r\sin\varphi = z$, Eq. (52) is transformed as

$$\frac{1}{z^2}\frac{dz}{d\phi} = \frac{1}{A^{(0)}}\left(L_1\frac{1}{\sin^2\phi} + L_2\frac{\cos\phi}{\sin^3\phi}\right)$$

which is integrated to have,

$$-\left[\frac{1}{z}\right]_{z_a}^{z} = \frac{1}{A^{(0)}}\left[-L_1\cot\phi - \frac{1}{2}\frac{1}{\sin^2\phi}\right]_{\phi_a}^{\phi}$$

where z_a and φ_a correspond to boundary condition $r = r_a\ (\theta_a)$, $\theta = \theta_a$. Eventually, the streamline is expressed as the following equation.

$$\frac{1}{r\sin(\theta + \alpha^{(0)})} = \frac{1}{r_a\sin(\theta_a + \alpha^{(0)})} + K(\theta) \tag{53}$$

with

$$K(\theta) \equiv \frac{1}{A^{(0)}}\left[L_1(\cot\phi - \cot\phi_a) + \frac{1}{2}L_2\left(\frac{1}{\sin^2\phi} - \frac{1}{\sin^2\phi_a}\right)\right] \tag{54}$$

where

$\phi_a = \theta_a + \alpha^{(0)}$.

We can see in Eq. (53) that without the $K(\theta)$ term this represents a straight line $r\sin\left(\theta + \alpha^{(0)}\right) = \text{const.}$, so that we have a uniform flow in the direction of $\theta = -\alpha^{(0)}$ in this case. Thus non-zero $K(\theta)$ term contributes to make a distortion from the straight line. This feature of the curve in use of $\mathbf{A}^{(0)}$, $\mathbf{A}^{(1)}$, $\mathbf{B}^{(1)}$ values given in Eq. (50) is illustrated in Fig. 4a. Comparison with the result based on the Boltzmann-BGK equation is also shown in Fig. 4b. Note that the present result shows very narrow region around the triple point.

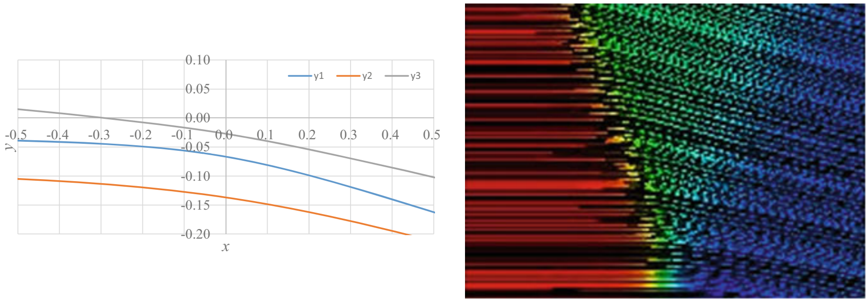

(a) **(b)**

Fig. 4 Results for stream line by **a** the present analysis, **b** the numerical calculation on the basis of Boltzmann-BGK equation [7]

Density Distribution

We have the density distribution in Eq. (46)

$$\rho = C^{(0)} + r[(2B_1^{(1)}C^{(0)}/A^{(0)})\cos(\theta+\alpha^{(0)}) + C^{(1)}\sin(\theta+\alpha^{(0)})] \tag{46}$$

This can be expressed simply in (x_γ, y_γ)-coordinate system which is a $\alpha^{(0)}$-rotated system from the original one in Fig. 1, and given as.

$x_\gamma = r\cos\phi,\ y_\gamma = r\sin\phi,\quad \phi = \theta + \alpha^{(0)}$.

Thus we have

$$\rho = C^{(0)}\Big[1 + \Big(2B_1^{(1)}/A^{(0)}\Big)x_\gamma + \big(C^{(1)}/C^{(0)}\big)y_\gamma\big)\Big] \tag{55}$$

So it represents a straight line in (x_γ, y_γ)-coordinates in the present approximation, while its distribution along a streamline through a point $r(\theta_a)$ on r_a, is expressed in using Eqs. (49), (53) as,

$$\rho = C^{(0)}\Big[1 + r(\theta, \theta_a)(2B_1^{(1)}/A^{(0)})(\cos\varphi + C'\sin\varphi)\Big],$$

where $C' = A^{(0)}C^{(1)}/\Big(2B_1^{(1)}C^{(0)}\Big)$. This expression provides the changing feature of the density along the streamline s in showing that its main change is sinusoidal with a distortion by the factor $r(\theta, \theta_a)$ as shown schematically [18] in Fig. 5a. It is compared also with the one in Fig. 5b which is given numerically by the Boltzmann-BGK equation [7, 17]. These density lines start from the same density of incoming uniform flow, and become different after passing through shock wave(s) on different streamlines. It looks similar to the one for one-dimensional flow in a finite region.

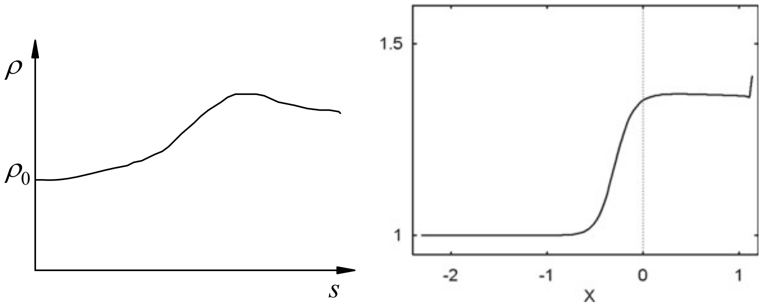

(a) (b)

Fig.5 **a** Schematic diagram of density distribution along a streamline, **b** numerical results [18] for number density distribution by the Boltzmann-BGK equation on $y = -1$

7 Concluding Remarks

We constructed a general solution of the 2D Navier–Stokes equations in cylindrical coordinates (r, θ)-system in the form of r-power expansion whose coefficients are functions of θ only, and we showed these functions are determined successively starting from the solution of the original equations along the line $r = 0$ in (r, θ)-plane.

It turned out that this zeroth order solution itself is found to represent a fan-like flow from an origin in ordinary (x, y)-plane and use of this solution for the determination of shock angles of Mach reflection is effectively equivalent to the current widely accepted proposal of replacing the slip flow line in the original three-shock theory by a fan-like flow for the solution of the "von Neumann paradox". As a result, present approach actually provides a kind of justification for the postulation in using viscous gas instead of perfect gas.

The solution was utilized to study the internal structure of the triple point. It is concerned with the flow in the non-Rankine-Hugoniot zone, to which we set two bounding hyperbola as seen in Fig. 3 and used the solution there in conformity with boundary conditions along bounding hyperbola as the incoming flow along front curve and the fan-like flow given by the zeroth-order solution at the rear. The last condition corresponds to the use of Rankine-Hugoniot condition to the plane shock structure case.

Since we can study the flow directly in the zone which can be set in advance and the present approach has an advantage in that we are free from the difficulty of making ever finer mesh to the zone moving with advancing time steps as the case in the conventional approach of computing entire flow field.

Use of the solution to this problem was found to be effective to have reasonable result even with an approximation of only a few terms of the expansion in comparison with numerical result [7] of the corresponding one by the Boltzmann-BGK equation.

References

1. Birkhoff G (1950) Hydrodynamics: a study in logic and similitude, 1edn. Princeton UP, Princeton, p 24
2. Bleakney W, Taub AH (1949) Rev Mod Phys 21:584
3. von Neumann J (1963) Collected works, vol 6. Pergamon, New York, p 238
4. Sternberg J (1959) Phys Fluids 2:179
5. Chen H, Zhang B, Liu H (2016) J Spacecraft Rockets 53:619
6. Harrison FB, Bleakney W (1947) ONR report, N6ori-105, Task II
7. Sakurai A, Kobayashi S, Tsukamoto M (2018) 23rd International Shock Interaction Symposium, Kruger National Park. South Africa, p 43
8. Courant R, Friedrichs KO (1948) Supersonic flow and shock waves. Interscience, New York, p 345
9. Sakurai A (1964) J Phys Soc Jpn 19:1440
10. Guderley KG (1953) Headquarters air material command Technical Report F-TR-2168-ND
11. Skews BW (1971) C.A.S.I. Transactions 4:99
12. Ben-Dor G (2008) Shock wave reflection phenomena, 2nd edn. Springer-Verlag, New York, p 205
13. Ivanov MS, Bondar YA, Khotyanovsky DV, Kudryavtsev AN, Shoev GV (2010) Prog Aerosp Sci 46:89
14. Kobayashi S, Adachi T, Suzuki T (1995) Fluid Dyn Res 17:13
15. Tesdall AM, Sanders R, Keyfitz L (2008) SIAM J Appl Math 68:1360
16. Lau-Chapdelaine SSM, Radulescu MI (2016) Shock Waves 26:551
17. Sakurai A, Tsukamoto M, Khotyanovsky D, Ivanov M (2011) Shock Waves 21:267
18. Sakurai A, Tsukamoto M, Kobayashi S (2017) On a problem of shock wave structure. In: Symposium on shock waves in Japan, 1C1–3

Akira Sakurai born in 1921. Graduated from Tokyo University, Dept. Physics, B. Sc. in 1944. Tokyo Denki University, 1948–1991. D. Sc. (Tokyo Univ.) in 1955. Professor Emertius 1991.

Susumu Kobayashi born in 1957. Graduated from Tokyo University, Dept. Aeronautics Astronautics, B. Engng. in 1979. Graduated from Graduate School of Engng, Tokyo Univ., D. Engng. in1984. Kanazawa Inst. Tech., 1984–1987. Saitama Inst. Tech., 1987–2022.